Proceedings : 4. ISUD

Fourth International Symposium on Ultrasonic Doppler Method for Fluid Mechanics and Fluid Engineering

Fourth   International Symposium
on Ultrasonic Doppler Methods
for Fluid Mechanics and Fluid Engineering
(4th ISUD)

6.- 8. September, 2004
Hokkaido University
Sapporo, Japan

Scientific Committee

Prof. M. Aritomi   (Tokyo Inst. Tech., Fluid Engineering/Nuclear)
Prof. E.Windhab   (ETHZ, Fluid Eng./Non-Newtonian)
Dr. G. King   Warwick Univ., Physics
Dr. G. De Cesare   (EPFL, Environmental)
Dr. M. Mori   (TEPCO, Industrial Applications)
Dr. Y Takeda   (Hokkaido Univ., Fluid Engineering/Mechanics)
Dr. A. Tokuhiro   (Univ. of Missouri, Nuclear)

Organizing Committee

Y. Takeda   (Hokkaido Univ.)
Y. Murai   (Hokkaido Univ.)
H. Kikura   (TIT)
N. Furuichi   (Gifu Univ.)

Fourth International Symposium

on Ultrasonic Doppler Methods

for Fluid Mechanics and Fluid Engineering

Timetable

		6. (Mon)	7.(Tue)	8.(Wed)
8:30	8:55	Registration	**Session 5**	**Session 8**
8:55	9:20		Industrial flow	Methodology
9:20	9:45	Opening	(4)	( )
9:45	10:10	Plenary lecture		
10:10	10:35		Break	
10:35	10:50	Break	10:30 12:15	Break
10:50	11:15	**Session 2**	Special session	**Session 9**
11:15	11:40	Fundamental		Fundamental
11:40	12:05	flow 1	Flow metering –	flow 2
12:05	12:30	(4)	present and future	(4)
12:30		Lunch	Lunch	Lunch
	13:30			
13:30	13:55	**Session 3**	**Session 7**	**Session 10**
13:55	14:20	Flow metering 1	Flow metering 2	Fundamental flow 3
14:20	14:45	(4)	(3)	(4)
14:45	15:10			Adjourn
15:10	15:40	Break	Group Photograph	
15:40	16:05	**Session 4**	Excursion &	
16:05	16:30	Environmental	Met-Flow Dinner	
16:30	16:55	Flow		
16:55	17:20	(5)		
17 20	17 45			

<u>Tentative Program</u>

6.9.2004

Time	
08: 30-09: 20	Registration
09: 20-09: 45	Opening
09: 45-10: 35	**Plenary lecture:** High Rayleigh number thermal convection: An overview and a new approach by ultrasonic measurements M. Sano Tokyo Univ.
10: 35-10: 50	Coffee Break
10: 50-12: 30	Session 2 : **Fundamental flow 1**
10: 50-11: 15	Study of vortex ring dynamics using UVP Y. Murai, H. Kitaura, Z. Xiao, P.J. Thomas, Y. Takeda Hokkaido Univ.
11: 15-11: 40	Observations of particle dispersion extracted from the UVP ultrasound signal G.P. King, N. Furuichi, Y Takeda Warwick Univ.
11: 40-12: 05	Experiments in an initial region of a circular free jet Y. Inoue, S. Yamashita, K. Kondo Gifu Univ.
12: 05-12: 30	UVP measurement on Taylor-Couette flow of magnetic fluids with small aspect ratio H. Kikura, S. Kishikawa, D. Ito, M. Aritomi, Y. Takeda TIT
12: 30-13: 30	Lunch Time
13: 30-15: 10	Session 3 : **Flow metering 1**
13: 30-13: 55	Industrial applications of new type flow-metering system by Ultrasonic-Doppler Profile-Velocimetry (1) Effects of surface roughness and asymmetric pipe flow on accuracy of profile factor K. Tezuka, M. Mori, Y. Takeda, M. Aritomi, H. Kikura TEPCO
13: 55-14: 20	Industrial applications of new type flow-metering system by Ultrasonic-Doppler Profile-Velocimetry (2) Measurement experiences of flow on piping and industrial applications M. Mori, K. Tezuka, M. Aritomi, H. Kikura, Y. Takeda TEPCO
14: 20-14: 45	Development of flow rate measurement on open channel flow using Ultrasonic Doppler Method . Arimatsu, S. Wada, H. Kikura, M. Aritomi, M. Mori TIT
15: 45-15: 10	Characteristics of sound pressure distribution on Ultrasonic Doppler Method S. Wada, H. Kikura, Y. Koike, M. Aritomi, M. Mori TIT
15: 10-15: 40	Coffee Break
15: 40-17: 20	Session 4 : **Environmental flow**
15: 40-16: 05	Application of UVP transducers to measure bed geometry and velocity profiles in a hydraulic scale model with gravel pit . Nilipour, G. De Cesare, J.-L. Boillat LCH, ENAC, EPFL
16: 05-16: 30	Flow measurement in an open channel by UVP K. Yokoyama, N. Kashiwaguma, T. Okubo, Y. Takeda Hokkaido Univ.
16: 30-16: 55	Determination of Velocity profiles and bed morphology using UVP transducers to investigate the influence of lateral overflow on mobile bed B. Rosier, F. Jordan, G. De Cesare, J.-L. Boillat, A. Schleiss LCH, ENAC, EPFL
16: 55-17: 20	Vector measurement of environmental flow field by UVP T. Ohkubo, N. Kashiwaguma, K. Yokoyama, Y. Takeda, K. Ouchi Hokkaido Univ.
17: 20-17: 45	Ultrasonic measurements in ice slurry generation by direct contact evaporation D. Vuarnoz, D. Ata-Caesar, O. Sari, P.W. Egolf, ITSL

7.9.2004

Time	
08:30-10:10	**Session 5 : Industrial flow**
08:30-08:55	An industrial process control concept for microstructure-rheology related food product characteristics based on in-line ultrasound-Doppler and ultrasound attenuation measurements E. J. Windhab, J. Shaik, B.Birkhofer B. Ouriev ETHZ
08:55-09:20	In-line characterization and rheometry of concentrated suspensions using ultrasound B. Birkhofer, S.A.K. Jeelani, B. Ouriev, E.J. Windhab ETHZ
09:20-09:45	A comparative study between UVP and LDA techniques for highly concentrated pulp suspensions in pipe flow J. Wiklund, J. Pettersson, A. Rasmuson, M. Stading SIK
09:45-10:10	Using Ultrasonic Velocity Profile measurements in an Air-vessel type surge-tank model R. Klasinc, M. Larcher, A. Predin Graz Univ.
10:10-10:30	Coffee Break
10:30-12:15	**Special session: Flow metering – present and future**
10:30-11:05	Improving the international acceptability of flow measurements G.E. Mattingly NIST
11:05-11:40	Dreams about legal gas metering J.G.M. van der Grinten NMI
11:40-12:15	Flow measurement standards and traceability in Japan Y. Terao AIST
12:15-13:55	Lunch Time
13:55-15:10	**Session 7 : Flow metering 2**
13:55-14:20	Advanced Hybrid Type Ultrasonic Flow Meter Utilizing State-of-the-Art pulsed-Doppler method along with traditional transit time method H. Yao, Y. Oomuro, K. Hagiwara, M. Kishiro, A. Miyamoto, K. Yamada, N. Tadata, G. Ohgawara, T. Yamamoto, Y. Takeda Fuji Electric Instruments
14:20-14:45	Analysis of frequency characteristics on non-invasive Utrasonic-Doppler flow measurement for metal pipes M. Kishiro, N. Hirayama, H. Yao, T. Yamamoto, Y. Takeda Fuji Electric Instruments
15:45-15:10	Accuracy improvement on non-invasive Ultrasonic-Doppler Flow Measurement by utilizing shear waves in metal pipe N. Hirayama, T. Onodera, S. Suzuki, H. Yao, G. Ohgawara, T. Yamamoto, Y. Takeda Fuji Electric Instruments
15:10-15:40	Group Photograph
15:40-18:00	Excursion
18:00-21:30	Met-Flow Dinner

8.9.2004

Time	
08:30-10:35	**Session 8 : Methodology**
08:30-08:55	Surface Decoration of Stainless Steel for LBE Flow Measurement by Ultrasonic Techniques K Kikuchi, M. Tezuka, S. Saito, H. Oigawa, Y. Takeda JAERI
08:55-09:20	Application of multi-wave TDX for multi-phase flow measurement H. Murakawa, H. Kikura, M. Aritomi TIT
09:20-09:45	Spectral reconstruction method for liquid velocity measurement beyond the Nyquist limit S. Fischer, P. Schmitt, B. Schwaller IMFS
09:45-10:10	A new algorithm for low velocity measurement by UVP H. Kitaura, N. Tadata, Y. Tasaka, Y. Takeda Hokkaido Univ.
10:10-10:35	Fundamental study for development of vector UVP-(1) Concept and time information- H. Ohbayashi, Y. Takeda, K. Yamaguchi Hokkaido Univ.
10:35-10:50	Coffee Break
10:50-12:30	**Session 9 : Fundamental Flow 2**
10:50-11:15	Influence of chain-like clusters on oscillating pipe flow of a magnetic fluid T. In-nami, Y. Oshikawa, R. Hasegawa, T. Sawada Keio Univ.
11:15-11:40	Velocity measurement around a large bubble rising in stagnant water in a round pipe using the UVP H. Minagawa, M. Ibuki, S. Yamada, Y. Shiomi Univ. of Shiga Prefecture
11:40-12:05	An unsteady flow structure on the heated rotating disk under the mixed convection condition N. Furuichi, M. Yoshida, M. Kumada Gifu Univ.
12:05-12:30	UVP measurements of the flow behind a rotating circular cylinder Y. Inoue, A. Ito, S. Yamashita Gifu Univ.
12:30-13:30	Lunch Time
13:30-15:10	**Session 10 : Fundamental Flow 3**
13:30-13:55	UVP measurement of Taylor-Couette vortex flow with small aspect ratio D. Ito, S. Kishikawa, H. Kikura, H. Kawai, M. Aritomi, H.Takahashi TIT
13:55-14:20	An experiment on the flow in a hard disk drive N. Sugawara, J. Funaki, K. Hirata Doshisha Univ.
14:20-14:45	Spatial and temporal structure of a time dependent pipe flow Y. Sato, Y. Takeda, D. Sugiyama Hokkaido Univ.
14:45-15:20	Closing

Plenary Lecture

High Rayleigh number thermal convection:
An overview and a new approach by ultrasonic measurements

Prof. Masaki Sano

Department of Physics
The University of Tokyo
E-mail sano@phys.s.u-tokyo.ac.jp

Abstract

Understanding turbulence at high Reynolds and high Rayleigh number is one of the unsolved fundamental problems in science. Recently, new scaling behavior and structures have been discovered in thermal convection at very high Rayleigh number by utilizing low temperature gas or liquid metals. However, strong coupling between velocity and thermal field in convection was offering both experimental and theoretical difficulties. Measurement of velocity field in thermal convection has been a hard problem until very recently. In this work, we succeeded in measuring velocity field of thermal turbulence of mercury instantaneously by using ultrasonic velocimetry. Interesting fluctuating dynamics of the mean flow and universal nature of the kinetic energy cascade are elucidated utilizing spectral decomposition and reconstruction. Scaling properties of the structure functions and the energy spectrum are directly calculated without the use of Taylor's frozen-flow hypothesis for the first time. Despite the complex nature of the mean flow, it is found that the energy cascade process exhibits universal laws in thermal turbulence.

STUDY OF VORTEX RING DYNAMICS USING UVP

Yuichi Murai*, Hidekazu Kitaura*, Zhiying Xiao**, Peter J. Thomas**, Yasushi Takeda*

*Division of Mechanical Science, School of Engineering, Hokkaido University
N13W8, Sapporo, 060-8628, Japan, E-mail: murai@eng.hokudai.ac.jp
**Fluid Dynamics Research Centre, School of Engineering, University of Warwick
Coventry, AV4 7AL, UK, E-mail: pjt1@eng.warwick.ac.uk

ABSTRACT

The dynamics of a vortex ring generated at the tip of a nozzle which is fixed on the top of a cylindrical water tank are investigated using UVP (Ultrasound Velocity Profiler). The instantaneous velocity profiles on three ultrasound beams are obtained to reconstruct two-dimensional structure of vortex ring. The nozzle diameter is D_o=50mm and experiments were performed for varying piston speeds and strokes of the vortex ring generator. The measurement section is $5D_o$ from the vortex ring generator, at which the vortex ring involves the influence of transient structure before reaching developed state. The translational velocity, the diameter, and the length of the vortex ring are quantitatively evaluated from the two-dimensional velocity field as function of dimensionless piston stroke and Reynolds number. The results have shown that the vortex ring has a certain condition to be generated clearly in the initial developing region. The typical length scales coincide with earlier studies, and thereby the availability of UVP for the intermittent flow measurement has been confirmed.

Keywords: Vortex ring, UVP, Flow field reconstruction, Multi-dimensional flow measurement

INTRODUCTION

A vortex ring can be seen in various natural phenomena regarding intermittent fluid flow such as volcanic fumes and smoker's rings. It has a long history of research from various points of views from pure scientific study to advanced engineering application. Especially the vortex ring has been chosen as a good research target to obtain fundamental knowledge on flow transition or instability caused by nonlinear phenomena of fluid flow [1][2]. Recent topics associated with vortex rings are the mechanism of downburst as a motion of large vortex ring [3], the interaction of flame with vortex ring [4][5], the vortex ring generated by a bursting bubble [6], the sound noise generation by vortex-pairing [7], and the atomization of droplets in fuel injection for IC engines [8]. On the other hand, vortex rings have often been employed as paradigms to test flow measurement techniques such as LDV and PIV because the vortex ring is one of elementary structures of fluid flow expressed mathematically [9]. In the past characteristics of vortex rings, such as their translational velocity, the ring diameter, and the ring's axial length, was studied by means of dye visualization and LDV [10]. Recently velocity measurements based on digital image processing such as PIV was employed to investigate vortex rings [11][12].

In this study, UVP (Ultrasound Velocity Profiler,[13]) is used to acquire those parameters directly from the two-dimensional flow field, which is measured by three ultrasound transducers. Utilization of UVP allows us to measure the on-beam velocity profile at real time, thereby the suitable experimental condition for generating ideal vortex ring can be found in a short working time. In addition, the repetition of measurement for treating irregularity of the vortex is easily performed. In this paper we report first results on the flow measurement technique based on multiple channel UVP, the flow field reconstruction method, and the difference of internal structure accompanied with changing the piston speed and the piston stroke of a vortex ring generator.
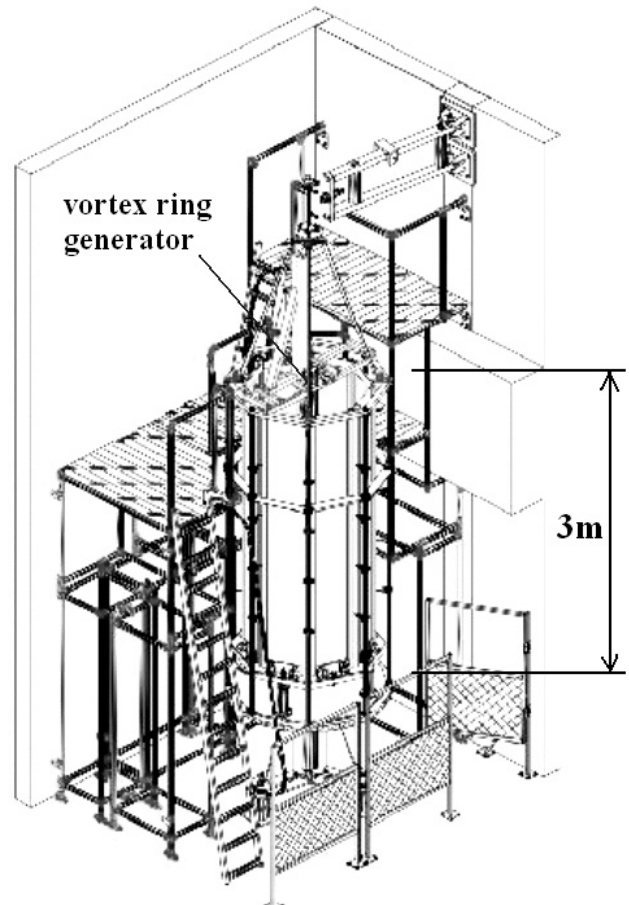

Fig.1 Overview of experimental facility

EXPERIMENTAL METHOD

Experimental facility

Fig.1 shows overview of experimental facility. A vortex ring generator, which is composed of a cylindrical nozzle and a reciprocating piston, is fixed on the top of a water tank with 3m heights and 1m widths. The vortex ring is emitted downward in water. The diameter of the nozzle D_0 is 50mm and the piston to push out the vortex ring is connected with a stepping motor controlled by computer, so the stroke S and the piston speed V are control parameters. The acceleration and the deceleration of the piston are fixed at 30m/s². The water temperature was 9.2 deg C, therefore, the kinematic viscosity is 1.30×10^{-6} m²/s and the density is 0.998×10^3 kg/m³. Vortex rings for 43 different parameter combinations were investigated – these test cases are summarized in Table 1. The numbers in the cells of Table 1 identify the number of the experiments.

Table 1. Experimental conditions

Piston Stroke D (mm)	Piston Velocity V (mm/s)						
	100	200	300	400	500	600	700
30	1	2	3	4	5	6	7
50	8	9	10	11	12	13	14
70	15	16	17	18	19	20	21
90	22	23	24	25	26	27	28
110	29	30	31	32	33	34	35
130	36	37	38	39			
150	40	41	42	43			

Injection of tracers

Hydrogen bubbles are used as fluid tracers for providing echo, i.e., ultrasound reflector. The bubbles are generated using two platinum wires of 0.5mm in diameter and 100mm in length. The wires are connected to a DC power by parallel circuit. 30V-DC power was enough to supply hydrogen bubbles with a sufficient number density around the target volume of the measurement. The mean bubble rise velocity was 20mm/s in quiescent water, so the mean diameter is estimated to be 0.27mm by assuming Levichi's drag coefficient (C_D=48/Re), which is around 1/5 of the wavelength of 4MHz ultrasound in water.
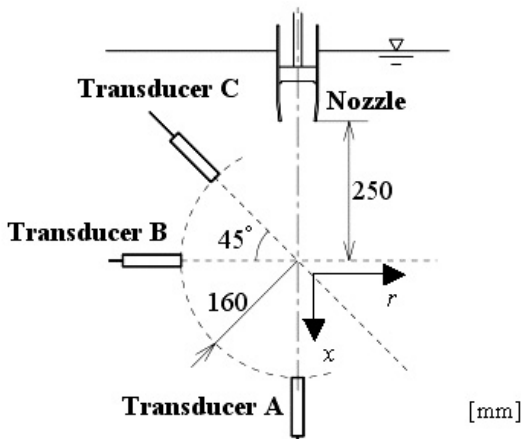

Fig.2 Definition of measurement space

Arrangement of ultrasound transducers

In order to obtain the velocity profiles on multiple measurement lines, three ultrasound transducers were mounted inside the tank as shown in Fig.2. The transducer A provides the axial (vertical) velocity component, the transducer B the lateral (horizontal), and the transducer C the oblique velocity component, respectively. The three ultrasound beams cross at x=250mm, i.e. 5 times the diameter of the vortex ring generator. The measurable radius from the cross point R is 160mm.
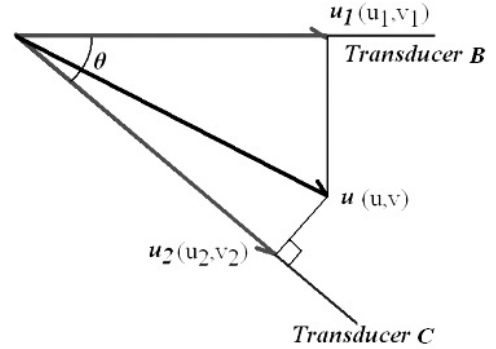

Fig.3 Velocity vector obtained by two velocity profiles

Reconstruction of two-dimensional flow

The vortex ring often has a three-dimensional structure in the initial region of the nozzle and in the transition region to turbulent flow before breaking up. However the primary flow is axisymmetic two-dimensional, and it is maintained in a certain distance from the nozzle. We have tried to measure the two-dimensional velocity vector field at the measurement space by combining multiple measurement data obtained in different direction. The velocity vector of the flow is calculated from two componential velocities, obtained by transducers B and C. As shown in Fig.3, the transducer B provides the lateral velocity $\mathbf{u}_1$ (u_1, v_1). Here u_1 is the lateral component, and v_1 the axial component. We set the transducer B in a horizontal plane so that v_1=0. The transducer C provides oblique components $\mathbf{u}_2$ (u_2,v_2) at the angle of θ=45 degree. Expressing the real velocity vector of the flow by $\mathbf{u}$ (u, v), the differential velocity vector ($\mathbf{u}_2$-$\mathbf{u}$) and $\mathbf{u}_2$ cross in perpendicular, therefore,

$$(\mathbf{u}_2 - \mathbf{u}) \bullet \mathbf{u}_2 = 0 \tag{1}$$

The velocity component u of $\mathbf{u}$ corresponds to u_1 or the direct measurement velocity U_B since the transducer B is set in a horizontal plane, i.e.,

$$u = u_1 = U_B . \tag{2}$$

Hence, eq.(1) can be rewritten with the components by,

$$(u_1 - u_2)u_2 + (v - v_2)v_2 = 0. \tag{3}$$

This equation gives the velocity component v by the following form,

$$v = v_2 - \frac{u_2}{v_2}(u_1 - u_2) . \tag{4}$$

The velocity components of $\mathbf{u}_2$ (u_2, v_2) are calculated from the velocity U_c measured by the transducer C as follows,

$$u_2 = U_C \cos\theta , \tag{5}$$

$$v_2 = U_C \sin\theta . \tag{6}$$

Thus, the velocity components u and v are calculated by,

$$u = U_B \tag{7}$$

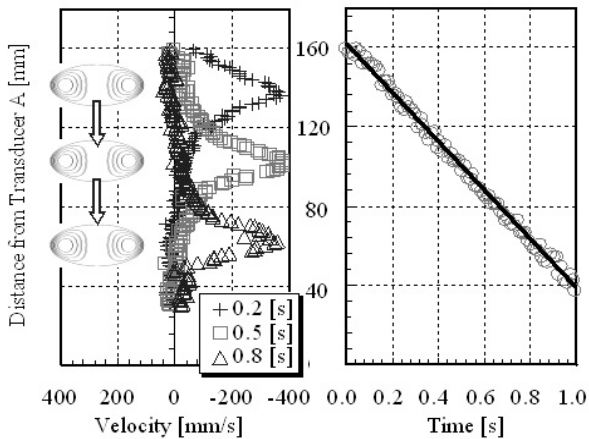$$v = U_C \sin\theta - (\tan\theta)^{-1}(U_B - U_C \cos\theta) \tag{8}$$

The velocity vector field of the vortex ring can be reconstructed by assuming that the vortex ring keeps its two-dimensional flow structure in a short period or in a short distance. Namely, the vortex ring to be measured must not change its own structure in the measurement space within R=160mm. Fortunately, ordinary vortex rings are stable for a

certain long distance up to hundreds times as its diameter. Using this assumption or the phenomenological fact, the velocity vector field is calculated even though the local measurement timing differs dependent on the alignment of the transducers.

RESULTS AND DISCUSSION

Translational velocity

The translational velocity of vortex ring is obtained from the temporal change of the vertical velocity profiles measured by the transducer A. Fig.4 (a) shows samples of instantaneous profiles of the axial velocity. The core part of the vortex ring has downward velocity as shown in the graph, and this profile migrates with a translational velocity. After the peak velocity location in each profile is obtained as function of time as shown in Fig.3 (b), the translational velocity and the deceleration are measured by fitting the data with second order function. The typical deceleration of vortex ring was 10^{-3} m/s^2 which provided around 3% reduction of the translational velocity in the measurement space within R=160mm. The decelerations measured in some cases (Cases 3, 7,and 33) were more than 30% in the measurement space due to very unstable ring structure, however the translational velocity was defined as the mean value within the measurement space.

Fig.5 shows the measurement data of the translational velocity U^* which is non-dimensionalized by the piston speed V. A Reynolds number for the vortex ring is defined by Re=$V D_0/\nu$. The dimensionless piston stroke is defined by S*=S / D_0. The grayscale map expresses larger U^* as white while smaller as the black. According to the measurement results, U^* increases almost linearly with S^* and also with Re at $Re < 2.0 \times 10^4$ while U^* becomes almost constant at $Re > 2.0 \times 10^4$. This implies that, 1) vortex ring is undeveloped at $Re < 2.0 \times 10^4$, and is developed enough at $Re > 2.0 \times 10^4$ in the measurement space, 2) the translational velocity relative to piston speed reaches around 0.5 only in certain optimum condition while it has smaller value in case of small S^*.
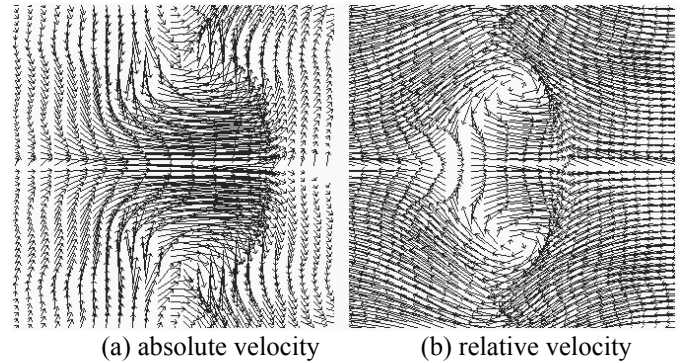

(a) absolute velocity   (b) relative velocity

Fig.6 Velocity vector field of vortex ring for Case 24

(a) velocity profiles   (b) peak velocity location
Fig.4 Velocity profile measured by transducer A
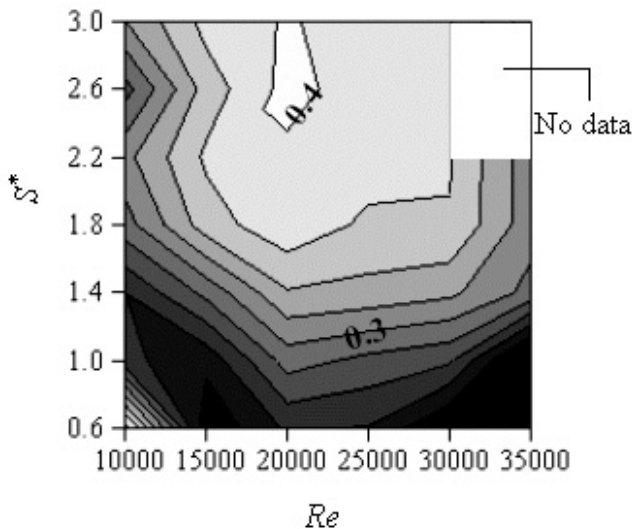
Fig.5 Map of dimensionless translational velocity
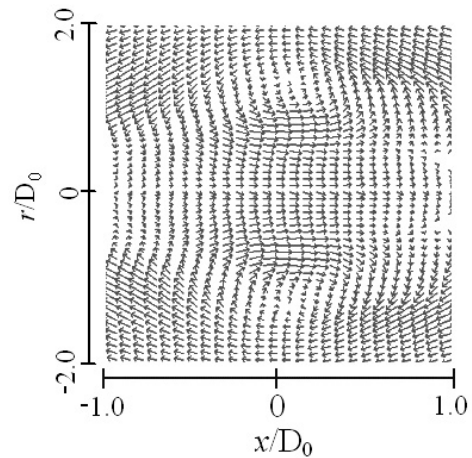

Fig.7 Vortex ring structure for S*=1.0 and Re=1.0x10^4.
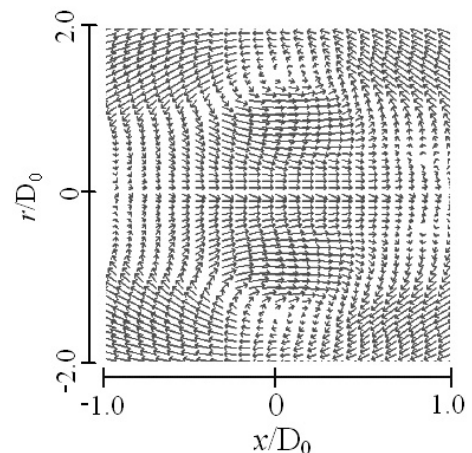

Fig.8 Vortex ring structure for S*=3.0 and Re=1.0x10^4.

3
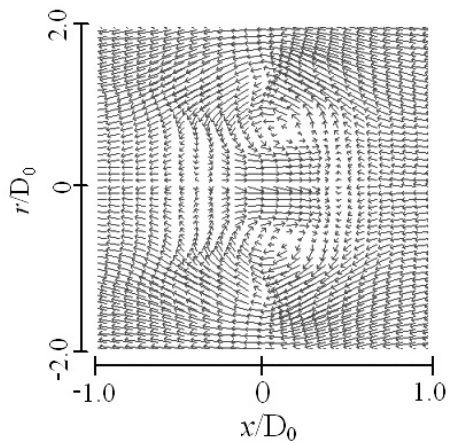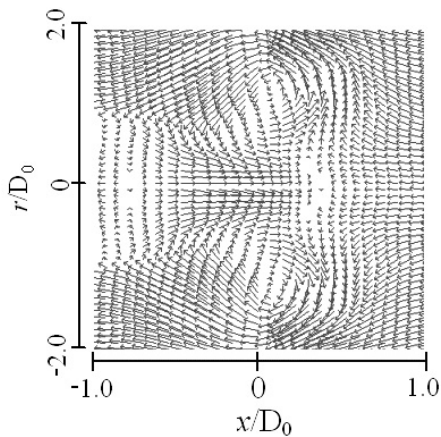
Fig.9 Vortex ring structure for S*=1.0 and Re=4.0x10^4.

Fig.10 Vortex ring structure for S*=3.0 and Re=4.0x10^4.

Two-dimensional flow field

Fig.6 shows two-dimensional velocity vector field obtained by three transducers. The velocity vector shown in (b) is relative velocity to the translational velocity measured by transducer A so that the circulation structure is easily identified.

Figs.7-10 shows four cases of the two-dimensional flow field in relative velocity. Fig.7 is the result of short stroke and low speed, Fig.8 just longer stroke, Fig.9 just higher speed and Fig.10 longer stroke and higher speed than (a). The result tells us that the increase of piston speed makes the structure of vortex ring clear and its circulation becomes strong while its size hardly changes. On the other hand, as the piston stroke increases, the diameter of the vortex ring becomes large.
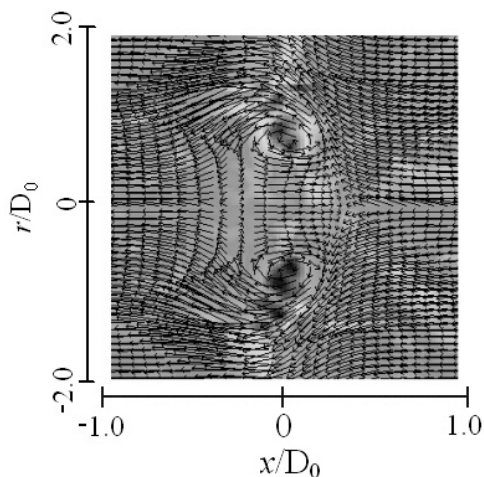
Fig.11 Vorticity distribution in Case 34

(S*=2.2, Re=6.0x10^4)

Fig.11 shows the vorticity distribution in Case 34 (see Table 1). The relative velocity vectors are overlapped on the vorticity color map. We can see that the peak vorticity appears approximately on the point at which the relative velocity vector gets zero. In the case of faster piston velocity given, multiple vorticity peaks emerge but the sign of the vorticity is the same. This implies that the vortex ring with a fast translational velocity would take a relaxation time to be stabilized. It means, the initial structure of the vortex ring, which involves short wavelength disturbance, remains in the present measurement volume. However the measurement error should be evaluated as well, which causes due to several factors including curved motion of vortex ring.
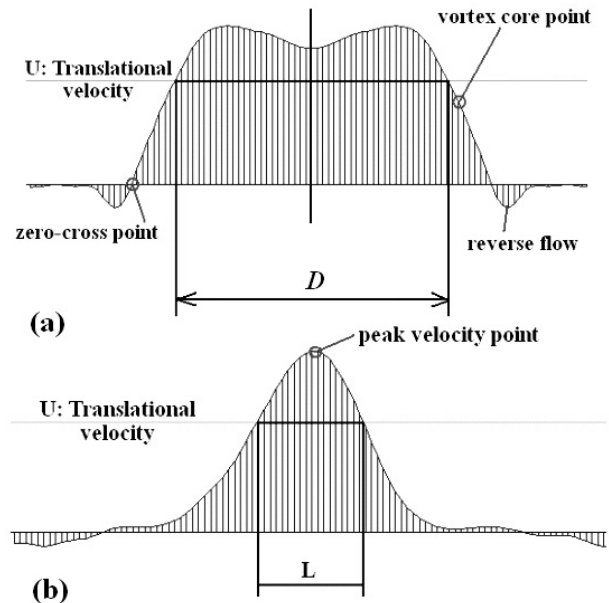

Fig.12 Definition of the diameter and the length of vortex ring

Typical length scales

Using the velocity vector field data of the vortex ring, the diameter and the length of vortex ring have been calculated. The diameter of vortex ring; D is defined by the distance between two points, on which the axial component of the relative velocity vector corresponds to zero. Namely, that is the point having the translational velocity. It is not defined with the point of vorticity peak (see Fig.12 (a)). The axial length of vortex ring; L is defined by the distance between the two points on the central axis, on which the axial component of the relative velocity gets zero (see Fig.12 (b)).
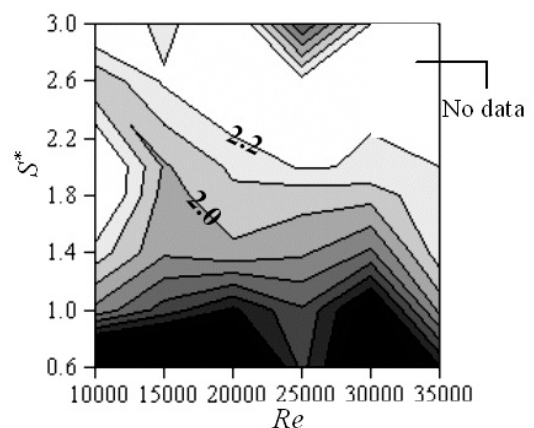

4

Fig.13 Dimensionless vortex ring diameter

Fig.13 shows the measurement results for the vortex ring diameter normalized by the nozzle diameter D_0, i.e. $D^*=D/D_0$. The grayscale map is drawn as function of dimensionless stroke and Reynolds number in the same way as in Fig.5. It is known that the spatial development of vortex ring is classified into four phases, i.e., generation region, laminar region, wavy region, and turbulent region before breaking up as shown in Fig.14. In the present measurement, the vortex ring from generation region to laminar region is measured. Roughly speaking, the diameter measured at $x=5D_0$ is reduced by increasing the piston speed V or Reynolds number. This is because initial circulation given by the piston gets large with increasing V, resulting in faster generation of vortex ring. However, in the case of V=100mm/s (Re=1.0×10^4), the diameter is exceptionally small because vortex ring itself was not formed clearly. For V>500mm/s (Re>5.0×10^4), the reduction of the diameter becomes blunt. On the other hand, increasing the piston stroke S^* for $S^* >1$ promotes the growth o the diameter. Diameters of more than twice the cylinder diameter were obtained for $S^*>2$.
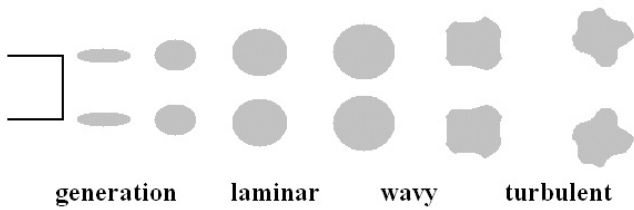

generation   laminar   wavy   turbulent

Fig.14 Spatial development of vortex ring in four phases
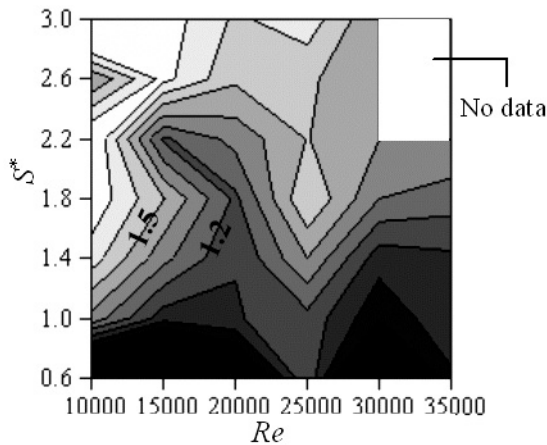

Fig.15 Dimensionless vortex ring length
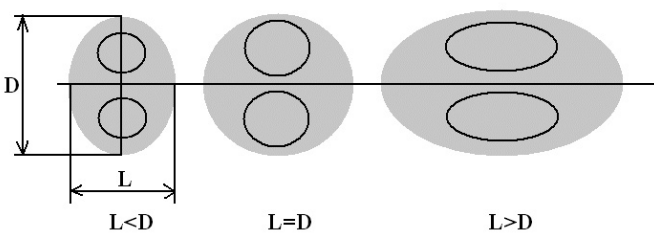

L<D   L=D   L>D

Fig.16 Translating region varied by length of vortex ring

Fig.15 shows the measurement result for the axial length of the vortex ring. The length is one of parameters represent the initial structure of vortex ring produced by piston-type vortex ring generator as shown in Fig.16. In general, the vortex ring length is elongated with increasing the piston stroke S^*. This is

because the total volume of translating fluid inside the vortex ring is proportional to the piston stroke. Supposing that any vortex ring is generated ideally and similarly, the vortex ring length must be completely proportional to the piston stoke. However, the actual length of the vortex ring is more complicated for two reasons. One is the fact that the diameter and the length of vortex ring are dependent on each other, and must satisfy the momentum given by the generator. Therefore, the relationship between the diameter and the length is not linear, resulting in non-symmetric structure generated as the piston stroke varies. This tells us simultaneously that there is a suitable relationship between the piston stroke and the piston speed to generate stable vortex ring in the initial region.

CONCLUDING REMARKS

The flow structures of single vortex rings in quiescent water have been successfully measured using UVP. At this time, the vortex ring is generated by a piston-type vortex ring generator, whose behavior varies with two parameters, i.e. the piston stroke D, and the piston speed V. The following points have been confirmed through the present experimental research.

(1) The two-dimensional velocity vector field of vortex ring can be reconstructed by combining three measurement data sets of UVP aligned at different angles. Using the vector maps, the basic characteristics of the vortex ring are quantitatively evaluated using the translational velocity U, the vortex ring diameter R, and the vortex ring length L.

(2) There is a suitable region to generate clear and strong vortex rings on the map of dimensionless piston stroke S^* and dimensionless piston speed denoted by Reynolds number. When the stroke S^* and Re numbers are too small, no clear vortex ring is identified. When the stroke S^* is too long, the flow becomes like a jet which does not induce vortex ring in a short time. When Re number is too large, the vortex ring is unstable and takes a relaxation time to become stable one.

(3) The vortex ring diameter D^* gets large as Re number increases. The diameter is approximately proportional to the piston stroke S^* for the range of $1<S^*<3$. The vortex ring length L^* increases with increase of Re number but it is not the monotonic function of Re number.

On the other hand, we encountered the following technical problems in UVP for the application to vortex ring. We have to consider these problems in the next step.

(a) The dynamic range of the velocity measurement by UVP is limited but the core part of the vortex ring had a very high-speed flow obeying the free vortex motion. In case of high piston speed for V>600mm/s, the core part of the vortex ring could not be measured, at which the velocity gets faster than 1m/s.

(b) In the case of slow piston speed or short piston stroke, the hydrogen bubble's buoyancy, which induces no uniform convection of water in the measurement volume, cannot be ignored relative to the main flow.

(c) In some cases, the trajectory of the vortex ring is curved and departs from the measurable radius R.

REFERENCES

1. Maxworthy, T., 1972, The structure of vortex rings, *J. Fluid Mech.*, 51, pp.15-32.
2. Maxworthy, T., 1977, Some experimental studies of vortex rings, *J. Fluid Mech.*, 81, pp.465-495.
3. Letchford, C.W., Chay, M.T., 2002, Pressure distributions on a cube in a simulated thunderstorm downburst, *J. Wind Eng. & Industrial Aerodynamics*, 90, pp.733-753.
4. Ishizuka, S., Murakami, T., Hamasaki, T., Koumura, K., Hasegawa, R., 1998, Flame speeds in combustible vortex rings, *Combustion & Flame*, 113, pp.542-553.
5. Renard, P., Thevenin, D., Rolon, J.C., Candel, S., 2000, Dynamics of flame/vortex interactions, *Progress in Energy and Combustion Sci.*, 26, pp.225-282.
6. Buchholz, J.H.J, Sigurdson, L.W., 2002, An apparatus to study the vortex ring structure generated by a bursting bubble, *Measurement Sci. & Tech.,* 13, pp.428-437.
7. Tang, S.K., Ko, N.W.M., 2001, Mechanism for sound generation in inviscid two-dimensional vortex interactions, *J. Sound & Vibration*, 21, 823-846.
8. Zhao, F., Lai, M., Harrington, D.L., 1999, Automotive spark-ignited direct-injection gasoline engines, *Progress in Energy & Combustion Sci.*, 25, pp.437-562.
9. Fukumoto, Y., 2002, Higher-order asymptotic theory for the velocity field induced by an inviscid vortex ring, *Fluid Dynamics Research*, 30, pp.65-92.
10. Shariff, K., 1992, Vortex rings, *Annu. Rev. Fluid Mech.*, 24, 235-279
11. Schram, C., Riethmuller, M.L., 2001, Vortex ring evolution in an impulsively started jet using digital particle image velocimetry and continuous wavelet analysis, *Meas. Sci. Tech.*, 12, pp.1413-1421.
12. Willert, C., 1997, Stereoscopic digital particle image velocimetry for application in wind tunnel flows, *Meas. Sci. Tech.,* 8, pp.1465-1479.
13. Takeda, Y., 1995, Instantaneous velocity profile measurement by ultrasonic Doppler method, *JSME Int. J., series B,* Vol.38 (1995) No.1.

OBSERVATIONS OF PARTICLE DISPERSION
EXTRACTED FROM THE UVP SIGNAL

G.P. King*, N. Furuichi **, Y. Takeda***

*Fluid Dynamics Research Centre, School of Engineering, University of Warwick, Coventry, UK CV4 7AL,
E-mail: greg.king@warwick.ac.uk,
**National Institute of Advanced Industrial Science and Technology
Center 3, Umezono1-1-1, Tsukuba 305-8563, Japan, E-mail: furuichi.noriyuki@aist.go.jp
***Laboratory for Flow Control, Hokkaido University, E-mail: yft@eng.hokudai.ac.jpT

ABSTRACT

An idea how to obtain qualitative information about particle dispersion by a flow from the UVP signal without further investment in instrumentation is described and illustrated in flow through an axisymmetric sudden expansion.

Keywords: Turbulent flow, Backward Facing Step, Vortex, Wake, and Separation

INTRODUCTION

In many fluid mechanical applications one desires to know not only the velocity field, but also how a tracer is stirred and dispersed by the flow. In work reported at the last ISUD meeting, Cellino described the development and application of an ultrasound system to measure the velocity and concentration fields simultaneously [1]. However, at the present time it is very expensive to implement their techniques. On the other hand if one is satisfied with less detailed knowledge, then the owners of a standard commercial ultrasound velocity profiler (UVP) can obtain some information about tracer dispersal at no additional cost.

The key to the idea is straightforward. Recall that in order to measure a velocity, particles capable of backscattering the incident ultrasound radiation must be present in the measurement volume. The UVP signal processing software counts the number of valid velocities measured during the profile sampling period. The number of valid velocities during the sampling period is called the success rate and here will be denoted by σ and is suitably normalized so that $0 \le \sigma \le 1$. Since the UVP carries out the measurement for a number of spatial positions in parallel, and as a function of time, we obtain $\sigma(x,t)$ where x denotes the US beam direction. Thus $\sigma(x,t)$ is a measure of the presence of tracer as a function of space and time along the beam direction. Clearly if one has more US transducers, more information about the space-time evolution of the tracers could be obtained. Also, the velocities at the positions where the success rate is large enough could be recorded and suitable averages of the particle flux could be obtained.

In this note we describe our idea (arrived at independently a few months before the last ISUD) and illustrate it with some experiments on the flow in an axisysmmetric sudden expansion.

EXPERIMENTAL METHOD

We use the experimental configuration and apparatus previously used by Furuichi, Takeda and Kumada [2] who investigated the flow transition in an axisymmetric sudden expansion using an ultrasound velocity profiler [3]. The flow configuration and coordinate system is shown in Figure 1. The flow emerging into the expansion section forms a separation bubble, and it is well known that the time averaged reattachment length varies as a function of Reynolds number, $\mathrm{Re}_d = V_b d/\nu$, where V_b is a bulk velocity estimated from the flow rate, d is the pipe diameter upstream of the step and ν is the kinematic viscosity. The transitional scheme is classified as laminar flow for $\mathrm{Re}_d < 1000$, transitional regime for $1000 < \mathrm{Re}_d < 4000$, and turbulent regime for $\mathrm{Re}_d < 4000$. Two large changes in the flow structure were observed in the transitional regime: the first at $\mathrm{Re}_d \approx 1500$ caused by a change in the spatial structure of the flow, and the second at $\mathrm{Re}_d \approx 2000$ where a change in the upstream flow occurred.

Air particles were produced by hydrolysis and used as scatterers/tracers, just as in the work by Furuichi et al [2]. The electrode was in the shape of a semi-circle and was positioned near the corner of the step in the lower half of the expansion section, as indicated in Figure 1. The transducer was aligned in the cross-stream direction at four different streamwise positions: $z/z_R = 0.67$, 1.0, 1.33 and 1.67, where z_R is the position of the time-averaged reattachment point.

The experimental protocol was as follows. First the flow rate was set to yield a pre-selected Reynolds number, and the US transducer was positioned at one of the pre-determined streamwise positions. Then a short duration current was sent through the electrode, thereby causing a pulse of small air bubbles to be released into the flow. A short time after the current was turned off the UVP data collection began, and the success rate $\sigma_k(r,t)$ was collected and stored as a function of radial position and time at a fixed streamwise position z_k. Next,

the position of the transducer was moved to a new streamwise position and the experiment repeated.

RESULTS AND DISCUSSION

Results of these experiments are shown in Figure 2 (space-time plots of $\sigma_k(r,t)$) and Figure 3 ($\overline{\sigma_k}(t) = \int \sigma_k(r,t)dr$).

Figure 2 is a measure of the residence time at different radial positions as a function of time. The figures require some care to interpret properly and this will be described in the presentation.

CONCLUDING REMARKS

In conclusion, the results are to be interpreted qualitatively, not quantitatively. The idea is highly suggestive that interesting information about how the flow disperses tracer particles in the flow can be obtained from the UVP signal, complementing the measured velocity field.

REFERENCES

1. M. Cellino, Ultrasonic measurements of instantaneous velocity and suspended concentration in open channel, ISUD3, 23-29, (2002), Lausanne.

2. N. Furuichi, Y. Takeda and M. Kumada, Spatial structure of the flow in an axisymmetric sudden expansion, Experiments in Fluids, **34**, 643-650, (2003) .

3. Y. Takeda, Development of ultrasound velocity profile monitor, Nuc. Eng. Des., **12 6**, 17 7, (19 90) .
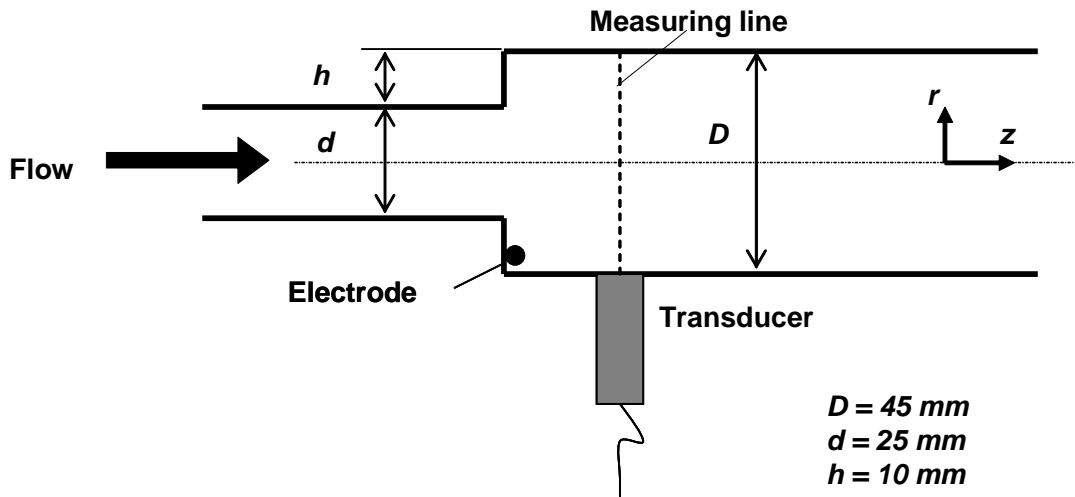
Figure 1: Experimental configuration of the axisymmetry sudden expansion.
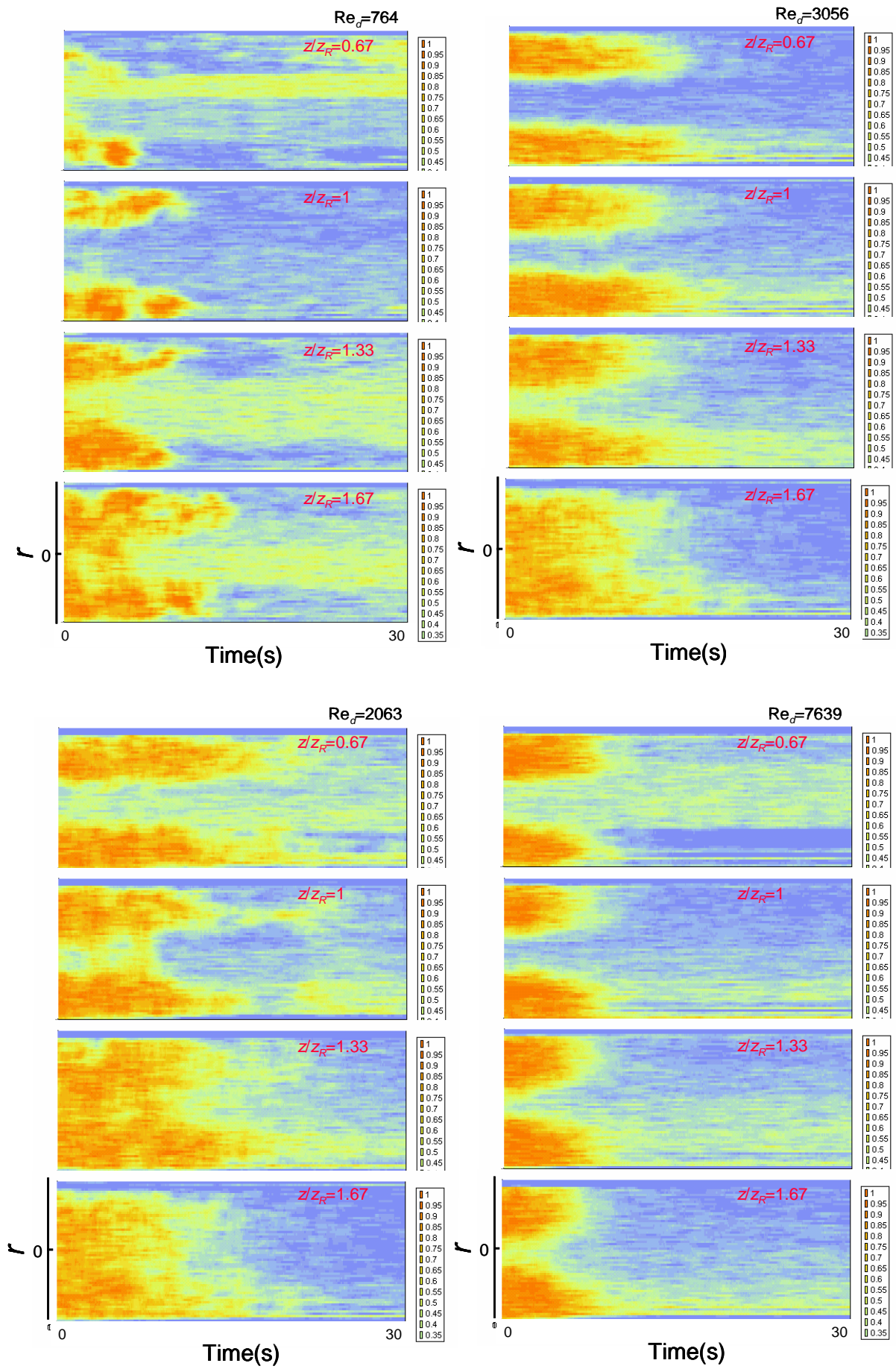
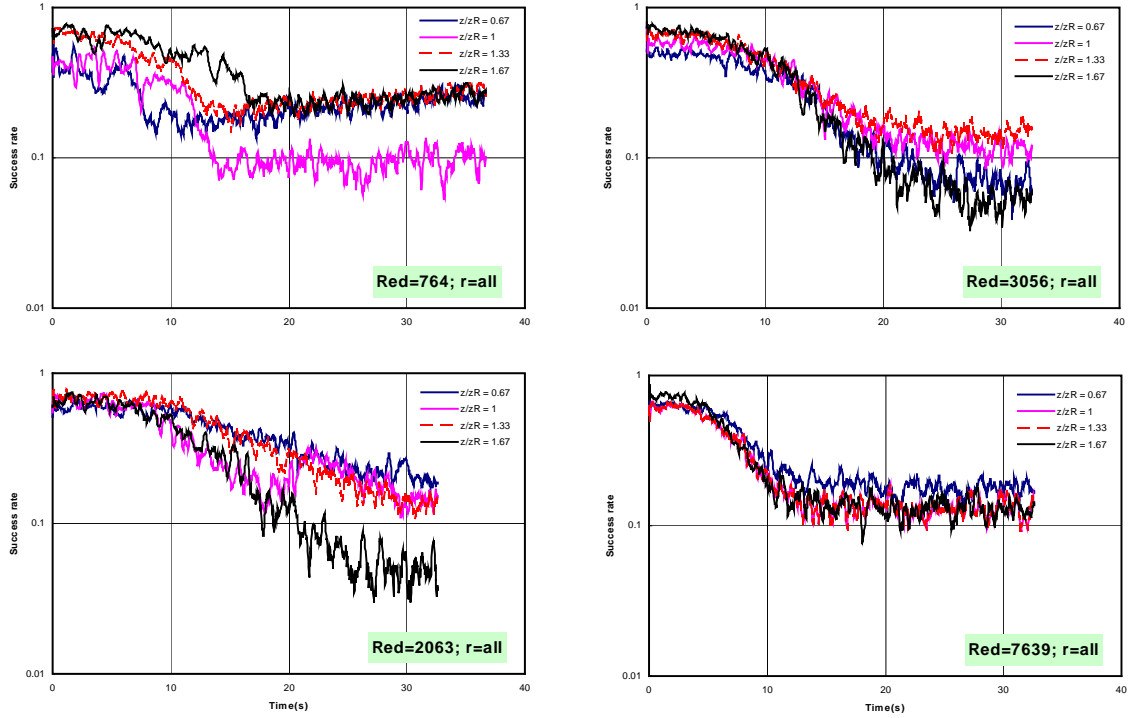Figure 2: Space – time color density plots of the success rate $\sigma_k(r,t)$

Figure 3: Plots of the radially integrated success rate, $\overline{\sigma_k}(t) = \int \sigma_k(r,t)dr$.

EXPERIMENTS IN AN INITIAL REGION OF A CIRCULAR FREE JET

Yoshihiro Inoue[*], Shintaro Yamashita[*] and Kunikazu Kondo[**]

* Dept. Mathematical & Design Eng., Gifu University, 1-1 Yanagido, Gifu 501-1193, Japan
E-mail: inouey@cc.gifu-u.ac.jp, yamasita@cc.gifu-u.ac.jp

** Dept. Mechanical Eng., Suzuka College of Tech., Shiroko-cho, Suzuka, Mie 510-0294, Japan
E-mail: kunikazu@mech.suzuka-ct.ac.jp

ABSTRACT

Coherent structures in the near field of an axisymmetric jet have been investigated in a water channel. Instantaneous velocity profiles were obtained in the axial and radial directions with the ultrasonic Doppler method. The UVP (ultrasonic velocity profile) monitor used in this study is Met-Flow model X3-PS with the ultrasonic transducers of the basic frequency of 4 MHz. Also, a multi-line measurement system was utilized. Two transducers were connected to the UVP monitor and alternately switched to acquire two profiles with different angles of azimuthal direction at the same streamwise position quasi-simultaneously. Dominant time-scale and averaged length-scale of velocity fluctuating fields are examined from DWT, and wavenumber-frequency spectrum is calculated by two-dimensional FFT along the axial direction. Coherent structures in the axial and radial directions are investigated in terms of POD. Axial variation in the amplitude and wavelength of $u(x, t)$ is well represented in the lower-order POD modes in the axial direction, and also the radial oscillation of the mixing layer is captured by the only first POD mode with about half a total energy. Azimuthal mode of radially oscillating mixing layer is estimated from a cross-correlation between the random coefficients $v^{(2)}(\boldsymbol{q}, t)$ and $v^{(2)}(\boldsymbol{q} + \boldsymbol{Dq}, t)$.

Keywords : Round Jet, Discrete Wavelet Analysis, POD, Azimuthal Mode

INTRODUCTION

A study of the jet that is one of a representative flow field of free shear flow has been done a lot so far, and the engineering application field is wide. There are various kinds for a three-dimensional free jet from a difference of shape of an outlet. Of these, a circular jet [1], an elliptical jet [2], a rectangular jet [3] are well examined as a comparatively simple model.

This study is aimed for elucidation of space-time flow structure of a three-dimensional free jet by water tank experiment using an Ultrasonic Velocity Profile Monitor (UVP), putting a center of interest in the flow field close to the nozzle outlet. The authors have made experiments on a square and a circular jet and reported the fluctuating flow field of a square free-jet [4]. In this report, the flow structure of a circular free jet is examined.

A study of a circular jet is started for a long time, and Hinze describes the prospects of those days in the first edition of his book [5]. Interest for this flow field does not run out, and, for example, many experiments such as Wygnanski & Fiedller [1] are done afterwards. With experimental environment fixed better, experimental studies are still continued with progresses of experimental methods [6-8], and the understanding of flow structure is deepened; these studies contribute to high sophistication of a calculation model. In particular, the development of space measuring methods promotes a breakaway from conventional methods like point measurements, conditional measurements and so on, and it contributes greatly to understanding of the spatial structure of various flows.

The advantage of the ultrasonic Doppler method used in this study is to be able to get an instantaneous velocity profile on a line of ultrasonic beam in time series; the principle of the UVP measurements and its performance should be referred to Takeda [9]. On the other hand, a particle imaging velocimetry has ability to acquire two- or three-dimensional information in space, but it is not easy to expand this in the time direction. Therefore, the UVP measurements set in an appropriate measuring position and direction are very effective to obtain the information of space-time correlation of the flow field. In this study, acquired data are analyzed by Fourier transform, discrete wavelet transform and proper orthogonal decomposition, and, from their results, the flow structure of the circular jet is clarified.

EXPERIMENTAL PROCEDURE

Apparatus

The outline of flow field and coordinate system are shown in figure 1. We take x- and y-axes in the jet-axis and radial directions, respectively. Test section of the water tank used in this experiment is an open channel of 0.7 m wide, 0.64 m deep of water and 3 m long, and jet nozzle is set up at the central portion on the partition of the test section and settling chamber. The exit diameter of the nozzle is 85 mm, and the contraction shape is a quadrant of a radius 12 mm added hereafter a straight line. In the experiment, Reynolds number Re_j based on the velocity U_j in the core of the jet and nozzle exit diameter D was set to about 0.9×10^4. Then the initial momentum thickness $\boldsymbol{q}_0$ of the shear layer at the position of $x / D = 0.2$ was about 1.0 mm, and $Re_\theta = U_j \boldsymbol{q}_0 / \boldsymbol{n} \approx 10^4$.

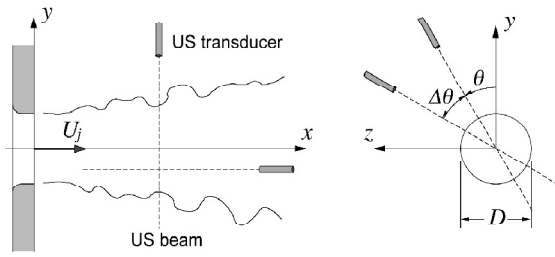Fig. 1. Coordinate system

Fig. 2 Distributions of mean and fluctuating velocity components.

UVP measurement method

In the UVP measurement, ultrasonic transducer comprising a function of transmission and reception is used and velocity component in the traveling direction of ultrasonic beam is detected almost instantaneously for 128 points on the beam. The basic frequency of ultrasonic wave used in this experiment was 4 MHz, and hydrogen bubbles generated successively from a platinum wire of diameter of 30 μm was used for scattering particles. An incidence direction of the ultrasonic beam, namely, the measuring line was chosen as each direction of x- and y-axes as shown in figure 1, and the profiles along the x- and y-directions for the instantaneous velocity components of axial direction u and radial direction v were obtained in time series. In working conditions of this experiment, the time interval of velocity data was about 38 ms, and the space intervals of adjacent measuring point were 2.94 mm in the x-direction, and 2.20 mm in the y-direction.

In addition to the experiment using one transducer mentioned above, to examine the correlation of flow structure in the circumferential direction the experiment using two transducers simultaneously was also made. Azimuthal angle of the fixed measuring line is assumed ***q***, and phase angle between the moving and fixed measuring lines is indicated by ***Dq*** (figure 1, right). In this case because multiplexer built in the UVP works, and sequential switching measurement is done, time delay of about 39 ms is occurred between the measuring lines in this measurement. The measuring position of the axial direction was $x / D =$ 2 and 3.

If a flight direction of ultrasonic beam is assumed ***x***, the quantity obtained by this measurement is space-time distribution of ***x*** component of the instantaneous velocity, and it is expressed

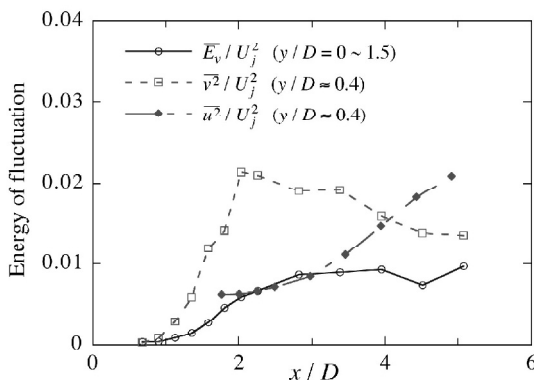with $V_\xi(\boldsymbol{x}) + v_\xi(\boldsymbol{x},t)$. Here $V_\xi(\boldsymbol{x})$ shows time-averaged velocity distribution and $v_\xi(\boldsymbol{x}, t)$ space-time distribution of fluctuating velocity. For data set of this space-time distribution, data analyses such as Fourier transform, discrete wavelet transform and proper orthogonal decomposition are performed as done in the previous report [4], and flow structure is examined.

RESULTS AND DISCUSSION

Mean flow field

Figure 2 shows the distributions of radial component of mean velocity V and r.m.s. value of fluctuating velocity v_{rms} within the flow region in this experiment. Mean and fluctuating velocity profiles become anti-symmetric and symmetric, respectively, because of the axial symmetry of the flow. At $x / D = 1$, a sharp change of V around $y / D = 0.5$ is seen. This region is located between the jet core and the fluid surrounding jet, and is initial mixing layer that is comparatively thin. The mixing layer rapidly increases its thickness as goes downstream, and the fluctuation intensity in the layer is augmented. The fluctuation intensity has a distribution with its minimum at $y = 0$, and a difference of this local minimum and the peak value is shortened for $x / D > 4$.

Fig. 3 Axial changes in the spatially and temporally averaged energy of velocity fluctuation.

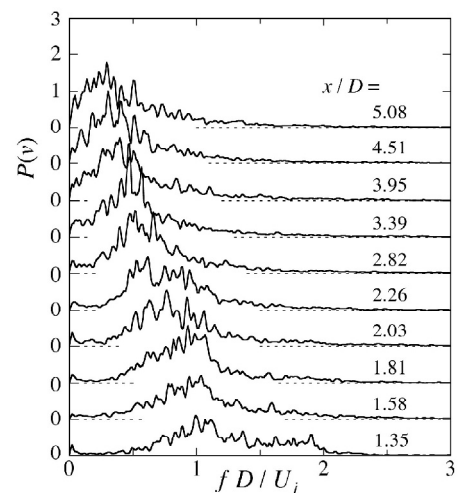Fig. 4 Power spectrum of v-fluctuation at $y / D \approx 0.4$.

In order to inquire the axial change in the fluctuation energy, the changes in $\overline{u^2}$ and $\overline{v^2}$ at the representative position $y / D \approx 0.4$ and in space average of the energy of y component of fluctuating velocity $\overline{E}_v$ are shown in figure 3. Characteristic change
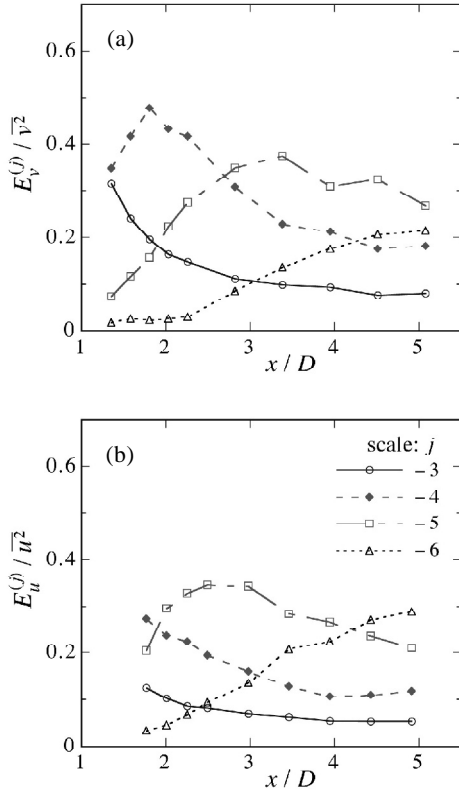

Fig. 5 Axial distributions of the wavelet spectrum of $v(t)$ and $u(t)$ at $y / D \approx 0.4$.
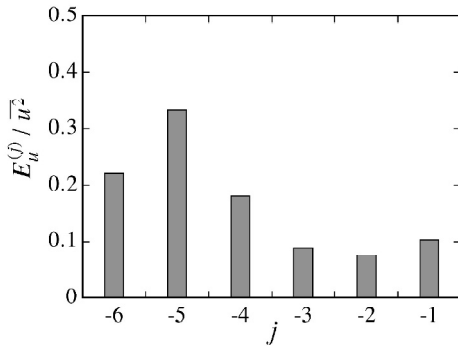

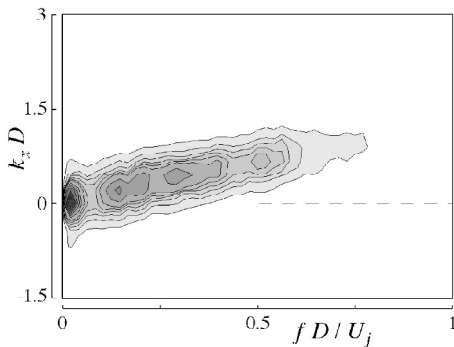Fig. 6 Wavelet spectrum of $u(x, t)$ in space.

Fig. 7 Wavenumber-frequency spectrum of $u(x, t)$.

is seen in $\overline{v^2}$ behavior in that it suddenly increases toward the maximum at $x / D = 2$, and thereafter it turns to decrease. Averaged fluctuating energy $\overline{E}_v$ increases in the range of $x / D < 3$, and becomes nearly constant afterwards. Unlike these, the distribution of $\overline{u^2}$ is monotone increasing in the measuring range. Figure 4 shows the power spectra of v-fluctuation. For $x / D < 2$, a high energy hump around the dimensionless frequency $f D / U_j = 1$ is seen, and this central frequency falls for $x / D > 2$. It seems that this change is caused by the distortion and/or coalescence behavior of the vortices formed in the mixing layer, and, as a result, the maximum of v-fluctuation energy at $x / D = 2$ is brought about.

Consequently, to examine the axial change in the fluctuation energy included in each time scale, an orthogonal wavelet expansion for u- and v-fluctuations is made about time axis, and the change in the energy density of each scale is shown in figure 5. Because a time interval of this measurement is $\boldsymbol{D}t = 0.038$ s, for example, the time scale of the analysis for $j = -4$ becomes 0.61 s, and the dimensionless Nyquist frequency is 0.67. In figure 5(a) showing the change in v-fluctuation energy, the result shown in figure 4 becomes clearer, and the manner that a predominant scale in the axial direction varies can be grasped. That is, the fluctuation energies of $j = -3$ and -4 for $x / D < 2$, of $j = -4$ and -5 for $x / D = 2$ to 3.5 and of $j = -4$ to -6 for $x / D > 3.5$ are predominant. On the other hand, the change of a similar predominant scale is shown also in figure 5 (b) related to u-fluctuation energy, but energy contribution rate of scale $j = -4$ is small compared with v-fluctuation.

Mixing-layer oscillation in the axial direction

From $u(x, t)$ measured at $y / D = 0.4$, nearly central position in the mixing layer, the characteristic of the oscillation of the mixing layer in the axial direction is examined. At first figure 6
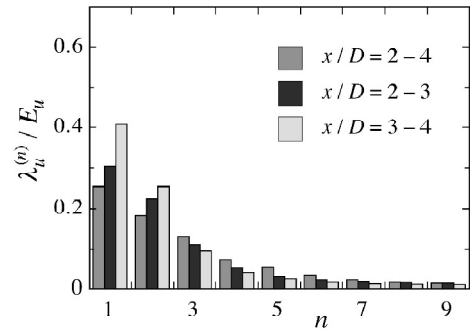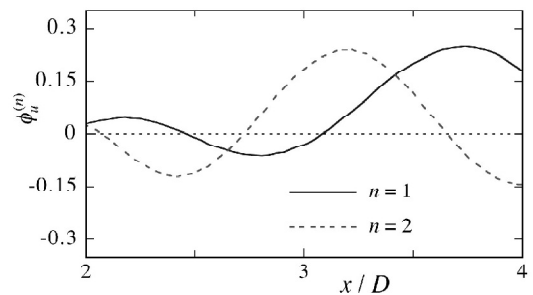

Fig. 8 POD spectrum of $u(x, t)$.

Fig. 9 Distributions of the eigenfunction at the first two POD modes in the axial direction at $y / D \approx 0.4$.
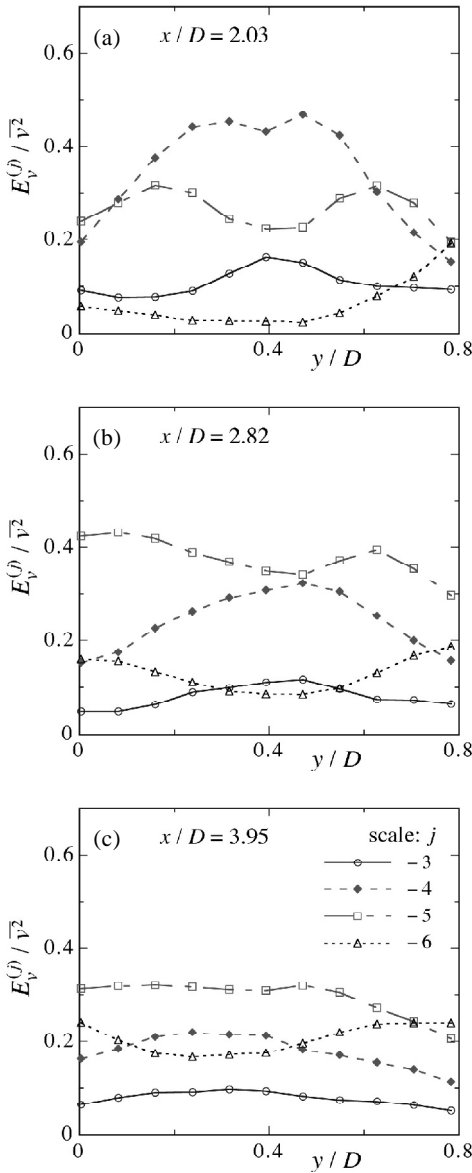
Fig. 10 Radial distributions of the wavelet spectrum of $v(y, t)$ in time. (a) $x / D = 2.03$, (b) $x / D = 2.82$ and (c) $x / D = 3.95$

Fig. 11 POD spectrum of $v(y, t)$.

Fig. 12 Distributions of the eigenfunction at the first two POD modes.

is the DWT spectrum obtained from the orthogonal wavelet expansion made in the direction of spatial coordinate axis in the range of $x / D = 2$ to 5. From this figure, it can been seen that the energy contribution from the scale $j = -5$, which is the dimensionless wavelength 2.2, is the highest, and that there exist waves around the mean wavelength in the mixing layer.

Next, the wavenumber-frequency distribution is sought from two-dimensional Fourier transformation in spatiotemporal space. In this case the range of analysis was assumed $x / D = 3$ to 5. Figure 7 shows this result in the form of a contour map, where frequency f and wave number k_x are made dimensionless. The region where the energy is high extends as a ridge linearly from the origin, and the phase velocity of the wave is estimated 0.77 U_j for $y / D = 0.4$ from this slope.

As for this flow field, the time scale varies in the flow direction as described in the previous section, and it seems that the spatial scale varies with this. However, two-dimensional Fourier spectrum mentioned above cannot express non-homogeneity in space, and also DWT spectrum cannot. Therefore the proper orthogonal decomposition is performed for the same data
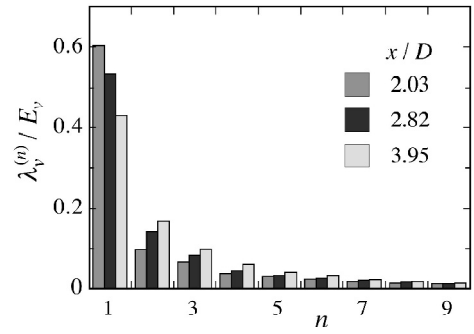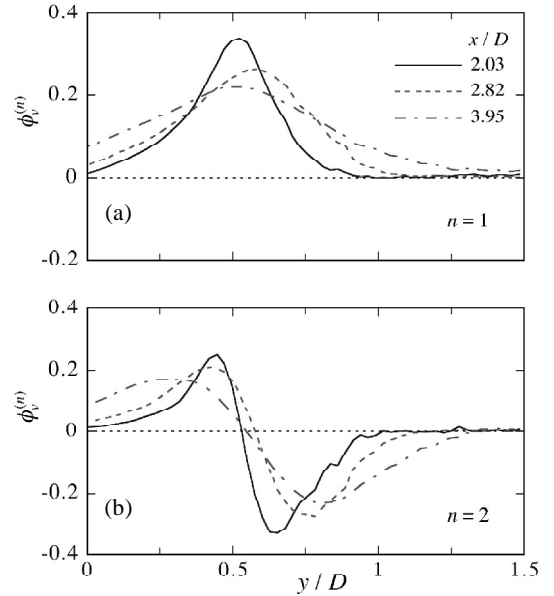
set, and at first the spatial mode in which the energy content is high is detected. The result analyzed in the range of $x / D = 2$ to 4 is given in figure 9, and the energy spectrum is shown in figure 8. It is understood that, from the distribution of eigenfunction, the variations of the amplitude and wavelength in the flow direction are captured. Even if analyzed after dividing the target range into $x / D = 2$ to 3 and 3 to 4, any difference between the distributions of eigenfunction was hardly seen, but as shown in figure 8 the energy density of lower order mode is higher when analyzed after dividing, and in particular for $x / D = 3$ to 4.

Velocity fluctuation in the radial direction

The change of the time scale of v-fluctuation in the radial direction is examined using the DWT in representative positions $x / D = 2.03$, 2.82 and 3.95. It can been seen from figure 10 (a) of position $x / D = 2.03$ that the energy contribution from the scale $j = -4$ holds more than 40 % in the mixing layer, and that from $j = -5$ is large next. At $x / D = 2.82$ (figure 10 (b)) the contribution from the scale $j = -5$ is predominant on the whole. Because the scale $j = -5$ is the nearest to a column mode with respect to time scale, it seems that the column mode is dominant on the whole cross section of the jet at $x / D = 2.82$. On the other hand, the scales $j = -4$ and -5 make contribution of the same degree in the center of the mixing layer, and the fluctua-
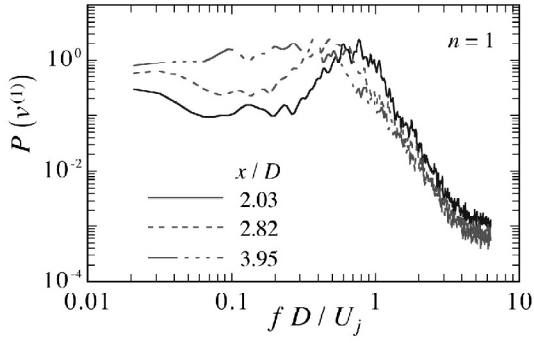
Fig. 13 Power spectra of the random coefficient at the first POD mode.

Fig. 14 Cross-correlation of the random coefficient of $v(y, t)$ in the azimuthal direction.

tion having a short time scale becomes stronger than in the jet center. The scale $j = -5$ is also predominant in $x / D = 3.95$ (figure 10 (c)), but its energy contribution becomes low, and the fluctuation of the scale $j = -6$ becomes relatively high compared with at the upstream positions.

For the radial distribution, the spatial mode was found by applying the proper orthogonal decomposition. Figure 11 gives the POD spectrum, and figure 12 shows the distributions of the eigenfunction for $n = 1$ and 2. The distributions of eigenfunction of low order mode in any position become similar, and only the radial width expands as goes downstream. From the energy spectra, extreme prominence of mode $n = 1$ is realized. However, this prominence becomes low in the downstream. It seems that the fluctuation of $n = 1$ corresponds to the inward and outward motions of the mixing layer from the distributions of the eigenfunction, and superposition of this fluctuation and that of $n = 2$ brings about a deviation of the radial position where v-fluctuation has a maximum value.

The power spectrum obtained from the FFT analysis of random coefficient $v^{(n)}(t)$ for $n = 1$ is shown in figure 13. From this spectrum, the time periodicity of the spatial variation of mode $n = 1$ can be examined. There exists a clear hill on the distributions of spectra for $x / D = 2.03$ and 2.82, and dimensionless frequency corresponding to each hill is about 0.8 and 0.5, respectively; these values accord with the peak frequencies seen in figure 4. On the other hand, the spectrum of $x / D = 3.95$ shifts more to the low-frequency side, but any hill with prominent frequency is not seen. Although the figure was omitted by limitation of the space, any prominent component in the spectra for $n = 2$ does not appear in all positions, and hence there seems to be little relevance between the generation of spatial fluctuation for $n = 2$ and the mechanism to produce the fluctuation for $n = 1$.

Velocity correlation in the azimuthal direction

The experiment on the flow structure in the circumference direction was made on the two measuring lines which are aligned to the radial direction and different in phase angle; the phase angle Dq was varied from 10° to 90°. As was also described in the previous section, the motion in the jet cross section can be well expressed by the lower-order POD mode of $v(y, t)$, and this time fluctuation can be contracted to the random coefficient $v^{(n)}(t)$. On the confirmation that the eigenvalue and eigenfunction do not change in the circumferential direction, we understand that the circumferential change affects only the random coeffi-
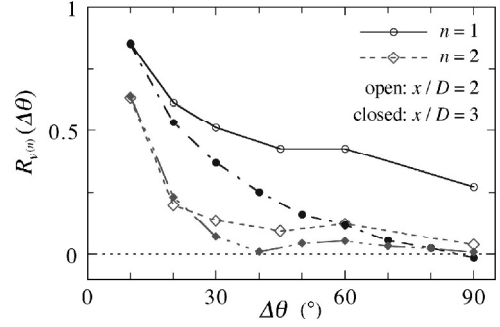
cient; we put this as $v^{(n)}(q, t)$. Here, a characteristic between the random coefficients with different phase angles is examined from cross correlation.

Figures 14 (a) and (b) stand for the circumferential cross-correlation coefficients of $v^{(1)}$ and $v^{(2)}$ at $x / D = 2$ and 3 respectively. Values of correlation coefficient of $v^{(1)}$ decrease with increase of Dq at all positions, and those for $x / D = 2$ maintain the value of 0.3 to 0.5 at $Dq = 90°$ whereas for $x / D = 3$ there is almost no correlation at the same phase angle. This means high axially-symmetric nature of the fluctuation at $x / D = 2$, and the decrease in correlation length namely the poorness of axial symmetry is exhibited at the downstream position. In addition, values of correlation coefficient of $v^{(2)}$ for $x / D = 2$ suddenly decrease to approximately 0 from $Dq = 0°$ to 40°, and correlation length in the circumferential direction is considerably short. If this spatial mode means the oscillation of the center of the mixing layer in the radial direction as mentioned in the above section, this flow has structures of scale of 60° to 80° in circumferential span, and it seems that five or six structures are arranged in the whole circumference. This result agrees well with the result of flow visualization made particularly as well as the experimental result of Toyoda [10].

CONCLUSIONS

Results of this study are summarized below.

(1) The energy of fluctuating velocity in the mixing layer began to rapidly increase from $x / D \approx 1$, and v-fluctuation grew up firstly. The time scale of fluctuation shifted to the lower frequency side in the process of this growth, and the difference of u- and v-fluctuations appeared in DWT scale $j = -4$, which is the dimensionless Nyquist frequency of 0.67.

(2) Mean wavelength of the fluctuation and phase velocity were estimated from axial velocity distribution at $y / D \approx 0.4$. In addition, the change of the wavelength in the flow direction was well expressed by the distribution of eigenfunction found with POD.

(3) Nearly 50 % of total energy of the fluctuation were contained only in the first mode of POD for $v(y, t)$, and this time scale was about 0.8 and 0.5 in dimensionless frequency at $x / D = 2.03$ and 2.82, respectively.

(4) It was shown that the axial symmetry became poor in the axial direction from the measurement of phase of $v(y, t)$ along the circumferential direction, and the scale of the flow structure in the circumferential span was estimated as 60° to 80° from the fluctuating component of the second mode of POD.

REFERENCES

1. I. Wygnanski, I., H. Fiedler, 1969, Some measurements in the self-preserving jet, *J. Fluid Mech.*, 38, pp. 577-612.

2. H.S. Husain, F. Hussain, 1993, Elliptic jets. Part 3. Dynamics of preferred mode coherent structure, *J. Fluid Mech.*, 248, pp. 315-361.

3. Y. Tsuchiya, C. Horikoshi, T. Sato, 1986, On the spread of rectangular jets, *Exp. Fluids*, 4, pp. 197-204.

4. Y. Inoue, S. Yamashita, K. Kondo, 2002, The ultrasonic velocity profile measurement of flow structure in the near field of a square free jet, *Exp. Fluids*, 32, pp. 170-178.

5. J.O. Hinze, 1959, "Turbulence. An Introduction to Its Mechanism and Theory," McGraw-Hill, New York.

6. N.R. Panchapakesan, J.L. Lumley, 1993, Turbulence measurements in axisymmetric jets of air and helium. Part 1. Air jet, *J. Fluid Mech.*, 246, pp. 197-223.

7. H.J. Hussein, S.P. Capp, W.K. George, 1994, Velocity measurements in a high-Reynolds-number, momentum-conserving, axisymmetric, turbulent jet, *J. Fluid Mech.*, 258, pp. 31-75.

8. G. Xu, R.A. Antonia, 2002, Effect of different initial conditions on a turbulent round free jet, *Exp. Fluids*, 33, pp. 677-683.

9. Y. Takeda, 1995, Velocity profile measurement by ultrasonic Doppler method, *Exp. Thermal Fluid Sci.*, 10, pp. 444-453.

10. K. Toyoda et al., 1999, Effect of axial azimuthal perturbations on entrainment, mixing and diffusion of a circular jet, *Proc. 3rd ASME/JSME Joint Fluids Eng. Conf.*, FEDSM99-7285.

UVP MEASUREMENT ON TAYLOR-COUETTE FLOW OF MAGNETIC FLUIDS WITH SMALL ASPECT RATIO

Hiroshige Kikura*, Shingo Kishikawa**, Daisuke Ito*, Masanori Aritomi* and Yasushi Takeda***

* Research Laboratory for Nuclear Reactors, Tokyo Institute of Technology,
2-12-1 Ohokayama, Meguro-ku, Tokyo, 152-8550 Japan, e-mail: kikura@nr.titech.ac.jp
**[2] Muroran Institute of Technology, 27-1 Mizumoto-cho, Muroran-shi, Hokkaido 050-8585, Japan,
*** Hokkaido University, Kita-13, Nishi-8, Kita-ku, Sapporo 060-0808, Japan

ABSTRACT

In this paper, the application of ultrasonic velocity profile (UVP) method to investigate magnetic-fluids flow is described. The objective of the research is to measure the internal flow of a magnetic fluid on Taylor-Couette flow with small aspect ratio using the UVP method and to analyze the influence of the applied magnetic field. The flow structure of a magnetic fluid in a concentric annular geometry with a small aspect ratio of 3 and a radius ratio of 0.6 for an inner-cylinder rotation was investigated. Axial velocity distributions were measured using the UVP measurement technique. A non-uniform magnetic field was applied to the flow field using a permanent magnet, located outside of the cylinders. The results demonstrated that the UVP method was capable to provide the information on the structure of Taylor-Couette flow with small aspect ratio in a magnetic fluid.

Keywords: Magnetic fluid, Taylor-Couette Flow, UVP, Ultrasound, Velocity Profiles, mode Bifurcation

INTRODUCTION

The magnetic fluids contain solid, magnetic, single domain particles coated with a molecular layer of a dispersant in a liquid carrier such as water or kerosene. Since the diameter of these particles lies in the size range of 5 - 15 nm, and due to the thermal agitation, the resulting random walk and random rotation, i.e. Brownian motion, the ferromagnetic particles remain suspended steadily. To achieve a stable dispersion in non-polar or polar solvent, the particles are coated with a single or double layers surfactant.

The importance of such magnetic fluids has been increasing in various fields of engineering application. This leads to the increased interests in studying flows of the magnetic fluids. Conventional methods for flow investigations, such as laser-Doppler-techniques (LDA) and Particle Image Velocimetry (PIV) are not applicable for investigating the magnetic fluid flows. Because, the dark colored liquid prevents the laser-light from penetrating the flow fields. In order to investigate the flow fields of liquids with optically non-transparent media, the Ultrasound Velocity Profile method (UVP method) has been developed [1][2]. Recently, the velocity information obtained from liquid-metal flows are available, i.e. measurements in mercury [3] and measurements in sodium [4]. Hence, the method for investigating the flow fields in the magnetic fluids has also been available [5] [6].

Taylor-Couette flow with small aspect ratio, which has the effect at the end of annulus, is an interesting physical phenomenon, typical to non-linear dynamics. Many researchers have carried out the investigations on mode bifurcation and flow pattern, applying laser Doppler anemometry, flow visualization or other methods. Benjamin [7] studied the change in mutation of primary flow at the length of comparatively short annulus. Mullin [8] investigated the evolution of primary flow and the transition from N-cell mode to (N+2)-cell mode by flow visualization. If we use a magnetic fluid as a test liquid, it is suggested the possibility of mode control by using an external magnetic field.

Some experimental investigations by mean of torque characteristics for cylindrical and spherical Couette flow on magnetic fluids had also been studied [9]-[11]. The UVP method was applied to the time-dependent Taylor-Couette flows obtained between two concentric rotating cylinders to measure time-dependent flow dynamics of a magnetic fluid by Kikura, et al.[12]. They found that under a non-uniform magnetic field, there is an angular dependence of the flow and the maximum velocity depends on the intensity of the magnetic field and is influenced by the level of the upstream velocity.

Thus, the aim of the present paper is to measure the internal flow of a magnetic fluid on Taylor-Couette flow with small aspect ratio using UVP method and to discuss the influence of an applied magnetic field on the flow mode bifurcation control.

SOUND PROPERTY OF MAGNETIC FLUID

Since the ultrasound properties, especially sound velocity, were unknown for the magnetic fluid used in this investigation, and its value is essential in the ultrasonic Doppler method, we measured the sound velocity [12]. In Fig. 1, the results are given for a magnetic fluid. The based test fluid W-40 is a water-based magnetic fluid and the weight concentration w% of fine magnetite particles is controlled by dilution. From Fig.1 we found that the velocity of sound in magnetic fluids decreases with the increase in weight concentration of magnetite particles. In the present study, we used the magnetic fluid of 23.35w% having a sound velocity of 1450 m/s.

Even though the magnetic fluids are composed of solid, magnetic, single domain particles coated with molecular layer
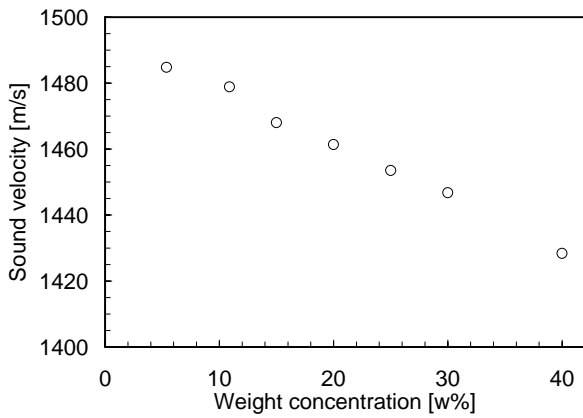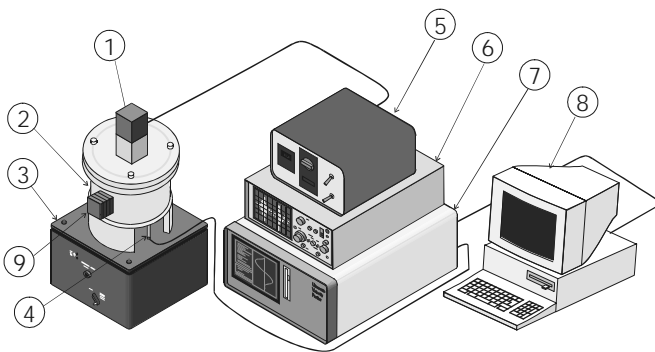
Fig. 1 Sound velocity of a water-based magnetic fluid

Fig. 3 Magnetic field and

1. Motor, 2. Taylor-Couette Vessel, 3. Isolator, 4. US transducer,
5. Controller, 6. Oscilloscope, 7. UVP monitor, 8. PC, 9. Magnet

Fig. 2 Experimental apparatus

Fig.4 Measuring position

of a dispersant, the diameter of particles in the size range of 5 to 15 nm is too small to emit strong ultrasound signals. Furthermore, the present investigations are based on the propagation of ultrasound waves in magnetic fluids possessing a large absorption of ultrasound. To acquire such a strong ultrasound signal, tracer particles (Micro Sphericalfeather: MSF10) were added to the flows. The tracer particles are made of a SiO2-shell having a spherical shape, uniform diameter particle of 0.9 mm with low effectiveness and specific gravity. Although these particles are much smaller than the wavelength of the ultrasound, the reflected-power is efficient to produce significant signal-to-noise ratio of the detected ultrasound wave and the measuring length in the magnetic fluid is 60 mm in the present case. The propagation of ultrasound in magnetic fluids was investigated by Gogosov et al [13]. They found out that the sound velocity in a magnetic fluid was smaller than that in the solvent. Additionally, the sound velocity changed when a magnetic field was applied. However, in the present configuration we had not found any deflectable change in the sound velocity due to the present magnetic field.

EXPERIMENTAL SET-UP

The schematic of experimental apparatus is shown in Fig. 2. The apparatus consists of two concentric cylinders, which are made of Plexiglas. The length of the cylinders are 48mm, the outer radius of the inner cylinder is $R_i = 24$mm and the inner radius of the outer cylinder is $R_o = 40$mm. They are positioned vertically adjacent and the gap between the two cylinders is
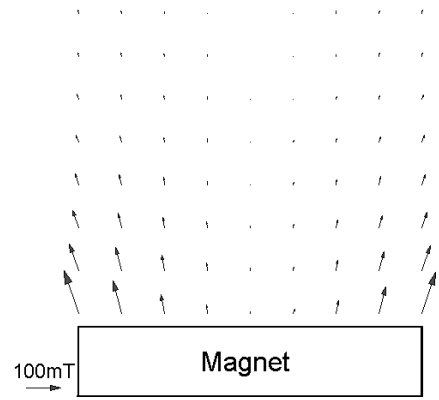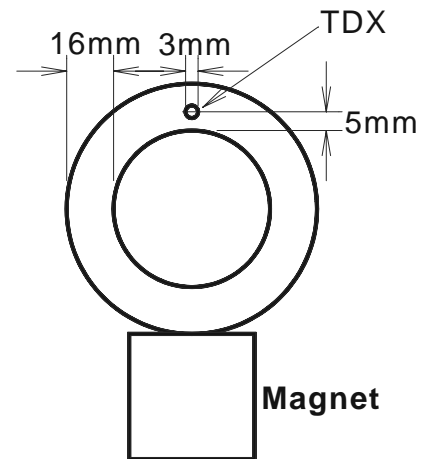
filled with a magnetic fluid. The UVP transducer (8K3I, INS 570, Japan Probe Co.)is installed from the bottom of container to measure the axial velocity distributions. In a system with fixed outer cylinder, the fluid in the annular gap moves in a plane perpendicular to the cylinder axis for small Reynolds number ($Re = \Omega R_i(R_o-R_i)/\nu$). Here, Ω is rotation rate of inner cylinder, and ν is kinematic viscosity of a magnetic fluid. The UVP monitor used in this work is the X-3 PSi model (MetFlow SA) with basic ultrasound frequency of 8MHz..

The non-uniform magnetic field was applied perpendicularly to the cylinder axis using a 40-mm×40-mm×45-mm permanent magnet, positioned outside the cylinders. Typical magnetic field distribution ($B_0 = 62$mT) around the cylinder is shown in Fig. 3a and the locations of ultrasonic transducer for measurements are shown in Fig. 3b. Here B_0 is mean magnetic field intensity on the surface of the magnet. The Hall-effect Gauss meter measured the vertical and horizontal magnetic inductions; hence the vector field of the magnetic field was obtained. We applied the magnetic fields with following two ways, one is that the magnet applied when the rotation of the cylinder $\Omega = 0$, and after the start of rotation the magnet was released from the cylinders (case-1). The other way is that after the rotation of the cylinder, the magnet was placed at the outer cylinder. Subsequently, the magnet was released from the cylinders (case-2).
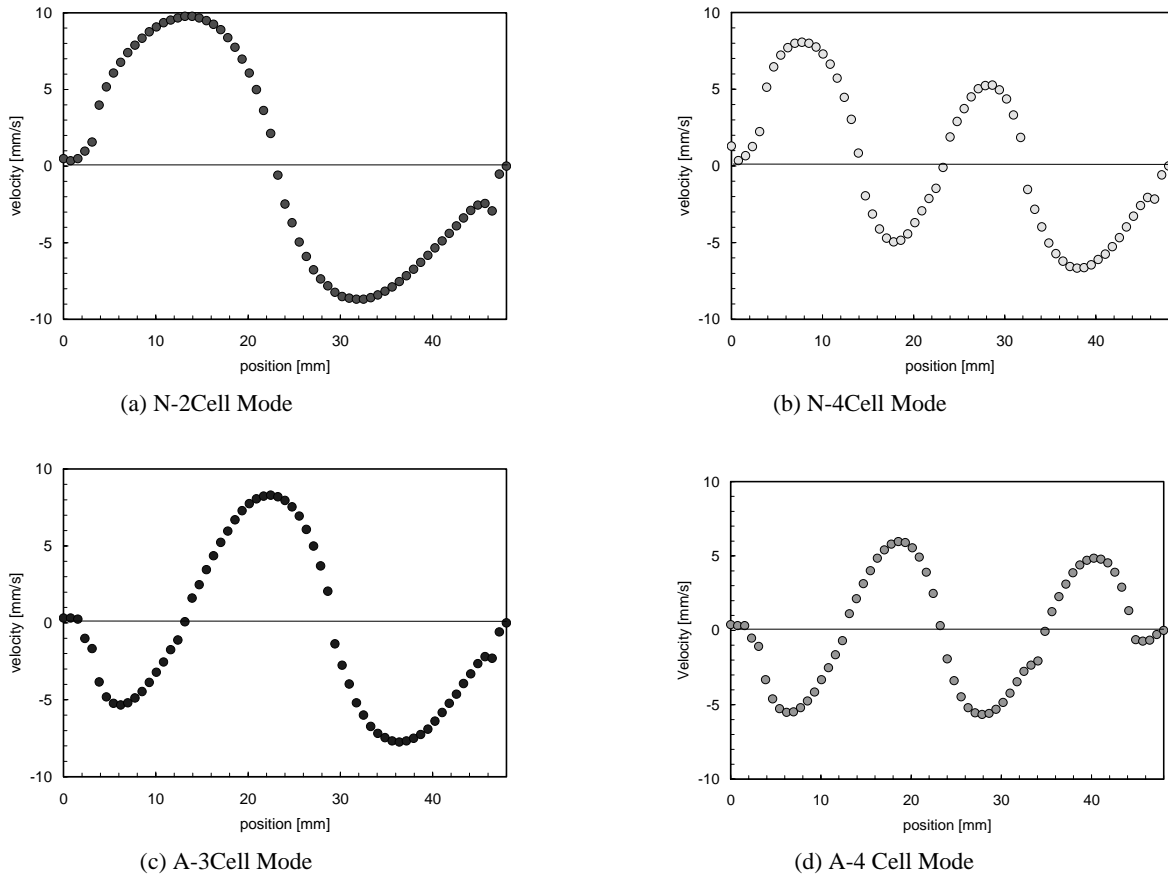
RESULTS AND DISCUSSION

(a) N-2Cell Mode

(b) N-4Cell Mode

(c) A-3Cell Mode

(d) A-4 Cell Mode

Fig. 4 Axial mean velocity profiles (Re=350, B_0=0)

(a) A-4 Cell (Re=420)

(B) A-4 to A3 Cell (Re=580)
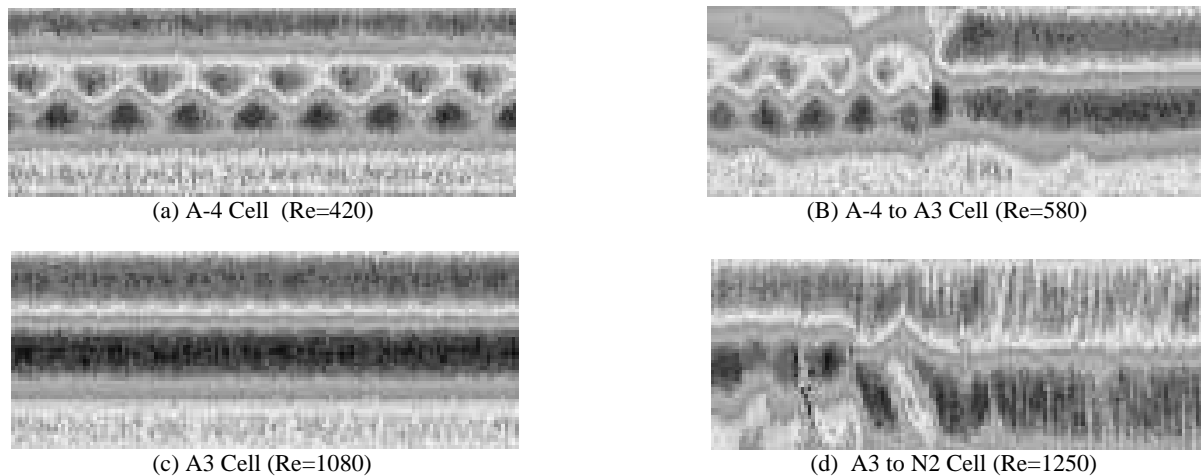

(c) A3 Cell (Re=1080)

(d) A3 to N2 Cell (Re=1250)

Fig. 5 Mode bifurcation from A-4Cell mode to N-2 Cell mode (B_0=0)

The velocity profile was obtained by setting up the ultrasound transducer on the outer wall of the end plate at the inner wall position, as illustrated in Fig. 3b. At very low Reynolds numbers in a rotating Taylor-Couette system, the flow is a two-dimensional circular Couette flow having the velocity profile $V=(0,V_\theta(r),0)$. At critical Reynolds number, Couette flow becomes unstable to Taylor-vortex flow (TVF), which has three dimensional, axisymmetric counter-rotating toroidal vortices. Taylor vortex flow occurs with small aspect ratio on various flow patterns. Fig. 4 shows the mean velocity distributions in different flow mode at same Reynolds number (Re = 350) without magnetic field. In Taylor-Couette flow with small aspect ratio, the flow is classified as primary mode and secondary modes. The primary mode flow (N-2Cell) is formed smoothly from Couette flow by a gradual increase in Re. The secondary mode (N-4Cell) occurs when the Re was abruptly increased until reaching a certain value. The number of vortices in the secondary mode is different from one in the primary mode. The primary mode and secondary mode are distinguished into normal mode and anomalous mode. On each end wall, the flow in the normal mode has a normal cell which gives an inward flow in the region adjacent to the end wall. The flows of the anomalous modes (A-3Cell and A-4 Cell) have anomalous cells, which give an outward flow near the end wall. Using UVP method we can obtain the instantaneous velocity profiles and understand the each mode from instantaneous and mean velocity profiles.

Mode bifurcation occurred depending upon the increase of Reynolds number. Fig 5 shows mode bifurcation of the anomalous 4-cell mode (A-4 Cell) for the measured velocity profiles. In each display, the ordinate represents position (64 data points for 0.74mm in width) and the abscissa is time (256
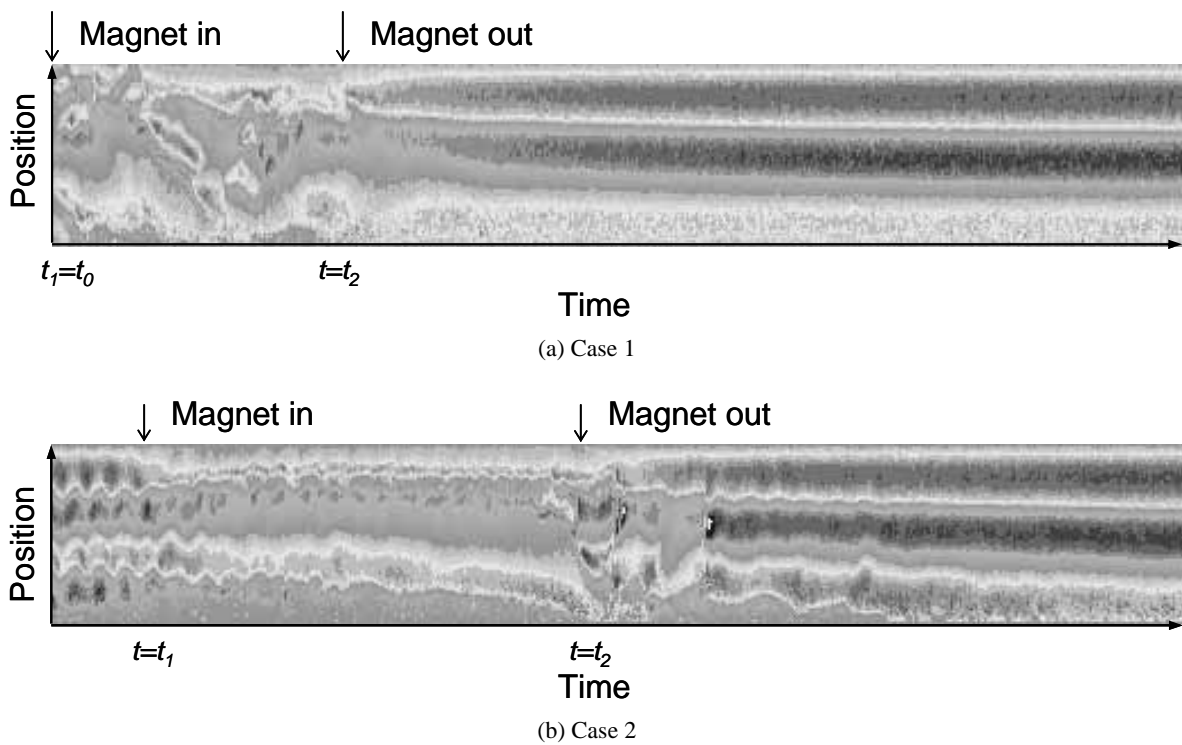
(a) Case 1

(b) Case 2

Fig. 6 Measured velocity profiles (Re=600, B_0=62mT)

points for 29s). The velocity values are color-coded: yellow and red being positive; green and blue, negative. The full-scales are of ±20mm/s, ±30mm/s, ±40mm/s and ±50mm/s, respectively.

Fig. 6 shows the measured velocity profiles for mode control using a magnetic field. In case-1, the magnetic field was applied from rotating start and the final flow mode was anomalous 3-cell mode. In the case 2, the magnetic field was applied during normal 4-cell mode; the final flow mode was also anomalous 3-cell mode. From each one of them, reliable control to 3-cell mode was obtained. The study clarified that the UVP method was capable to provide the information on the structure of Taylor vortex flow with small aspect ratio, in a magnetic fluid.

CONCLUDING REMARKS

The flow structure of the Taylor-Couette flow with small aspect ratio of a magnetic fluid has been investigated using the ultrasonic velocity profile (UVP) method. For checking the ultrasound properties of the magnetic fluid, the dependence of sound velocity on the weight concentration was studied. The velocity of sound in magnetic fluids decreases with increase in weight concentration of magnetite particles. However, in the present configuration we found no deflectable change in the sound velocity due to the magnetic field. From the experimental results on the Taylor-Couette flow with aspect ratio of 3 in a magnetic fluid under the no external field, 4 type of flow modes(N-2cell, N-4Cell, A-3Cell and A-4Cell mode) have been understood from instantaneous and mean velocity profiles. Mode bifurcation occurred depending upon the increase of Reynolds number. Influence of an applied magnetic field on the flow has been carried out and we found that the possibility of mode bifurcation control using magnetic field.

REFERENCES

[1] Takeda, Y., *Int. J. Heat Mass Flow*, **7** (1986), pp.313-318.

[2] Kikura,H, Yamanaka, G. and Aritomi, M., *Experiments in Fluids*, **36**-1 (2004), pp.187-196.

[3] Takeda, Y. and Kikura, H., *Experiments in Fluids*, **32**-2 (2002), pp.161-169.

[4] Kamoshida, H. et al., *Proc. Japan Soc. Nucl. Engin. Spring Meeting* (1995), p.363 in Japanese.

[5] Kikura, H., Takeda, Y. and Sawada, T., *J. Mag. Mag. Mat.*, **201** (1999), pp.276-280.

[6] Sawada, T., Kikura, H and Tanahashi, T., *Experiments in Fluids*, **26** (1999), pp.215-221.

[7] Benjamin, T. B., *Proc. R. Soc. London*, Ser. A, **359** (1978), pp.27-43.

[8] Mullin, T., *J. Fluid Mech.*, **121** (1982), pp.207-218.

[9] Yamaguchi,H. and Koori,I., *J. Mag. Mag. Mat.*, **122** (1993), pp.221-222.

[10] Niklas,M., *Zeitschrift fuer Physik* B (1987), pp.493-501.

[11] Hart, J. E., *J. Fluid Mech.*, **453** (2002), pp.21-38.

[12] Kikura, H., Takeda, Y. and Durst, F., *Experiments in Fluids*, **26** (2002), pp.161-169.

[13] Gogosov,V.V. et al., *J. Mag. Mag. Mat.*, **122** (1993), pp.70-73.

Industrial Applications of New Type Flow-metering System by Ultrasonic-Doppler Profile-Velocimetry

(1) Effects of Surface Roughness and Asymmetric Pipe Flow on Accuracy of Profile Factor

Kenichi Tezuka, TEPCO, 4-1 Egasaki-cho, Tsurumi-ku, Yokohama, 230-8510
Michitsugu, Mori, TEPCO, 4-1 Egasaki-cho, Tsurumi-ku, Yokohama, 230-8510
Yasushi Takeda, Hokkaido University
Masanori Aritomi, Tokyo Institute of Technology
Hiroshige Kikura, Tokyo Institute of Technology

As nuclear power plants are highly aging, readings of flowmeters for reactor feedwater systems drift due to the changes of flow profiles. The causes of those deviations are caused by the change of wall roughness of inner surface of pipings. To cope with those concerns, time-of-flight ultrasonic flowmeters are being introduced to nuclear power plants in the United States. However, flow profile factors (PFs), which adjust measurand to real flow rates, also strongly depend on flow profiles. To determine profile factors for actual power plants, manufactures of flowmeters usually conduct factory calibration tests under ambient flow conditions. Indeed, flow measurements with high accuracy for reactor feedwater require them to conduct calibration tests under real conditions, such as liquid conditions and piping layouts. These make it inevitable in quite a few measuring errors for large, hi-Reynolds number pipings in power plants. Therefore, the measurement accuracy of flow rate by conventional time-of-flight ultrasonic flowmeters is questionable. This paper discussed the effects of surface roughness and asymmetric pipe flow on accuracy of Profile Factors.

Key Words: *pipeflow profile; ultrasonic; Pulse-Doppler*

1. Introduction

Figure 1 shows the changes in PFs due to the changes of pipe roughness. These calculations are done using the numerical simulation code (Star-CD) and logarithmic law under the same hydraulic conditions as 480MW class reactor feedwater system. Two kinds of flowmeters are selected for the calculations of PFs, cross flow type and transit time. As the equivalent sand-grain surface roughness gets rougher, PFs deviate with a few percentage points against the PFs of smooth pipings in both systems. Up to around 6 % deviation is observed in case of cross flow measurement system that measures the center line velocity of pipings. In case of transit time flowmeter, the PF deviates up to 3% against the smooth pipings. Therefore, if nuclear power plants get aging, we are supposed to experience those PF deviations in both systems. These deviations directly affect to the accuracy of flowmeters.
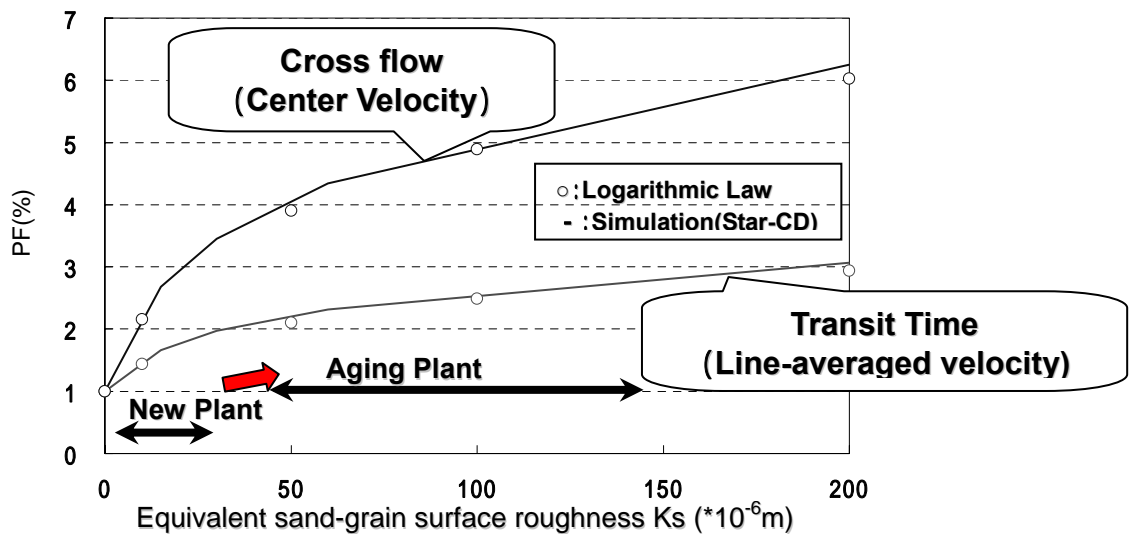

Fig.1 Percentage Changes in Profile Factors vs. Surface roughness

This paper discussed the effects of surface roughness and asymmetric pipe flow on accuracy of Profile Factors.

2. Experimental procedure

Experiments are conducted with water flow system under ambient temperature in 151 mm diameter stainless steel pipes at three different Reynolds numbers, $1.5*10^5$, $2.8*10^5$ and $4.4*10^5$, by changing a circulation pump speeds. Inner surfaces of those pipes are sanded by alumina powders or machined to obtain three different surface roughness; $5.3*10^{-6}$m, $11.9*10^{-6}$m and $22.7*10^{-6}$m. Surface roughness is represented by root mean square value, Rq, of a surface roughness curves. The configuration of the test section is shown in Figure 2. Velocity profiles are measured with the Ultrasonic Doppler Flow Meter (UdFlow) at the horizontal diameter positions of 12D and 30D from tube-type flow conditioner placed after the pipe elbow. As ultrasonic reflectors, miniaturized bubbles are injected through the bubble injector ring with the volumetric void flow rate of 0.003%.
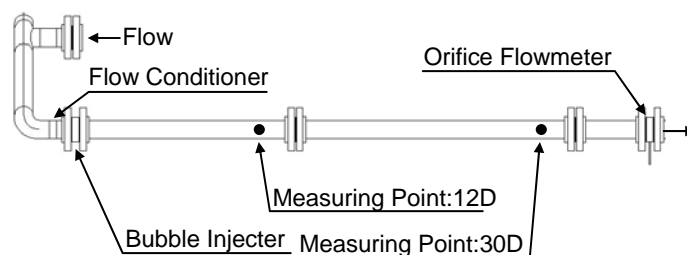

Fig.2 Sketch of the test section

3. Results

3-1 Flow pattern

Figure 3 shows the comparison of flow patterns of pipe cross section at different positions. Spatial resolutions of velocities along the radius directions are around 0.75mm. Velocities are normalized by the maximum velocity to compare the shape of velocity profile. Almost fully developed flow patterns are established at the horizontal diameter position of 30D. However, at the position of 12D, effect of elbows still produces asymmetric flow patterns which result in large errors in measurements in time-of-flight ultrasonic flow meters. In actual power plans, time-of-flight ultrasonic flow metes are usually installed at the horizontal diameter position of around 10-12D with the limitation of piping configurations, we should take these flow asymmetricity into account for determining PFs.
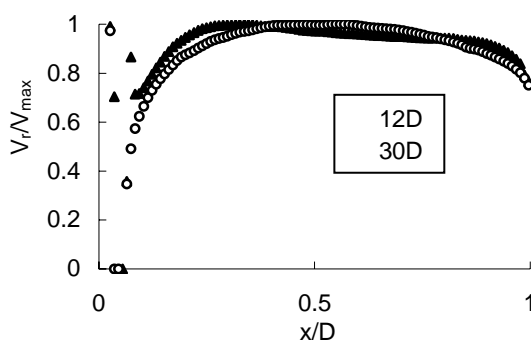

Fig.3 Flow profiles along horizontal diameter positions for Rq=5.3*10^{-6}m

Figure 4 shows the comparison of flow patterns at different Reynolds numbers. The shape of asymmetric flow patterns are strongly depending on Reynolds numbers. It may also depend on the flow conditioner configurations. In this experiment, the flow patterns change all of sudden when Reynolds number exceeds $1.5*10^5$. This result shows that we cannot extrapolate Reynolds number to determine the PFs in a real plant due to the sudden change of flow patterns. If very high accuracy, such as within 1%, is required, factory tests to determine the PFs of time-of-flight type ultrasonic flowmeters have to be conducted under

the same thermal hydraulic conditions, pipe roughness, pipe confabulations and flow conditioners as feedwater system of actual nuclear power plants.
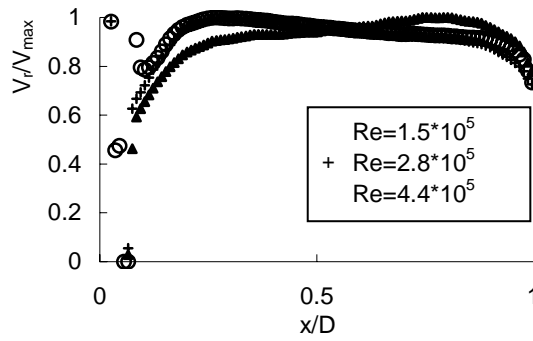
Fig.4 Flow profiles of different Reynolds number for Rq=5.3*10^{-6}m at horizontal diameter position 12D

3-2 Surface Roughness

Figure 5 and 6 show the comparison of flow patterns at three different pipe roughnesses. We can know that pipe roughness strongly affects to the flow patterns both at 12D and 30D. In both cases, the flow velocities near the pipe walls gets steeper as the increase of surface roughness which results in the increase of friction factors between fluid and pipe wall. We can hardly know how the surface roughness of a feed water piping changes during plant life time. Therefore, Even if factory tests are conducted with the piping roughness simulating the actual power plants before being installed to the actual plants, the changes of PFs as same as the flow nozzle of reactor feed water system will be observed as plants get aging.
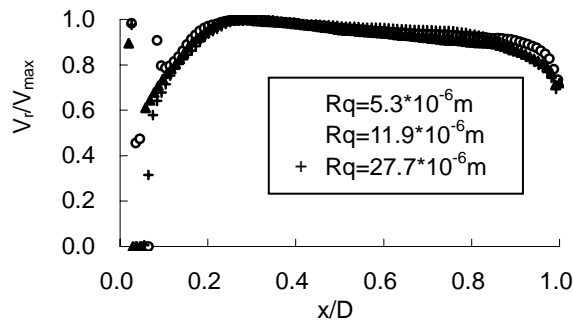
Fig.5 Flow profiles of different surface roughness at horizontal diameter position 12D
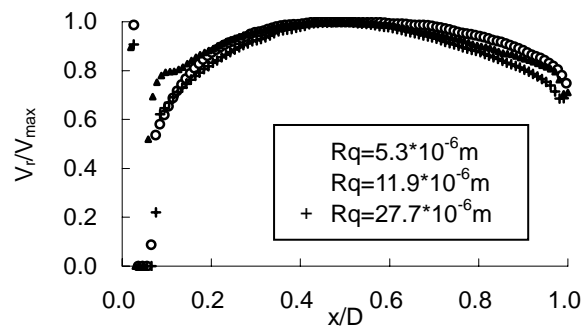and Re number is 4.4*10^5

Fig.6 Flow profiles for different surface roughness at horizontal diameter position 30D
and Re number is 4.4*10^5

3-3 Effects on Profile Factors

Figure 7 and 8 show the deviations of PFs due to the changes of Reynolds numbers and pipe roughnesses. A PF is defined as a ratio of the area-averaged velocity obtained by an orifice flowmeter to the line-averaged velocity calculated from velocity profile measured by UdFlow. The deviation of PF is calculated with the most smooth case of Rq is $5.3*10^{-6}$m and Re=$1.5*10^5$ as a reference PF value. As a result, changes of pipe roughnesses result in the changes of PFs by 6.5% at the maximum at the horizontal diameter poison 12D. Furthermore, the changes Reynolds numbers result in the changes of PFs by 2.5% at the maximum at the same surface roughness. Therefore, we should take into account those effects in order to measure the flow rates of feedwater with the accuracy better than 6.5% at the position of 12D in actual power plants.
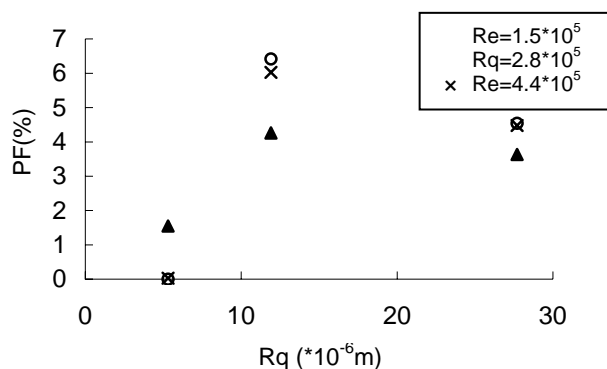

Fig.7 Percentage changes in profile factors for Rq and Re number at horizontal diameter position 12D
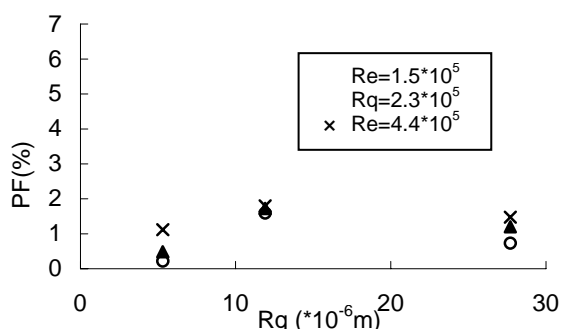

Fig.8 Percentage changes in profile factors for Rq and Re number at horizontal diameter position 30D

4. Conclusions

With an ultrasonic Doppler flow meter, we can quantify the changes of flow profiles and PFs due to pipe elbow, pipe roughness and Reynolds numbers. According to the results of this experiment, deviation of PFs could be around 6-7% at maximum, which directly affects to the estimation of flow rates.

5. Reference

(1) Tezuka, et al., Development of flow rate and profile measurement using ultrasonic Doppler method, Atomic Energy Society of Japan 2003
(2) T.T. Yeh, G.E.Mattingly, Effects of pipe elbows and tube bundles on selected types of flowmeters, Flow Measurement Instrument 1991
(3) A.Calogirou at el., Effect of wall roughness changes on ultrasonic gas flowmeters, Flow Measurement and Instrumentation 12 2001

Industrial Applications of New Type Flow-metering System by Ultrasonic-Doppler Profile-Velocimetry

(2) Measurement Experiences of Flow on Piping and Industrial applications

Michitsugu Mori[1], Kenichi Tezuka[1],

Masanori Aritomi[2], Hiroshige Kikura[2], and Yasushi Takeda[3]

[1] Tokyo Electric Power Co., Inc., Yokohama 230-8510, Japan
[2] Tokyo Institute of Technology, Tokyo 152-8550, Japan
[3] Hokkaido University, Sapporo 060-8628, Japan

Keywords: ultrasonic-Doppler, velocity profile, flowmeter, industrial application, calibration

ABSTRACT

Electric power plants with thousands of flowmeters measure the flow rates in their major processes. The circulating water (CW) pump system, which locates in the intake structure providing a continuous supply of turbine-condenser cooling water, does rarely have flowmeters due to its pipe size exceeding almost one meter, where profile factors can hardly be determined for these large pipes and high flow rate because of the difficulty of factory tests. Conventional flowmeters such as time-of-flight (TOF) ultrasonic flowmeters are sometimes used but cannot achieve the high accuracy of flow rate measurements for large pipes.

Instead of installing any flowmeters, plant operators usually estimate the flow rates to evaluate the cooling performance of the condenser with the Q-H design curve of the pump. However, this Q-H curve often drifts due to the deterioration of pump itself.

In order to achieve the high accurate flow measurement, the measurement of a flow profile should be required to eliminate a profile factor. We have conducted fields test using an ultrasonic pulse-Doppler flowmetering system to measure the flow profile of CW cooling pump flow for the case of a pipe diameter of 1.7m, where the flow rate was around 270 m^3/min. Instantaneous flow profile is widely fluctuating by almost double of the average velocity due to the turbulence of pipe flow and pulsation of CW discharge. Next step of the application of the ultrasonic pulse-Doppler system is to measure the flow rate of nuclear feed water system, with a temperature of 220 degrees C and the pressure of 7.5MPa.

1. INTRODUCTION

Integration of instantaneously-determined flow velocity-profiles, obtained from performing continuous line-measurement over piping is considered to provide an accurate flow rate measurement system as an advanced flowmeter, superior to the conventional flowmeter using a profile factor. The conventional one based on the TOF method depends largely on the accuracy of a profile factor as it finally determines the flow rate of a fluid by multiplying it. This is also true of a one-point ultrasonic-Doppler flowmeter. Accordingly, these conventional methods are limited in the scope of application as they are effective only in measuring flows with steady-state developed flow. In other words, the methods have to use an approximation that is applicable only in a narrow flow range. (**Takeda Y**., 1987, 1995).

Meanwhile, the feedwater and CW cooling systems of a power plant are generally exposed to high temperature and/or pressure condition(s) with large pipes. Therefore,
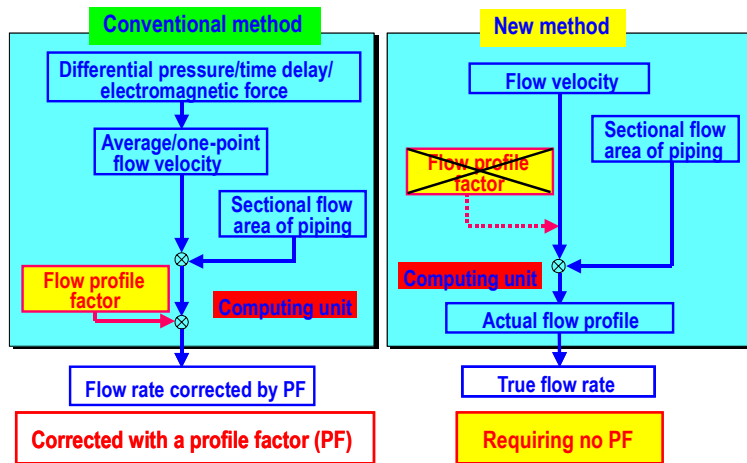
Figure 1. Conceptual Comparison between Conventional Flowmeter and Ultrasonic-Doppler Flow Velocity-Profile Flowmeter.

determining a profile factor under the same flow conditions and the configurations like large pipe diameters and curve bends is impracticable and results in certain errors in measurement. In fact, it is impossible at the present stage to determine a profile factor by a high-precision calibration loop using a weighing method under such high temperature and pressure conditions as in the feedwater or large-bore piping as in the CW cooling system for a nuclear or a fossil-fired power plants. Consequently, the profile factor has to be determined with a Reynolds number approximately one digit smaller than that of the actual plant. In the case of the CW system with a piping bore of ~3 meters for instance, a profile factor determined with the piping bore set at a fraction of the actual size is applied to the system because of constraints from the calibration facilities. The conventional ultrasonic flowmeters as described above round off all indeterminate errors by a profile factor as shown in Figure 1. To get rid of these errors, efforts are needed to eliminate the profile factor by determining flow rates based on the calculation of true flow profile in the piping. This concept is described in Figure 1. (**Takeda Y**., 1998, **Mori M**., et al., 1999, 2002)

2. APPLICATIONS FOR INDUSTRIAL POWER PLANT

In electric power plants, thousands of flowmeters are installed to measure the flow rates in major processes. Example of Applications of flowmetering systems for Boiling Water Reactor (BWR) is shown in Figure 2, in which, except for the main-steam flow rate, W_{ms}, to a turbine system, the feedwater flow rate, W_{fw}, condenser flow rate, W_c, CW cooling pump flow rate, W_{wc}, are water flows. The feedwater flow rate is significant since it affects the regulated thermal output power. The temperature of feedwater is ~220 degrees-C and the pressure is ~7.5MPa, where Reynolds Number is more than 20,000,000. These conditions hardly realize in the weighing method for calibration to determine PFs. The CW cooling flow rate is necessary to evaluate the plant efficiency; however, flowmeters are rarely found in the CW line because of its difficulty to measure the flow rates and pipe sizes beyond one meters.
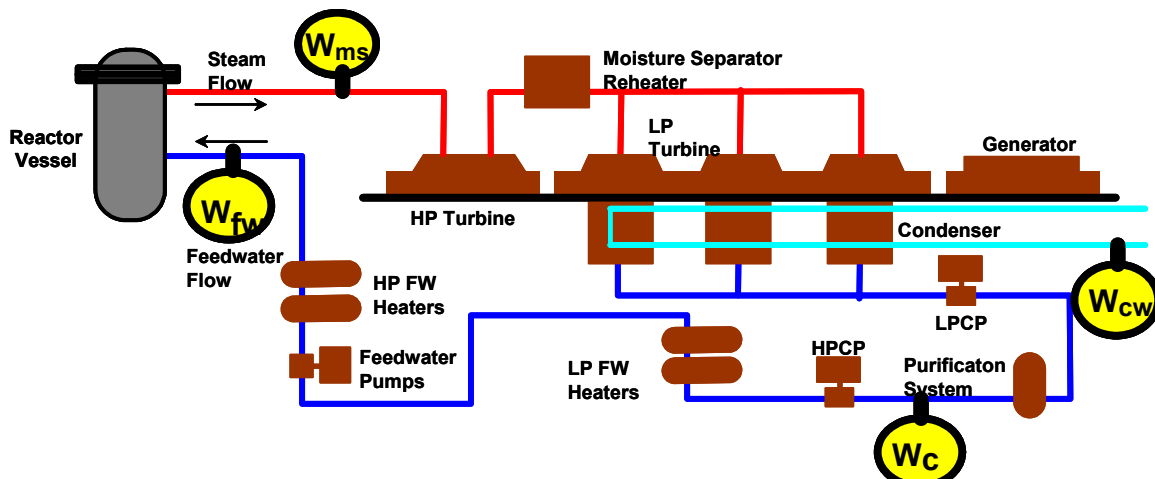

Figure 2. Example of Applications of flowmetering system for Boiling Water Reactor.
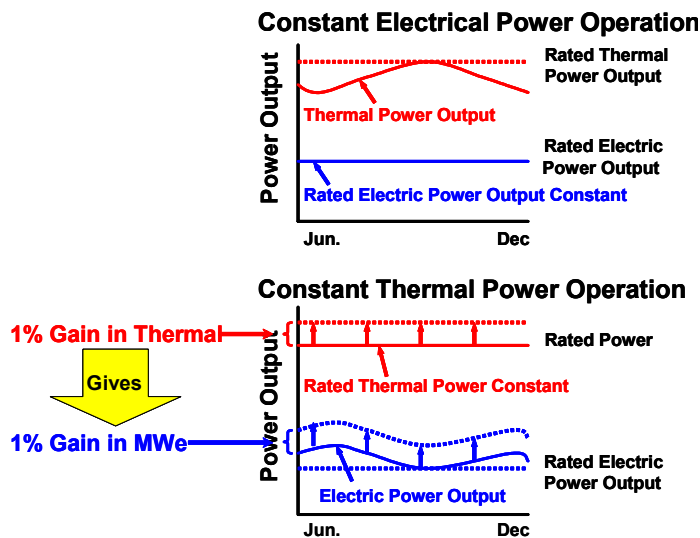
Constant Electrical Power Operation

Constant Thermal Power Operation

Figure 3. Effects of constant thermal power operation on gained electricity compared with constant electrical power operation.

Figure 3 shows effects of constant thermal power operation on gained electricity compared with constant electrical power operation. Under the constant electrical power operation, the rated electric power output is regulated as constant; on the contrary, the electric output power depends on the effective-ness of the CW cooling system by seawater temperatures in the case of the constant thermal power operation. In the latter case, any gain in thermal power provides certain gain of electricity. However, the thermal power output of a nuclear power plant is strictly regulated, which surely requires an accurate measurement of feedwater flow rates. Aged flow nozzles are considered to indicate higher values than real ones due to its deterioration and erosion. As shown in the following equation, the reactor thermal power output, Q, is significantly affected by the flow rate of feedwater, W_{fw}, the fact of which shows that it is absolutely necessary for the accurate measurement of feedwater to increase the plant availability.

$$W_S \times h_s = (Q - Q_{loss}) + W_{fw} \times h_{fw} + W_{cr} \times h_{cr} - W_{cu} \times (h_{cui} - h_{cuo}) + W_{rec} \times \Delta h_{pump}$$

Q	=	**Reactor Thermal Power**
W_S	=	**Flow Rate of Main Steam**
W_{fw}	=	**Flow Rate of Feedwater**
W_{cr}	=	**Flow Rate of Control Rod Drive System**
W_{cu}	=	**Flow Rate of Reactor Water Clean-up System**
W_{rec}	=	**Flow Rate of Recirculation System**
h_s	=	**Enthalpy of Steam**
h_{fw}	=	**Enthalpy of Feedwater**
h_{cr}	=	**Enthalpy of Control Rod Drive System**
h_{cui}	=	**Enthalpy of Reactor Water Clean-up System Inlet**
h_{cuo}	=	**Enthalpy of Reactor Water Clean-up System Outlet**
h_{pump}	=	**Recirculation Pump Heating**
Q_{loss}	=	**Heat Loss**

3. CALIBRATION TESTS

Measuring tests were conducted at the National Institute of Standard Technology (NIST), a unit under the U.S. Department of Commerce. The flow rate of water per unit length of time can be determined by accumulating in the tank the fluid flowing down the test section in a given period of time and dividing the volume of the fluid thus accumulated by the time elapsed. The nominal measurement error is 0.12%. In this test, the flow of water was measured at the part where it reached the stage of full development. The proposed ultrasonic-Doppler flow velocity-profile flowmeter was found to meet the approved values of the standard loop with an error well within 1%, proving to have sufficient accuracy. Table 1 compares the approved values of the NIST standard loop and corresponding data on the ultrasonic-Doppler flow velocity-profile flowmeter at Re = 400,000. The values of the NIST loop are based on the average of weighing time while those of the ultrasonic-Doppler flow velocity-profile flowmeter are based on the time average of instantaneous values. As

indicated in the table, the measuring test found a deviation of only 0.03% between the two devices in terms of the average of the values recorded by five rounds of measurement. From the results of measurement conducted with Re number varied, it was found that the overall average deviation between the two devices was no more than 0.2%. (**Takeda**, 2000; **Mori**, 2002)

Table 1. Comparison of the approved values of the NIST standard loop.

Table 2. Comparison of the approved values of the NMIJ standard loop.

NIST - U.S. National Institute of Standards & Technology

Run No.	UdFlow	NIST	Deviation	
			L/s	%
#1	69.760	69.600	-0.161	-0.23%
#2	69.670	69.613	-0.057	-0.08%
#3	69.725	69.612	-0.113	-0.16%
#4	69.444	69.622	0.178	0.26%
#5	69.569	69.609	0.040	0.06%
Average	69.634	69.611	-0.022	-0.03%

NMi-J - Japan National Institute of Advanced Industrial Science and Technology

Reference Flowrate Q_1 (m³/h)	Output of Flowmeter under Test Q_{fn} (m³/h)	Ratio of Flowrate and Uncertainty	
		Ratio Q_{fn}/Q_1	Expanded Uncertaintly (k = 2)
2000.5	2008.9	1.004	0.4%
1512.7	1508.2	0.997	0.1%
986.1	984.6	0.999	0.3%

Further calibration tests were conducted on the ultrasonic-Doppler flow velocity-profile flowmeter by a liquid flowmeter calibration facility, a verification loop, at the National Metrology Institute of Japan (NMIJ), suborgan of the National Institute of Advanced Industrial Science and Technology (AIST), an independent governmental corporation, and Nederlands Meetinstituut (NMI). In NMI, the calibration tests were carried out for water and kerosene. The calibration facility (made to the national standard) has the standard uncertainty set at 0.02% of the reference flow rate. The calibration tests on the ultrasonic-Doppler flow velocity-profile flowmeter were carried out with a measuring instrument attached to the 400A piping section of the facility. The results of the test at NMIJ and NMI are summarized in Table 2, and Table 3, respectively. The test findings indicate the uncertainty of the flowmeter examined in terms of the average of the results recorded in 10 rounds of measurement, compared with the reference flow rate set as a target. Based on the measuring test, the ultrasonic-Doppler flow velocity-profile flowmeter was given a calibration certificate showing an uncertainty range of 0.1% to ~0.5% for water.

Table 3. Comparison of the approved values of the NMI standard loop for water (left) and kerosene (right).

NMi - Nederlands Meetinstituut

Reference Flow-rate [l/min]	Reference Velocity [m/s]	Indicated Flow-rate [l/min]	Indicated Velocity [m/s]	Deviation [%]
1276.7	1.2041	1273.1	1.2007	-0.28
1276.6	1.2040	1280.7	1.2079	+0.32
1276.8	1.2042	1271.7	1.1994	-0.40
953.76	0.8995	959.4	0.9048	+0.59
953.41	0.8992	952.8	0.8986	-0.07
953.74	0.8995	949.1	0.8951	-0.49
632.02	0.5961	633.9	0.5979	+0.30
631.82	0.5959	628.5	0.5928	-0.52
632.04	0.5961	630.1	0.5943	-0.30

Reference Flow-rate [l/min]	Reference Velocity [m/s]	Indicated Flow-rate [l/min]	Indicated Velocity [m/s]	Deviation [%]
1276.6	1.2040	1279.5	1.2067	+0.22
1276.4	1.2038	1281.3	1.2084	+0.38
1276.5	1.2039	1281.5	1.2086	+0.39
956.19	0.9018	949.3	0.8953	-0.72
956.54	0.9022	959.1	0.9046	+0.27
955.92	0.9016	955.4	0.9011	-0.06
639.51	0.6032	641.1	0.6046	+0.23
639.49	0.6031	643.6	0.6070	+0.65
639.30	0.6029	643.90	0.6073	+0.73

4. FIELD APPLICATION EXPERIMENTS

The field tests were carried out to extend the applicability of the ultrasonic-Doppler flow velocity-profile flowmeter. Table 4 shows the field application experiences of Ultrasonic-Doppler flow velocity-profile flowmeter. The flow rates of the condenser circulation water (CW) were successfully measured for the pipe sizes of 1.5m and 1.7m, where the sufficient ultrasonic reflectors existed in the flow of the pipes to measure the velocity profiles because of low system pressure. The following all cases in Table 4 were measured with a clamp-on type ultrasonic-Doppler flow velocity-profile flowmeter.

Figure 4 shows the measurement result of fields test using an ultrasonic pulse-Doppler flowmetering system for CW cooling flow for the case of a pipe diameter of 1.7m. The time-averaged flow velocity-profile of large pipe with D=1.7m well predicted the parabolic flow profile. Integrating the flow velocity-profile by half over the pipe section provides the flow rate. Figure 5 shows the instantaneous flow profile widely fluctuating by almost double of the average velocity due to the turbulence of pipe flow and pulsation of CW discharge. The parabolic flow profile shown in Figure 4 comes from averaging the instantaneous flow profiles widely fluctuating by almost double of the average velocity. These information could be blind for conventional TOF ultrasonic flowmeters.

Table 4. Field application experiences of Ultrasonic-Doppler flow velocity-profile flowmeter.

| System	Pipe Size (m)	Wall Thickness (mm)	Wall Material	Fluid Type	Flow Rate (m^3/min)	Results
Feedwater Pump Bearing Seal Water	0.1	6	Carbon Steel	Condensate Water	0.5	Succeeded
Turbine EHC	0.05	4	Stainless Steel	Mineral Oil	0.01	Succeeded
Plant Discharge Water	0.1	6	Carbon Steel	Water	0.5	Succeeded
Condenser Circulation Water	1.5	14	Carbon Steel	Seawater	450	Succeeded
Condenser Circulation Water	1.7	14	Carbon Steel	Seawater	520	- Succeeded - Bubbles Injected
Hydro Turbine	3.8	12	Carbon Steel	Water	2400	- On-going
Reactor Feedwater Pump Discharge	0.36	28	Carbon Steel	Condensate Water	800	- On-going
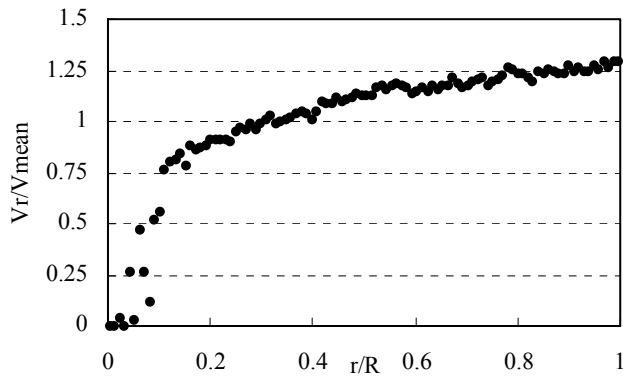
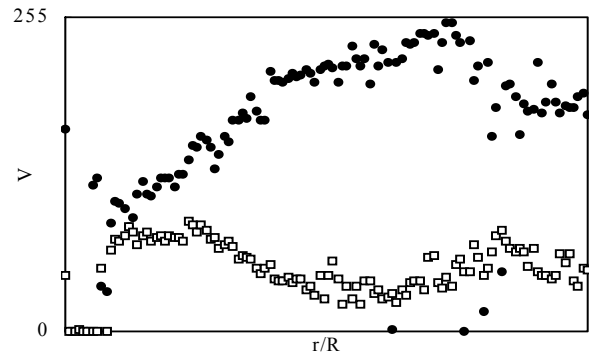**Fig.4 Time-averaged flow profile of large pipe D=1.7m**

Fig.5 Instantaneous flow profile of large pipe D=1.7m

5. REMARKABLE SUMMARY

The ultrasonic-Doppler flow velocity-profile flowmeter proposed is a new device which, unlike the conventional flowmeters, theoretically dispenses with a profile factor (i.e., adjusting factor) and is capable of accurately measuring true values at the work site of a plant without using some arbitrary adjusting factors. Field applications using the ultrasonic-Doppler flow velocity-profile flowmeter were tested in the various flow and pipe conditions. It is expected that the ultrasonic-Doppler flow velocity-profile flowmeter, with these advantages, will be applied to on-site measurement of true flow rates in large-bore pipes or the calibration of existing flowmeters and pumps installed in pipelines, thereby contributing to the improvement of plants and equipment in efficiency and to the reduction of their maintenance costs.

REFERENCES

Takeda Y.(1987). *Measurement of velocity profile of mercury flow by ultrasound Doppler shift method*, Nuclear Technology, 79, pp 120-124.

Takeda Y. (1995). *Velocity profile measurement by ultrasonic Doppler method,* Experimental Thermal and Fluid Sci., 10, pp 444-453

Takeda Y. et. al. (1998). *Development of flow rate measurement using ultrasonic Doppler method (1) Theoretical background,* 1998 Fall Meeting of AESJ, F16, p.343

Mori M. et. al. (1999). *Development of ultrasonic-Doppler velocity profile method for flow rate measurements of power plant,* ICONE-7, FP7429

Takeda Y. et. al. (2000). *Development of a new flow metering system using UVP, Preliminary performance assessments using NIST flow standards,* Proceedings of ASME FEDSM'00, ASME 2000 Fluids Engineering Division Summer Meeting, June 11-15, Boston, Massachusetts.

Mori M. et. al. (2002). *Development of a novel flow metering system using ultrasonic velocity profile measurements,* Experiments in Fluids, 32, pp.153-160

Mori M. et. al. (2002), *Industrial Application Experiences of New Type Flow-metering System based on Ultrasonic-Doppler Flow Velocity-Profile Measurement,* 3rd ISUD

DEVELOPMENT OF FLOW RATE MEASUREMENT ON OPEN CHANNEL FLOW USING ULTRASONIC DOPPLER METHOD

Takashi Arimatsu*, Sanehiro Wada*, Hiroshige Kikura*, Masanori Aritomi*
and Michitsugu Mori**

*Research Laboratory for Nuclear Reactors, Tokyo Institute of Technology, 2-12-1 Ohokayama, Meguro-ku, Tokyo, 152-8550 Japan, e-mail: arimatsu@2phase.nr.titech.ac.jp
**Tokyo Electric Power Company, 4-1 Egasaki-cho, Tsurumi-ku, Yokohama, 230-8510 Japan

ABSTRACT

This paper presents the velocity profiles and the accurate flow rate measurements on open channel flow using Ultrasonic Doppler method. In this study, the accurate flow rate was calculated by integrating the velocity distributions over the cross section. The flow rate measurements were carried out on three different conditions. The flow rate measured by this method was compared with the flow rate measured by Electromagnetic flow meter and the results show the errors were less than 6%.

Keywords: ultrasonic Doppler velocity profiler, open channel, velocity profile, multiline measurement, flow rate

INTRODUCTION

Many instruments, working on a variety of principles, have been developed to measure velocity profiles in an open channel. The information of liquid velocity distribution over the cross section is necessary for the flow physic study. For the measurement in an open channel, many attempts [1] have been conducted such as hot film anemometry [2] and Laser Doppler anemometry [3]. However, those devices provided only the local information in a single point. The multi-dimensional properties such as velocity profile and time-dependent flow rate is still difficult to measure simultaneously. This limitation becomes worse in the case of the measurement in the application with time dependent cross-sectional area change, i.e. the measurement in the river with sand bottom and with sludge accumulation.

Recently Ultrasonic Velocity Profiler (UVP) has been developed and applied to measure local instantaneous flow properties along the measuring line [4][5]. Thus, it is able to improve the flow metering performance and to be applied for a transient flow rate measurement. In this measuring system, flow rate was calculated using the velocity profiles that were obtained by UVP. Wada et al. [6] applied three transducers to evaluate the more accurate time-dependent liquid flow rate in developing regime in vertical circular pipe. The results show that the errors were less than 1%. Tezuka et al. [7] investigated the effect of the inner surface roughness of a pipe on the velocity profiles and flow rate measurement. They showed that the error was up to 8%. However, the assumption of velocity profiles was required to measure the time-dependent flow rate.

According to the available literatures, the multi-line measurement has been conducted mostly in the pipe flow where the cross-section area is constant. From this point of view, the objective of this paper is to develop the multi-line flow rate measurement using Ultrasonic Doppler in an open channel where the cross-section area is varied in time domain.

EXPERIMENTAL APPARATUS

The experimental apparatus are illustrated in Fig.1.The experiment was carried out in the open channel. The open channel was made of acrylic resin, with length 3200mm, height 200mm, and width 100mm. The flow rate in open channel was adjusted by the flow rate in bypass using valve. The water level was adjusted by the supplied flow rate into open channel and the height of dam at the downstream end of the channel. The height of dam was 50mm in this experiment. Due to the area expansion at the entrance, the water level fluctuation would be induced. In this case, the surface flow was kept stable by the rectifier at the entrance of the open channel. The flow rate in open channel was monitored by electromagnetic flow meter (MGK1010K, Tokyo Keiso).
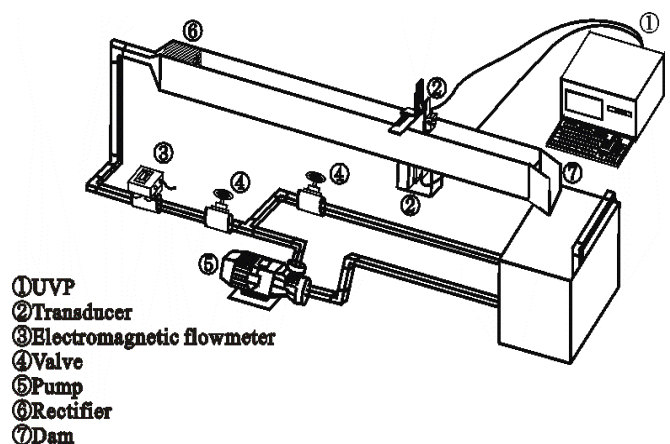

①UVP
②Transducer
③Electromagnetic flowmeter
④Valve
⑤Pump
⑥Rectifier
⑦Dam

Fig.1 Experimental apparatus

VELOCITY MEASURMENT

The measuring system consists of the ultrasound velocity profile monitor (UVP model X3-Psi, Met Flow). The working frequency of the ultrasonic transducer is 8 MHz. The transducer was set up at the free surface with an angle of 70 ° with respect to the mean flow parallel to the open channel axis. The nylon micro tracer particles (WS-200P, Daicel Hüls) are utilized to trace the liquid velocity. Their average diameter was 80 μ m. Experiments were carried out at atmospheric temperature, water temperature was kept at 22   using the sub cooler. In order to indicate flow condition, liquid velocities along the centre-plane at the position of 100mm, 200mm, 400mm, 800mm, 1600mm, and 2400mm were measured. Furthermore, liquid velocity distribution over the entire cross-section was also measured at the position of 2400mm downstream from the entrance with 31 measuring points in the span wise direction.

In order to clarify the effect of transducer position, the comparison of the velocity profiles obtained from upper and lower position of the channel was performed. The measuring configuration was shown in Fig.2. Transducer for lower position was placed in small acrylic resin box below the channel. The space of the box was filled with the water and covered with acrylic resin wall with 2 mm thickness. For the upper position, transducer was placed at the free surface with an angle of 70 ° with respect to the mean flow direction. The accuracy measurement of Ultrasonic Doppler method using both upper and lower transducer position was also verified by comparing with the standard device, Electromagnetic Current Meter (VP1000RT and VPT-400-09PS, KENEK). The comparison was performed at the distance of 2100 mm from the entrance on the centre plane of the channel.
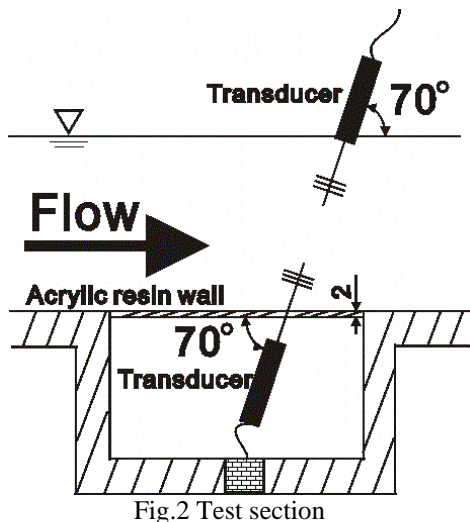
Fig.2 Test section

FLOW RATE MEASUREMENT

It is known that the variation of transducer position and angle affects directly to the measurement of velocity distribution and water level. In this case, liquid velocity distribution and water level shall be reported by changing the transducer position in traverse direction with the constant measuring angle.

By using the obtained liquid velocity distribution, the liquid flow rate can be calculated by integrating the local velocity distributions bover the entire cross section using the upper transducer. The velocity at the wall was treated as no-slip condition. The flow rate was calculated by Eq. (1). [8]

$$Q=\sum_{p=1}^{m}\sum_{i=1}^{n}\frac{\Delta l \cdot \Delta z}{4}\left(v_{p,i}+v_{p,i+1}+v_{p+1,i}+v_{p+1,i+1}\right) \quad (1)$$

m: Number of measurement points on cross section,
n: Number of measurement cubic in axial direction,
  l: Spatial resolution in span wise direction,
  z: Spatial resolution in vertical direction,
v: Local time-averaged liquid velocity

The measurements were carried out on steady (normal condition) and unsteady condition (condition A and B). The unsteady flow was generated, in this case, by applying the solid obstacle to disturb the flow. The utilized obstacle that was made of acrylic resin has the dimension of 30x50x200 mm³. The obstacle configuration for condition A and B is illustrated in Fig. 3.
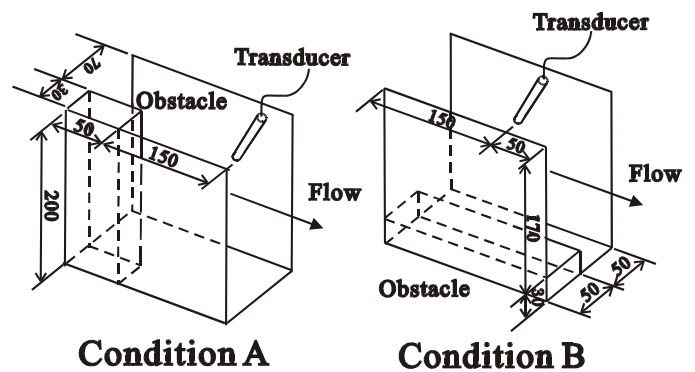

Condition A   **Condition B**
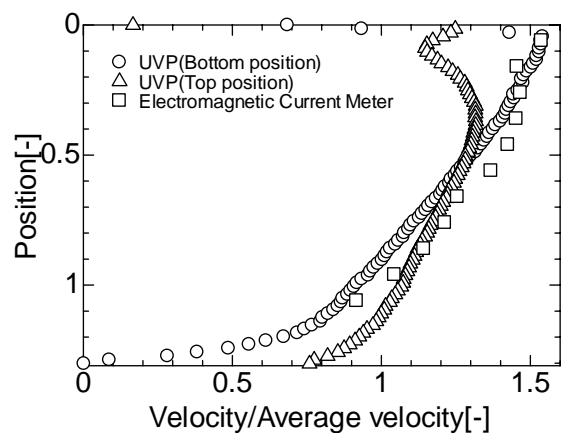Fig.3 Experimental condition A and B

Fig.4 Liquid velocity distribution between upper and lower position of transducer comparing with Electromagnetic current meter
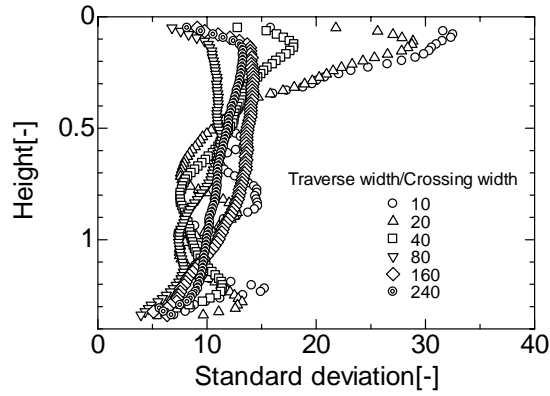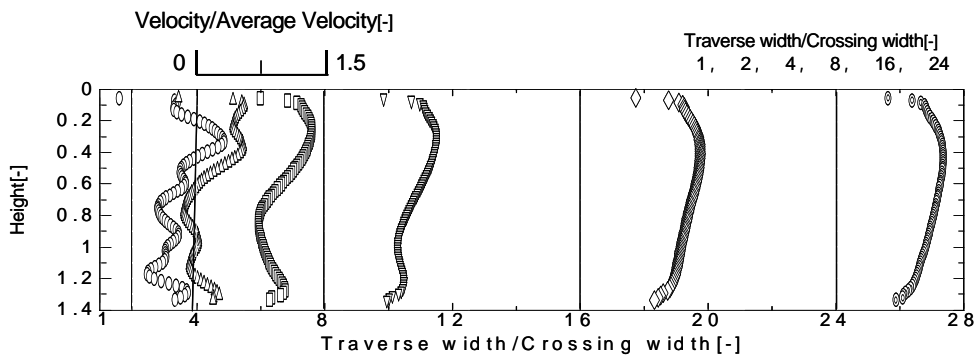
Fig.5 Standard deviation of profiles

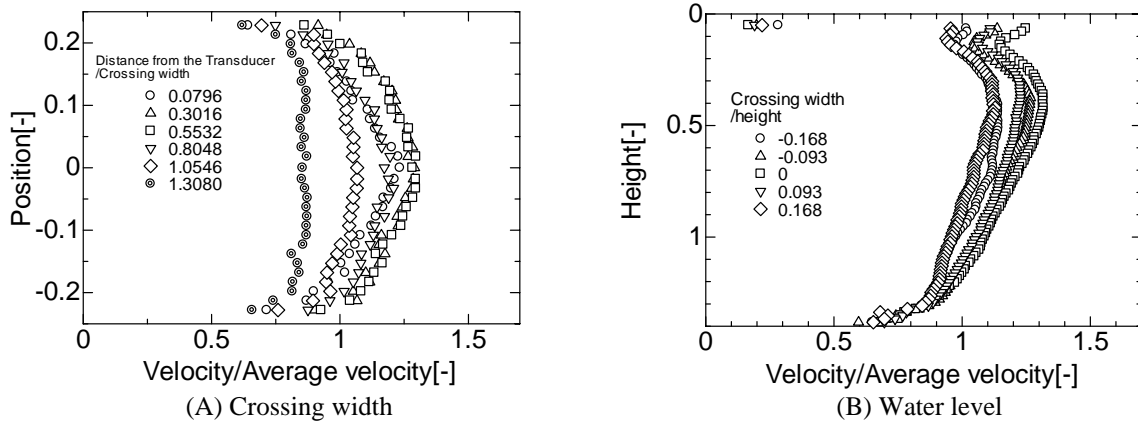Fig.6 Velocity distributions on the centre-plane

(A) Crossing width

(B) Water level

Fig.7 Velocity distributions on normal condition

(A) Crossing width

(B) Water level

Fig.8 Velocity distributions on condition A
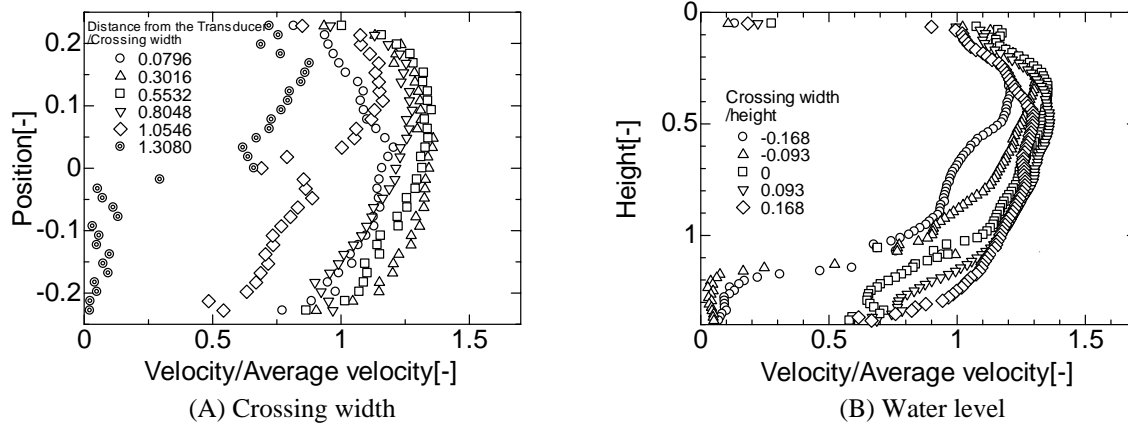
(A) Crossing width   (B) Water level
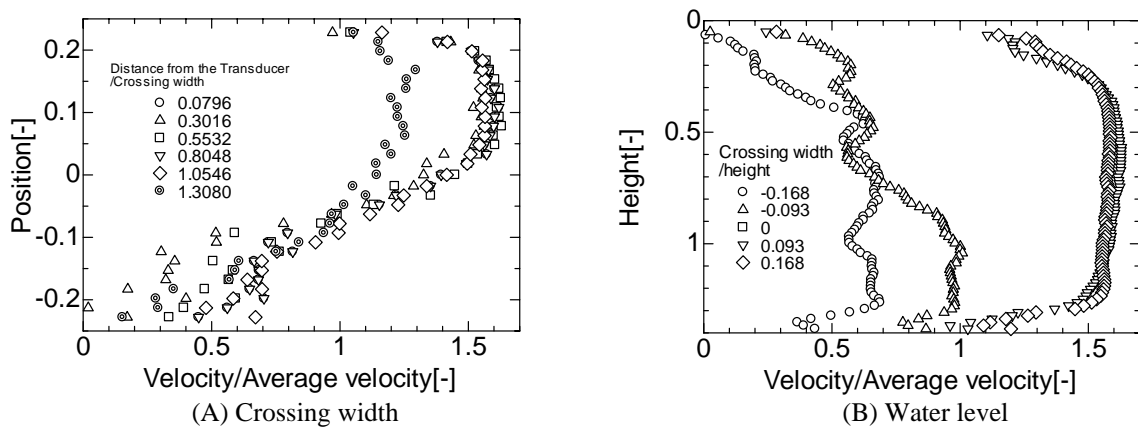
Fig.9 Velocity distributions on condition B

RESULTS AND DISCUSSION

The results of mean velocity distributions obtained by UVP and Electromagnetic current meter were shown in Fig.4. The good agreement was found for lower transducer position, while the slightly deviation was observed for the upper transducer position. The larger deviation for the upper transducer comparing with the lower one can be explained by the water level fluctuation of the free surface near the ultrasonic transducer.

Fig.5 shows the standard deviation of velocity profiles on the centre-plane. It can be seen that the scattered velocity was enhanced particularly near the entrance, water surface and bottom regime. Fig.6 shows the velocity distributions on the centre-plane. It can be seen that the velocity distributions near the entrance has no exactly flow pattern. Furthermore, the fully-developed velocity distribution is observed at the position of 1600mm downstream from the entrance quite far from the inlet.

The flow rate measurement was performed at the distance of 2400mm from the entrance to avoid the unsteady condition near the entrance. Fig.7 shows the velocity distributions in span-wise direction (Fig.7 (A)) and the variation of water level (Fig.7 (B)) under normal condition. It can be seen the small deviation between each profile referring to the steady condition. Similar to Fig.7, the results of unsteady condition A and B is illustrated in Fig. 8 and Fig. 9 respectively. As the results, large deviations are observed between each profile due to the high unsteady level generated from the obstacle.

Table 1 shows the result of the liquid flow rate calculation according to Eq. (1) and compared with the standard device using electromagnetic flow meter. The overall deviation is less than 6 %. These errors probably cause by the water level fluctuation on the free surface. This can be seen from the larger deviation of steady normal condition and unsteady condition B comparing with unsteady condition A. Therefore, it is possible to measure not only the steady flow rate but also the unsteady flow rate.

Table 1. Result of the flow rate measurements

Condition	Electromagnetic flowmeter (l/min)	This method (l/min)	Error (%)
Normal condition	56.7	54.4	4.1
Condition A	55.3	54.3	1.8
Condition B	55.0	52.0	5.5

CONCLUSION

Ultrasonic Doppler method was applied to the open channel flow. The information of velocity distribution and water level in term of the transducer position and its angle were obtained. The velocity distributions obtained by UVP were applied to calculate the liquid flow rate particularly under the unsteady condition. The results show that it is possible to measure not only the steady flow rate but also the unsteady flow rate accurately. Finally, the effect of water level fluctuation near the transducer is revealed. In this case, some measrument correction is required to minimize the overall error generated during the measurement.

REFERENCES

1. U.Lemmin , T.Rolland, 1997, Acoustic Velocity Profiler for laboratory and field studies, *J. Hydr.Engrgl.,* pp. 1089-1098.
2. M. Bayazit,1976, Free surface flow in a channel of large relative roughness, *J. Hydr.Res.,* 14(2), pp. 115-126.
3. I. Nezu , W.Rodi, 1986, Open channel flow measurement with a Laser Doppler Anemometer, *J. Hydr.Engrg.,* 112(5), pp. 335-355.
4. Y. Takeda, 1987, Measurement of velocity profile of mercury flow by ultrasound Doppler shift method, *Nucl. Technol.,* 79, pp. 120-124 .
5. Y. Takeda, 1995, Velocity profile measurement by ultrasonic Doppler method. *Exp. Therm. Fluid Sci.,* 10, pp. 444-453.
6. S. Wada, et al., 2004, Development of pulse ultrasonic Doppler method for flow rate measurement in power plant (Multilines flow rate measurement on metal pipe), *Nuc. Sci. Technol.,* vol. 41, No. 3, pp. 1-8.
7. K. Tezuka, et al., 2003, Development of flow rate and profile measurement using ultrasonic Doppler method (17) Effects of pipe elbows on swirl and Reynolds number changes" *Fall Meeting of the Atomic Energy Society of Japan*, F43, pp.24-26.
8. S.Wada, et al., 2003 Environmental flow mapping using ultrasonic Doppler method, *FLUCOME*, 7th,CD-R paper No.ID-85, pp.1-6.

CHARACTERISTICS OF SOUND PRESSURE DISTRIBUTION ON ULTRASONIC DOPPLER METHOD

Sanehiro Wada*, Hiroshige Kikura*, Yoshikazu Koike**, Masanori Aritomi* and Michitsugu Mori***

* Research Laboratory for Nuclear Reactors, Tokyo Institute of Technology,
2-12-1 Ohokayama, Meguro-ku, Tokyo, 152-8550 Japan, e-mail: sane@2phase.nr.titech.ac.jp
, ** Shibaura Institute of Technology, 3-9-14 Shibaura, Minato-ku, Tokyo, 108-8548, Japan,
e-mail: koikey@sic.shibaura-it.ac.jp
*** Tokyo Electric Power Company, 4-1 Egasaki-cho, Tsurumi-ku, Yokohama, 230-8510 Japan,
e-mail: michitsugu.mori@tepco.co.jp

ABSTRACT

Ultrasonic Doppler method (UDM) for a flow metering system has been developed. The method has the capability to obtain instantaneous velocity profiles along the ultrasonic beam. Our purpose is to apply UDM to a flow rate measurement of a circular pipe flow. The principle of the flow measurement method is based on the integration of an instantaneous velocity profile over a pipe diameter. Hence, the accuracy of the flow rate directly depends on the accuracy of velocity profiles measured by UDM. Reflection, diffraction and inflection of ultrasound occur at the boundary of two materials, which have different acoustic impedance. And the transmission coefficient depends on the incident angle of ultrasonic beam, the difference between their acoustic impedance, the thickness of the pipe wall, and the basic frequency of the ultrasound. In this paper, a sound pressure distribution through a metallic plate at each incident angle has been investigated, and considering the results a precise flow rate could be measured when the difference of the acoustic impedance is large and the wall thickness is not same order of the wavelength.

Keywords: sound pressure distribution, transmission of ultrasound, ultrasonic Doppler method, velocity profiles, and metallic pipe wall

INTRODUCTION

As a new flow metering system in a circular pipe, ultrasonic Doppler method has been developed [1][2]. This method has a capability of measuring the instantaneous velocity profile in a pipe over a diameter directly, so it is expected to improve the flow metering performance to be applicable for a transient flow measurement. In order to establish the technique and investigate its absolute accuracy, the comparison among experimental results has been performed at the National Institute of Science and Technology (NIST) flow standards located in Gaithersburg, MD, USA [3]. These results showed that the difference between the averaged ultrasonic Doppler method values and NIST gravimetric measurement were about 0.18%.

The laboratory experiments appeared that for fully developed flow condition an accurate measurement of flow rate was achievable using only a single measuring line, and additionally, for non developed flow which is located just below the bend pipe the multilines method was successfully applied and the errors were less than 1% [4]. However, the results of that the velocity profiles in both near region from the metallic pipe wall were disturbed using nylon powder as ultrasonic reflectors also have been reported. Therefore, when this method applies to a metallic pipe increased the diameter or the thickness, there is a possibility to decrease the precision of a flow rate measurement. This is because that an echo reflected from a boundary of a pipe wall and resonated especially in a metallic pipe wall is very strong. Additionally, an ultrasound

through a large metallic pipe might be attenuated, so that the signal-to-noise ratio of detected echo is reduced.

The available ways to overcome these challenges are to consider the effects of a material and thickness of a pipe, a ultrasonic frequency, and an incident angle to a transmission coefficient. The experimental results showed that when a metallic pipe wall is one half-wave length of ultrasound, the velocity profiles and the flow rate would give the most promising accuracy [5].

Therefore, we described about the effects of an incident angle in this paper, when the difference of the acoustic impedance is large and the wall thickness is not same order of the wavelength. A sound pressure distribution through a carbon steel plate at each incident angle has been investigated. And then considering the results, precisions of velocity profiles and flow rates have been estimated.

SOUND PRESSURE DISTRIBUTION

As the container material of the pipe in power plants and industrial plants is a metallic, the transmission of the ultrasonic beam through the metallic wall is important. The propagation and transmission of ultrasound wave follow the common optical law. Reflection, diffraction, inflection and so on occur at the boundary of two materials that have different acoustic impedance. And in solids, both of a longitudinal and a shear wave, which refractions are different, are generated. Table 1 shows the critical angles of both a longitudinal and a shear wave in carbon steel from water.

Table 1 Critical angle of a longitudinal and a shear waves in plexiglass and carbon steel from water

	US velocity [m/s]		Critical angle [deg.]	
	Long.	Shear	Long.	Shear
Water	1,480	-	-	-
Plexiglas	2,350	1,460	39.0	-
Carbon steel	5,950	3,240	14.4	27.2

Experimental setup and method

Fig.1 is the schematic diagram of the measuring a sound pressure distribution, which consists of a transmitting and receiving system of ultrasound, and a test section. Fig.2 shows the photographs of the test section. Pulse ultrasound is transmitted from a transducer connected to X-3 PS-i model

Ultrasonic Velocity Profiler
Transducer
    oscilloscope
Ultrasonic hydrophone

Trigger line
Plexiglass box
    stage
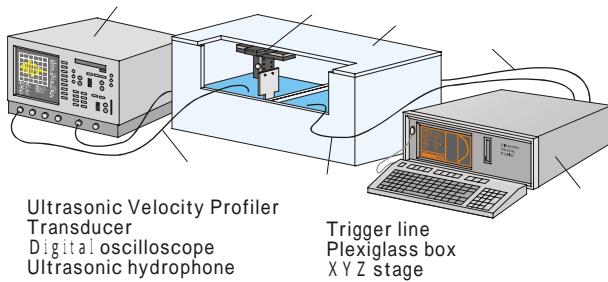
Fig.1 Experimental setup for measuring ultrasound pressure distribution

640 mm
250 mm
350 mm

2MHz Transducer

Ultrasonic hydrophone
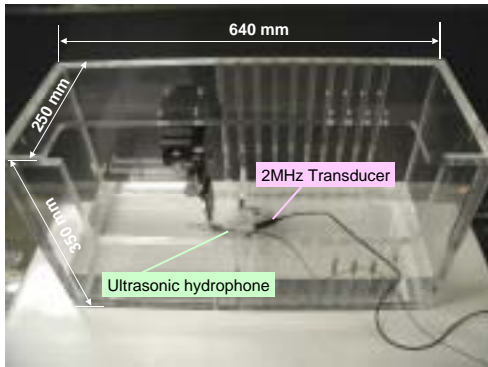
(a) Water box
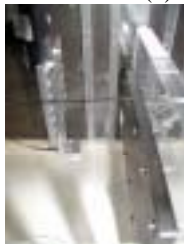
(b) Ultrasonic hydrophne   (c) Transducer
Fig.2 Phtographs of the test section
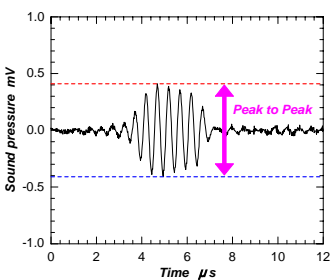
Fig.3 A typical example to calculate a sound pressure
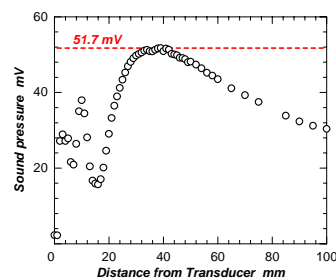
Fig.4 Sound pressure distribution along a center line of a beam without plates

Ultrasonic Velocity Profile monitor (Met Flow AG). The beam diameter and the basic frequency are 10 mm and 2 MHz respectively. And then, the pulse is received using a ultrasonic hydrophone connected to a digital oscilloscope (LeCroy: C574AL). The effective and outer diameters of the hydrophone are 0.5 mm and 1.4 mm respectively, and since the hydrophone is placed on a XYZ stage, this system can scan the detail sound pressure filed.

As a metallic plate, carbon steel (SS400) is applied and the thickness is 10 mm. To estimate the effect of an incident angle, the transducer is set up from 5 to 28 degrees, and the hydrophone is traversed along the plate keeping 10 mm from the plate surface.

A transmitted pulse ultrasound from the transducer is detected like Fig.3 by the hydrophone. In this study, a sound pressure of this signal is calculated adopting the peak to peak value. And to difine a transmission coefficient of ultrasound through a metallic plate, the value of the peak to peak is nomalized by a maximal value of a transmissted beam. Fig.4 shows an experimental result of a sound pressure distribution along a center line of the ultrasonic beam without plates.We emploied the maximal value of the sound pressure, 51.7 mV for normalizing.

Results and discussion

The transmission coefficients at each incident angle are plotted against the distance from the edge of the transducer in Fig.5. At 5 and 10 degrees, some maximal peaks are appeared because of the pulses reflecting in the plate and the existence of the both longitudinal and shear waves in the plate. On the other hand, at from 15 to 20 degrees, one strong and narrow peak is formed. Considering the longitudinal ciritical angle is 14.4 degrees (Table 1), this strong and narrow peak is attributed to the shear wave. At 25 and 28 degrees, the peak width becomes broader as increasing the angle due to the beam width on the scanning line increases.

Fig.6 shows the maximum values of the transmission coefficients at each incident angle in Fig.5. It can be seen that at small angle, around 5 degrees, the coefficient has a maximal peak owing to the longitudinal wave, and additionally at around 18 degrees, another maximal peak which is higher than at 5 degrees is expressed due to the shear wave.

VELOCITY PROFILES AND FLOW RATES

Experimental apparatus and method

Considering the results described above, velocity profiles and flow rates have been measured using UDM. The experimental apparatus consists of a water circulation system, a test section and a measurement system. Fig.7 is the schematic diagram of this apparatus, which was designed and built in to emphasize on the formation of fully developed turbulent pipe flow in both downward and upward directions. In this study, single-phase turbulent pipe flow in upward direction was investigated. Water is circulated by a centrifugal pump from the storage tank into the pipe. The vertical pipe is made of plexiglass, which total length, inner diameter and wall thickness were 6 m, 50 mm and 5 mm, respectively. The flow rate is regulated by the needle valve and monitored by flow orifices and pressure sensor located upstream of the test section. The measuring point was located at 90D downstream from the pipe inlet. The material of the test section is carbon steel (SS400) and the wall thickness is 5 mm.

Velocity profiles were collected using UVP monitor at each incident angle. The basic frequency, beam diameter and distance of measurement volumes are 2 MHz, 10mm, and

(a) 5 deg.

(b) 10 deg.

(c) 15 deg.

(d) 17 deg.

(e) 18 deg.
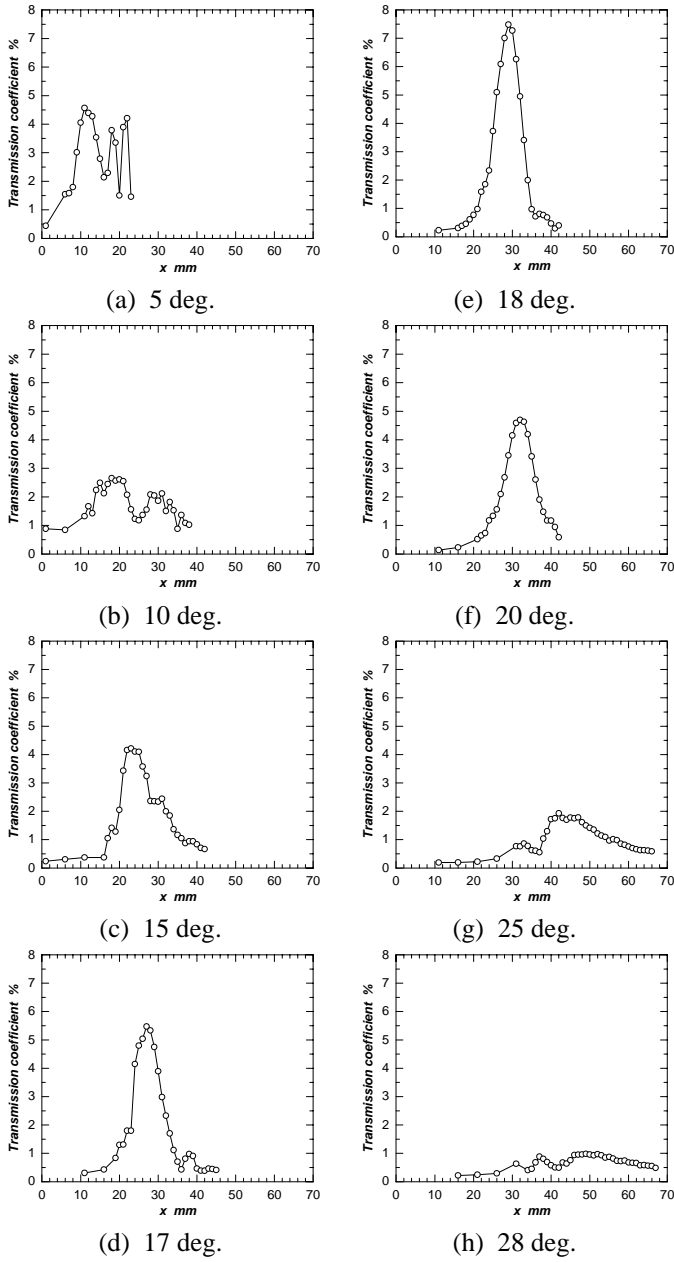
(f) 20 deg.

(g) 25 deg.

(h) 28 deg.

Fig.5 Transmission coefficients of ultrasound
through a carbon steel plate (thickness = 10 mm)

Fig.6 Maximum of transmission coefficients
at each incident angle in Fig.5

0.74mm respectively. For reflectors of ultrasound, small bubbles mixing in the pump is suspended in water with the Reynolds number of 24,000.

UDM for a flow rate measurement requires only a single transducer whereby the measurement line goes through the center of a pipe. If a flow is axially symmetric, the flow rate can be obtained accurately by integrating the half of the velocity profile using Eq. 1, which is obtained from the measuring line on the diameter:

$$Q(t) = \frac{\pi}{3}\left\{ \frac{R_0^3 - R_1^3}{R_0 - R_1} v_0 + \sum_{i=0}^{n-2}\frac{R_{i+1}^3 - R_{i+2}^3}{R_{i+1} - R_{i+2}}(v_{i+1} - v_i) + R_n^2 v_n \right\} \qquad (1)$$

where R_i is the distance from the center of the pipe to the measuring point, and v_i is the velocity of the point.

Results and discussion

The mean velocity profiles at each incident angle are illustrated in Fig.8. The typical data set consists of 1024 instantaneous velocity profiles. As shown in Fig.8, The left half velocity profiles, which are near side from the transducer, is disturbed, and especially at under 15 degrees the disturbed area is larger. Because when the incident angle is small the reflection from the front pipe wall and ringing in the pipe is very strong. Compared Fig.8 with Fig.5, it can be seen that the accuracy of velocity profiles depend on the strength of the transmission coefficient.

As mentioned above, since the left half velocity profile is disturbed, a flow rate is calculated by the right half velocity profile in this paper. The comparison of errors and standard deviations between the measured flow rate using UDM and the volumetric flow rate with respect to the incident angle is illustrated in Fig.9 and Table 2. At less than 15 degrees, the error value increases as increasing the incident angle, due to the longitudinal wave strength becomes weaker. In the opposite, at more than 15 degrees the error decreases, and at around 19 degrees it takes the minimal value, 1.6 %. This is because that the transmission coefficient of the shear wave generated in the pipe wall has the maximum value. Then, over

1. Pump
2. Storage tank
3. Overflow tank
4. Test pipe
5. Needle valve
6. Flow orifices
7. Subcooler
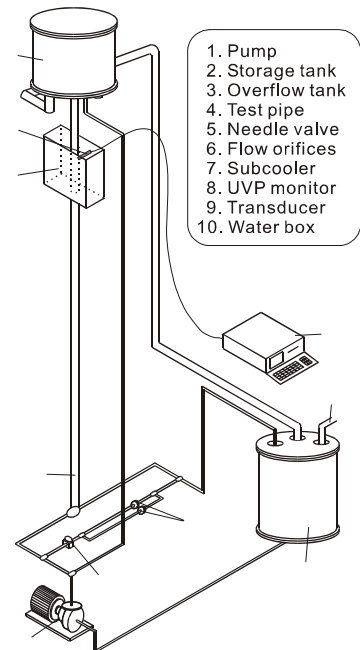8. UVP monitor
9. Transducer
10. Water box
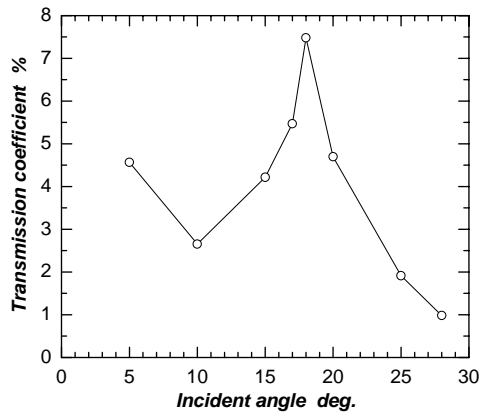
Fig.7 Experimental apparatus for measuring a velocity
profile and a flow rate

19 degrees the strength of ultrasound occurred by the shear wave in the pipe wall becomes weaker, so that the error of the flow rate increases.

(a) 5 deg.

(b) 10 deg.

(c) 15 deg.

(d) 18 deg.

(e) 19 deg.

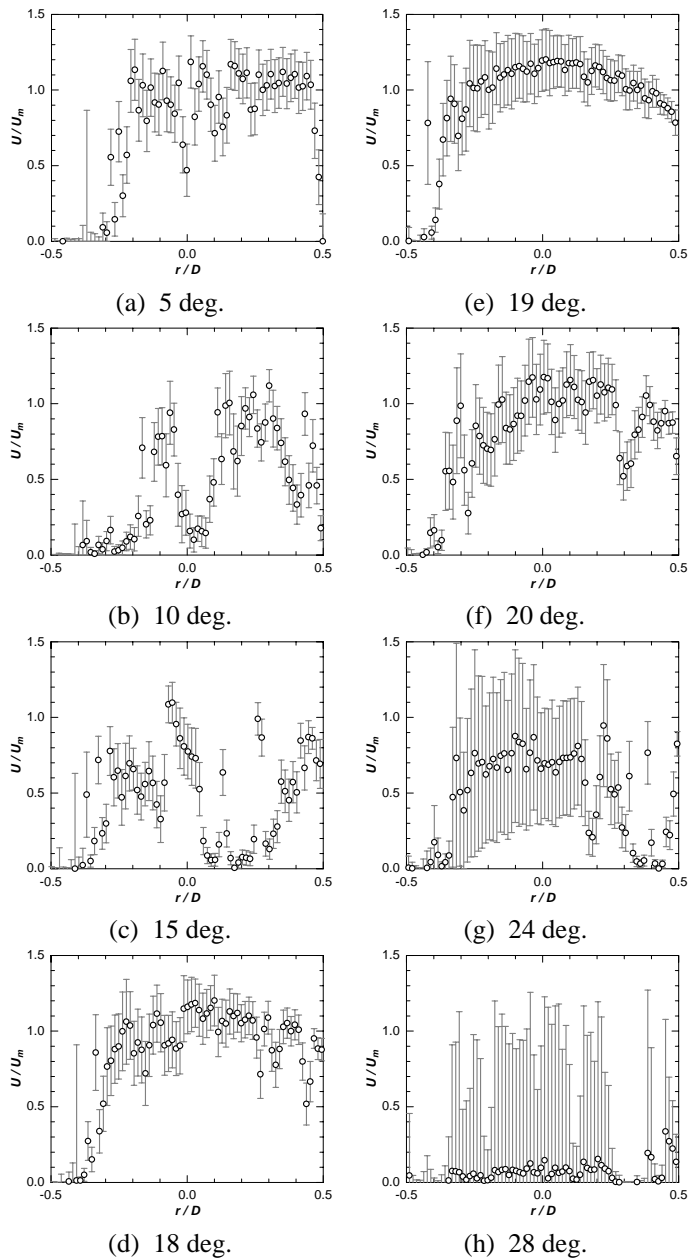(f) 20 deg.

(g) 24 deg.

(h) 28 deg.

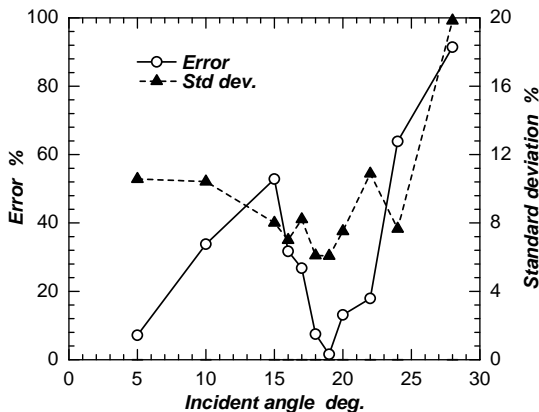Fig.8 Mean velocity profiles at each incident angle using carbon steel pipe (Thickness = 5 mm)

Fig.9 Errors and Standard deviations of flow rate at each incident angle

However, the standard deviation of the flow rate shows the different tendency. At more than 15 degrees, the characteristic between the error and the standard deviation is similar. On the other hand, at less than 15 degrees, as decreasing the incident angle, the standard deviation increases. In this experiment, owing to the pulse repetition frequency of UDM is fixed (2426 Hz), the resolution of the velocity is large in the case of the incident angle is small.

CONCLUDING REMARKS

The effect of the incident angle on measuring velocity profiles and flow rates using ultrasonic Doppler method is investigated in the case of the pipe material is carbon steel. The laboratory experiments appeared that the transmitted ultrasound, which generated by the longitudinal wave in carbon steel, becomes weaker as increasing the angle, and the accuracies of the velocity profile and the flow rate are also reduced.

On the other hand, it is clear that the ultrasound generated by the shear wave has the maximum strength at about 18 degrees, and additionally higher accurate values of the velocity profile and the flow rate are obtained at that angle.

REFERENCES

1. Y. Takeda, 1987, Measurement of velocity profile of mercury flow by ultrasound Doppler shift method, *Nucl. Technol.*, 79, pp.120-124.

2. Y. Takeda, 1995, Velocity profile measurement by ultrasonic Doppler method, *Exp. Therm. Fluid Sci.*, 10, pp.444-453.

3. M. Mori, Y. Takeda, T. Taishi, N. Furuichi, M. Aritomi, H. Kikura, 2002, Development of a novel flow metering system using ultrasonic velocity profile measurement, *Exp. Fluids*, 32, pp.153-160.

4. S. Wada, H. Kikura, M. Aritomi, M. Mori, Y. Takeda, 2004, Development of pulse ultrasonic Doppler method for flow rate measurement in power plant (Multilines flow rate measurement on metal pipe), *J. Nucl, Sci. Technol.*, 41, pp.339-346.

5. M. Mori, Y. Takeda, H. Kikura, M. Aritomi, 1999, Development of ultrasonic-Doppler velocity profile method for flow rate measurements of power plant, *7th Int. Conf. on Nuc. Eng.* (*ICONE7*), Tokyo, Japan, 19-23 April, 1999, ICONE-7429.

Table 2 Errors and Standard deviations of the flow rate at each incident angle

Incident angle [deg.]	Error [%]	Std dev. [%]
5	-7.2	10.6
10	-33.8	10.4
15	-52.8	8.0
17	-26.8	8.2
18	-7.5	6.1
19	-1.6	6.1
20	-13.1	7.5
24	-63.8	7.7
28	-91.4	19.8

APPLICATION OF UVP TRANSDUCERS TO MEASURE BED GEOMETRY AND VELOCITY PROFILES IN A HYDRAULIC SCALE MODEL WITH GRAVEL PIT

Nima Nilipour*, Giovanni De Cesare**, Jean-Louis Boillat***

*Formerly: Postgraduate student, LCH, ENAC, EPFL, Presently: Engineer, STUCKY Ltd, nnilipour@stucky.ch
**Senior research associate, Laboratory of Hydraulic Constructions (LCH), EPFL, giovanni.decesare@epfl.ch
***Senior research associate, LCH, EPFL, jean-louis.boillat@epfl.ch

ABSTRACT

As part of the project of the third correction of the Rhone River in Canton of Valais in Switzerland, the effect of gravel extraction from the riverbed in the Rarogne Region was studied. A 1:45 scale physical model with mobile bed was constructed and a series of experimental tests were conducted in order to investigate downstream erosion and changes in sediment transport due to the dredging pit. Three combinations of pit and contraction due to dredging were studied for three flood discharges. The velocity profile was measured in different locations, using UVP (Ultrasonic Velocity Profiler) probes. Having velocity profiles, evolution of the bed geometry and development of the mining pit can be instantly determined during the test. The main difficulty of the analysis was interpretation of the velocity profile in order to detect bed position. Installing four probes along the width of the model, lateral effect of contraction and mining pit on flow velocity was analyzed. Finally, based on results of the tests, recommendations are given for the mining operator, taking into account the local conditions and downstream structures.

INTRODUCTION

Disruption of sediment transport in rivers caused by sand and gravel pits can change bed geometry and endanger the stability of the banks and downstream structures, e.g. bridges. Sediment transport is affected by sudden change in the river section geometry and consequently erosion is anticipated in the downstream of the pit. Therefore, geomorphic and also environmental effects of material extraction are one of the main concerns in river training projects [1].

The 3rd correction of the Rhone River is a project at national scale which deals with all kind of hydraulic activities and structures in the Swiss part of the river. Sand and gravel extraction is carried out in few locations along the river among them in the Rarogne Region.

In the study the evolution of bed geometry due to a mine pit is investigated. A 1:45 scale physical model with mobile bed was constructed and a series of experimental tests were conducted in order to investigate downstream erosion and changing in sediment transport due to the dredging pit model The main goal of this study is to determine the depth and extend of the erosion in the affected zone in order to establish criteria for the mine operator.

Although research was carried out in the past based on laboratory tests and numerical modeling [2], [3] and [4], due to complexity of this phenomenon, scale hydraulic modeling is necessary for each project in order to obtain accurate results. Lee and Song [2] proposed formulas, derived from the experimental results, for different parameters and tried to find an empirical solution to this problem. This set of formulas has been obtained for a rectangular mining pit composed of uniform sediments over the whole river width and for a limited extend of Froude numbers (0.40-0.47).

Its application is limited to cases presenting no lateral contraction and only within the range of the original study.

Referring to these investigations, two different stages can be distinguished in the mining pit migration process, the convection and the diffusion phase (Figure 1). The transition occurs when the lowest point of the pit coincides with the downstream extremity of the pit.
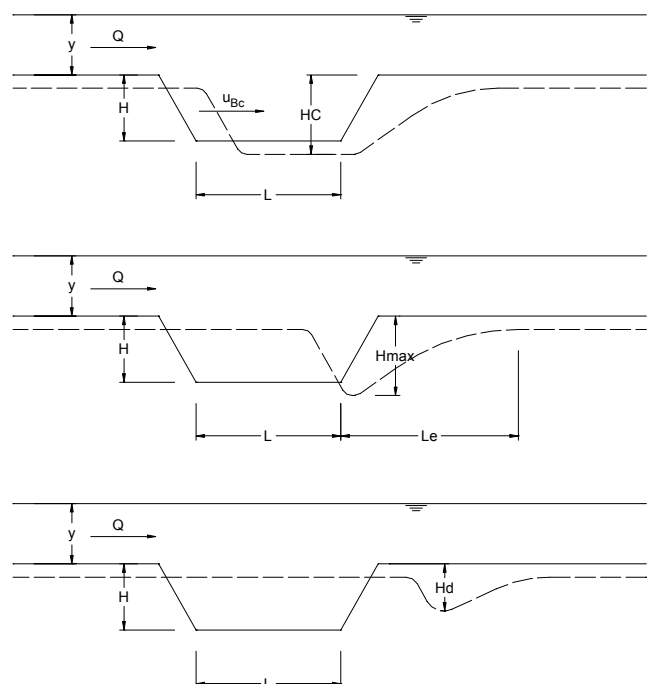

Figure 1: Migration of a rectangular mining pit composed of uniform sediments according to [2]

The Ultrasound Doppler Velocity Profile method (UVP method) has been chosen in the presented model study in order to measure the hydraulic flow characteristics and the bed profile during the transient phenomena. The principle of the method is straightforward; echography and Doppler effect. Originally developed in medical engineering to measure blood flow, its applications nowadays extend to non-medical flow measurements in general fluid mechanics. Due to the inherent constraints of classical anemometry, there has been a clear need to develop and dispose a measurement technique by which one can obtain velocity fields in space and time valuable for the hydraulic engineer. The Method has been applied since 1995 at the Laboratory of Hydraulic Constructions (LCH) to monitor initially the time-depended flow field of turbidity currents, velocity profile measurements for surface roughness determination, modeling of muddy debris-flows and roughness effects in sediment transporting mountain rivers.

PHYSICAL MODEL

The simulated river reach extends to some 800 m (Figure 2) which was modeled at a scale of 1/45 giving the length and width of the model as 16 m to 2.4 m, respectively.

In order to find out the impact of the dredging pit during different flood events, a series of tests were carried out for three discharges listed in Table 1.

Table 1. Three discharges adopted in this study

Return period (yr)	10	50	100
Discharge in prototype (m^3/s)	580	740	820
Discharge in model (l/s)	42.7	54.5	60.4

Since during the mining operation, material deposits causing contraction have also been observed for the mentioned discharges, the three following configurations of dredging pit geometry were tested:

- Big dredging pit, 2 m long, 10 cm deep
- Big dredging pit with contraction, 2 m long, 10 cm deep
- Small dredging pit, 1 m long, 10 cm deep

The contraction is maximum, half of the width, in the beginning of the pit and reaches to zero at the end of the pit. The geometry of the pit was chosen based on observations and measurements performed in different periods of the mine operation in the last 14 years. The hydraulic model constructed for this study is schematically shown in Figure 3.
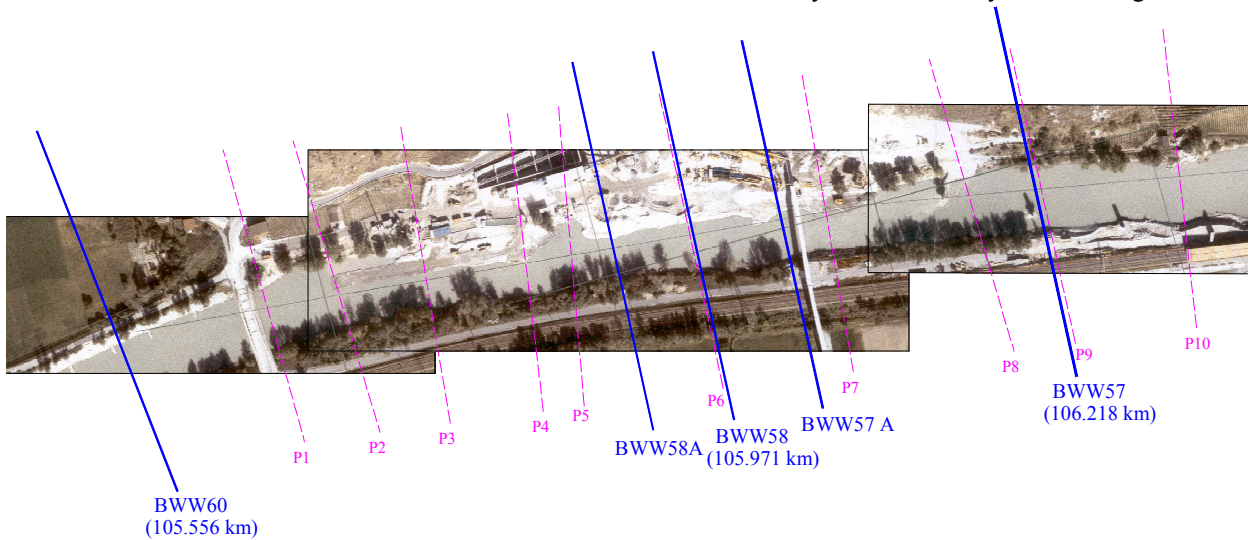
Figure 2: Limits of the hydraulic model and available cross sections of Rhone River used in this study
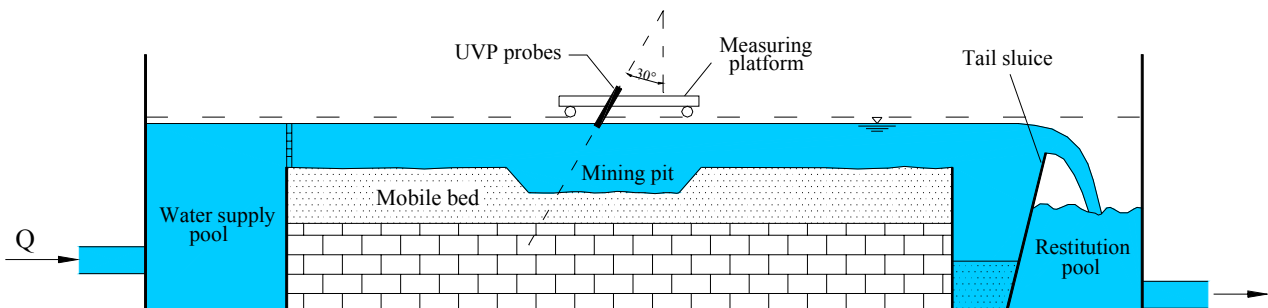

Figure 3: Schematic presentation of the hydraulic model

In order to meet the similarity laws in case of mobile bed modeling, grain diameter used as bed load should be chosen considering the riverbed roughness and type of the bed form. Total roughness must be calculated taking into account roughness by size of the grains and the bed form. Based on the empirical formulas and charts determining the bed form [5], in case of the Rhone River the bed form consists of dunes. Considering total roughness, uniform graded fine sand of 0.2

mm diameter was adopted as bed load. Using very fine sand, saturation of the model become very delicate and local erosion may occur.

Sediment feeding was evenly done on the upstream limit of the model during the tests. The sediment discharge has been calculated for each case based on empirical relations of Smart & Jaggi and Schoklitsch (from [6]). Average values of the above mentioned methods were applied as sediment discharge, Table 2.

Table 2. Sediment feeding discharge

Water discharge (l/s)	Solid discharge (l/s.m)
42.7	0.0060
54.5	0.0075
60.4	0.0100

INSTRUMENTATION

Four UVP (Ultrasonic Velocity Profiler) transducers were mounted on a mobile measurement platform moving along the model, Figure 4.

2 MHz transducers were adopted for the test taking into account the three following parameters:
- Measurement distance range
- Maximum estimated velocity range
- Required accuracy in terms of width of the measurement channel and velocity resolution

Table 3. UVP transducer configuration used in this study

Start point	Channel distance	End point	Maximum depth	Maximum velocity	Velocity resolution	Frequency
(mm)	(mm)	(mm)	(mm)	(mm/s)	(mm/s)	(Hz)
9.4	2.22	293.6	338	809.6	6.3	2188

Velocity profile measurement was conducted every 25 cm close to the pit and every 50 cm in the other parts.

In each measurement station, 100 profiles were measured by each of the four probes, having one second delay to activate the next probes. One full set of measurement over the model was performed at an interval of half an hour.

Figure 4: UVP transducers mounted on the measurement platform supported itself by rails

Having velocity profile measured in different distances from the upstream limit of the model, geometry of the bed was determined by detecting the bed position. Velocity profiles can be analyzed using MFX-XW software [8]. The methodology of velocity profile analysis is described as follows:

- Zero velocity
- Zero standard deviation
→ Obvious bed position

- Zero velocity
- Non-zero standard deviation
or
- Non-zero velocity
→ Manual bed detection

In the first case bed position can be easily detected, whereas in the second case more visual attention and work is required in order to accurately find the bed elevation using UVP.

Considerations regarding the application of UVP in mobile bed studies

- Correction of the velocity values due to inclination of the probes with respect to the vertical should be taken into account if real velocity values are required (can be automatically done by MFX-XW software [8]).
- For measuring velocity in a certain position, a number of profiles has to be measured in order to obtain a realistic average profile representing the actual average velocity profile (in this study 100 measurements each time to cover turbulent fluctuations in the steady state flow field).

- Accuracy of the measurement is limited to the width of the measurement channel.
- Sound reflection in the fixed part of the bed (in this case concrete foundation of the model) should be detected and removed while analyzing the water velocity profile.
- Upper part of the velocity profile should also be omitted as it is affected by the turbulence on the surface caused by water flow around the probe end.
- Since the probe is inclined with respect to the vertical, bed elevation detection can be influenced by bed form, e.g. dunes, ripples, etc. This has two aspects: Firstly, the average bed elevation can be wrongly determined by the height of the local dune, secondly if the dunes are relatively big compared to the water depth, bed level reference points are in different positions for aligned probes in the cross section.
- If bed geometry or flow field changes rapidly, it is recommended to install probes at fix positions so that the time needed to place the probes at the right position does not affect the accuracy of the measurements of a transitional phenomenon.

Advantages of UVP transducers:

- Online measuring of velocity profile
- Online measuring of bed elevation without stopping the test, especially in case of transient phenomena.
- Turbulence measurement, limited to acquisition frequency
- 3-D flow field analysis

AUTO BED DETECTION USING UVP

Based on the criteria mentioned above, auto detection of the bed was investigated and the results are presented in Table 4.

Table 4. Results of average velocity profile analysis

Q (l/s)	Case 1		Case 2		Case 3		Case 4	
	No.	%	No.	%	No.	%	No.	%
42.7	39	98	0	0	1	2.5	0	0
54.5	34	85	0	0	6	15	0	0
60.4	16	40	7	17.5	14	35	3	7.5

Case 1: Auto detection of the bed is possible
Case 2: Non-zero velocity
Case 3: Non-zero standard deviation
Case 4: Difficult to detect the exact position of the bed

As it can be seen the possibility of the bed auto detection decreases as the discharge increases. With higher discharges, solid discharge also increases, causing higher sediment transport rate and more indistinct bed position. Therefore, due to the bed load transitional zone (moving bed), a precise bed level almost does not exist any more. By reducing the velocity resolution, the auto bed detection can be more reliable, as in most of the velocity profiles categorized as case 2, minimum velocity is equal to the velocity resolution. It should be said that having less material transport rate inside the dredging pit, bed position could be automatically detected for all the velocity profiles measured inside the pit.

RESULTS

Applying the methodology explained above, bed geometry along the model was determined in different times by measuring velocity profiles and interpreting them, Figure 5. The evolution of the dredging pit was investigated under different discharges. The pit location for Q_{50} (model) at different instances is shown in Figure 6. As it can be seen the upstream face of the pit remains parallel to its initial slope (1:1). Figure 7 shows the evolution of the dredging pit in the physical model.
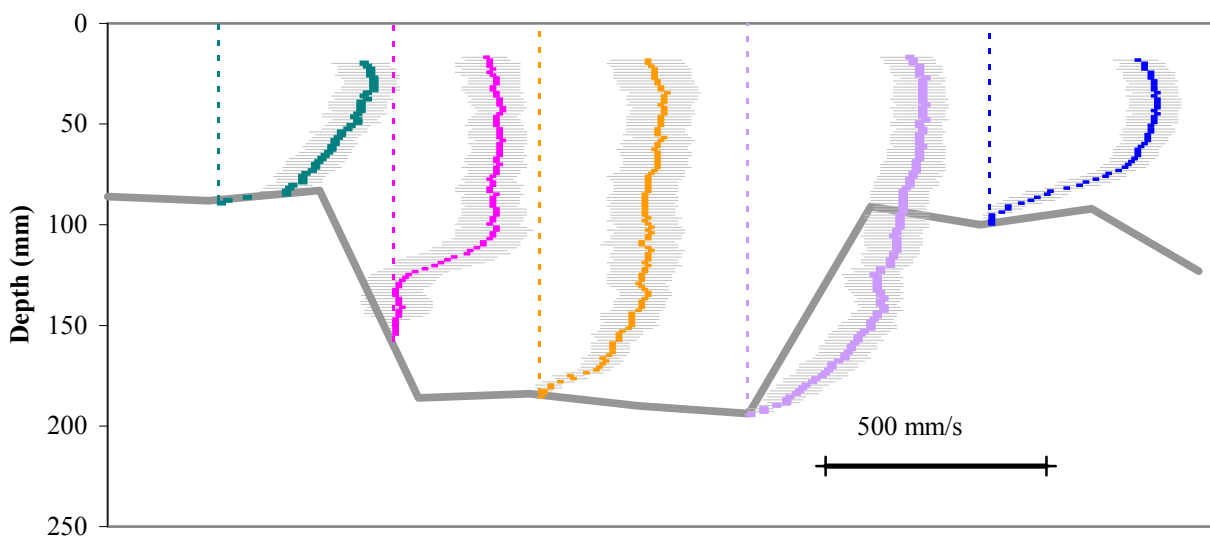

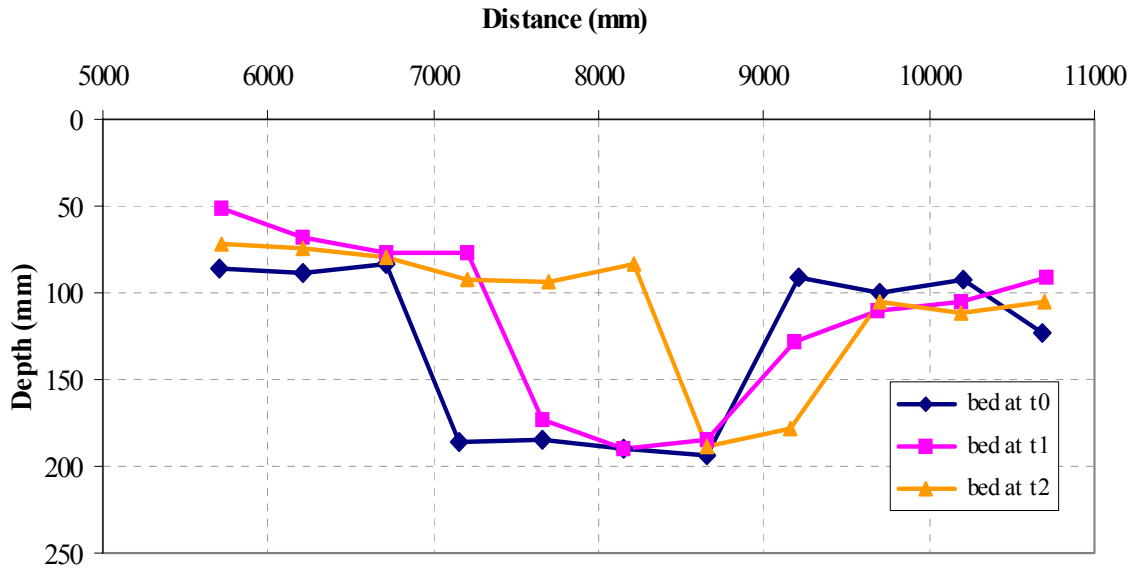Figure 5: Velocity profiles and standard deviation measured by UVP probes in the pit

Figure 6: Bed geometry measured by UVP probes at $t_1=0$, $t_2=1$ and $t_3=3$ hours for $Q_{50}=54.5$ l/s (prototype 740 m^3/s)

Time increasing erosion is observed downstream of the pit. This is due to disruption in the bed load transport, as all the sediments coming from upstream trap in the pit, whereas shear velocity remains the same downstream of the pit and consequently causes erosion. The depth of the erosion decreases towards downstream. It is a transient phenomenon and the extent and depth of the erosion depend on the time required to fill the whole pit by sediments, returning the bed to its equilibrium state. The required time depends on the solid discharge and volume of the pit. Hence, by limiting the size of the dredging zone, the downstream erosion can be controlled with respect to the selected flood event.

Since sediment transport depends on the corresponding shear velocity and sediment size, the pit moves faster with increasing discharge producing higher shear velocity, Table 5. Although the pit moves faster and the required time to fill it is shorter, the downstream erosion does not necessarily decrease as the higher shear velocity causes more erosion in a shorter time.

Table 5. Comparison of the test results for different discharges

Q (l/s)	Pit movement (m/hr)	shear stress τ_o (Pa)	Downstream Erosion extent (m)
42.7	0.20	0.63	6.0
54.5	0.52	0.75	6.9
60.4	1.04	0.88	7.5

Having contraction in addition to the dredging, test results show that local erosion can occur in the pit due to 3-D flow field. Also the shape of the moving pit front is not straight anymore and it advances faster in the center, making a curved pit front.

With a pit size used in this study, downstream erosion on prototype scale can be expected up to 300 m downstream of the pit during major flood events. For the given simulated pit size, dredging operations should take place at least 300 m

upstream from any important hydraulic structure (e.g. bridge pier) on the river in order to limit the impact of bed erosion.
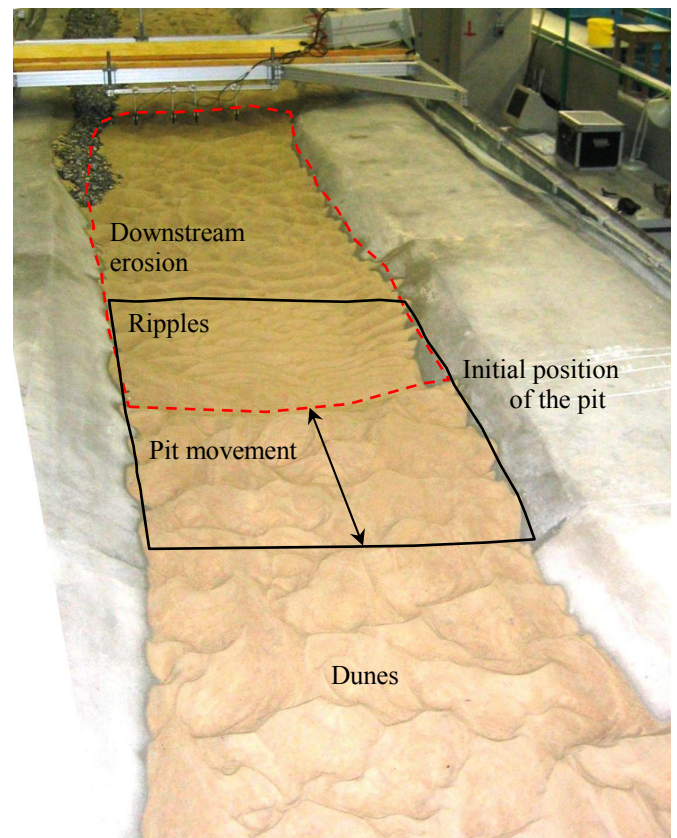
Figure 7: Picture of the pit movement on the river bed

Further investigations are needed in order to asses the effect of dredging pits with other dimensions under different flood events and solid transport conditions.

CONCLUSIONS

A hydraulic model with mobile bed at a scale of 1/45 was constructed to study the effects of a dredging operation on the Rhone River in the Rarogne Region, Canton of Valais, Switzerland. Four UVP transducers mounted on a mobile platform were used to monitor the evolution of the bed geometry and movement of the dredging pit.

Analyzing the average velocity profiles, the possibility of auto bed detection by interpretation of the velocity profiles measured using UVP probed was investigated. In most cases auto detection is feasible. The possibility increases with lower discharges where less bed movement occurs.

Downstream degradation caused by dredging operations was determined for different discharges and recommendations are provided regulating gravel extraction activities.

Further studies are needed to evaluate the effect of different pit dimensions, solid transport conditions and sediment sizes. Numerical modeling, calibrated based on the result of this work, are currently carried out in order to evaluate the sensitivity of the results to effective parameters.

REFERENCES

1. Kondolf G.M. (1994) "Geomorphic and environmental effects of instream gravel mining", Landscape and Urban Planing, 28,225-243

2. Lee, H-Y., Song, M-H. (1993) "Migration of rectangular mining pit composed of uniform sediments", Journal of Hydraulic Engineering, , Vol. 119, No. 1, January, p. 64-80

3. Bianco G., Cargnelutti M., Gadin A.C. (1997) "Study of local phenomena in natural rivers: comparison among experimental results in a flume with mobile bed and numerical simulations with a MIKE 11 - ST model", 2nd DHI Users Conference, June 9-11, 1997

4. Gill M.A. (1993) "Hydrodynamics of mining pits in erodible bed under steady flow", Journal of Hydraulic Engineering, Vol. 120, n° 11

5. Larras J. (1972) "Hydraulique et granulats". Collections du centre de recherches et d'essais de Chatou, N° 15, Eyrolles, Paris

6. Graf, W.H., Altinakar M.S. (1998) "Fluvial Hydraulics: Flow and Transport Processes in Channels of Simple Geometry". John Wiley and Sons, England, ISBN 0-471-97714-4

7. Hersberger, D. S. (2002) "Measurement of 3D flow field in a 90° bend with ultrasonic Doppler velocity profiler", Proc. Of the 3rd International Symposium on Ultrasonic Doppler Methods for Fluid Mechanics and Fluid Engineering, p. 59-66, Lausanne, Switzerland, Sept. 2002

8. Met-Flow (2000) "UVP Monitor – Model UVP-XW. Users guide", Met-Flow SA, Lausanne, Switzerland

DETERMINATION OF VELOCITY PROFILES AND BED MORPHOLOGY USING UVP TRANSDUCERS TO INVESTIGATE THE INFLUENCE OF LATERAL OVERFLOW ON MOBILE BED

Burkhard Rosier*, Frédéric Jordan*, Giovanni De Cesare**,
Jean-Louis Boillat** and Anton Schleiss***

*Research associate, Laboratoire de Constructions Hydrauliques LCH, EPFL – ENAC - LCH, Switzerland,
secretariat.lch@epfl.ch
**Senior research associate, LCH, EPFL – ENAC - LCH, Switzerland
***Professor and director, LCH, EPFL – ENAC - LCH, Switzerland

ABSTRACT

Lateral side weirs on channels are widely used in irrigation engineering and flood regulation. They are installed at the wall along the side of the main-channel to spill water over them when the water level in the channel rises above their crest. This lateral loss of water is responsible for the reduction of sediment transport capacity in the main-channel by decreasing the bottom shear stress. This yields to the formation of sediment deposits which raise the bed level locally. The design discharge to be diverted over the side weir is therefore increased and consequently sediment transport capacity is further decreased. This interaction between lateral overflow and sediment transport has to be known in order to avoid undesirable consequences. With the help of an experimental setup the physical processes in the main-channel and on the side weir were analyzed systematically confirming the processes mentioned above. They are strongly transient showing a tendency towards an equilibrium state of the river bed. The presence of mobile bed material forms an important part of these processes. Without paying attention to detail, resulting errors may be in the order of 25 %.

Keywords: Ultrasonic Velocity Profiler (UVP), velocity profile, lateral overflow, side weir, bed morphology, bed-load transport

INTRODUCTION

The content of the present paper results from the multidisciplinary flood protection research project *DIFUSE* (**Di**gues **Fu**sibles et **S**ubmersibl**e**s, Fuse plugs and overflow dams at rivers) involving governmental offices, private companies and four research institutes. The task of the *Laboratory of Hydraulic Constructions* (*LCH*) is to study the effects of a side overflow on the sediment transport in a natural channel.

At the current stage of research, the available published work is limited to only one of these aspects. Lateral overflow, sediment transport and bed morphology are treated as a single problem and nearly no publications relate these phenomena to each other. Due to this lack of knowledge, the particular objectives of the *LCH* contribution are to collect experimental data which can be used to conduct a non-dimensional parameter analysis to predict the hydraulic behaviour of the diverting weir. Combined with a photogrammetrical approach, the purpose is to determine river bed changes and to find empirical relationships. Furthermore, the collected data serves as main-input to generate a 3D numerical model.

EXPERIMENTAL MEASUREMENTS

Channel facility and tested parameters

With the help of a 30 m long and 2.0 m wide flume, the hydraulic and geometric characteristics of the main-channel and the side weir were analyzed systematically to determine the influence of laterally placed side weirs on sediment transport, erosion and deposits in the main-channel. The flume was subdivided longitudinally into two separate channels by a vertical 0.9 m high smooth wall. The first channel, being 1.5 m wide, represents the actual testing facility including the mobile bed and the side weir on the right river bank. The second one, 0.47 m wide, constitutes a lateral channel permitting to evacuate the laterally diverted discharge. A general layout of the experimental setup is shown in Figure 1. The main-channel discharge (117 – 220 l/s) including flood hydrographs, diverted discharge, channel slope (0.1 – 0.4 %), length of the lateral weir crest (3.0 m, 2 x 2.5 m), number of weirs (1 or 2) and sill height (0.09 m, 0.10 m,) were considered as test parameters.
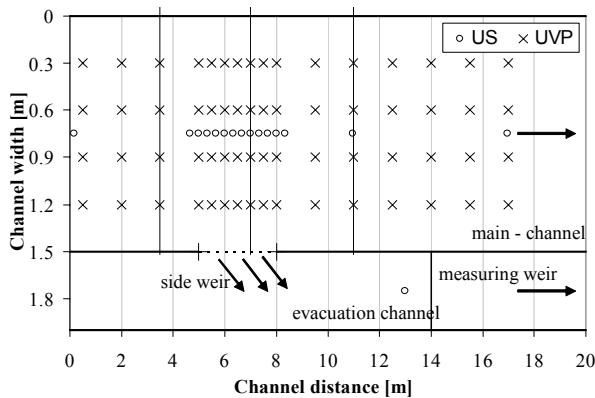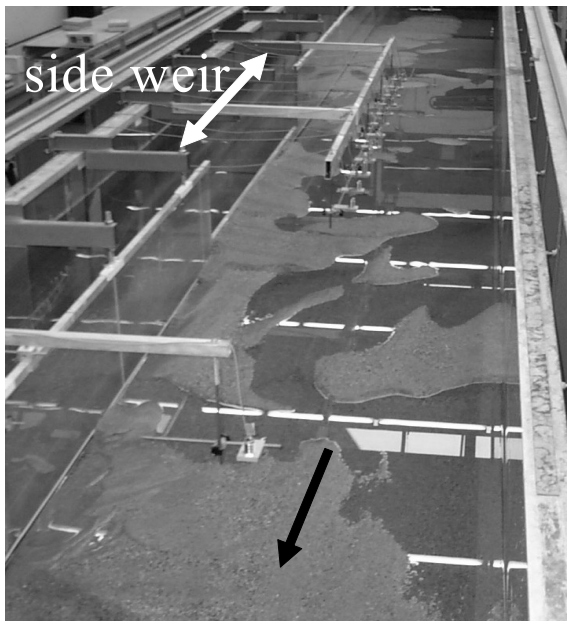
Fig. 1 General view of the test facility with the main channel, the lateral side weir, the mobile bed and evacuation channel (top) and disposition of water level (US) and velocity (UVP) recording (bottom)

Measuring procedure

The channel facility is originally horizontal. The bottom slope is created by adjusting the mobile bed to the requested slope. The mean thickness of the sand layer is 0.24 m. The bed material used in all tests consists of sand having a mean diameter of $d_m = 0.75$ mm. The sediment quantities to be supplied at the upstream end of the flume have been estimated according to the formula of Smart & Jäggi [1]. Sediment feeding was adjusted during the test in order to maintain a constant water level for a certain discharge thus maintaining uniform flow conditions in the upstream stretch of the flume. The upstream discharge was delivered by the use of three pumps feeding one pipe controlled by an electromagnetic flow meter.

A steady flow rate could therefore be easily set and maintained accurately throughout the duration of each test. The diverted discharge was measured by a standard sharp-crested weir installed in the evacuation channel.

Water depth along the main-channel as well as on the sharp-crested weir in the lateral channel were recorded continuously with a frequency of one measurement per second by the use of an ultrasonic gauge (voltage between 0 and 10V). The voltage was transformed into a distance to a reference level located at the crest of the side weir. The error of the level measurement is less than 1 mm (average ± 0.5 mm). Altogether,

15 ultrasonic gauges were installed longitudinally in the centre line of the channel, one located upstream of the side weir, 12 in the reach of the side weir (every 0.33 m), two downstream of the weir and one upstream of the measuring weir in the evacuation channel (Fig. 1).

Velocities were measured with an Ultrasonic Doppler Velocity Profiler (Metflow SA, Model UVP-XW) allowing to obtain instantaneously a 1D-velocity profile over the whole channel depth [2]. For each 1D-profile, 128 data points in time were recorded with a spatial resolution of 128 points over flow depth. Eight probes, each inclined by 25°, were mounted on a measuring frame fixed on a traversing beam whereof four probes were orientated in the longitudinal channel direction and four perpendicular to the main-channel axis, thus allowing to constitute a 2D velocity field (Fig. 2). The used probes had an emitting frequency of 2 MHz. Velocity profiles were recorded every 30 minutes for 16 cross sections, whereof three were located upstream of the weir, seven in the array of the weir (every 0.5 m) and six in the downstream section of the channel (Fig. 1). The velocity measurements were also used to detect the bed. The surface was obtained from the signal for which the velocity as well as the variance were close to zero [3] [4].
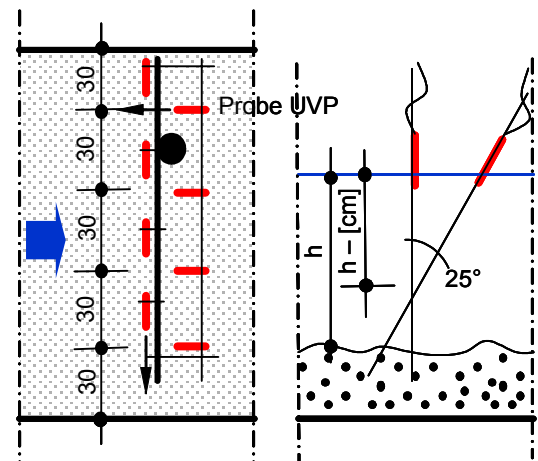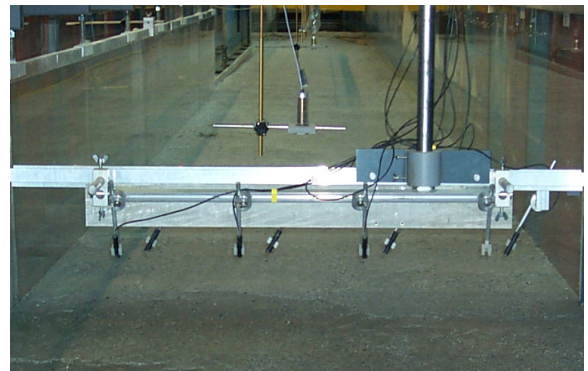

Fig. 2 Disposition and configuration of UVP probes on the measuring frame

As far as the monitoring of the river bed topography is concerned, a photogrammetrical approach has been applied serving as a three-dimensional surface measurement tool. For the present study five photographs with an overlap of 60 % have been taken to cover the whole channel. This has been done for the initial flat bed situation and after each experiment for the final bed situation after controlled drainage of the channel. 18 photocontrol points distributed along the channel facility and in the laboratory were used for the orientation and triangulation process. For the creation of the DTM a grid resolution of 2,5 x 2,5 cm has been chosen.

RESULTS AND DISCUSSION

Water level and diverted discharge

Due to the passage of dunes, water level measurements reveal strongly transient processes owing an oscillatory character. At the beginning of each experiment the water level in the main channel as well as the one over the measuring weir in the evacuation channel increases. With elapsing experiment time the level reaches a maximum before tending towards an almost constant value. This behaviour is more or less distinctive depending on the initial discharge. As far as the diverted discharge (Q_D) is concerned, the water level in the evacuation channel has been transformed into a discharge using the equation for sharp-crested weirs. Compared to the initial discharge introduced upstream (Q_1), Q_D amounts on average to 17 % of the total discharge introduced (Fig. 3, top).
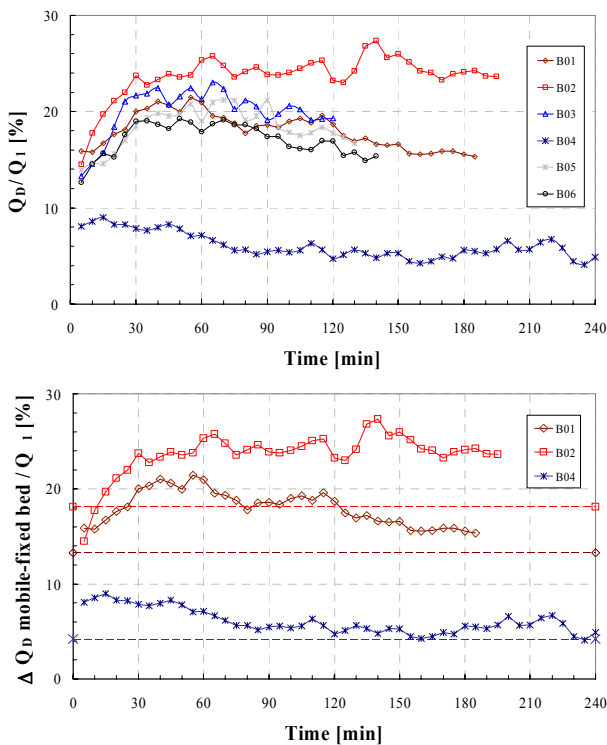
Fig. 3. Temporal evolution of diverted discharge (Q_D) in percentage of total discharge (Q_1) (top) and comparison of Q_D for mobile and fixed bed conditions with Q_1 (bottom)

The lowest value of 4 % is obtained for the smallest discharge, the largest one of 28 % for the highest discharge. Compared to fixed bed conditions (Fig. 3, bottom) it can be noticed that the ratio Q_D/Q_1 averages to be 25 % higher with a mobile bed thus corresponding to [5].

Velocities

The velocity recordings revealed an interesting effect of the Doppler measurement device which has been described earlier [3]. If the measured velocity was higher than the maximum velocity, the UVP shifts the measured value by minus 2 times the velocity range to the negative domain of the measurement and vice versa. If the sign of the velocity is known, the recorded velocity can be corrected by shifting the negative (positive) values again to the positive (negative) domain [4]. Qualitative and corrected velocity profiles in channel axis and perpendicular to the weir for three cross sections situated upstream, in

the weir alignment and downstream are plotted in Figure 4. For each cross section, a profile at the beginning and at the end of the test has been measured at 0.9 m channel width (Fig. 1).

The profiles in flow direction (Fig. 4, top) at the beginning of the experiment are almost homogenous to become significantly disturbed in the weir alignment as well as in the downstream channel section. The distance to the free water surface is nearly equal for all profiles indicating an almost similar water depth. From this, a rather regular and undisturbed bed morphology can be concluded. At the end of the test, a typical velocity distribution is encountered for the upstream part whereas further downstream distortions come across. The distance to the free water surface decreases. Assuming a horizontal water surface level, the bed level has therefore increased.
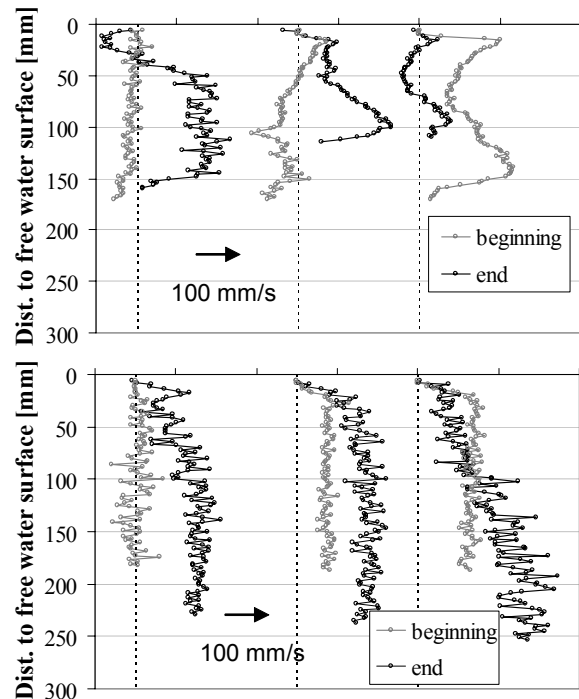

Fig. 4. Velocity measurements parallel to channel axis (top) and perpendicular (bottom) upstream, in the weir alignment and downstream at the beginning and at the end of test run B02. Dashed line: v = 0 mm/s

The velocity profiles perpendicular to the weir (Fig. 4, bottom) are nearly constant over flow depth for the beginning of the test run. With elapsing time the velocity component towards the weir increases.

The velocity measurements have also been successfully used for the detection of the bed surface (see next paragraph). Therefore the development of the bed over time can be determined, which is not possible with the photogrammetrical treatment since only the final bed situation can be measured. The information about the ground is less dense because only eight points for the eight probes are obtained instead of 1.5 m/0.025 m = 60 points from the photogrammetry. Nevertheless, it helps to get an idea about the development of the bed over time.

River bed morphology

After introducing the flow to the prepared initial flat bed by a small discharge, a rapid change of bed roughness due to the formation of dunes appears. Upstream of the side weir the dunes are of quite uniform character whereas in the reach of the weir and downstream the regular formation is clearly disturbed.

Based on the photogrammetrical analysis the DTM for the final bed situation has been determined. Typical cross-section profiles for different locations along the main channel are shown in Figure 5. The formation of sediment deposits in particular in the reach of the side weir are clearly apparent leading to a reduction of the cross section of about 33 %. A volumetric balance for a 7.0 m stretch reveals a deposited volume of 0.044 m^3 or 116 kg. Due to the reduction, the flow velocity opposite to the weir is increased resulting in an oscillatory erosion process before attenuating. In Figure 1 these observations are pointed up in a qualitative way. Outgoing from the weir side, an erosion gutter, at the end of the test still filled with water, is running to the right and again to the left. Sedimentation reaches on the right bank are followed by eroded reaches on the left bank.
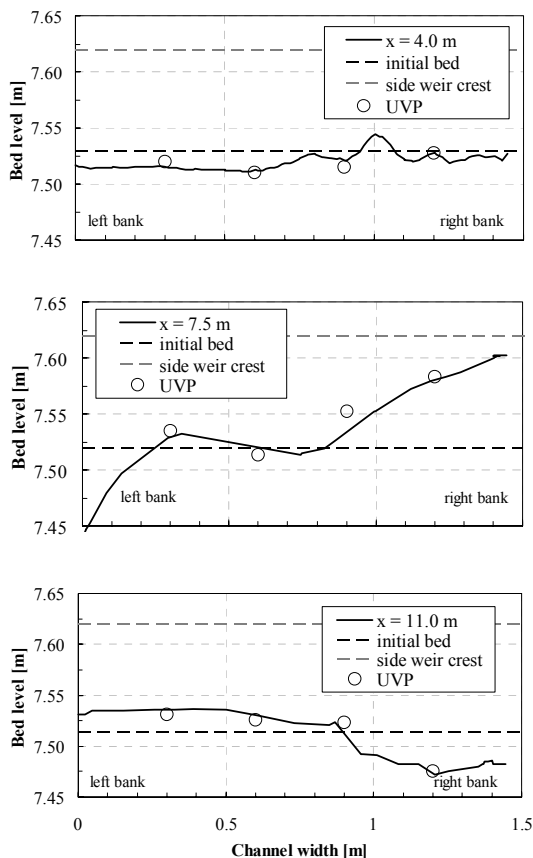
Fig. 5. Cross sectional profiles for the final state of the river bed upstream, in the weir alignment and downstream (from top to bottom)

The detection of the ground using UVP measurements are in fairly good agreement with those obtained from photogrammetry thus permitting an analysis of the temporal evolution of the bed morphology.

CONCLUSION AND PERSPECTIVE

An essential prerequisite in the field of flood protection is the capability to design and to predict accurately the behaviour of flood control devices such as lateral side weirs. In many cases the behaviour of mobile bed material will form an important part of this process. It has already been demonstrated that without paying attention to detail, errors in calculating can be of the order of 30 % [5].

The analysis of experimental test series confirms the formation of local deposits of sediments in the reach and downstream of lateral side weirs, particularly on the weir side of the channel. The flow is attracted by the lateral side weir leading to

progressive modification of the bed morphology and an elevation of the bed near the weir alignment. On the one hand the deposits increase the flow velocity opposite to the weir resulting in additional stress to the bank since the cross section is reduced up to 30 %. On the other hand the bed elevation is combined with an elevation of the water level leading to an increased diverted discharge over the side weir. Compared to fixed bed conditions the ratio diverted discharge/ main channel discharge is about 25 % higher. Due to the migration of dunes this process is strongly transient since at the beginning of the experiment the diverted discharge/main-channel discharge ratio is low, then rapidly increases to a maximum before reaching almost a constant value. A tendency towards an equilibrium state of the river bed is observed which is also indicated by a strongly wavy water surface in the reach of the side weir at the beginning of each test which becomes smoother with elapsing experiment time.

Based on the examination of the first test series, the remaining experiments will be analysed according to the same procedure to finally perform a non-dimensional parameter analysis and to develop empirical relationships for the hydraulic and sedimentary behaviour. The collected data will also serve to calibrate a 3D numerical model in order to analyze the observed effects in detail and to widen the application range.

A better understanding of the interaction between sediment transport and lateral overflow will allow to develop and to provide appropriate design criteria for engineers involved in the design of fuse plugs on rivers in the framework of flood protection projects.

REFERENCES

1. **Smart, G.M. & Jäggi, M.N.R** (1983). *Sedimenttransport in steilen Gerinnen*. In Vischer, D. (ed.), Mitteilungen der Versuchsanstalt für Wasserbau, Hydrologie und Glaziologie (VAW) 64. Zürich: Eidgenössische Technische Hochschule Zürich (ETHZ).

2. **Metflow** (2000). *UVP Monitor – Model UVP-XW*. Users guide, Metflow SA, Lausanne, Switzerland.

3. **Hersberger, D.S.** (2002). *Measurement of 3D flow field in a 90° bend with ultrasonic Doppler velocity profiler*. Third International Symposium on Ultrasonic Doppler Methods for Fluid Mechanics and Fluid Engineering. PSI Proceedings 02 -01, ISSN 1019 – 6447: 59 – 66. Ecole Polytechnique Fédérale de Lausanne (EPFL), Lausanne, Switzerland, September 9 – 11, 2002.

4. **Hersberger, D.S.** (2003). *Wall roughness effects on flow and scouring in curved channels with gravel bed*. In Schleiss, A. (ed.), Communications du Laboratoire de constructions hydrauliques (LCH) 14. Lausanne: Ecole Polytechnique Fédérale de Lausanne (EPFL).

5. **Wormleaton, P.R.; Sellin, R.H.J.; Bryant, T.; Loveless, J.H.; Hey, R.D. & Catmur, S.E.** (2004). *Flow structures in a two-stage channel with a mobile bed*. Journal of Hydraulic Research, IAHR 42 (2): 145-162.

An experiment on the flow in a hard disk drive

N.Sugawara*, J.Funaki** & K.Hirata***

*Dept. Mech. Engng., Doshisha Univ., Kyoto 610-0321, Japan, E-mail: dtd0372@mail4.doshisha.ac.jp
, **Dept. Mech. Engng., Doshisha Univ., Kyoto 610-0321, Japan, E-mail: jfunaki@doshisha.ac.jp
, *** Dept. Mech. Engng., Doshisha Univ., Kyoto 610-0321, Japan, E-mail: khirata@doshisha.ac.jp

ABSTRACT

The authors attempt flow and thermo visualizations on a real HDD. Additionally, the authors attempt measurements based on UDM (Ultrasonic Doppler Method), using a geometrically-symplified model. Thermo visualizations shows no obvious increase of disk-surface temperature during first 60[min.]. We confirm the existence of the solid-rotation core with some obstructed flows. But, there is no core at higher brockage ratio of the obstruction. The comparison between LDV and UDM shows the effectivity of UDM. Using UDM, the authors showed the disk flow, qualitatively.

Keywords: HDD, UDM, UVP, Disk flow, Rotating disk, Flow visualization, and Thermal image

1. INTRODUCTION

Hard-disk drives are the most popular storage devices in modern PCs. Recently, for higher speed and higher capacity, the accurate positioning operation of read/write magnetic heads becomes required. As the inside flow often causes pressure and velocity fluctuations, more accurate research have been needed.

Our present interest is the flow between two disks. Namely, we consider a pair of disks of the same radius in a stationary cylindrical enclosure. Disk spacing is much narrower than disk radius. Disks are connected with a common shaft, and corotate. Such a flow is often non-axisymmetric, and consists of two regions, that is, the region in solid-body rotation and the region of secondary flow. Until now, various studies have been carried out in order to resolve the flow. For example, Gor et al. (1994) measured the combined effect of an obstruction which is inserted from the enclosure, using a laser Doppler anemometry. Recently, Suzuki and Humphrey (1997) have performed three-dimensional numerical simulations for corotating-disks flow with two types of obstructions, such as a magnetic head arm support and an air lock.

There have been no experiments on real devices. So, in the present work, the authors attempt flow and thermo visualizations on a real HDD. Additionally, because there have been less experiments (for example, hot-wire, LDV and flow visualization), the authors attempt measurements based on UDM (Ultrasonic Doppler Method), using a geometrically-symplified model.

2. REAL DISK-DRIVE UNIT TEST

2-1. EXPERIMENTAL METHOD

2-1-1. Apparatus

Configuration of experimental apparatus is shown in Fig.1. Flow visualizations are performed with an obstructed or an unobstructed configuration. A real hard-disk drive used in the present work rotates at 7,200rpm (Re=1.13 × 10^5, δ=G/R_d=0.0423 and λ=R_w/R_d=1.0. For definitions, see below.). An original enclosure wall and rotating disks are replaced by acrylic ones, for observation. An obstruction is simplified by removing fine parts such as magnetic heads. The obstruction is joined with adhesive on the enclosure-wall. A high-speed video camera is used.

2-1-2. Parameters

Important parameters are as follows (see Fig.2). Reynolds number based on the disk radius is
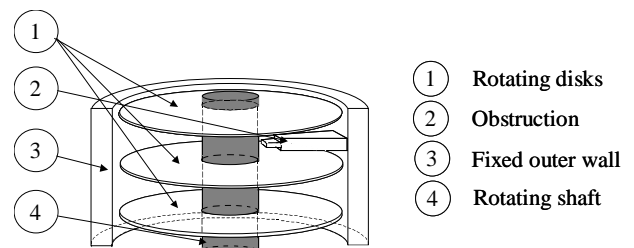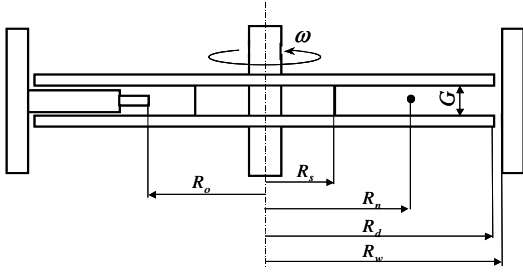
$$Re = \frac{\omega R_d^2}{\nu}. \qquad (1)$$

1	Rotating disks
2	Obstruction
3	Fixed outer wall
4	Rotating shaft

Fig.1. Schematic diagram of HDD.

Fig.2. Definitions of experimental parameters.

G : gap
R_o : radius to an obstruction tip
R_d : radius of rotating disk
R_n : radius to a nichrome smoke wire
R_s : radius of shaft
ω : angular velocity
R_w : radius of fixed outer wall
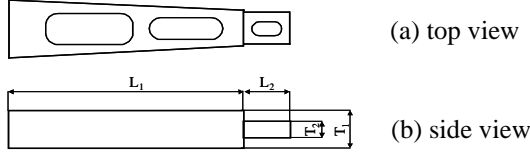

(a) top view

(b) side view

Fig.3. Parameters of obstruction.

The ratio of gap to disk radius is

$$\delta = \frac{G}{R_d} . \qquad (2)$$

In this work, $\delta = 4.23 \times 10^{-2}$.

Dimensionless radius of the enclosure-wall is

$$\lambda = \frac{R_w}{R_d} . \qquad (3)$$

In this work, 1 and $(R_w - R_d)/R_d = 0.004$.

The obstruction is shown in Fig.3. Dimensionless length of the obstruction is

$$\alpha = \frac{L_1 + L_2}{R_d} . \qquad (4)$$

Blockage ratio of the obstruction is

$$\beta = \frac{L_1 T_1 + L_2 T_2}{R_w G} . \qquad (5)$$

2-1-3. Thermo-visualization procedure

In order to observe the surface temperature on the real disk unit, we try thermal-image measurements. Pictures are taken at a frame rate of 120[fps]. We remove a top plate covering the device interior, and replace the special glass plate through which infrared rays pass efficiently.

2-1-4. Flow-visualization procedure

We lighted up by a halogen lamp, which is fixed as to prevent the reflection. The device has three disks. So, we have painted a middle disk black, and visualized an upper disk space. Flame rate of the camera is 6,000[fps]. In order to confirm the accuracy of the frame rate, we have checked the position of a mark on the disk.

The smoke-wire method is adapted, using liquid paraffin. We used a pair of nichrome wires twisted (diameter: 0.2mm), for more smoke. We take pictures at the time enough after the starting up.

(a) $t=0$ [min.]   (b) $t=10$

(c) $t=30$ (d) $t=60$ [min.]
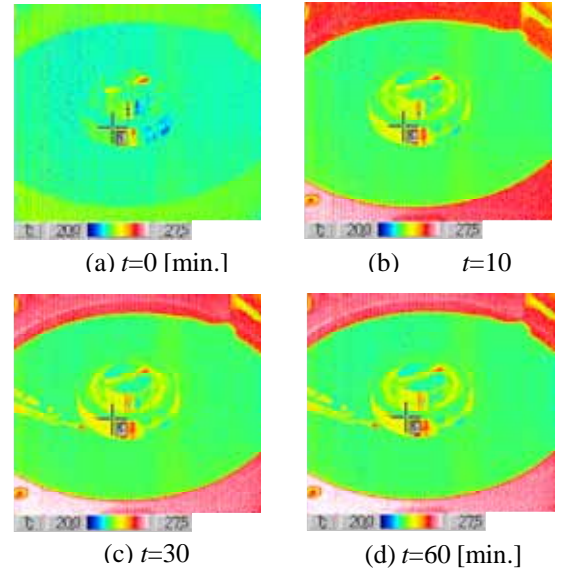
Fig.4. Surface temperature on a rotating disk of a ...HDD...
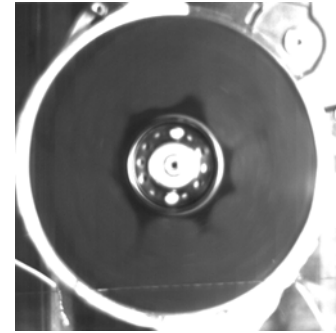
Fig.5. Visualization without obstruction $(Re=1.13\times10^5)$.

We drilled two 0.5mm holes on the enclosure wall, for the nichrome wire. The position of the nichrome wire is at $R_n/R_d=80\%$.

2-2. RESULTS AND DISCUSSION

2-2-1. Disk-surface temperature

We observed disk-surface temperarure during 1 hour after the starting up. Results are shown in Fig.4. Here, temperature is not absolutely but relatively, in exact meaning. The enclosure-wall temperature increases by about 3 degrees after 30 minutes later. But, we can observe no clear increase of disk-surface temperature during 60[min.].

2-2-2. Unobstructed Flow

Fig.5 shows a steady state at the time enough after the starting up. We are able to confirm the existence of a solid-body-rotation core. The core is almost polygonal with 6 to 7 apexes (circumferencial mode 6 to 7).
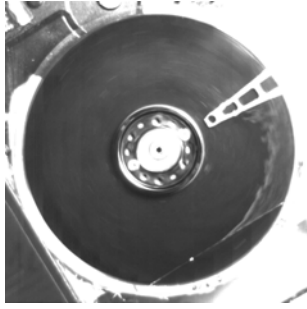
2-2-3. Obstructed Flow

Fig.6 shows obstructed flows with the obstructing length $\alpha=20$, 40 and 60%. The obstruction is about 90 downstream from a nichrome wire. The core size in Fig.6(a) ($\alpha=20\%$) is roughly the same as that in Fig.5.

(a) α=20%, β=11%   (b) α=40%, β=31%
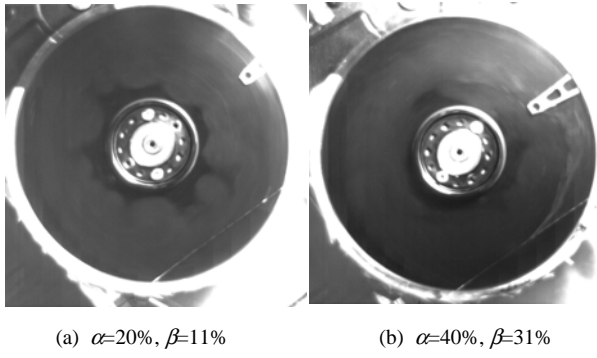
(c) α=60%, β=50%

Fig.6. Visualization with obstruction (Re=1.13$\times$10^5).

In Fig.6 (b) (α=40%), we can see the core, but the core dimension is much smaller than those in Fig.5 and Fig.6(a). It is difficult to determine the circumferential mode, because the apexies disappear just downstream the obstruction.

In Fig.6(c) (α=60%), we can not see the core. On the upstream of a thick part of the obstruction, smoke stagnates. On the other hand, there is no smoke on the upstream of a thin part of the obstruction. Humphrey et al. (1997) reported that there exists a reversed flow region on the immediate downstream of the obstruction. However, we couldn't confirm the reversed flow.

3. MODEL TEST

3-1. Experimental Method

For UDM measurements (Takeda, 1986), we use a geometrically simplified apparatus, which is made of acrylic resin. We use three UDM transducers in order to measure three velocity components u_r, u_θ and u_z. As particles to reflect ultrasonic waves, we use polyethyrene beads, whose specific gravity is 0.918, and whose mean diameter is 12μm. To measure the radial velocity u_r, one transducer is fixed outside the enclosure-wall toward the centre. To measure the circumferencial velocity u_θ, another transducer is fixed outside the enclosure wall eccentrically. To measure the axial velocity u_z, the other transducer is above the rotational disk.

3-2. RESULTS AND DISCUSSION

We conducted LDV (Laser Doppler Velocimetry) measurements and UDM measurements, simultaneously, in order to check UDM accuracy. We measured the circumferential velocity u_θ (shown in Fig.7). Vertical axis is dimensionless time-mean circumferencial velocity. Horizontal axis is dimensionless radial position. UDM results agree well with LDV results.
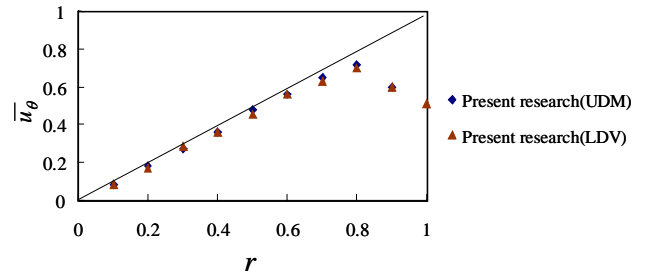
Fig.7. Comparison UDM with LDV at z=0.5 (Re=1.0$\times$ 10^5, λ=1.0, δ=0.3, mode4).
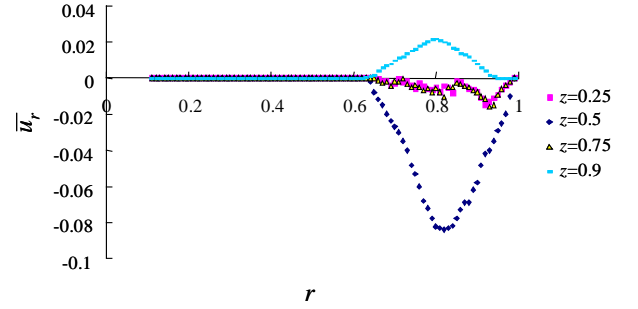
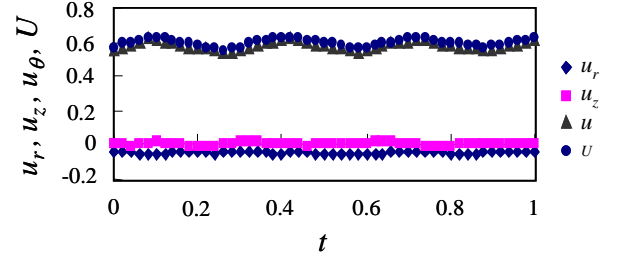Fig.8. Velocity u_r by UDM at z=0.25~0.9 (Re=5.0$\times$10^4, λ=1.0, δ=0.2, mode5 to 6).

Fig.9. Time histories of velocity components by UDM at r=0.9, z=0.5 (Re=1.0$\times$10^5, λ=1.0, δ=0.3, mode4).

Fig.8 shows radial velocity profiles at several vertical positions. Vertical axis is dimensionless mean radial velocity. Horizontal axis is dimensionless radial position. It is confirmed that centripetal flow exists near a midplane between disks, and centrifugal flow exists near disk-surfaces.

Fig.9 shows radial, axial and circumferencial velocities at r=0.9 and z=0.5. Vertical axis is instantaneous dimensionless velocities. Hrizontal axis is dimensionless time. We can confirm that periodic fluctuations correspond with the circumferencial mode.

4. CONCLUDING REMARKS

The following conclusions are obtained.

1. We can observe no obvious increase of disk-surface temperature during first 60[min.].

2. We confirm the existence of the solid-rotation core at α=0, 20 and 40% (at β=0, 11 and 31%, respectively). But, there is no core at α=60% (at β=50%).

3. The comparison between LDV and UDM shows the effectivity of UDM. Using UDM, we observed the disk flow qualitatively.

REFERENCES

1. Gor, Humphrey and Greif, 1994, "Ventilated Flow Between Corotating Disks with Large Obstructions," Transactions of ASME, Journal of Fluids Engineering, Vol. 116, pp.828-834.

2. Suzuki and Humphrey, 1997, "Flow Past Large Obstructions Between Corotating Disks in Fixed Cylindrical Enclosures," Transactions of ASME, Journal of Fluids Engineering, Vol. 119,   pp.499-505.

3. Takeda, 1986, "Velocity profile measurement by ultrasound doppler shift method, " Int. J. Heat Fluid Flow, Vol. 7, pp.313-318

Flow Measurement in an Open Channel by UVP

Kaoru Yokoyama*, Naoya Kashiwaguma, Tomoyuki Okubo, Yasushi Takeda,

*Hokkaido University, North-13 West-8 Kitaku Sapporo, E-mail: yo-k@ring-me.eng.hokudai.ac.jp

ABSTRACT

Measuring velocity distribution is required in order to understand the structure of environmental flow well, because environmental flow is complex in structure in comparison with industrial flows. Velocity distribution is obtained by measuring velocity at some points in space or the depth of the river, using several kinds of assumptions. Because many of the existing velocity meters can measure velocity only at a single point in space, velocity distribution measured by the existing velocity meters includes the time lag of measurement. Therefore velocity distribution estimated by these methods must include some error. UVP has been used for a measurement of discharge in a pipe etc because it can measure the instantaneous velocity distribution on a measurement line. And high accuracy of measurement of pipe flow has been certified. From this feature, it is thought that UVP is useful to measure environmental flow. So in this study, discharge in an open channel was estimated by UVP. It was quantitatively evaluated by comparison with discharge in a pipe. Its adaptability to environmental flow was evaluated. Discharge in an open channel estimated by UVP agreed well with that of a pipe, with a difference between both less than 10 %

Keywords: Flow in an open channel, Velocity distribution, Discharge and UVP

INTRODUCTION

In river management, it is important to forecast areas that have possibility of a flood by measuring temporal change of flow rate of the river. Controlling a spread of pollutant is a key issue in environment management. For these purposes, measurement of flow field is essential. From such a viewpoint, requirement of a precise measurement (time dependent if possible) of environmental flow like river or lake is rapidly increasing.

Concerning flow velocity measurement in the river, flow varies according to conditions like the bottom surface or shape of the cross section. So environmental flow field is strongly distributed in three-dimensional space in comparison to industrial flows which can be mostly modeled as one or two-dimensional in space. In order to measure velocity distribution more accurately, measuring the velocity at many points is required. But, because many of the existing flow meters like electromagnetic meter are pointwise measurement, only at a single point in space, a long time is needed to obtain velocity distribution and the measured result includes errors due to a time lag of long measurement. In order to avoid such temporal inaccuracy, various hydrological methods have been used based on strong simplifications and assumptions like Manning's formula[1] Based on such assumptions, discharge is estimated using the measured value of the velocity at only some point in space or the depth of the river. Since assumptions are very crude and actual velocity distributions are different from theoretic value, this becomes one of the causes that enlarge measurement uncertainty of discharge. Therefore, development of new techniques of measuring instantaneous velocity distribution like Ultrasonic Velocity Profile measurement method (UVP) or Acoustic Doppler Current Profiling instrument (ADCP) has been strongly required.

The aim of the present investigation is to apply the UVP to several environmental flows. Actually, though river discharge has been measured using ADCP by Morlock (1996)[3] or Kizawa (2001)[4] etc., the measurement uncertainty has not been examined properly, because actual river discharge is unknown. As a first step, the discharge in an open channel was estimated from velocity distributions measured by UVP, and it was quantitatively evaluated by comparison with discharge in the pipe (reference value) also measured by UVP. Though UVP can measure velocity vector at an intersection of two or three measurement lines, vector measurement takes more time than the one-dimensional (1D) velocity distribution measurement. As a method that requires smaller time lag of measurement, measurement of 1D velocity distribution was performed in this experiment. Firstly, a flow that could be assumed well to be 1D flow was measured. Next, a flow that is 2D was measured. The errors from reference values in each test were estimated. Based on the results of this test, adaptability of UVP to environmental flow was evaluated.

EXPERIMENTAL METHOD

Experimental equipment

Figure 1 illustrates the test channel of this experiment. In order to make a flow steady, water was filled in an overflow tank by a pump and flowed to the open channel through the vinyl chloride pipe (1) from overflow tank. Discharge was controlled by a manually operated valve (2). The inside diameter of the pipe is 194 mm. Test section 1 is located at the

end of this pipe and reference discharge of the channel was measured there. A transducer was set at the angle of 8 degrees leaning from a vertical line. The main channel has a reservoir tank at the upstream (3) and a dam at the down stream (4). Height of the dam was 268 mm. Two partition boards are set up on it (5). Their width is 70 mm. The distance from the end of the tank to the tip of the dam is 4000 mm, and the width is 620 mm. The section from the tank to the dam was defined as an open channel. The bottom surface and the interior wall of the open channel are made of wood. The x-axis, y-axis, z-axis were defined to the direction of the main stream, the direction of the vertical line of the wall, the direction of the vertical line of the bottom. The origin was set at the end of the tank. Test section 2 was located in an open channel. As shown in figure 2, a single transducer was set at the position of 2410 mm from the dam (9 times of a height of the dam) with the angle equal to 16 degrees leaning to an upstream side from a vertical line. Its head was immersed in water. It was moved by a sliding motor in order to obtain velocity profiles at any y-coordinates.
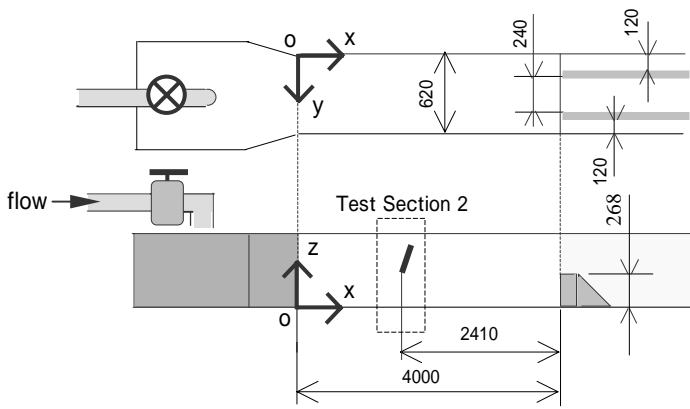
Figure 1: The test channel.
*1 Pipe (Test section 1) 2 Valve 3 Reservoir Tank 4 Dam
5 Partition boards 6 Open channei (Test section 2)
7 Transducer*
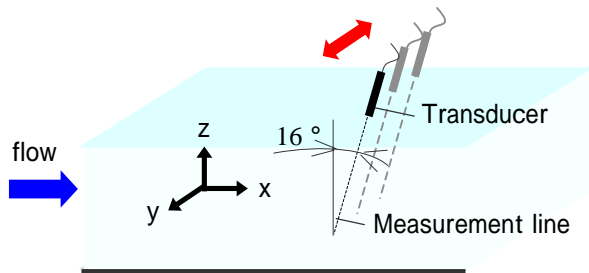
Figure 2: Test section 2.
(Transducer was moved flom y=10 to 310)
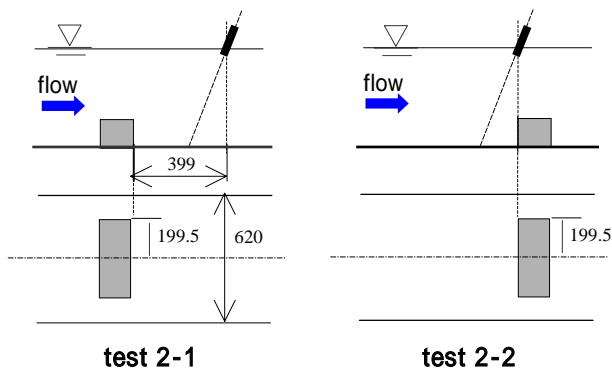
Figure 3: Setting of the block in test 2-1 and test 2-2.

At the test section 2, firstly, velocity distribution was measured without any obstruction in the channel, being assumed as 1D flow (called test 1). Secondly, a block was placed on the bottom in order to measure flow that was disturbed and not 1D flow (called test 2). The size of the block; length was 399 mm, width was 99 mm, height was 99 mm. The setting of the block is illustrated in figure 3. It was set perpendicular to the wall at the center of the channel. Measurement was made for two places of the block. In the test 2-1, the block was located at 399 mm (equal to length of the block) upstream from the head of the transducer. In the test 2-2, the block was located down stream of the head of the transducer.

Experimental method

At the test section 1, discharge of pipe flow was measured by udFlow (Tokyo Electric Power Company). It was a flow meter applying the principle of UVP, and its high accuracy was certified in the several certification tests[5]. So this discharge was adopted as a reference discharge of this channel. Basic frequency of transducer for emitting ultrasonic pulse was 2 MHz.

At the test section 2, velocity distribution was measured by using an Ultrasonic Doppler Velocity Profiler (Met-flow, UVP DUO). Symmetrical flow to a center was assumed. Measurement was made on 30 lines, where y-coordinate was 5 mm interval from 10 to 60, 10 mm interval from 60 to 220 and 20 mm interval from 220 to 310. In the test 1 and 2, basic frequency of transducer was 4 MHz. Velocity resolution of UVP DUO was set as about 5.0 mm/s and its spatial resolution was set as about 3.8 mm. Mean velocity distributions on each measurement line were obtained as an average of 512 profiles (about 50 sec).

The test 1 was performed in four cases by changing discharge, and called case 1, 2 ,3 and 4. The smallest discharge was 22 l/s (case 1), and the largest discharge was 46 l/s (case 4). In the test 2, discharge was same as case 3 (about 36 l/s).

Both the test section 1 and 2, tiny bubbles in water were used as tracer to reflect an ultrasonic pulse. Measurements were performed simultaneously at the test section1 and 2, and the discharge at test section 2 was compared with the reference value at the test section 1.

Data Treatment

UVP can obtain the velocity component along a measurement line, but the direction of actual velocity vector is unknown by a single transducer. In this study, flow in an open channel was assumed as 1D flow. The y- and z-components of velocity (v_y and v_z) were assumed to be nearly 0. The component of a measurement line of velocity was converted to the x-component of velocity. The x-component of velocity was calculated as,

$$v_x = v_0 / \sin \theta \qquad \text{(a)}$$

where v_x is the x-component of velocity, v_0 is the component of a measurement line of velocity, is an angle of the transducer.

Discharge of the open channel was then calculated by integrating velocity distribution about the direction of y and z.

$$Q = \iint v_x dz dy \qquad .$$

The error of discharge in the open channel was defined as a difference from the reference discharge in the pipe, and was calculated as,

$$e = \frac{\left|Q_{Pipe} - Q_{Channel}\right|}{Q_{Pipe}} \times 100$$

where Q_{Pipe} is a discharge in the pipe, $Q_{Channel}$ is a discharge in the open channel.

RESULTS AND DISCUSSION

Results of test 1

Figure 4 shows a 1D velocity profile at the center of the channel (y = 310) in case 2. The horizontal axis is v_x, and the vertical axis is a distance from the head of the transducer. Each point shows the average v_x, and each error bar shows a standard deviation of v_x at each position. Distance equal to 0 is the head of the transducer and the point that v_x nearly equal to 0 (about 399 mm) is decided as the bottom surface. The more close to the bottom, standard deviation is larger. This is because departure from 1D assumption of flow might be large by the influence of roughness of the bottom surface near the bottom. If UVP is used, not only average discharge but also time fluctuation of discharge can be estimated by standard deviation of velocity.

Next, the 2D velocity distribution in the cross section was measured. Figure 5 shows such velocity distributions in case 2 and case 4. The figure is for the region from the side wall to the center of the channel (half of the cross section). The horizontal axis is y-coordinates, and the vertical axis is z-coordinates. V_x is expressed by gray scale. Because of friction on the solid surfaces, flow velocity is small near the bottom surface and the side wall. Velocity near the free surface is also small. The reason might be that the head of the transducer changed the flow direction. The velocity component along a measurement line was nearly 0 because direction of a flow became nearly parallel to the surface of the transducer near its head. Because of the time lag of measurement, current measurement methods using the existing flow meter could not obtain such 2D distributions. But if UVP is used, the 2D distribution can be obtained with smaller time lag, and 2D flow structure which has not been understood correctly until now can be clarified.

Based on the 2D velocity distributions, flow discharge was estimated. Figure 6 shows the result. Horizontal axis is reference discharge measured by udFlow. Horizontal bars mean its standard deviation. The vertical axis is discharge in the open channel. Vertical bars mean standard deviation estimated by the standard deviation of velocity. As a tendency, discharge in the open channel agrees well with the reference discharge line. Since the range of standard deviation bars overlap with the reference discharge line, it is thought that discharge estimated by UVP is highly reliable. The error was estimated to be about 7% in case 1&2 and about 2.5% in case 3&4. The main cause of this error might be an inaccuracy of the angle of the transducer. In this experiment, v_x was calculated by formula (a). So when is small, the influence of the inaccuracy of an angle becomes larger. The second cause of the error was the unmeasured region. Because the head of the transducer was immersed in water, flow velocity was not measured in the region between the head of the transducer and the water surface. The length under water of transducer was about 5 mm. Since the water depth was about 400 mm, the unmeasured region was less than 2%. Therefore if the measurement field has deep water depth, the influence of the unmeasured region may be negligible. Consequently in order to make an error of discharge smaller, countermeasures must be taken. For example, making the angle of fixing equipment correctly, or increasing the angle .
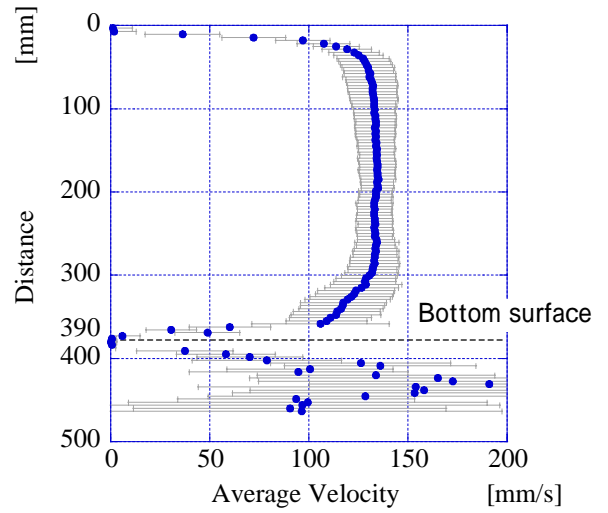

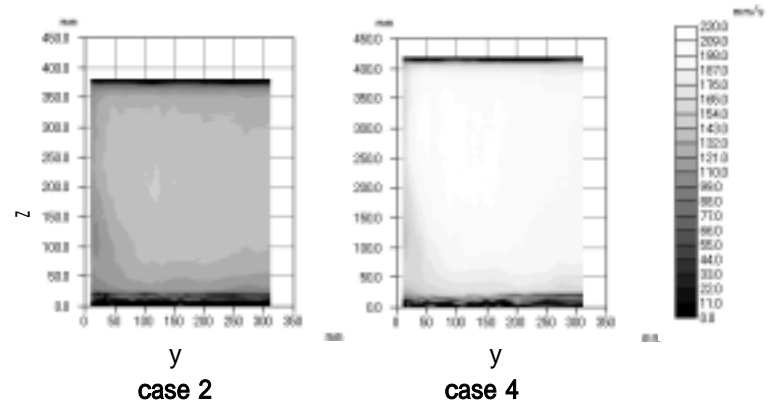**Figure 4: 1D mean velocity profile at y=310 mm (center of the channel) in case 2.**

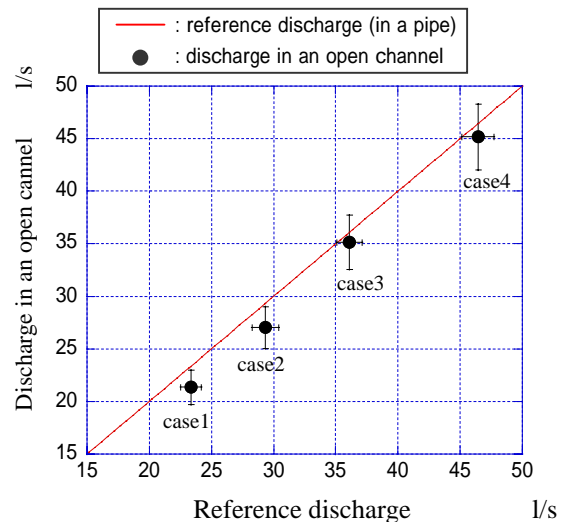**Figure 5: Velocity distribution in case 2 and case 4.**

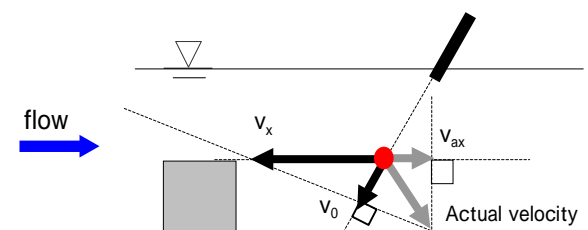**Figure 6: Discharge of pipe flow and open channel**

Figure 7: model of test2-1

(v_0: the component along a measurement line of velocity, v_x: the x component of velocity, v_{ax}: the x component of actual velocity)
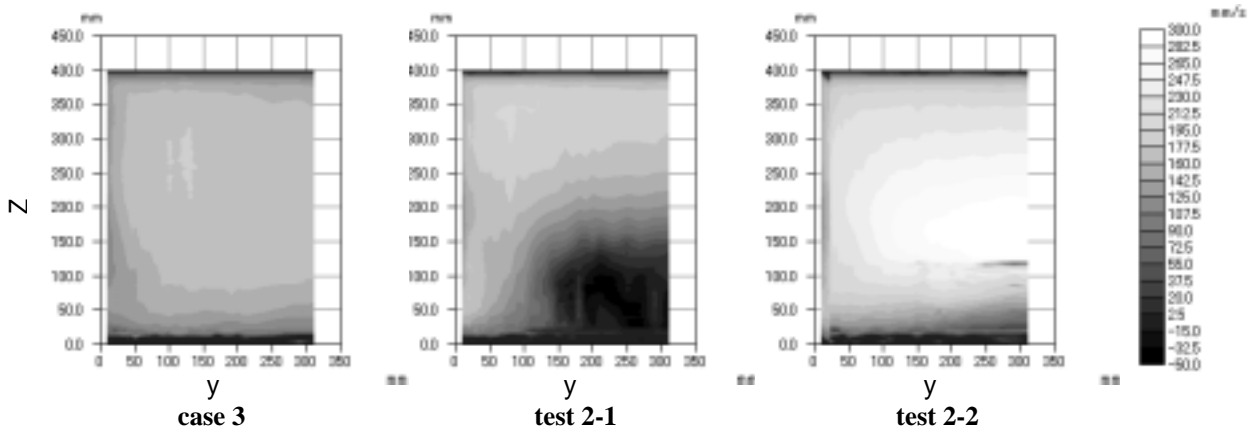
Figure 8: Velocity distributions in case 3,test 2-1,and test 2-2

Results of Test 2

In this test, the block was placed on the bottom of the open channel and 3D flow was prepared. The aim of this test was to measure a flow that is not 1D flow by single transducer, and to evaluate the accuracy.

Figure 8 shows the velocity distributions. Horizontal axis is y-coordinates, and the vertical axis is z-coordinates. Case 3 is the case measured without obstruction in the channel. In test 2-1, v_x is negative in the region behind the block. The reason might be the change of the direction of actual velocity vector by the block. The model of test 2-1 is shown in figure 7. In this region, it flows downward and the flow is not 1D flow. As shown in figure 7, v_x is estimated as negative if the component along a measurement line of velocity is changed into v_x by formula (a), though x-component of an actual velocity vector is positive.

In test 2-2, v_x is larger in the whole region compared with case3. In this region, it flows upward. As shown in figure 9, v_x is estimated larger than the x-component of actual velocity vector if v_x is calculated by formula (a).

Thus when 2D or 3D flow is measured by a single transducer, v_x measured by UVP is different from the x-component of actual velocity.

Based on the velocity distribution so obtained, the discharge in the channel was estimated. The result of discharge is shown in figure 10. Vertical axis is a discharge in the pipe (reference value) and in the open channel. Discharge in the test 2-1 is larger than the reference value. Discharge in the test 2-2 is smaller than the reference value. Because v_x was different from the actual value as discusses above, a difference of discharge is fairly large. The error is about 2.7 % in case 3, while they are about 23 % and 29 % in test 2-1 and 2-2. This result indicates that, in order to perform highly precise measurement using a single transducer, it is very important to choose a measurement point which could be assumed well as 1D flow. Furthermore, in order to measure 2D or 3D flow correctly, velocity vector must be measured using two or three transducers.

CONCLUDING REMARKS

The conclusions of this study are the 1) the error of discharge based on velocity distribution by UVP could be less than 10 % if appropriate measurement point is chosen, and 2) in order to perform highly precise measurement using a single transducer, a measurement point which could be assumed well as 1D flow must be chosen.

Velocity distribution in the cross section measured by UVP was very useful to understand the structure of environmental flow.

The results concluded, when single transducer is used, UVP might be very applicable for environmental flow that could be assumed as 1D flow.
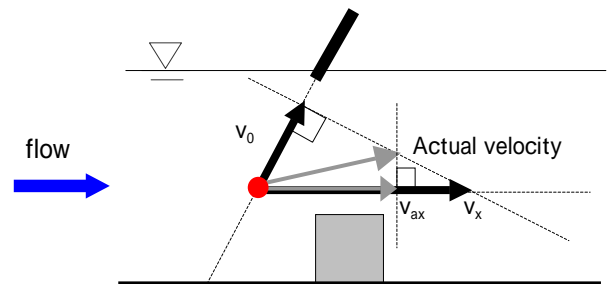

Figure 9: model of test 2-2

(v_0: the component along a measurement line of velocity, v_x: the x component of velocity, v_{ax}: the x the actual velocity vector)
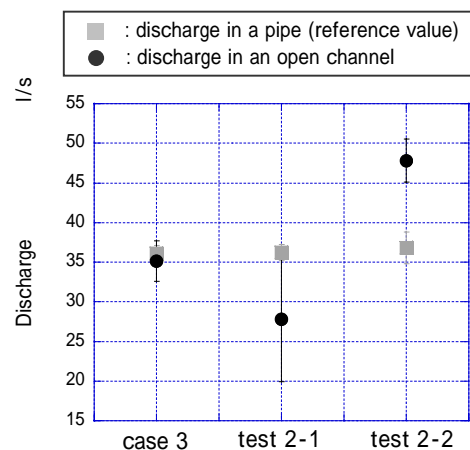

Figure 10: Discharge of pipe flow and open channel in case 3, test 2-1, and test 2-2.

REFERENCES

1. Japan Society of Civil Engineers, 1957, *The collection of formulas of hydraulics*, pp 8-14
2. Y Takeda, 1995, Instantaneous Velocity Profile Measurement by Ultrasonic Doppler Method. *JSME International Journal, Series B, Vol.38, NO.1,* pp.8-15
3. Morlock, S.E., 1996, Evaluation of acoustic Doppler current profiler measurements of river discharge, *U.S. Geological Survey Water-Resources Investigations Report 95-4218*, 37pp
4. K.Kizawa and Y Ide, 2001, The Suggestion of New Observation Techniques about River Discharge, *Symposium about the technique of river maintenance and management*, pp 251-256
5. M Mori et al, 2002, Development of a novel flow metering system using ultrasonic velocity profile measurement, *Experiments in Fluid* 32, pp 153-160.

Vector Measurement of Environmental Flow Field by UVP

Tomoyuki Ohkubo*, Naoya Kashiwaguma, Kaoru Yokoyama, Yasushi Takeda , Kazuo Ouchi**

*Hokkaido University, N13W8, Kitaku, Sapporo, E-mail: totsu@ring-me.eng.hokudai.ac.jp
**Tohoku Afforestation & Environmental Protection CO., LTD, 5-1, Honcho 2-chome, Aoba-ku, Sendai,
E-mail: ouchi-k@tohoku-aep.co.jp

ABSTRACT

In recent years, environmental flow fields have various problems such as pollution, flood etc. Therefore, request of measurement of environmental flow fields has been increasing. In general currently, these flow fields are measured by electromagnetic current meters or propeller meters. But those techniques are time consuming and of high cost to obtain flow field because they are point measurement. Furthermore their accuracy is too low. The aim of this study is to measure velocity vector in open channel flow field above the dam model. Flow rate was estimated from the measured vector field. The applicability of vector measurement for environmental flow field was confirmed qualitatively and quantitatively.

Keywords: environmental flow field, UVP, velocity vector, open channel

INTRODUCTION

The measurement of environmental flow fields is very important for river conservation works. If flow field information is not acceptable in their works, various problems, for instance, pollution and flood etc. may occur. Therefore, an increasing number of sectors and authorities are interested in the measurement of environmental flow fields. A lot of measurement techniques were developed for environmental flow. For example, Utami, T and Ueno, T. measured two dimensional stream line of river surface by visualization [1].

Flow rate of rivers is one of the most important quantities by which water management is well performed. It has two essential characteristic factors; accuracy and temporal change. Both factors are required to be satisfactory simultaneously.

Essentially, environmental flow is highly three dimensional. However, at present, flow rate of river is measured, in most cases, using electromagnetic current meters or propeller meters which are pointwise and no flow structure is taken into account. This is the reason why high accuracy cannot be attained.

The Ultrasonic Velocity Profiler (UVP) [2] has been used in various environmental flow configurations. V. Bares and V. Boza carried out flow mapping at river model [3]. D. S. Hersberger measured three dimensional flow field in a 90 degrees bend of open channel [4].

In this study, we attempted to make a vector measurement as a basis for flow measurement using an open channel loop with dam model, which is a model of river flow. Flow rate was estimated using the obtained vector field. As a result, applicability of UVP for environmental flow measurement was evaluated in quality and quantity.

EXPERIMENTAL SETUP AND METHOD

Experiments were performed with an open channel loop in the R&D center of Tohoku Electric Power Company, as illustrated in Fig.1. It consists of an overflow tank, a pipe, a valve, a reservoir tank, an open channel and a dam model. Water is circulated via the overflow tank by the pump. It flows through the pipe, collected in the reservoir tank, the open channel again, and then it overflows the dam model. The pipe diameter is 196 [mm]. Open channel is 4000 [mm] long, 620 [mm] wide and 1120 [mm] high between the reservoir tank and the dam model. Flow rate is controlled by the valve as about 8.5,14.0 and 21.1 [l/s]. Dam is 268 [mm] high and has two piers. Therefore the flow is three dimensional near the dam.
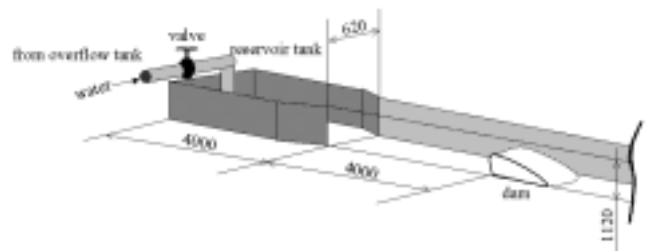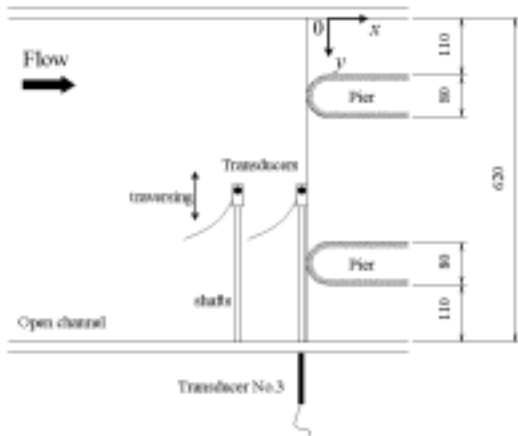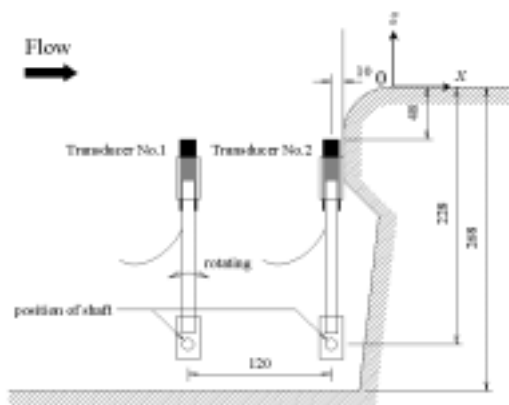

Fig.1 Open cannel loop with dam model

(a) ground plane

(b) front view

Fig.2 Overflow measurement system
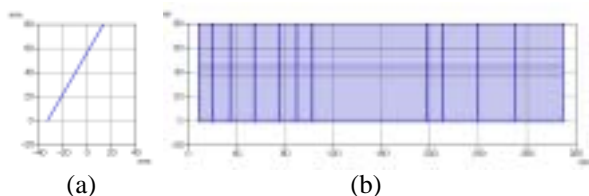

(a)   (b)

Fig.3 Cross section of measurement field in a single transducer measurement, (a) is view of x-z plane, (b) is view of y-z plane
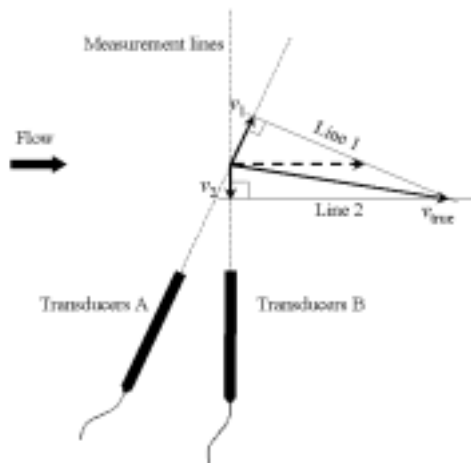

Fig.4 Velocity vector at cross point

In this study, flow rate was measured by UdFlow in pipe flow (TEST SECTION 1) and by UVP-DUO at overflow beyond the dam (TEST SECTION 2).

TEST SECTION 1   UdFlow was developed by Tokyo Electric Power Company for measurement of flow rate in a pipe. Its uncertainty has been approved to be less than 1% [5]. Therefore, the measured flow rate by TEST SECTION 1 was used to be a reference value to compare with the results of TEST SECTION 2. A transducer was fixed on the pipe at 8 degrees to vertical line on outside surface. The basic frequency was 2 [MHz]. Entrained bubble was used for reflecting particles. Sampling time was 300 [msec] and the number of profiles recorded was 1024 (Measuring time was about 5 minute). Their profiles were averaged at each point for calculating flow rate.

TEST SECTION 2   UVP-DUO (Met-Flow, Lausanne) can perform multiple line measurement for vector velocity mapping on flow field. Overflow measurement system is shown in Fig.2. (a) is a ground plan and (b) is a front view. The coordinate is set that zero point is an intersection point on the dam and the side wall, x direction is a flow direction, y direction is a spanwise direction and z direction is a vertical direction. Two transducers (No.1 and No.2) were located in the open channel for measurement of x and z velocity components (v_x and v_z). Transducer No.3 was set outside of the side wall to measure y component (v_y). The basic frequency was 2 [MHz]. Transducer No.1 could be rotated in x-z plane for stepping motor. Transducer No.2 was fixed on a shaft. No.1 and 2 were set to parallel and could be traversed to y direction by a sliding motor. The unit was controlled automatically by computer. Transducer No.3 was moved manually on the side wall.

For most simple measurement of flow field using UVP, a single transducer (Transducer No.1) was used. It was inclined at 29.8 degrees to vertical line. Data were collected at twelve lines to y direction between y=0 to 320 [mm]. However lines were avoided near the pier between y=110 to 190 [mm]. Furthermore flow was assumed to be symmetric to the center of width. A cross section of measurement field is shown as Fig.3. Sampling time was 150 [msec] for one profile. The number of profiles collected was 512. Their velocity distributions were converted to v_x and averaged. Flow rate was estimated using the average profile.

Vector measurement of flow field was carried out using three transducers (Transducer No.1, No.2 and No.3). Vector is calculated at a cross point of three profiles. The configuration of vector measurement using two transducers is illustrated in Fig.4. Transducer A obtains v_1 at a cross point of measurement lines. The v_{true} appears on the Line 1, similarly, appears on the Line 2 by obtained v_2. Therefore the v_{true} is estimated as 2D vector from the cross point of measurement lines to the cross point of Line 1 and Line 2. Moreover using another transducer, vector is taken as three components.

Data were collected each cross point that was set the fifteen lines to y direction between y=0 to 320 [mm] at a cross section of y=-50 [mm] (above Transducer No.2) and the interval of 10 [mm] from z=-10 [mm] to z direction. Sampling time was 450 [msec] for a profile. The number of profiles collected was 512. Vector was calculated and averaged at each point. Flow rate was estimated using the average profile.

RESULTS AND DISCUSSION

Flow rate was set for three cases (Case1, 2 and 3). These were measured at TEST SECTION 1 and 2.

Results of TEST SECTION 1

Results are summarized in Table.1. Reynolds number for all cases is larger than 10^4 and in turbulent flow in the pipe.

Results of TEST SECTION 2

A measured velocity distribution using Transducer No.1 is shown in Fig.5 (Case3). The horizontal axis is distance from transducer and the vertical axis is velocity. Error bar is standard deviation of averaging. The transducer was located at y=310 [mm] with inclination angle of 21.3 degrees. A free surface must appear on a velocity distribution because it was measured from inside of water. We took a following way to determine the location of free surface. Velocity increases from the transducer to near the dam and then it decreases. Large fluctuation appears at about 160[mm]. It was checked that this point corresponds to the free surface by a scale. In this study, the location of free surface was determined by a large fluctuation on the average velocity distribution.

The velocity distribution by a single transducer measurement is shown in Fig.6 (a), (b) and (c) for Case1, Case2 and Case3 respectively. The horizontal and vertical axes are y and z. The shaded rectangular shows area of no data near the pier. Magnitude of velocity is shown by colors.

In Case1, the velocity is lower near the pier and free surface and higher near the dam. Furthermore the depth of water is out of the horizontal. Other cases also indicate a similar tendency. Usual measurement techniques assume that the depth of water is fixed and a flow is steady for y direction. But in the actual conditions, this assumption must not be valid. Therefore it is necessary for accurate environmental flow measurement to obtain a detailed velocity distribution. The present result indicates that UVP is a more powerful measurement method than others.

Velocity vector as a result of the three transducers measurement in case3 is shown in Fig.7 (a), (b) and (c). (a) is the horizontal plan, (b) is the side view and (c) is the front view. Arrows and colors give velocity vectors. It shows that the flow diverges as escaping from the pier and the dam. Comparatively fast flow appears near the free surface. This is different from the results of a single transducer measurement. In a single transducer measurement, a v_x calculated is given as an arrow of broken line in Fig.4. Therefore it occurred that the v_x is different from the v_{true}.

Table.1 Flow rate in a pipe

	Case1	Case2	Case3
Q_{pipe}[l/s]	8.5	14.0	21.1
Standard deviation [l/s]	1.0	1.1	1.6
Re	$4.80*10^4$	$7.62*10^4$	$1.08*10^5$

Fig.5 Velocity distribution using Transducer No.1

(a) in Case1 (Q_{pipe} is 8.5 [l/s])

(b) in Case2 (Q_{pipe} is 14.0 [l/s])

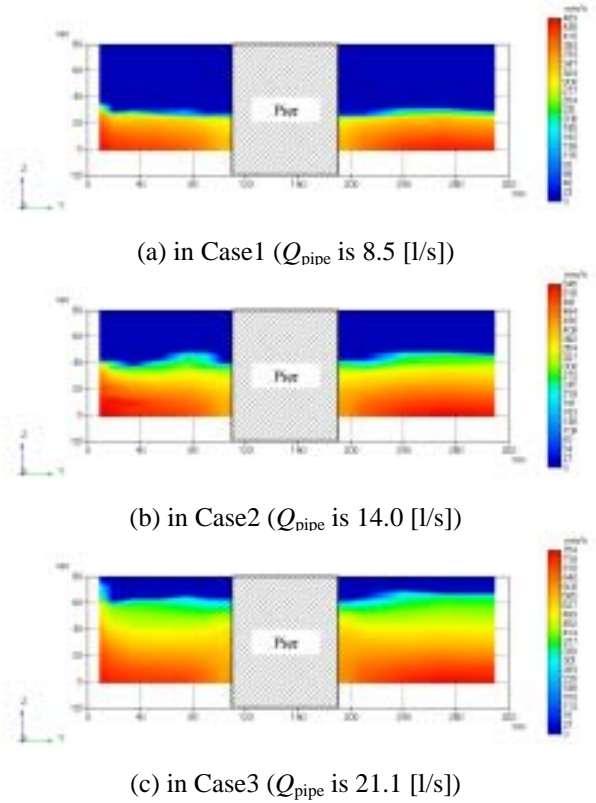(c) in Case3 (Q_{pipe} is 21.1 [l/s])
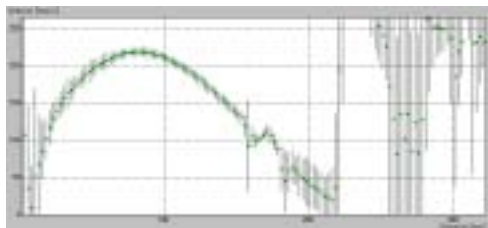
Fig.6 Velocity distribution of flow field in a single transducer measurement
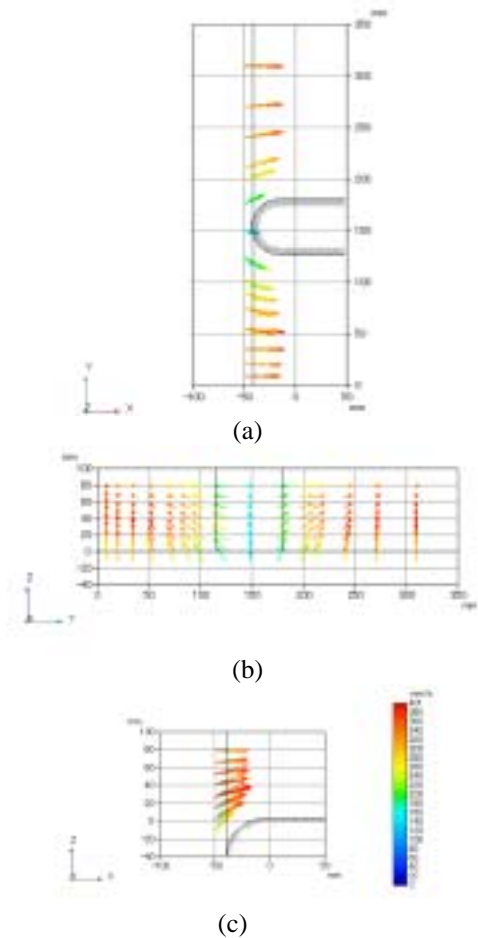

(a)

(b)

(c)

Fig.7 Velocity vector on a cross section of flow field in the three transducers measurement, (a) is the horizontal plan, (b) is the side view and (c) is the front view
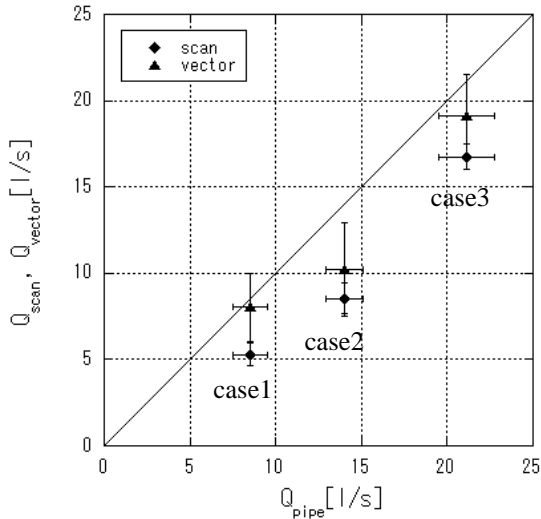
Fig.8 In comparison with Q_{scan} and Q_{vector} to Q_{pipe}

In order to make a quantitative comparison, flow rate was estimated from the measured velocity distribution. Q_{scan} is a flow rate from a single transducer measurement. Q_{vector} is a flow rate estimated from the three transducers measurement. Results are plotted in Fig.8. The horizontal axis is Q_{pipe} and the vertical axis is in Q_{scan} and Q_{vector}. Error bar is a standard deviation for each axis. In all cases Q_{vector} is closer to the diagonal line than Q_{scan}. Especially, a good agreement was attained in case1 and case3. A one dimensional flow cannot be assumed since the flow had three dimensional components in consequence of pier and dam. Therefore, Q_{vector} from a more detailed measurement is better than Q_{scan}.

CONCLUDING REMARKS

In this study, velocity vector was measured in an open channel flow field near the dam model. Flow rate was estimated using the vector flow fields. Furthermore, applicability for environmental flow measurement was evaluated at qualitatively and quantitatively.

It is concluded that UVP is powerful technique for quantitative or qualitative measurement of environmental flow. When flow cannot be assumed as a one dimensional flow, measurement has to be made for velocity vector by multiple transducers.

REFERENCES

1. T. Utami, T. Ueno, 1984, Visualization and picture processing of turbulent flow, *Exp. in Fluids*, 2, pp.25-32.
2. Y.Takeda, 1995, Velocity profile measurement by ultrasonic Doppler method, *Exp. Therm. & Fluid Sci.*, 10, pp.444-453.
3. V. Bares, V. Boza, 2002, ELBE RIVER MODEL: UVP FLOW MAPPING, *Proc. of the 3rd ISUD*.
4. D. S. Hersberger, 2002, MEASUREMENT OF #D FLOW FIELD IN A 90 ° BEND WITH ULTRASONIC DOPPLER VELOCITY PROFILER, *Proc. of the 3rd ISUD*.
5. M.Mori, et al., 2002, Development of a novel flow metering system using ultrasonic velocity profile measurement, *Exp. in Fluids*, 32, pp.155-160.

AN INDUSTRIAL PROCESS CONTROL CONCEPT FOR MICROSTRUCTURE-RHEOLOGY RELATED FOOD PRODUCT CHARACTERISTICS BASED ON IN-LINE ULTRASOUND-DOPPLER AND ULTRASOUND ATTENUATION MEASUREMENTS

E.J. Windhab*, J. Shaik*, B. Birkhofer* and B. Ouriev**

*Food Process Engineering Laboratory, Swiss Federal Institute of Technology, Technoparkstrasse 1, CH-8005 Zurich, Switzerland, E-mail: erich.windhab@ilw.agrl.ethz.ch
**Bühler AG, CH-9240 Uzwil, Switzerland, Email: mailto:ouriev@buhlergroup.com

ABSTRACT

The main quality characteristics of multiphase liquid food systems and various non-food industrial products depend on microstructure and rheological properties which mirror the dynamic properties of microstructure. If the development of rheology and microstructure during different stages of production processes can be monitored, acess will be given to tailormake products with well defined quality characteristics by rheology-microstructure based control of processing parameters. As In-line rheometers do not exist for non-transparent concentrated suspensions, conventionally off-line rheometers, which do not always represent the process flow conditions, are often used to determine the rheological properties. In a similar often also non-representative way microstructure is measured off-line.

Consequently, it has been proposed to (i) develop a Compact In-line Rheometer based on pulsed Ultrasound Velocity Profile (UVP) and Pressure Difference (PD) measurement, which can monitor or control the rheology/microstructure related quality parameters at multiple locations in a process under transient and steady-state conditions, to (ii) investigate the In-line rheology of model and real suspension based food systems in an industrial process using the Compact UVP-PD in-line Rheometer, and (iii) apply in addition coupled ultrasound in-line attenuation measurements to get information on the system microstructure (e.g. particle size distribution) for the investigated suspension systems.

The process control concept, the UVP-PD in-line rheometer, the Ultrasound spectroscopy principle and results from laboratory and industrial measurements are presented and discussed.

IN-LINE CHARACTERIZATION AND RHEOMETRY OF CONCENTRATED SUSPENSIONS USING ULTRASOUND

B. Birkhofer*, S.A.K. Jeelani*, B. Ouriev**, and E.J. Windhab*

*Food Process Engineering Laboratory, Swiss Federal Institute of Technology, Technoparkstrasse 1, CH–8005 Zurich, Switzerland, E-mail: beat.birkhofer@ilw.agrl.ethz.ch
**Bühler AG, CH–9240 Uzwil, Switzerland, E-mail: ouriev@buhlergroup.com

ABSTRACT

In this work characterization of model and industrial suspensions is done using ultrasound technique. Experimental investigation of the acoustic properties of the suspensions helps to explain suspension microstructure and its flow behavior. The model fluids consist of corn starch particles suspended in water or oil based systems. Cocoa butter crystalline fat suspensions are selected as industrial suspensions. They are produced in a shear crystallization process with defined solid content. The solid phase of the fat suspensions is determined using Nuclear Magnetic Resonance technique. The sound velocity is found to be a linear function of the solid cocoa butter content and temperature. A software was developed to integrate on-line measurement of flow profiles, pressure difference, temperature and acoustic properties such as velocity of sound.

Beside in-line sound velocity measurements, the shear rate dependent viscosity of suspensions flowing through a pipe is determined by means of pulsed ultrasound based anemometry (UVP: Ultrasound Velocity Profiler) and pressure drop (PD) methods. The measured time delay and frequency of the ultrasound reflected by particles flowing along the axis of the ultrasound beam are used to obtain the velocity profile in the flowing suspension. The rheological models are applied for characterization of the flow velocity profiles determined using the in-line UVP-PD technique. The model parameters can be compared with those obtained from off-line rotational rheometers.

Keywords: Flow profiling, in-line rheometry, suspensions, ultrasound, velocity of sound

INTRODUCTION

A novel method for in-line rheometry involving the measurement of an Ultrasound based Velocity Profile (UVP) using the Met-Flow UVP Monitor [1] and Pressure Difference (PD) in a pipe section was developed and tested at our laboratory by Ouriev and Windhab [2,6] for the flow of a wide variety of model and industrial suspensions. Industrial suspension systems such as chocolate, fat, shampoo and cellulose fibers in water suspensions were characterized by the in-line UVP-PD method. The in-line rheological results were compared with those measured by conventional off-line rheometers [2-9].

The feasibility study of the shear crystallization process and its influence on cocoa butter crystallization is currently under investigation. The result of this research will be used straightforward in the industrial chocolate production. The shear crystallization process developed at our laboratory [10] strongly influences the solid fat content of the cocoa butter suspension. It can be increased from 0% (liquid cocoa butter at 45°C) to almost 30%. Therefore the acoustic properties (attenuation, sound velocity, signal distortion due to multiple scattering) vary drastically. Beside the acoustic properties, the process parameters of the crystallization influence the rheology of the fat suspension and consequently change shape of the flow velocity profiles.

MATERIALS AND METHODS

Ultrasound transducer adapter cells

For acoustic investigations an in-line double wall steel adapter was constructed (figure 1). The suspension flows inside a 25 mm diameter tube. The adapter construction allows the installation of two transducers opposite to each other and can be also used for static acoustic measurements. In this case the adapter tube is closed from one side and a small sample (50ml) is sufficient for the acoustic measurement. Based on this design, a PVC cell for two transducers with a Doppler angle of 20° was developed. This cell allows a simultaneous measurement of the flow velocity profile and monitoring of the transmitted pulse (thus velocity of sound calculated from the time of flight of the pulse and the transducer distance, and signal quality). Pressure and temperature dependencies of the sound velocity in water were used for calibration purpose. Measuring the sound velocity at different temperatures gives precise information about the actual distance between the two opposite transducers. Such distance calibration was applied to both steel and PVC flow adapters. The transmitting and receiving ultrasound transducers have a 4 MHz base frequency and are equipped with a 5mm active diameter acoustic element. One of them is connected to the Ultrasound Velocity Profile (UVP) Monitor and the other to the oscilloscope.
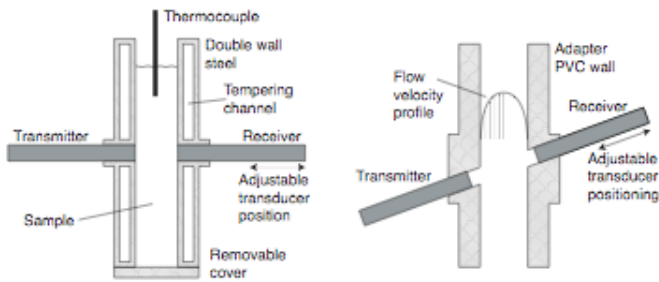
Figure 1: Measurement cells: double wall stainless steel adapter (left) in the configuration for a static measurement and PVC adapter with 20° Doppler angle (right). The transmitting transducer is used for velocity profile and echo amplitude measurement while the second transducer is used as receiver to measure the velocity of sound and other acoustic properties.

Data acquisition and control software

The current measurement setup (figure 2) consists of the UVP instrument (Met-Flow UVP-DUO), oscilloscope (Yokogawa DL 1520, 200 MS/s, 20 GS/s in repetitive mode, 150 MHz), thermocouples and pressure sensors connected to a National Instruments "FieldPoint" data acquisition system and a thermostat for the temperature control of the static measurements in the flow adapter. All the devices are controlled from a National Instruments LabView application. The communication with the UVP-DUO is implemented with an ActiveX library provided by MetFlow SA. As discussed earlier, the velocity of sound in cocoa butter depends on the temperature and the crystal content. Therefore the UVP parameters are set-up in time instead of distance units. For the display of the current state of the flow profile (average and standard deviation), a variable size first-in-first-out buffer was implemented. The waveform data of the transmitted pulse from the oscilloscope are used to calculate the instantaneous velocity of sound. This parameter is automatically applied to calculate the distances along the velocity profile and the volume flow rate. The amplitude and power spectra are used for characterization of the received signal quality.
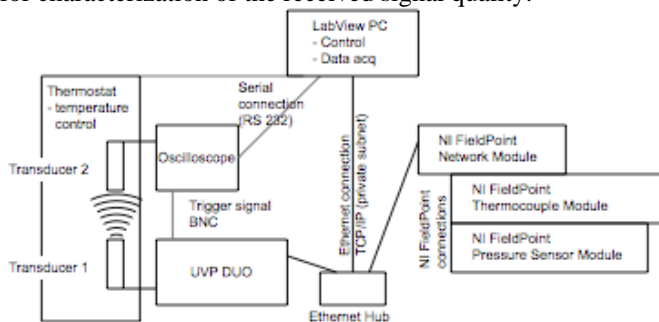
Figure 2: Scheme of the data acquisition and control hardware.

The temperature of a thermostat is controllable from LabView. This allows the automated measurement of the dependency of acoustic properties of liquids by using the double wall cell and driving a temperature ramp over several hours. Figure 3 shows an example of such a measurement.
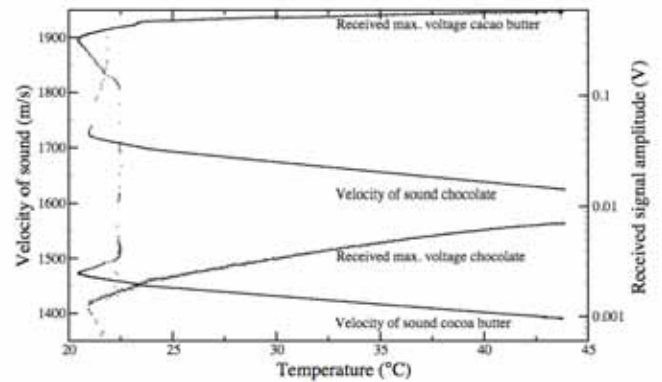

Figure 3: Velocity of sound and amplitude of the received signal plotted as a function of the fluid temperature.

The whole LabView application is implemented as a flexible modular system. The single modules abstracting the peripheral hardware, run in separate threads and can be activated according the requirements of the measurement. A central part of the application provides the graphical user interface for the adjustment of the parameters and the real time display of the measurement data, data logging and the infrastructure for the communication amongst the modules (e.g. the velocity of sound from the oscilloscope that is needed by the UVP module).

Cocoa butter fat suspension

Cocoa butter used for chocolate production is a mixture of triglycerides with a polymorphic crystallization behavior that has a melting range between 33 and 37°C. During the shear crystallization developed at our laboratory the crystal content is increased to up to 30%. The processing of cocoa butter results in the growth of crystals creating a needle like microstructure, which builds up to agglomerates. As the cocoa butter solidifies at room temperature, it is necessary to implement a temperature control of all the measurement equipment in direct contact with the cocoa butter.

Flow loop and crystallization procedure

The temperature controlled flow loop shown in figure 4, discussed in detail elsewhere [10], consists of a stirred cocoa butter feed tank, shear crystallizer and double wall steel transducer adapter cell.
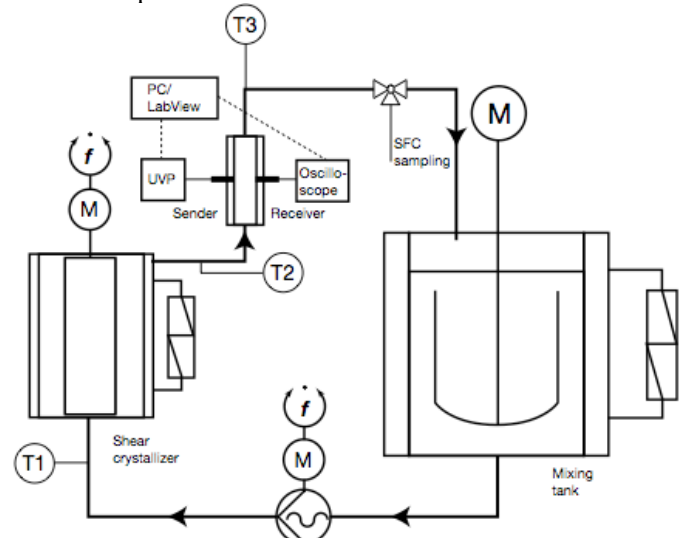

Figure 4: Crystallizer flow loop and instrumentation.

Prior to the crystallization process, cocoa butter was melted in the feed tank at 45°C. The molten suspension was pumped through the shear crystallizer flow loop for at least one hour. This was necessary to ensure that all cocoa butter in the flow loop was melted and a steady state was reached. In order to start the crystallization, the temperature of the shear crystallizer cooling water was set to 15°C and the shear crystallizer was switched on. The feed tank, pipes, and the ultrasound cell were all kept at 32.5°C in order to avoid solidification of cocoa butter.

The temperature, velocity of sound and signal amplitude of the ultrasound pulse were recorded as a function of time. An off-line Nuclear Magnetic Resonance (NMR) instrument was used to determine the corresponding solid fat content (SFC) of the cocoa butter suspension, which is the concentration of the cocoa butter crystals formed by drawing a sample at the outlet of the shear crystallizer.

Model suspensions

For a better understanding of the influence of suspension properties (e.g. kind of the continuous phase, concentration and microstructure of the disperse phase) on acoustic properties and finally the quality of the profile measurements, the model suspensions were used. In contrast, such acoustic investigations would be difficult due to the complexity of the cocoa butter. The temperature dependency of the kinetics of the rheological and micro-structural parameters makes it difficult to compare in-line and off-line measurements.

In a first series of experiments three model suspensions of corn starch particles (size range between 5 to 35 µm) dispersed in (i) sucrose solution with different sugar concentrations, (ii) silicon oil with different shear viscosities and (iii) rapeseed oil were considered. Concentration of disperse phase was varied between 0 and 40%w.

RESULTS AND DISCUSSION

Effect of solid fat content on sound velocity in cocoa butter

During crystallization, the cocoa butter temperature was kept constant over a wide range of crystal content. Therefore it was possible to measure the sound velocity c as a function of the solid fat content (SFC). In figure 5 this measured dependency (symbols) is represented by the straight line: $c = 1349.7 + 4.862$ SFC with a correlation coefficient of 0.993. It can be seen that 1% increase in SFC results in an increase of sound velocity by 5 m/s. The temperature dependency of the velocity of sound in the liquid cocoa butter is 3.5 m/s per °C.

The velocity of sound in a suspension of particles or emulsion of droplets depends on the mean density and mean compressibility and is given by the Urick equation [11]:

$$c = \frac{1}{\sqrt{\kappa \rho}}, \quad \kappa = \sum_j \phi_j \kappa_j, \quad \rho = \sum_j \phi_j \kappa_j \qquad (1)$$

where c: velocity of sound, κ: adiabatic compressibility, ρ: density, ϕ: volume fraction of the dispersed phase.

For a two phase system (e.g. solid cocoa butter crystals dispersed in liquid cocoa butter) one gets

$$\kappa = \phi \kappa_s + (1 - \phi) \kappa_l, \quad \rho = \phi \rho_s + (1 - \phi) \rho_l \qquad (2)$$

where subscript l: liquid/continuous phase; subscript s: solid/dispersed phase.

According to equations (1) and (2) it is possible to determine the composition of a suspension when the velocity of sound c, the adiabatic compressibility κ and the density ρ of the solid and liquid phases are known. The densities of liquid and solid cocoa butter are known. In the present case, the velocity of sound in solid coca butter had to be extrapolated. Compressibility of the liquid and solid cocoa butter can be also calculated. The velocity of sound from equation (1) is nearly linear for the range between 0% and 30% SFC. This corresponds qualitatively to the measured data shown in figure 5.
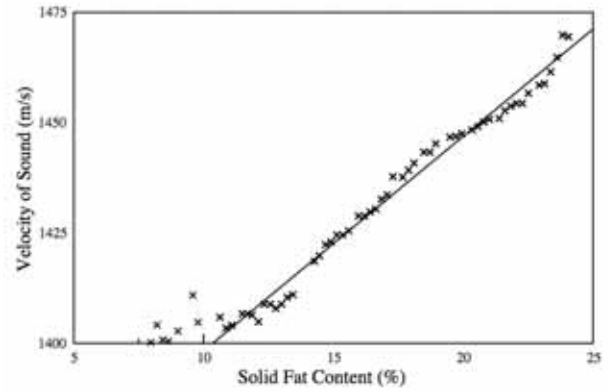

Figure 5: Velocity of sound as a function of the solid fat content (both quantities originally measured as functions of the time).

Acoustic properties of oil and water based model suspensions

Table 1 gives an example of the basic acoustic properties of suspensions degassed under vacuum with the same concentration of corn starch as dispersed phase. The signal transmitted through silicon oil based suspension is visibly distorted. Even for a 4 cycle pulse the amplitudes of the trough and crest are smaller in the center probably due to signal deletion caused by multiple scattering.

Table 1: Acoustic properties of model suspensions (S) of 10%w corn starch and their continuous phases (C) at 27 °C.

	Sound velocity, c		Ampl., a		Freq. Peak, f	
	C	S	C	S	C	S
	m/s		mV		MHz	
Sucrose solution (60%w)	1798.5	1876.1	4653	546	4.0	4.0
Rapeseed oil	1450.0	1479.0	3980	214	4.0	4.0
Silicon oil AK5000	1009.3	1055.5	2950	166	4.0	3.5

CONCLUSIONS

The sound velocity in cocoa butter is found to be a linear function of solid fat content and temperature. The attenuation of sound in model suspensions is found to be affected by the continuous phase - particle interface and whether the continuous phase is hydrophilic or hydrophobic. For instance, rapeseed and silicon oils when used as continuous phases contributed to the significant attenuation compared with that

for sucrose solutions. The UVPPD technique developed at our laboratory [2,6] can be used for in-line characterization and rheometry of concentrated suspensions. The present work involved the further development of a new software which integrated the simultaneous in-line measurement of flow velocity profiles, pressure difference, temperature and acoustic properties such as velocity of sound.

REFERENCES

[1] Met-Flow SA, 2002, UVP Monitor Model UVP-DUO, Met-Flow SA, Lausanne, Switzerland.

[2] Ouriev, B., 2000, Ultrasound Doppler based in-line rheometry of highly concentrated suspensions, Ph.D. Dissertation ETH No. 13523, Swiss Federal Institute of Technology, Zürich.

[3] Ouriev, B., Windhab, E., Braun, P., Yuantong, Z., Birkhofer, B., Industrial application of UVP-PD technique: Steady shear pipe flow of chocolate suspension in pre-crystallisation process, accepted for publication in journal: Review of Scientific Instruments, (September 2003)

[4] Ouriev, B., Windhab, E., Transient flow of highly concentrated suspensions investigated using UVP-PD method, accepted for publication in journal: Measurement, Science and Technology, (September 2003)

[5] Ouriev, B., Windhab, E., Novel ultrasound based time averaged flow mapping method for die entry visualization in flow of highly concentrated shear- thinning and shear-thickening suspensions, Measurement, Science and Technology Journal, Vol. 14, N° 1, pp. 140 - 148, (January 2003)

[6] Ouriev, B., Windhab, E., Rheological study of concentrated suspensions in pressure driven shear flow using a novel inline ultrasound Doppler method, Journal Experiments in Fluids, Vol. 32, N° 2, pp. 204 - 211, (2001/2002)

[7] Ouriev, B., Breitschuh, B., Windhab, E., Rheological Investigation of Concentrated Suspensions using a Novel inline Doppler Ultrasound Method, Colloid Journal, pp. 234 - 237, (February 2000)

[8] Johansson, M., Wiklund, J., Stading, M., Shaik, J., Ouriev, B., Windhab, E.J., Fischer, P., In-line Rheometry of Shear-Thinning and Shear-Thickening Complex Fluid Systems by UVP-PD Method, Annual Meeting of the Swiss Polymer Society/Rheology Group, Lausanne/Switzerland, 4.9.2001

[9] Wiklund, J., Johansson, M., Shaik, J., Fischer, P., Windhab, E., Stading, M., Hermansson, A.M., 2002, 3rd-International Symposium on Ultrasonic Doppler Methods for Fluid Mechanics and Fluid Engineering, pp. 69-76, EPFL, Lausanne, 9-11 September.

[10] Y. Zeng, 2000, Impf- und Scherkristallisation von Schokoladen, Ph.D. Dissertation ETH No. 13798, Swiss Federal Institute of Technology, Zürich.

[11] R. J. Urick, 1947, A Sound Velocity Method for Determining the Compressibility of Finely Divided Substances, Journal of Applied Physics, pp. 983-987

A COMPARATIVE STUDY BETWEEN UVP AND LDA TECHNIQUES FOR HIGHLY CONCENTRATED PULP SUSPENSIONS IN PIPE FLOW

J. Wiklund*, J. Pettersson**, A. Rasmuson** and M. Stading*

*SIK - The Swedish Institute for Food and Biotechnology, PO Box 5401, SE-402 29 Göteborg, Sweden,
johan.wiklund@sik.se, mats.stading@sik.se
**Dept. of Chem. Eng. & Environm. Sci., Chalmers University of Technology, SE-412 96 Göteborg, Sweden

ABSTRACT

UVP and LDA techniques have been used simultaneously to perform velocity profile measurements in highly concentrated pulp fibre suspensions. Experiments were carried out non-invasively through a 5 mm thick Polymethyl methacrylate, (PMMA), pipe measurement section in an experimental pipe flow loop. Pulp suspension concentrations ranging from 0.74 %(w/w) up to 7.8 %(w/w) were analyzed at four different volumetric flow rates. Instantaneous radial velocity profiles showing pronounced plug-flow behavior and sharp velocity gradients close to the pipe wall were obtained using the UVP technique. Results show that both techniques can be used with good agreement and that accurate velocities thus were obtained in much more concentrated pulp fibre suspensions than what has been reported so far in the literature. Results further show that the LDA technique can work even in strongly opaque systems such as a 7.8 %(w/w) pulp suspension with a sustained penetration depth of up to several millimeters, but with loss of velocity gradient information at high concentrations.

Keywords: *UVP, LDA, velocity profile, pulp, fibre, non-invasive, plug-flow*

1. INTRODUCTION

Pulp suspensions are very complex opaque aqueous systems which contain regions of relatively high fibre concentration called flocs. These tend to form a continuous network structure throughout the suspension above a certain critical concentration and shear rate. The chemical and physical complexity has led to the fact that the relationship between the applied stress and microstructure (rheology) during flow remains poorly understood, despite extensive study for nearly half a century, according to Li et al. [11].

Pulp suspensions are subjected to strong shear forces during processing and detailed knowledge about the flow properties are in fact essential for controlling a modern pulp process.

Competition in the paper pulp industry has increased over the past years. The annual turnover currently surpasses many other industrial branches in countries such as Canada and Sweden. The ability to develop innovative and new competitive products also largely depends on the ability to understand and control the manufacturing process. Since the velocity profile contain the shear rate information, it is thus of great importance if it can be measured. Nevertheless, very little reliable data on velocity profiles in concentrated pulp suspensions during pipe flow can be found in literature.

Until recently, it has been difficult to determine instantaneous radial velocity profiles under actual process conditions. Various flow visualization, as well as sophisticated particle tracking/imaging velocimetry techniques has been continuously improved in the academic field. However, most of them still require extensive experimental know-how; require rather time consuming data acquisition; are essentially limited to transparent fluids and are not applicable to pulp fibre suspensions at concentrations outside the dilute range.

The optical point-wise Laser Doppler Anemometry (LDA) technique [5], the Nuclear Magnetic Resonance Imaging (NMRI) method based on the paramagnetic properties of the nuclei [4], and the Ultrasonic Velocity Profiling (UVP) technique, which employs the pulsed Doppler echo method, [24-26], constitute some of the most promising techniques for pulp suspensions.

NMRI has been used for measuring time-averaged velocity profiles of dilute pulp suspensions, [11-14], in up to 0.86 %(w/w) fibre concentration. Some drawbacks of the method used were, compared to UVP and LDA, expensive equipment and long observation times. More differences between these three techniques are discussed e.g. in [3].

Arola et al. [2], managed to investigate velocity profiles of an aqueous 0.5 %(w/w) pulp suspension using relatively short observation times in the order of milliseconds. Seymour et al. [20] performed measurements of time-averaged velocity profiles in the steady flow of more concentrated 3 %(w/w) pulp suspensions using NMRI. At present, NMRI is not likely going to be implemented in industrial applications.

LDA was used by [6], to investigate air containing low concentrations of pulp in pipe flow. Kerekes et al. [10], studied water-pulp suspensions of 0.5 %. Steen, [21-22], later used transparent model pulp suspensions in order to study higher concentrations, 1.2 and 12 grams of fibres per liter in pipe flow. The same model system were later used by both [1] and [17-18] where measurement were also performed in a stirred tank using concentrations ranging from 3-20 %(w/w).

Few studies with comparative LDA and UVP results can be found in the literature. Some examples are [27], [28], [33], [19] and [16].

The UVP technique has been extensively used over the past few years to obtain instantaneous velocity profiles, but very few studies on pulp suspensions can be found in the literature. Hirsimäki, [7], used an early ultrasonic profiling technique to obtain radial velocity profiles in pulp suspensions of concentrations up to 1 %(w/w). Karema et al. [8-9], characterized velocity fluctuations and studied paper formation by fluidization and reflocculation in wood pulp suspensions of concentrations up to 1 %(w/w) using UVP.

Wiklund et al. [30-31], obtained instantaneous velocity profiles in a steady laminar flow of 0.5-3 %(w/w) and later up to 7.8 %(w/w) paper pulp suspensions using UVP. Rheological data were obtained using non-linear regression analysis and the integrated form of the Herschel-Bulkley model and pressure drop data.

The aim of the present study was to perform velocity profile measurements non-invasively using UVP and LDA in highly concentrated, opaque aqueous pulp suspensions in pipe flow. A further aim was to evaluate the use of the techniques in this type of suspension through comparison.

2. MATERIALS AND EXPERIMENTAL METHODS

2.1 Materials

Fully bleached kraft pulp samples were provided on two different occasions by Värö Bruk (mill), Sweden, but the composition was the same; 30-35 %(w/w) pine and 65-70 %(w/w) spruce. The pulp suspension taken from the mill had a concentration of about 18 %(w/w) of fibres. Fibre length measurements showed that the fibres were not milled during the pipe flow experiments and that the length-weighted mean fibre-length was about 2.4 mm. The tests were performed on two different occasions, with 0.61, 1.0, 1.9, 2.4 and 3.8 %(w/w) in fibre concentration during the first sequence and 0.74, 2.5, 4.4, 6.0 and 7.8 %(w/w) during the second one. During the first test sequence the concentration was changed by adding more of the concentrated 18 %(w/w) pulp. In the latter test sequence with higher concentrations, the concentrated pulp was diluted to 7.8 %(w/w) and lower concentrations in smaller vessels by adding water when the concentration was changed before being placed in the tank.

2.2 Experimental flow loop and Set-up

The experimental set-up and procedure is described in detail in [31]. However, relevant details are given here. The experimental flow loop consisted of a closed circulation system containing a tank, a pulp screw pump, stainless steel pipes, a contraction and finally a smaller pipe made of Polymethyl methacrylate (PMMA), which constituted the measurement section, as shown in Figures 1 and 2. The open tank was placed on top of the pump, thus supplying the pump continuously with fluid from the outlet at the bottom.

The PMMA pipe section had an inner diameter of 40 mm, a wall thickness of 5 mm and a total length of 50 cm. the UVP transducer was mounted at an inclination angle above the pipe inside the surrounding box fluid. The box served two purposes; first, the water-filled box formed an acoustic coupling between the wall and the UVP transducer, thus increasing the transmitted acoustic energy. Second, it made the laser beams enter the water media from the air or water through a plane surface, not a curved one and reflections were thus decreased.
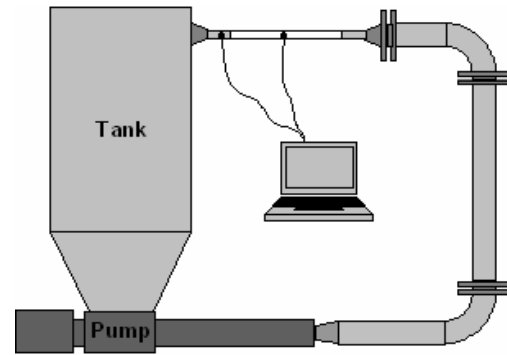

Figure 1. Schematic of the experimental flow loop.

The ultrasonic and laser beams were arranged so that the intersection between the beams was as close as possible to the centre of the pipe. Temperatures in the surrounding box and the test section were kept as equal as possible, 22-24ºC, in order to minimize differences in sound velocity and thus the acoustic impedance between the box fluid and the continuous phase in the suspensions studied.

UVP/LDA velocity measurements were performed, 70 mm from the tank inlet (i.e. upper left side of the PMMA pipe test section in figure 1). The pressure drop over the measurement section was measured continuously and the pressure gauges used ranges from atmospheric pressure up to 4 bar overpressure with an error of 0.5 % of the higher limit.
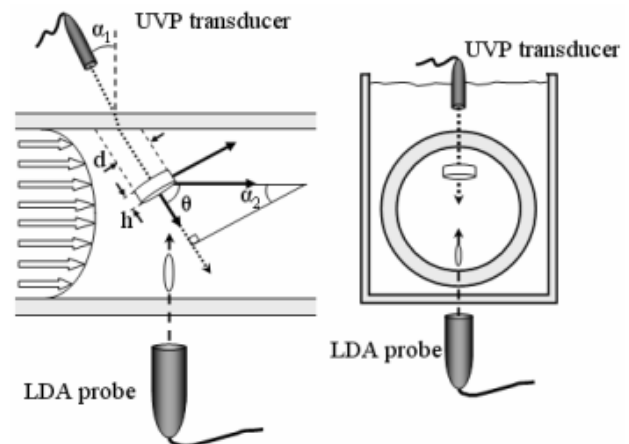

Figure 2. Schematic of the measurement section, ultrasound transducer and LDA probe configuration.

2.3 UVP and LDA equipment and Parameters

The UVP-DUO-MX Monitor with Multiplexer and software, version 3.0 from Met-Flow SA, Switzerland was used in this study. The UVP instrument was connected to a master PC for data acquisition, analysis and post-processing of raw data. Emitted ultrasonic pulses and the received echo were continuously monitored using a digital oscilloscope, Agilent Technologies, model 54624A, USA.

The Laser Doppler Anemometry instrument utilized in these experiments was a DANTEC FiberFlow Series 60X, Denmark, connected to two Burst Spectrum Analysers (BSA), i.e. a DANTEC 57N10, which interpret the Doppler signal to velocities. The equipment was controlled by DANTEC's software Burst Ware, version 3.0. The laser connected to this device was a Spectra-Physics laser, model 2060A-64, Germany.

Table 1: Experimental UVP and LDA parameters

Ultrasound frequency	2 MHz
Number of cycles per pulse	2
Active element diameter	10 mm
Pulse repetitions per profile	90
Number of recorded channels/profiles	110 -128 / 1024
Number of recorded profiles/flow rate	1024
Sound velocity	1485-1531 m/s
Doppler angle in suspensions	68.5-73°
Spatial resolution in suspensions	0.74 - 0.77 mm
Time resolution (single profile)	24-54 ms/profile
Pulse repetition rate	2.2 KHz - 6.2 KHz
Velocity resolution	10-24 mm/s
LDA measurement volume in suspension (radial direction)	950 μm
Number of LDA repetitions per point	5000

2.4 Experimental procedure

The tank was filled with the suspension, agitated mildly, the pump was then set to the desired flow rate and the flow was allowed to attain the steady-state. Four volumetric flow rates were investigated; 0.87, 1.45, 2.04 and 2.63 L/s. The test sequences started with the lowest flow rate and were then increased during the experiments at each concentration. UVP and LDA data acquisition were triggered simultaneously but UVP data acquisition was much faster. The wall positions and thus the first and last UVP channel number located inside the test pipe section were determined from a procedure that involves monitoring the echo amplitude, velocity gradient and several statistical steps in each recorded channel over time.

A few correction procedures of the effect on measurement volumes at the wall-liquid interface have recently been suggested by [32], [15] and [23] but they are still under debate. This effect and the effect of the curvature of the tube wall were therefore neglected in this study, the latter in accordance with mentioned papers.

In order to reduce the signal noise induced by e.g. mechanical vibrations, a statistical procedure was employed in which fluctuations larger than two standard deviations from the median value in each channel were removed. Arithmetic time-averaged velocity profiles were then calculated from the remaining radial velocity profiles.

3. RESULTS AND DISCUSSION

The applicability and limitations of LDA technique for investigated pulp suspensions is discussed. The velocity profiles obtained using UVP and LDA as well as key findings from using the techniques are then presented, compared and discussed for the investigated flow rates and concentrations.

3.1 LDA applicability in pulp suspensions

The LDA technique requires a transparent system, but correct measurements are still performed some distance into the apparently opaque pulp suspensions. In the concentrations presented in the figures, a maximum penetration depth of up to 7 mm was achieved. However, in a suspension as high as 7.8 %(w/w) the penetration depth was reduced to 3-4 mm, as shown in Figure 6. The most reasonable explanation for LDA to work in this system is that even though these pulp suspensions, at first sight, look more or less opaque, they contain only a couple percent of fibres by volume, and the rest is water. This means that the laser beams can reach some millimeters into the suspension by means of passing between the fibres. What happens is somewhat similar to ordinary LDA measurements of water when the water is seeded with particles that have a rather low concentration. If the seed particle concentration is increased, there will be a loss in penetration depth, but the performed measurements will still be correct.

**3.2 General comparative results for the pulp suspensions**

When comparing the UVP and LDA results over the range of investigated concentrations, it was found that the absolute values of the velocities agree well. This is clearly shown in Figures 3-6. The velocity gradient information in the recorded velocity profiles on the UVP transducer side were clearly visible for all investigated flow rates, but completely lost in the LDA measurements for all but the lowest concentrations. It was also found that all investigated suspensions exhibited various degrees of plug flow behavior and as the flow rate decreased, the plug-flow region increased in size, that is, larger plug radius R_0 for all but the highest concentration 7.8 %(w/w). A decrease in the plug-flow region was also found as the concentration decreased.

Since the obtained velocities from two different independent techniques (UVP and LDA)agrees very well with those calculated from volumetric flow rate measurements, the obtained results implies that both techniques give, indeed, accurate velocity results for the investigated pulp suspensions.

However, the results also show, e.g. in Figures 4-6, a decrease in penetration depth for LDA and the effect of various artifacts (discussed below) for the UVP method.

3.3 Flow behavior at < 2 %(w/w) pulp concentrations

Good agreement for the two techniques in the shape of the velocity gradient close to the far end wall from the UVP transducer side was found for low concentrations and high flow rates in this study, as shown in Figure 3.
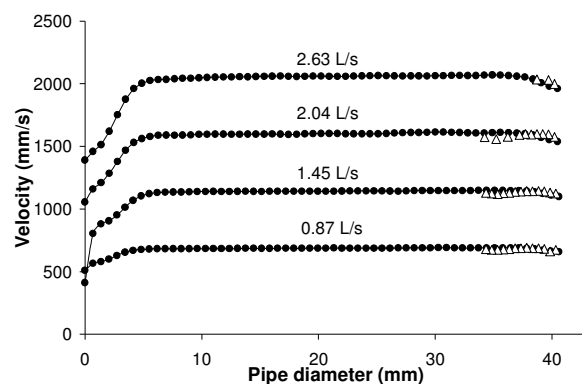
Figure 3. Velocity profile data for 1.9 %(w/w) pulp suspension for four volumetric flow rates. UVP (filled circles) and LDA (open triangles).
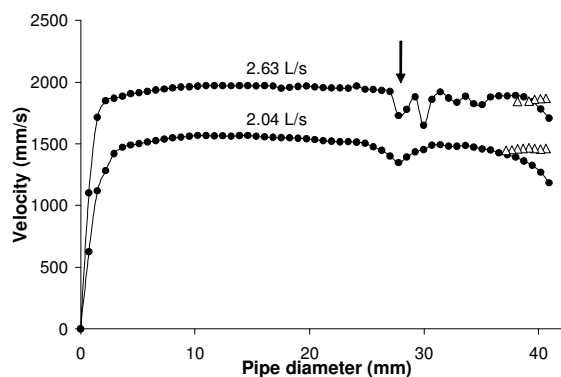
However, the velocity gradient information in the recorded velocity profiles on the UVP transducer side were quite distorted for the lowest flow rates, but less for the two highest flow rates. This effect was difficult to account for but mechanical vibrations were observed in this experiment which may have pushed the UVP transducer slightly from its optimal position in such way that the first points close to the wall were actually recorded within the near field zone. This effect may also have been caused by wall effects, but no such phenomena were observed for other concentrations and flow rates.

3.4 Flow behavior at 4-6 %(w/w) pulp concentrations

When comparing the UVP and LDA results over the intermediate concentration range, it was found that the absolute values of the velocities agree very well. This is clearly shown in Figures 4-5. The velocity gradient information in the recorded velocity profiles on the UVP transducer side were clearly visible for all investigated flow rates, but completely lost in the LDA measurements.
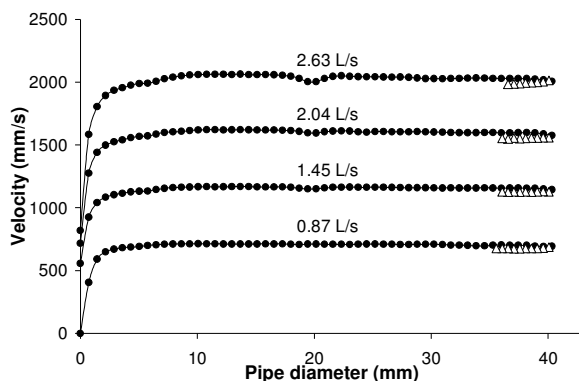
Figure 4. Velocity profile data for 4.4 %(w/w) pulp suspension for four volumetric flow rates. UVP (filled circles) and LDA (open triangles)
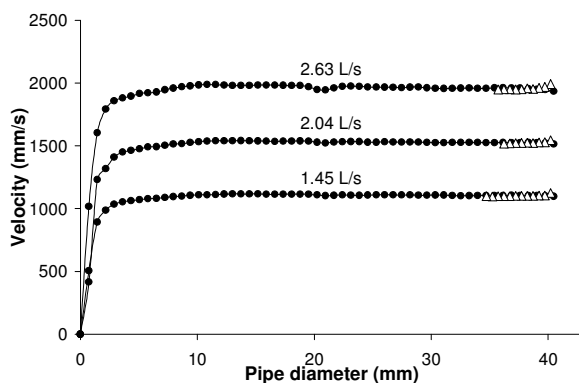
Figure 5. Velocity profile data for 6.01 %(w/w) pulp suspension for three volumetric flow rates. UVP (filled circles) and LDA (open triangles)

It was also found that investigated suspensions in this concentration range exhibited pronounced plug flow behavior. As the flow rate decreased, the plug-flow region increased in size, that is, larger plug radius R_0.

In addition, the results also showed the effect of various artifacts for the UVP method which resulted e.g. in a visible constant plug behavior of the recorded velocity profile, in which the velocity gradient information is lost towards the far end wall from the transducer side.

3.5 Flow behavior at >7.8 %(w/w) pulp concentrations

Pronounced plug flow behavior was also found for the highest pulp concentration of 7.8 %(w/w), as shown in Figure 6. It is interesting to note that the plug-flow region seemed to decrease in size (smaller plug radius, R_0) as the flow rate decreased for this concentration, which is in contrast to lower concentrations.

Furthermore, the local drop in velocity for both volumetric flow rates which is indicated by an arrow in Figure 6, which corresponds to the highest concentration, is also believed to be a UVP measurement artifact. This artifact was most likely caused by, multiple reflections from e.g. the pipe walls and not caused by a decrease in penetration depth due to attenuation of ultrasound.

Figure 6. Velocity profile data for 7.81 %(w/w) pulp suspension for two volumetric flow rates. UVP (filled circles) and LDA (open triangles).

Although the velocity gradient information in the recorded velocity profiles on the far UVP transducer side was visible for both investigated flow rates, it was also influenced by wall effects and ultrasound attenuation. Therefore, especially in Figure 6, it would be more accurate to compare the LDA measurements with the UVP results from the opposite side of the pipe, i.e. close to the UVP transducer. Doing this, good agreements were found even at the highest concentration in absolute velocities.

3.6 Time-averaging effects on UVP velocity profiles

Figure 7, which corresponds to a pulp concentration of 6.0 %(w/w), clearly demonstrates that it was possible to obtain a single instantaneous and complete velocity profile across the pipe test section with high accuracy using the UVP technique for only a couple of milliseconds.

Results in Figure 7 indicate that an arithmetic average of 10 sequential profiles (open circles) describes the plug flow behavior in great detail and that only slightly better profiles are obtained if more ~1000 profiles (filled circles) are used in arithmetic average calculations. The trend was the same for all suspensions.
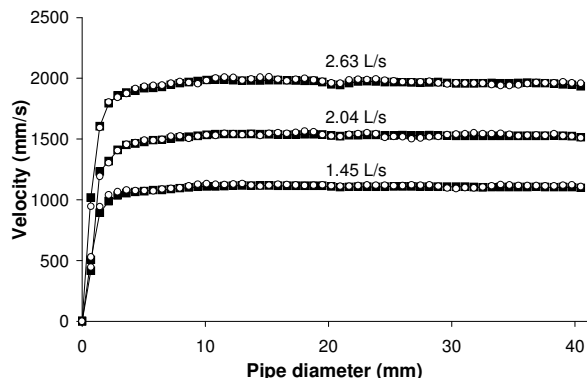
Figure 7. Arithmetic mean velocity profile data over ~1000 (filled circles) and 10 sequential (open circles) UVP profiles for 6.01 %(w/w) pulp suspension for three volumetric flow rates.

3.7 UVP related measurement artifacts and effects

As mentioned above, it was observed in this study that almost all of the obtained velocity profiles exhibited visible constant plug behavior throughout the pipe towards the far end wall from the transducer side. In this far region the velocity gradient information was lost. This artifact was most likely caused by e.g. multiple reflections from e.g. the pipe walls and the large number of scattering fibres and not by a decrease in penetration depth due to attenuation of ultrasound.

Fixed and moving interfaces reflect and modify the field of the acoustic pulse. In the wall region close to the transducer, multiple reflections by the wall and the irregular shape of the ultrasonic pulse beam in the near-field region may imply that the results are less reliable in this region in contrast to the LDA technique which does not suffer from this effect. In this study, the focal point was therefore positioned as close to the wall-liquid interface inside the tube as possible and this effect was therefore minimized.

However, mechanical vibrations were observed, e.g. for the lowest concentration which may have pushed the UVP transducer slightly from its optimal position in such way that the first points close to the wall were actually recorded within the near field zone. The non-zero velocity phenomenon and irregular shape of the velocity profile at the interface wall close to the transducer was therefore observed only for the 1.89 %(w/w) concentration in this study, as shown in Figure 3.

It is well known that the ultrasonic pulse beam can be forward-scattered by a moving seeding particle (fibre in this case) contained in the flowing suspension towards the far pipe wall interface. This acoustic energy is thus backscattered a second time in the direction to the transducer. The distance associated with the path transducer far pipe wall interface-scatterers is therefore located outside the flowing liquid. As a result, imaginary velocity components were most likely added to the real velocity profile, especially near the far pipe wall interface as pointed out by, e.g. Wang et al. [29].

The local drop in velocity for both volumetric flow rates indicated by an arrow in Figure 6, which corresponds to the highest concentration, is believed to be caused by this effect.

It was also found that the velocity profiles thus did not reach the expected zero velocity at the far interface wall and thus often appear to be slightly wider than the actual pipe diameter due to mentioned measurement artifacts. The illusion of velocity profiles being slightly wider than the actual pipe could also be enlarged by error in sound velocity and Doppler angle determination.

However, when comparing the UVP and LDA absolute velocity values it was found that they agree very well. Since the entire beam path was calculated and accounted for these findings implies that the correct sound velocity and Doppler angles were used when calculating the velocity and radial distance. Other phenomena than those discussed may also be involved in this case.

The intensity of the acoustic field received from a location inside the flowing suspension depends on the material, the shape and the number of these interfaces along the beam path. In addition, ultrasonic waves reflected multiple times inside a solid wall interface enlarge the ultrasonic beam inside the flowing suspension and modify its shape. These reflections, thus, make it more difficult to accurately predict the exact size and the shape as well as the location of the measuring volume when performing non-invasive measurements through multiple interfaces or thick wall materials.

In most commercial software, such as the one used with the UVP equipment used in this study, the ultrasound refraction and difference in sound velocity in multiple media are not taken into consideration, as pointed out by Wang et al. [29].

Consequently, these findings imply that measurements of the profile close to the pipe wall interface at the far end from the transducer side are less reliable due to mentioned artifacts since many of those are not compensated for. All velocity profiles were therefore truncated at the last measuring volume that originated from a position inside the pipe measurement section.

Further investigations are needed to fully explain, predict and compensate for the effects of mentioned artifacts for the investigated and similar pulp suspensions.

4. CONCLUSIONS

In this study, UVP and LDA techniques were used simultaneously to perform velocity profile measurements in highly concentrated pulp fibre suspensions in an experimental pipe flow loop. It was shown that both techniques can be used with good agreement to obtain accurate velocity (LDA) and velocity profile (UVP) data in much more concentrated fibre suspensions than what has been reported so far in the literature. No special seeding particles were needed as the

pulp fibres were found to work sufficiently for both LDA and UVP techniques. It was also demonstrated that LDA had a sustained penetration depth of up to several millimeters for these seemingly opaque systems such as a 7.8 %(w/w) pulp suspension. Furthermore, results showed that the UVP technique was sensible to various artifacts that could result in a visible constant plug behavior of the recorded velocity profile, in which the velocity gradient information is lost towards the far end wall from the transducer side. However, the UVP method could be optimized in such way that the penetration depth was sustained almost through the entire measurement section even for the highly concentrated 7.8 %(w/w) pulp suspension.

5. ACKNOWLEDGEMENTS

6. REFERENCES

1. Andersson, S., and Rasmuson A., "Flow Measurements on a Turbulent Fibre Suspension by Laser Doppler Anemometry" *AIChE J.*, **46** (6), 1106-1119 (2000).

2. Arola, D. F., Powell R. L., McCarthy M. J., Li T.Q., and Ödberg L., "NMR imaging of pulp suspension flowing through an abrupt pipe expansion" *AIChE J.*, **44**(12), 2597-2606 (1998).

3. Choi, Y.J., McCarthy K.L., and McCarthy M.J., "Tomographic techniques for measuring fluid flow properties" *J. Food Sci.*, **67** (7), 2718-2724 (2002).

4. Chaouki J., Larachi F., and Dudukovic M.P., "Noninvasive tomographic and velocimetric monitoring of multiphase flows" *Ind. Eng. Chem. Res.*, **36**(11), 4476-4503 (1997).

5. Durst, F., Melling A., and Whitelaw J. H., *Principles and Practice of Laser-Doppler Anemometry*, Academic Press, New York, USA (1981).

6. Ek, R., Möller K., and Norman B., "Measurement of velocity and concentration variations in dilute fiber/air suspensions using a laser Doppler anemometer" *TAPPI J.*, **61** (9), 49-52 (1978).

7. Hirsimäki, O., "Determination of Radial Velocity Profile and Flow Disturbance of Pulp Suspension by Ultrasonic Echo Correlation" *Paperi ja Puu*, **60** (2), 95-97 (1978).

8. Karema, H., Kataja M., Kellomäki M., Salmela J., and Selenius P., "Transient Fluidisation of Fibre Suspension in Straight Channel Flow" *TAPPI Int. Paper Phys. Conf.*, San Diego, USA, 369-379 (1999).

9. Karema, H., Salmela J., Tukiainen M., and Lepomäki H., "Prediction of Paper Formation by Fluidisation and Reflocculation Experiments" *12th Fund. Res. Symp.*, Oxford, UK, 559-589 (2001).

10. Kerekes, R.J., and Garner R.G. "Measurement of Turbulence in Pulp Suspensions by Laser Anemometry" *Trans. Tech. Sect. CPPA*, **8**, TR53-TR60 (1982).

11. Li, T.Q., Seymour J. D., Powell R. L., McCarthy M. J., McCarthy K. L., and Ödberg L., "Visualization of flow patterns of cellulose fiber suspensions by NMR imaging" *AIChE J.*, **40** (8), 1408-1411 (1994a).

12. Li, T.Q., Powell R. L., Ödberg L., McCarthy M. J., and McCarthy K.L., "Velocity measurements of fiber suspensions by the nuclear magnetic resonance imaging method" *TAPPI J.*, **77** (3), 145-149 (1994b).

13. Li, T. Q., and Ödberg L., "Flow properties of cellulose fiber suspensions flocculated by cationic polyacrylamide" *Coll. and Surf. A: Physiochem. Eng. Aspects*, **115**, 127-135 (1996).

14. Li, T. Q., and Ödberg L., "Studies of Flocculation in Cellulose Fibre Suspensions by NMR Imaging" *J. Pulp Pap. Sci.*, **23** (8), 401-405 (1997).

15. Nowak, M., "Wall shear stress measurement in a turbulent pipe flow using ultrasound Doppler velocimetry" *Experiments in Fluids*, **33**, 249-255 (2002).

16. Ozaki, Y., Kawaguchi T., Takeda Y., Hishida K., and Maeda M., "High time resolution ultrasonic velocity profiler" *Exp. Therm. Fluid Sci.,* **26**, 253-258 (2002).

17. Pettersson, J., and Rasmuson A., "LDA Measurements on a Turbulent Gas/Liquid/Fibre Suspension" *Accepted for publication in Can. J. Chem. Eng.*, (2004a).

18. Pettersson, J., Wikström T., and Rasmuson A., "Near Wall Studies of Pulp Suspension Flow Using LDA" *Submitted for publication*, (2004b).

19. Sato, Y., Mori M., Takeda Y., Hishida K., and Maeda M., "Signal processing for advanced correlation ultrasonic velocity profiler" Third International Symposium on Ultrasonic Doppler Methods for Fluid Mechanics and Fluid Engineering, September 9-11, 2002, Lausanne, Switzerland, 5-11 (2002).

20. Seymour, J. D., Maneval J. E., McCarthy K. L., McCarthy M. J., and Powell R. L., "NMR velocity phase encoded measurements of fibrous suspensions" *Phys. Fluids A: Fluid Dyn..*, **5** (11), 3010-3012 (1993).

21. Steen, M., "The Application of Refractive Index Matcing for Two-phase Flow Measurements in Turbulent Fibre Suspensions by Laser Doppler Anemometry" *Nord. Pulp Pap. Res. J.*, **4** (4), 236-243 (1989a).

22. Steen, M., "On Turbulence Structure in Vertical Pipe Flow of Fiber Suspensions" *Nord. Pulp Pap. Res. J.*, **4**(4), 244-252 (1989b).

23. Taishi, T., Kikura H., and Aritomi M., "Effect of measurement volume in turbulent pipe flow measurement by the ultrasonic velocity profile method (mean velocity profile and Reynold stress measurement)" *Experiments in Fluids*, **32**, 188-196 (2002).

24. Takeda, Y., "Velocity Profile Measurement by Ultrasonic Doppler Shift Method" National Heat Transfer Conference, *American Society of Mechanical Engineers*, **112** (106), 155-160 (1989).

25. Takeda, Y., "Development of an ultrasound velocity profile monitor" *Nucl. Eng. Design*, **126**, 277-284 (1991).

26. Takeda, Y., "Velocity Profile Measurement by Ultrasonic Doppler Method" *Exper. Therm. Fluid Sci.*, **10**, 444-453 (1995).

27. Teufel, M., Trimis D., Lohmuller A., Takeda Y., and Durst F., "Determination of veloctiy profiles in oscillating pipe-flows by using laser Doppler velocimetry and ultrasonic measuring devices" *Flow Meas. and Instr.*, **3** (2), 95-101 (1992).

28. Tokuhiro, A., "Experimental investigation of a vertical jet by ultrasound and laser Doppler velocimetry" *J. Nucl. Sci. and Tech.*, **36** (6), 540-548 (1999).

29. Wang, T., Wang J., Ren F., and Jin Y., "Application of Doppler ultrasound velocimetry in multiphase flow" *Chem. Eng. J.*, **92**, 111-122 (2003).

30. Wiklund, J., Johansson M., Shaik J., Fischer P., Windhab E., Stading M., and Hermansson A.-M., "In-Line Ultrasound based Rheometry of industrial and model suspensions flowing through pipes" *Third International Symposium on Ultrasonic Doppler Methods for Fluid Mechanics and Fluid Engineering*, September 9-11, 2002, Lausanne, Switzerland, 69-76 (2002).

31. Wiklund, J., Pettersson, J., Stading M., and A. Rasmuson, "A Comparative Study of UVP and LDA Techniques for Pulp Suspensions in Pipe Flow" *Submitted for publication*, (2004).

32. Wunderlich, T., and Brunn P. O., "A wall layer correction for ultrasound measurement in tube flow: comparison between theory and experiment" *Flow Meas. and Instr.*, **32**, 63-69, (2000).

33. Yamanaka, G., Kikura H., Takeda Y., and Aritomi M., "Flow measurement on oscillating pipe flow near the entrance using the UVP method" *Experiments in Fluids*, **32**, 212-220 (2002).

7. NOTATION

α_1 = transducer inclination angle

α_2 = angle between direction of flow and measurement axis

c = sound velocity, m/s

θ = Doppler angle

d = diameter of the measuring volume of the UVP, m

f_0 = basic ultrasonic frequency, MHz

h = thickness of UVP measurement volume, m

L = distance between pressure sensors, m

L/s = Volumetric flow rate, liters per second

N = number of ultrasonic cycles per pulse

r = radial coordinate, m

R = pipe radius, m

R_0 = plug radius, m

v = velocity, m/s

(w/w) = mass percentage pulp fibers

USING ULTRASONIC VELOCITY PROFILE MEASUREMENTS IN
AN AIR-VESSEL TYPE SURGE-TANK MODEL

R. KLASINC, M. LARCHER, A. PREDIN*

Graz University of Technology   roman.klasinc@tugraz.at, Larcher@hydro.tu-graz.ac.at
*University of Maribor

ABSTRACT

The downstream (turbine) portion of a pumped storage station was reproduced in a hydraulic scale model. Water was supplied through three simulated Pelton turbines. The problem to be solved by the model tests was the fact that for structural reasons the turbines are located below the water level of the lower reservoir. As water must be kept away from the turbine rotor, it is necessary to produce overpressure (compressed air). This, however, involves problems which need to be analysed in the physical model by defining the surge movement, because the rotor must by all means be prevented from being submerged. Part of the compressed air escapes together with the turbine outflow. Therefore, it is necessary to optimise the geometries (turbine casing) with a view to minimising this air flow. An ultrasonic measuring instrument (UVP) was used to monitor these processes. Three parameters were considered: the velocity profiles in the surge tank, the movement of the surge, and an attempt was made to identify the distribution of air bubbles.

Keywords: surge tank, air flow, velocity profiles, air bubbles

EXPLANATORY COMMENTS

Hydraulic scale model tests have been carried out at the Hermann Grengg Laboratory of the Department for Hydraulic Engineering and Hydro Resources Management at the Graz University of Technology since 1964. More than 300 tests have so far been performed for projects throughout Austria and abroad as well as for fundamental research purposes.

The studies described in this report were conducted as part of a test on the model of an air-vessel type surge-tank situated in the tailwater system of a pumped-storage scheme. The hydraulic tailwater system (Figure 1) consists of three separate air-vessel type surge chambers uniting in a connection gallery and linked with the lower reservoir by the tailwater gallery.
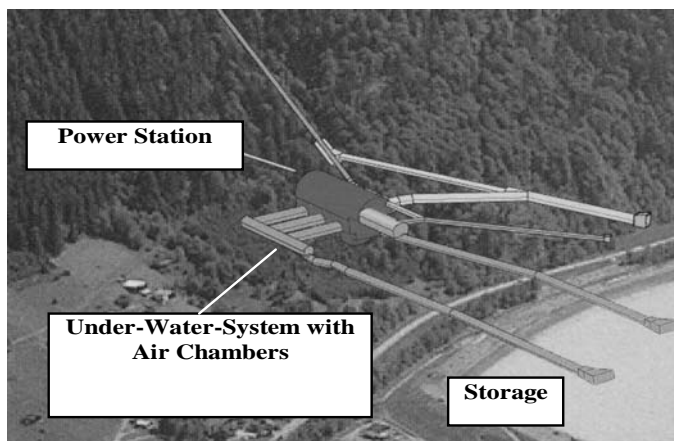
Fig. 1 Tailwater system scheme

As the water surface level of the lower reservoir is always above the axis of the impulse turbines, it is necessary to maintain a pressure of up to 3 bar above atmospheric in order to draw down the water surface within the surge chambers.

The two principal functions of the air-vessel type surge chamber are to dampen the water level fluctuations between the lower reservoir and the surge chambers in the case of mass oscillation and to absorb the air taken in by the turbines and degassing into the surge chamber(Figure 2).
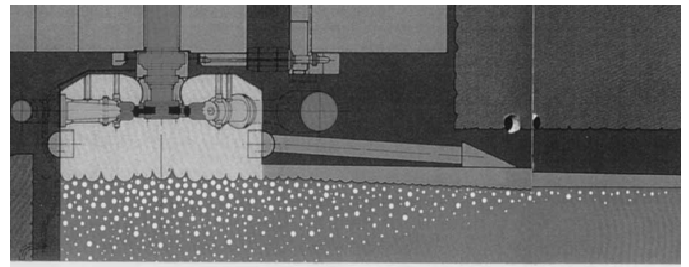
Fig. 2 Degassing into the surge chamber

The problem of such plants is that the air taken in actually does not entirely degas into the surge chamber, but is evacuated from the system through the tailwater gallery and is thus lost to the system. This question is of vital importance, especially where the turbine gallery is joined with the pump inlet line, that is, in the case of a „short-cut", as this may cause damage to the mechanical equipment (pumps, turbines, etc.).

The plexiglass model shown in Figure 3 was constructed to scale 1:22.5 at the Department and installed in its laboratory.
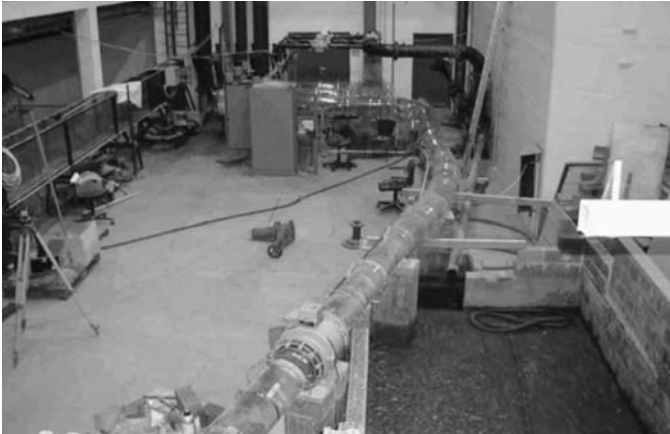
Fig. 3 Plexiglas model in the laboratory

THE MEASURING METHOD

The studies were carried out by use of the XW-3_Psi ultrasonic velocity profile measuring instrument made by Met-Flow. This measuring system consists of a computer (Main Unit) with an integrated keyboard, a display unit and multiplexed ultrasonic transducers. A maximum of four 4MHz transducers, 5mm in diameter, were available.

Fig. 4 Measureequipment XW-3Psi

The measurement window was designed as a function of the instrument parameters within the boundaries of the chamber cross-section. Results from the fringe zones near the contact between water and plexiglass (8mm in thickness) were omitted to avoid including imaginary results and unwanted reflections from the opposite wall.
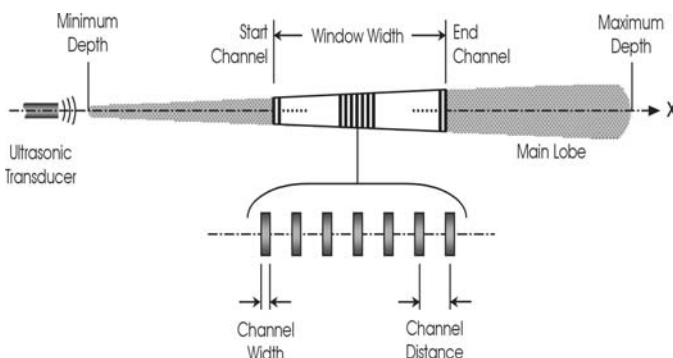
Fig. 5 Measureequipment XW-3Psi

The angle the transducer made with the flow direction (Doppler angle), which is important for defining the measurable velocity range, mainly depended on the structures installed at the entrance to the surge chamber. This angle was 75° for both horizontal and vertical measurements. The feasible measuring range of a 4MHz transducer was between –750 and 750mm/s for a maximum measuring depth of approximately 350mm, .
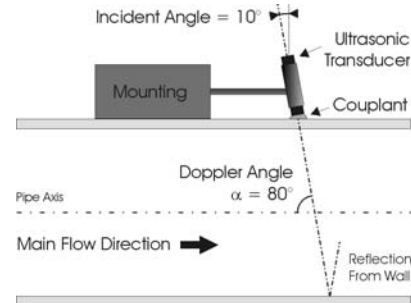
Fig. 6 Measureequipment XW-3Psi

As visual inspection had already suggested that swirl flow and, hence, turbulent flow conditions would occur, the instruments were tested, or "calibrated", by trying them first in positions where steady flow was expected. A further check of the instrument parameters was made by making comparable measurements at two opposite locations in the surge chamber.

The characteristic features of turbulent flow conditions are irregular secondary velocity components diverging from the main flow direction. The reflections of the fluid particles moving in all spatial directions affect the results of UVP measurements. Increased measuring durations proved effective in obtaining better results.
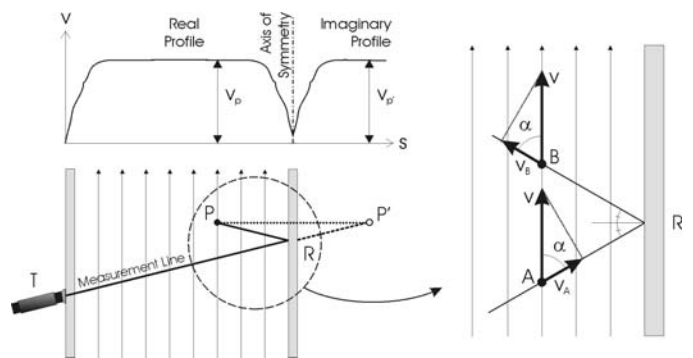
Fig. 7 Measureequipment XW-3Psi

UVP MEASUREMENTS AND RESULTS

During the first phase of the model tests it was important to study different turbine shaft configurations and their influence on the flow conditions. The main criteria of assessment were the length of the degassing zone as well as the velocity curve along the surge chamber. The UVP measurements were intended in the first place to describe the velocity curves in the surge chamber and, secondly, to provide additional information on the boundaries of the zone in the centre of the chamber cross-section where the undissolved air fraction

degases. By way of example, the measurements made in a non-symmetric turbine shaft will be described in the following paragraphs.
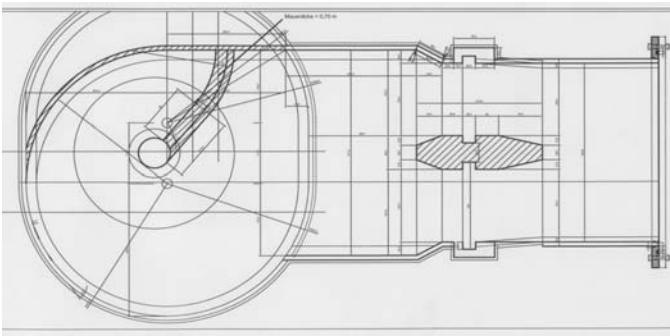
Fig. 8 Non-symmetric turbine shaft

Velocity curve

The velocity curve was described by means of measurements made in 7 cross-sections provided along the surge chamber. The surge chamber is approximately 3.50m long and has a horseshoe cross-section with a maximum internal width of 32.8cm and an internal height of 35.5cm. Allowance had to be made for the geometry of the structures installed within the surge chamber in positioning the measuring cross-sections. The maximum spacing was 50cm.
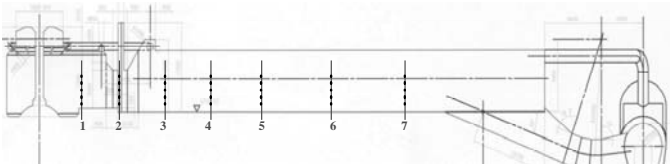
Fig. 9 Chamber-section

The water depth within the surge chambers selected for a certain stationary operating condition was about 24cm. In each cross-section measurements were taken in 5 horizontal planes with a constant spacing of 4.5cm. The measured velocity curves in Profile 1, in the entrance zone of the chamber, are shown plotted in Figure 10. The curves indicate the presence of some reverse flow in the two lower measuring planes as well as unsteadiness in the velocities measured in the foam zone.
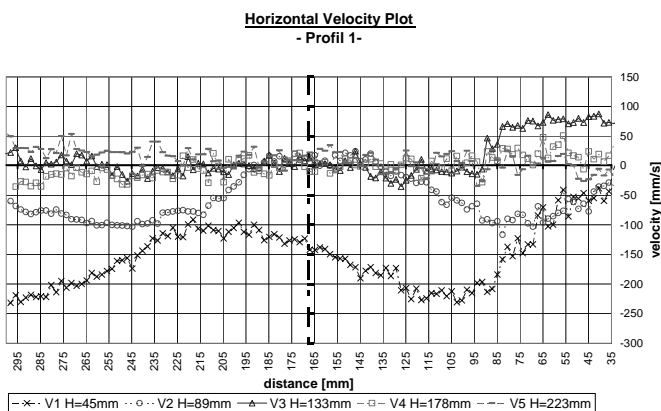
Fig. 10 Velocity plot in Profile 1

Figure 11 is a graph showing horizontal velocities measured in Profile 2. The influence of the asymmetrical inlets to the turbine shafts on outlet flow is clearly seen when comparing the weir openings, which are separated by piers in this area.
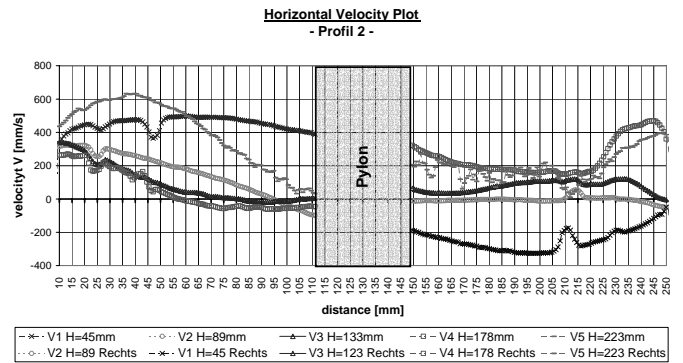
Fig. 11 Velocity plot in Profile 2

This asymmetry in the velocity curve continues, though decreasing, as far as Profile 7 (Figure 12). The results from each measuring cross-section were summarised in tables and diagrams, which served as a basis for the qualitative assessment of the velocity curve.
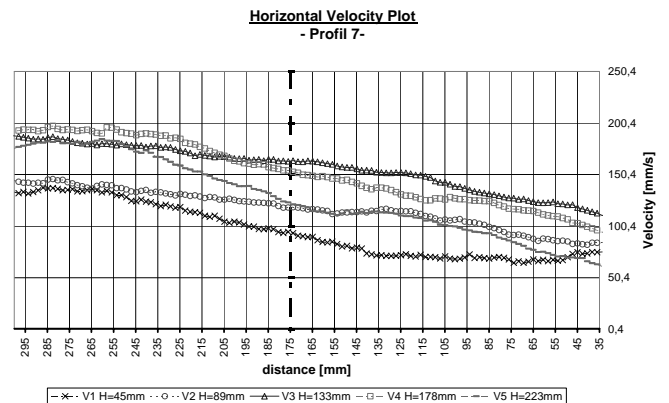
Fig. 12 Velocity plot in Profile 7

Reverse-flow swirls at the chamber floor were seen to extend to the middle of the chamber length. The turbulent swirl flows within the measuring cross-sections have only a minor influence on the velocity curve in general, they do, however, affect the quantitative result of the measurements.

Defining the boundaries of thedegassing zone

Degassing was studied by means of photographic evaluation of the chamber walls supported by the evaluation of the degassing zone in the middle of the cross-section using UVP measurement. The measurements were made at 4 points with a constant spacing of 4.5cm.
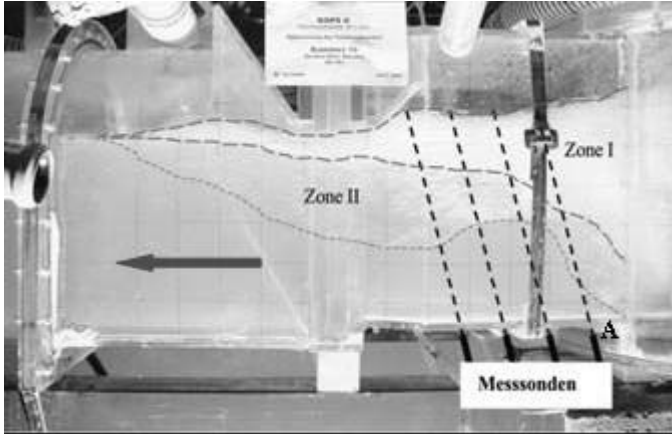
Fig. 13 Picture with degassing zones

The degassing area, shown in Figure 13, falls into two zones: An upper foam zone (Zone I), with a bubble size of up to 15mm and a high proportion of air in the water/air mix, moves at a low velocity.

In the lower area (Zone II), with a smaller proportion of bubbles, the air bubbles are characterised by jerky movement.

Figure 14 is a graph showing the velocities measured during a test as a function of depth, demonstrating, by way of example, a vertical UVP measurement made by Transducer A. The foam area (Zone I) is characterised by extremely fluctuating velocity levels, ranging in this case between 110mm and 270mm.
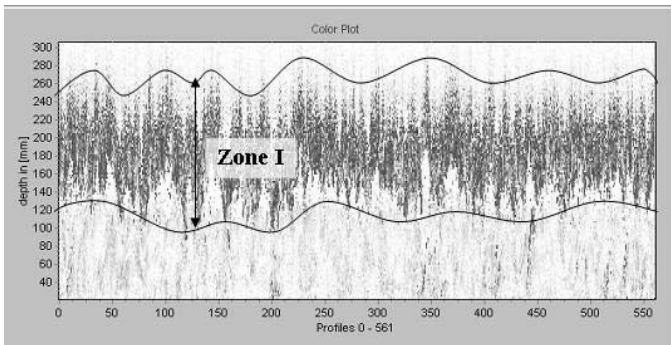
Fig. 14 Example of a vertical UVP measurement

In combination with photographic evaluation of the degassing process, UVP measurement proved a suitable method for a qualitative assessment of the turbine-shaft configuration. As, however, the size of the air bubbles in the model is relatively too large, quantitative transfer of the results to prototype conditions is either very difficult or impossible.

CONCLUDING REMARKS

A complex study programme was required for the scale model test on a compressed-air surge tank. This included identifying the velocity field and the wave movement resulting from the surge phenomena as well as zones characterised by a two-phase water/air mix.

The results of the velocity measurements showed qualititative agreement with the numerical analysis. Greater accuracy in determining the velocity curve would have been obtained if additional transducers had been purchased for the multiplex system. The two-phase zone was largely defined; the boundaries of the foam zone were clearly determined. Irregular two-phase zones were defined by the additional use of photographic analysis.

REFERENCES

1. Klasinc R., Geisler T., Predin A.: XXIX IAHR Congress 2001: Special seminar, Instrumentation for hydraulic Engineering: Measurement of Flow Velocities and Interfacial Wave Profiles by Use of the Ultrasonic Velocity Profile monitor

2. Met-Flow, (2000): Manual, UVP Monitor model UVP-XW, www.met-flow.com

3. Geisler, T., (2001): Ultrasonic Velocity Profile Measurements in Experimental Hydraulics; Diploma Thesis; www.cis.tugraz.at/wb/

4. Knoblauch, Klasinc, Geisler, Breitenstein,: Third Int. Symposium on Ultrasonic Doppler Methods for Fluid Mechanics and Fluid Engineering EPFL: Lausanne (2002): Ultrasonic velocity profile measurements in pipes and flumes in a hydraulic laboratory

IMPROVING THE INTERNATIONAL ACCEPTABILITY
OF
FLOW MEASUREMENTS

G. E. Mattingly*

*Chairman, CIPM/CCM/Working Group for Fluid Flow
and Deputy Chief, Process Measurements Division
National Institute of Standards and Technology Gaithersburg, MD
USA, E-mail: gmattingly@nist.gov

ABSTRACT

Rapid advances in technology–communications, the internet, tele–marketing, travel, etc. are accelerating the globalization of the world's market places. To facilitate this globalization, the Committee on International Weights and Measures (CIPM) has produced a Mutual Recognition Arrangement (MRA). This Arrangement, signed into existence in Oct 1999, has the objectives:

1. to establish the degree of equivalence of national measurement standards maintained by the National Metrology Institutes (NMIs),
2. to provide for the mutual recognition of calibration and measurement certificates issued by the NMIs, and thereby
3. to provide governments and other parties with a secure technical foundation for wider agreements regarding measurements that relate to international trade, commerce, and regulatory affairs.

Information on the CIPM, and the MRA can be found on the website: www.bipm.org

Degrees of equivalence between national measurement standards are based on the results of comparisons conducted within the Consultative Committees of the CIPM. Flow measurement efforts are being addressed by the newly formed Working Group for Fluid Flow (WGFF) of the CIPM Consultative Committee on Mass and Related Quantities (CCM). The member National Metrological Institutes (NMIs) of the WGFF are organized into specific measurement areas. In each of these areas, and according to MRA rules, the efforts are to design and conduct Key Comparison (KC) tests that quantify the equivalence of the flow standards maintained in the participating NMIs. To determine appropriate operating ranges for KC's, the WGFF is reviewing the Calibration and Measurement Capabilities (CMCs) of the participating NMIs.

This keynote presentation will briefly describe the MRA and the WGFF plans and programs to conduct the KC tests. The techniques planned for the KCs will be to design tandem flow meter transfer standards in the selected fluid and flow test conditions to quantify the performance of NMI flow standards under actual conditions of use. Youden analysis of variance techniques are planned to guide the resulting data analysis.

The results of these efforts are expected to make it feasible for flow measurements made anywhere in the world to be understood and acceptable anywhere else.

DREAMS ABOUT LEGAL GAS METERING

Jos G.M. van der Grinten*

*Nmi Certin B.V., P.O. Box 394, 3300 AJ Dordrecht, The Netherlands, E-mail: JvanderGrinten@nmi.nl

ABSTRACT

The future of gas metering is determined by past, present and future developments in the areas of metrology, economy and metering technology. This paper will show for each of these areas the current developments and development that are likely to occur or to be wished from a user perspective. This view will cover metrological, economical and technological aspects.

Generally, introduction of the concept that there are two types of information in metrology, will simplify the understanding of the background of taking measurements.

Economically, the supply of natural gas will be metered on an energy basis. New miniaturised, fast responding and cheap gas composition measurements will contribute to this market demand.

Not only the development of new and improvement of existing metering principles is important but also the measurement of flow profile, swirl, pulsations, acoustic noise, vibration and the thermodynamic properties of natural gases are important.

For the future the research area for flow meters, energy measurement, natural gas properties, disturbance testing and new metrological phenomena will remain interesting and challenging.

Keywords: Metrology, Gas meters, Energy

INTRODUCTION

Legal gas metering is the activity where gas meters are used to measure the amount of gaseous fuel or industrial gasses for custody transfer purposes, i.e. money transactions for gas supplies and fiscal purposes: taxes, levies and duties. Many counties in the world have for gas meters legal requirements that are based on the current OIML recommendations R6 [1], R31 [2] and R32 [3]. In most European countries these recommendations were implemented in their weights and measures legislation. In countries like e.g. Japan and Australia OIML recommendations are implemented via standards that are compulsory for custody transfer measurements. OIML is the International Organisation for Legal Metrology, a treaty organisation established in 1955. The countries that signed the treaty have the moral obligation to implement the OIML recommendations in their national legislation. The objective is to establish coherent metrology legislation in countries, which makes trade between countries easier. Today, OIML counts the membership of 59 countries and the corresponding membership of another 50 countries from all over the world.

The current OIML recommendations are technology oriented: diaphragm meters R31 [2], rotary piston and turbine gas meters R32 [3], supported by general provisions R6 [1]. For other technologies (e.g. ultrasonic and coriolis) there are no recommendations. Today, in the Dutch legislation only diaphragm, rotary piston and turbine meters are allowed for custody transfer. Other meter types are possible but only via a

dispensation procedure, which takes approximately 6 weeks longer to complete than a regular type approval.

With technology changing at an increasing pace it will serve market interests if legislation is technology independent, a development that was recognised as one of the key issues of the new Measurement Instrument Directive (MID) [4] in the European Union. To this end the current OIML recommendations for gas meters are under revision, which has resulted in a first committee draft [5], which is technology independent. Gas meters are generally part of an entire installation and so a new recommendation for gas metering systems is being developed [6]. These new recommendations necessarily form a compromise between the dreams of experts and the interests of countries participating. However, we know that these are going to be revised in the future. So today is an excellent starting point to dream about legal gas metering.

Walt Disney, famous for his creations of Mickey Mouse and Donald Duck, used for his creative work a method that was later called the Disney strategy. Any problem is viewed from three different perspectives: the dreamer, the critic and the realist. The dreamer thinks of anything that would be nice. The sky is even no limit. The critic tells why the new ideas are not possible or why they are actually bad ideas. The realist looks at what can be achieved and how problems can be solved. When changing his perspective Walt Disney actually changed seats and body posture in order to stimulate the new line of approach in his thinking.

For the purpose of this paper we will concentrate on dreaming. Criticism and realism will be postponed to a later

occasion. Since gas metering is a combination of metrology, economy and technology, we will focus in our dreams on these three areas.

METROLOGY

The first field of developments to be mentioned here is metrological. Metrology is the science of taking measurements. In scientific metrology metrologists focus on the development of new standards or the improvement of existing standards. Here scientists are dreaming of a couple of new quantum phenomena that will contribute to the development of standards based on fundamental physical constants. In industrial metrology people working in research and development need measurement standards to test the equipment developed. The focus here is the development of more accurate instruments. Legal metrologists focus not only on the application of measuring methods for custody transfer purposes but also on the regulation required for fair trade, health, safety, environment and consumer protection. A concise overview of the different metrology areas can be found in *Metrology – in short* 7, a publication issued by DFM, the Danish national metrology institute.

In the past decades metrology has undergone a paradigm shift leading to the publication in 1993 of the Guide to the expression of Uncertainty in Measurement 8 (GUM). The major implication of the GUM is that uncertainties are part of the measurement results. Instead of saying the length of the table is 1.80 m, we represent the length of the table by (1.80 ± 0.01) m, 0.01 m being the measurement uncertainty.

Also terminology has changed. Terms like *true value* and *error* have lost their practical significance in metrology. Instead of *error* the word *deviation* is used and *true value* is changed to *value*. The best-known estimate of the *value* of a quantity is the reference value obtained from a standard, which is used to determine the deviation of an instrument reading. *Maximum permissible error* is now better replaced by *tolerance*.

Terminology is an important aspect of the language in which we communicate measurement results. In metrology there are currently two dictionaries that contain terminology and definitions that are currently agreed on in metrology. The *Vocabulaire International de Métrologie* VIM 9 is general to metrology; the other is the *Vocabulaire International de Métrologie Légale* VIML 10, which is specific to legal metrology. In these vocabularies a number of terms exist that are not defined in a quantitative way: accuracy, inaccuracy, precision, repeatability, reproducibility.

Some terms actually demonstrate the opposite of their intention. E.g. if we look by repetitive measurements for *repeatability* or *reproducibility* we will find that the instrument show small fluctuations in reading that makes it not entirely repeatable or reproducible. In fact our search for repeatability leads to the opposite. Consequently, *repeatability* and *reproducibility* are nowadays treated as uncertainty sources.

In this information era it is an idea to divide all terms into two categories. One group of terms represent *available information*. Here we have *measured value*, *reference value* and *deviation*. The other group of terms refer to *missing*

information, i.e. *measurement uncertainty*. Here we can put all terminology that result in measurement uncertainty: *repeatability*, *reproducibility*, *drift* and *uncertainty*. Now it is also clear that if you do not correct for a known deviation this will result in an additional uncertainty. Terms like *accuracy* and *inaccuracy* have a bit of both categories, which make them confusing. On one hand accuracy expresses a small deviation, on the other hand an accurate instrument also has a low uncertainty. The term inaccuracy has the same ambiguity.

The concept of uncertainty as a measure of missing information has proven to be very useful instrument to help people to master the basic concepts of metrology. Illustration of this idea with examples can be found in a paper by the author 11.

Uncertainties cannot be avoided and that means that these play a role when taking measurement based decisions 12. Examples are speeding tickets for people that drive too fast and approval of instruments with respect to legal tolerances. The probability that a decision is taken correctly is called *confidence level*. The probability of taking an erroneous decision is called *risk*, which is 1 – confidence level. If the instrument deviation equals the tolerance the probability of taking a correct decision is 50%. So the point of standardisation in legal metrology is the minimum confidence level (e.g. 95%) required for metrological decisions.

ECONOMY

Apart from any metrological and technological developments, the gas markets are liberalized in some countries. As a result the trade and transport responsibilities are separated into different companies. Gas transportation and gas distribution companies will not own the gas and get only a fee for transporting the gas to the end user. As a result the gas balance of these companies will get more attention, requiring more accurate gas meters.

Another consequence of the liberalised market is that gas will be supplied from many more different sources than today. As each source has a different gas quality with different calorific value there will be a tendency to bill the supplied gas on an energy basis. However, normal gas appliances like stoves and central heating boilers are not capable of handling entirely different gas qualities. A stove manufactured for a calorific value of 35 MJ/m^3 will get damaged if gas of 42 MJ/m^3 is used. So a constant gas quality is of importance to domestic users of natural gas. The solution here is an intelligent pressure regulator that reduces the gas pressure on the appliances if a higher quality of gas is supplied. This will be possible after the development of a new and miniaturised measurement method for determining the gas composition, which will be also useful for gas metering on an energy basis.

The prices of energy are expected to rise in the near future and this will stimulate a market demand for more accurate meters, new measurement principles, gas meters that meter on an energy basis, automatic reading or telemetry through the internet, gas meters with multiple tariff registers.

However there is another development that will require new metrological methods. The person that manufactures a product or provides services has to demonstrate that his products or services comply with regulations, standards and consumer specifications. Quality systems have been accepted as a means to control design, production, and final product inspection.

Product malfunction will lead more and more to liability lawsuits, which involves high costs of lawyers and possible compensation payments. These payments have increased in the past decades and there is no indication that this tendency will change in the next years. Especially, the new economies will implement legislation on liability according to principles that are used in other countries. The manufacturer wants to know the risk he runs. Statistical and metrological methods will be further developed to assist the manufacturer to maintain his risk at a preset level.

Manufacturers will act on a global market with local needs. Language support will be of vital importance, not only for documentation but also in interpreting error messages that are transmitted in case of instrument malfunction or maintenance requests.

The consumers that are offered a free choice of gas supplier may become owner of the gas meter in which case they will become much more interested in possible meter deviations and measurement uncertainty. Consumers will appreciate more and more clear invoices based on transparent measurement systems that measure gas quantities traceably in energy units.

TECHNOLOGY

The last decade has shown rapid technological developments in the field of gas metering. Compared to the existing diaphragm, rotary piston and turbine gas meters a range of new metering technologies has been developed. Ultrasonic meters and coriolis meters are now used for custody transfer purposes, the latter one measuring gas quantities in mass units. New metering principles are being developed that have potential for custody transfer measurements and existing mechanical measurement principles will be upgraded with electronics to add diagnostic and telemetric functions. Velocity based gas meters, like the turbine gas meter and the ultrasonic meter will be able to compensate asymmetric velocity profiles and even swirl. Clamp-on meters have been developed that are able to measure the flow rate from the vortex noise of the gas flowing in the pipeline 13.

Recently, manufacturers try to develop compact equipment to measure gas in energy units. Although the response time of miniaturised gas chromatographs is much better than the existing process gas chromatographs 14, further miniaturisation is to be expected with almost real time determination of the gas composition. From the gas composition the calorific value of the natural gas can be determined using the ISO 6976 algorithm 15.

The technological and metrological challenges associated with these developments are plenty. As many gas meters are sensitive to flow disturbances, velocity profiles, pulsations and acoustic disturbances adequate tests need to be developed and standardised. Currently, only standardised tests exist for flow disturbances 3, 5. Laser Doppler velocity profile measurements for these disturbance tests under high-pressure conditions is described in 16. Objective of this study is to find flow conditioning methods. These methods can be used to provoke in a straight pipe the velocity profile and swirl typical to two out of plane 90° bends. Such devices will actually reduce the cost of full-scale tests of large diameter gas meters under high-pressure conditions. Ultrasonic Doppler methods are already used for instant determination of velocity profiles in liquids 17.

The influence of pulsating flows 18 and pipe vibrations 19 was investigated by TNO in The Netherlands. These test are not yet performed on a routine basis as part of the product certification of flow meters, but this is likely to change in the future.

A special chapter in technology is the determination of thermodynamic properties of natural gases. Today there are several standards to calculate the real gas factors of natural gases from the full gas composition 20 or some components and the calorific value 21. Also for the speed of sound a standard is available 22. However despite the many computer programs that determine from the gas composition, pressure and temperature the viscosity, the isentropic coefficient, etcetera, the traceability is still poorly documented. Especially, for differential pressure devices the accuracy of the measurement is depending on the uncertainty of the calculated values of thermodynamic properties.

CONCLUSION

At the end of this overview of the metrological, economical and technological aspect our dreams are summarised as follows.

As new insights in metrology become clearer to metrologists, developers and users of instruments, this will give an impulse to improvement of instrumentation and the quality of products improve. The introduction of the concept of available information (deviation, measured value) and missing information (uncertainty) helps people to find their way in the terminology that exists in metrology today.

In a competitive liberalised market consumers will be more aware of value for money. As a result there will be a market demand for metering the energy of gas supplied. Also gas meter accuracy will get more attention, certainly if the prices of energy increase.

Technologically gas meters will be developed that are based on new metering principles. Also energy meters will be developed. Instrumentation to measure the gas composition will become much smaller in size, faster in response and cheaper. For the prototype testing of new gas meters standardised tests will be developed for pulsations, vibrations and acoustic noise. Disturbances test of flow profile and swirl generation can be performed with devices that can be installed in straight pipe lengths, thus avoiding the costs of full-scale tests with large diameter gas meter under high-pressure conditions. Thermodynamic properties of natural gases need to be known in a traceable way in order to improve metering accuracy.

The research on gas metering and adjacent areas will be certainly very interesting for the future.

REFERENCES

1. OIML R6 (1989): General provisions for gas volume meters, OIML, Paris, 1989.
2. OIML R31 (1995): Diaphragm gas meters, OIML, Paris, 1995.
3. OIML R32 (1989): Rotary piston gas meters and turbine gas meters, OIML, Paris, 1989.
4. EU (2004): Measurement Instrument Directive, Directive 2004/22/EC on measuring instruments, Official Journal of the European Union L135/1, 30 April 2004.

5. OIML TC8/SC8 (2004): Gas meters, First Committee Draft of a recommendation to replace the existing R6, R31 and R32, secretariat The Netherlands.

6. OIML TC8/SC7 (2004): Measuring Systems for Gaseous Fuel, Third Committee Draft of a new recommendation, secretariat: Belgium and France.

7. BNM, CEM, CMI, DFM, IPQ, OFMET, PTB, SMIS, SMU, SP (2000): Metrology – in short, edited by Preben Howarth, DFM, Euromet project no. 595, Lyngby Denmark, first edition 2000.

8. BIPM, IEC, IFCC, ISO, IUPAC, IUPAP and OIML (1993): Guide to the expression of uncertainty in measurement (GUM), second edition, International Organization for Standardization, Geneva, 1995.

9. BIPM, IEC, IFCC, ISO, IUPAC, IUPAP and OIML (1993): International Vocabulary of Basic and General Terms in Metrology, *Vocabulaire International de Métrologie* (VIM), bilingual edition, International Organization for Standardization, Geneva, 1993.

10. OIML (2000): International vocabulary of terms in legal metrology, *Vocabulaire International de Métrologie Légale* (VIML), bilingual edition, OIML, Paris, 2000.

11. Jos G.M. van der Grinten (1997): Recent developments in the uncertainty analysis of flow measurement processes, 13th North Sea Flow Measurement Workshop, Kristiansand, Norway, October 1997.

12. Jos G.M. van der Grinten (2003): Confidence levels of measurement based decisions, OIML Bulletin Volume XLIV • Number 3 • July 2003, http://www.oiml.org/bulletin/2003/07/technique.pdf

13. Daniel L. Gysling and Douglas H. Loose (2003): Sonar-based, clamp-on flow meter for gas and liquid applications, ISA Expo 2003 Technical Conference, October 2003, Houston, Texas, USA.

14. Johan Bats (2003): The application of MEMS technology to on-line analyzers for natural gas, Proceedings of Flomeko XIII, 13-15 May 2003, Groningen, The Netherlands.

15. ISO 6976 (1995): Natural gas, calculation of calorific values, density, relative density, Wobbe index from composition, ISO, Geneva, 1995.

16. Gabriel Moniz Pereira, Bodo Mickan, Rainer Kramer, Dietrich Dopheide and Ernst von Lavante (2003): Investigation of flow conditioning in pipes, Proceedings of Flomeko XIII, 13-15 May 2003, Groningen, The Netherlands.

17. Yasushi Takeda (1995): Instantaneous velocity profile measurement by ultrasonic Doppler method, JSME International Journal, Series B, Vol. **38**, No. 1, 1995, pp. 8-16.

18. M.C.A.M. Peters, E. van Bokhorst and C.H.L. Limpens (1998): Impact of pulsations on vortex flow meters, paper presented at the Flomeko '98, Lund, Sweden, 15 – 17 June 1998.

19. E. van Bokhorst, M.C.A.M. Peters and C.H.L. Limpens (1998): Impact of pipe vibrations on vortex flow meter under operating conditions, paper presented at 4th International Symposium on Fluid Flow Measurement, June 1999, Denver, Colorado, USA.

20. ISO 12213-2 (1997): Natural gas — Calculation of compression factor — Part 2: Calculation using molar-composition analysis, ISO, Geneva, 1997.

21. ISO 12213-3 (1997): Natural gas — Calculation of compression factor — Part 3: Calculation using physical properties, ISO, Geneva, 1997.

22. AGA Report No. 10 (2003): Speed of sound in natural gas and other hydrocarbon gases, American Gas Association, Washington DC, USA, 2003.

ADVANCED HYBRID TYPE ULTRASONIC FLOW METER UTILIZING STATE-OF-THE-ART PULSED-DOPPLER METHOD ALONG WITH TRADITIONAL TRANSIT TIME METHOD

Hironobu Yao*, Yoshinori Ohmuro**, Kouji Hagiwara**, Masami Kishiro*, Akio Miyamoto*, Kazuyuki Yamada*, Norihiko Tadata*, Gunji Ohgawara*, Toshihiro Yamamoto*, Yasushi Takeda***

* Fuji Electric Instruments Co., Ltd., 1, Fuji-machi Hino-city, Tokyo 191-8502, Japan, e-mail: yao-hironobu@fujielectric.co.jp
** Fuji Electric Advanced Technology Co., Ltd. 1, Fuji-machi Hino-city, Tokyo 191-8502, Japan,
*** Div. Mechanical Science Graduate School of Engineering Hokkaido University, Kita-13 Nishi-8 Sapporo 060-8628 Japan,

ABSTRACT

This time, new hybrid type ultrasonic flow meter has been developed worldly at first as non-intrusive type one, utilizing UVP (Ultrasonic-Doppler Velocity Profile) method along with transit time method. For its configuration, a pair of clamp-on type ultrasonic transducers is located opposite to each other on a pipe surface. It enables diametric measurement of velocity profiles in case of UVP method, and measurement of time difference in case of transit time method, where these methods would be automatically switched over to each other yielding to conditions of measured liquid and magnitude of velocity. The basic study was done on switchover algorithm, and also the authors have got the prospect of achieving high accuracy (±0.5% of rate) for UVP method by taking measures against various types of acoustic interference and performing actual flow tests.

Keywords: UVP, Transit Time, Hybrid ultrasonic flow meter, Clamp-on, Velocity profile

1. INTRODUCTION

In terms of UVP method, some papers have been reported recently, aimed at industrial flow measurement [1]-[5]. UVP method can measure velocity profiles directly without any correction coefficient which is usually needed for the other flow meters such as ultrasonic transit time meter. Therefore it enables highly accurate flow rate measurement even for undeveloped flow. However, it has to be recognized that there are a few limitations due to its measuring principle. Firstly, to get enough intensity of echo signals with Doppler shift, UVP method requires bubbles and/or particles as tracers of velocity field in measured liquid. Secondly, the measurable maximum velocity is limited to rather a lower value than that of the other flow meters due to the sampling theorem. For example, the maximum velocity is 10 m/s for EMF (electromagnetic flow meter), but it is limited to less than 10 m/s for UVP method. Thirdly, when applying it to non-invasive flow metering, diametric measurement of velocity profiles cannot be done due to acoustic noises nearby ultrasonic transducer, and this time it was confirmed that velocity profiles are affected by various types of acoustic noises, especially for metal pipes.

On the other hand, transit time method has been commonly adopted for industrial non-invasive ultrasonic flow meter so far. In general, it is adequate for clean liquids such as ultra pure water in semiconductor use because it utilizes penetration of ultrasonic waves in liquid. There will be no limit for the maximum velocity without aeration. However, this method has some limitations as well. Firstly, it needs a conversion factor of average velocity with the assumption of fully developed flow. Secondly, although transit time method has been improved for aeration problems by utilizing digital signal processing technology, it is not so tough enough as to be applicable to all kinds of bubbly and/or opaque liquids.

Both methods have strong and weak points as above, but they have complementary roles to each other. New hybrid type ultrasonic flow meter has been developed as non-invasive type flow meter, utilizing UVP method along with transit time method. For its configuration, a pair of clamp-on type ultrasonic transducers is located opposite to each other on a pipe surface. It enables diametric measurement of velocity profiles in case of UVP method, and measurement of time difference in case of transit time, where these methods would be automatically switched over to each other yielding to conditions of measured liquid and magnitude of velocity.

In this paper, main specifications and configuration of newly developed hybrid type ultrasonic flow meter are reported. Also actual flow test results of UVP method are reported, showing examples of radius/diametric measurement of velocity profiles with clamp-on type ultrasonic transducers located on a few kinds of materials' pipes.

2. NEW HYBRID ULTRASONIC FLOW METER

As industrial ultrasonic flow meters, transit time method and conventional Doppler method, which cannot measure velocity profiles, have been mainly adopted until today. Transit time method is relatively high accuracy (±1 to ±2%), but it is not suitable for liquids that include a lot of bubbles and/or particles. On the other hand, conventional Doppler method is tougher against them than transit time method, but it has poorer accuracy (±3 to ±5%) than transit time method. Ultrasonic flow meter utilizing both methods is called "hybrid type" one in general.

This time, new hybrid type ultrasonic flow meter has been worldly at first developed, utilizing UVP method along with transit time method, and realizing higher accuracy than the above-mentioned traditional one.

The measuring principle of transit time method is that ultrasonic pulses are transmitted and received between a pair of transducers obliquely and alternately, and that bi-directional

transit time and the time difference induced by carry effect of fluid motion are measured, calculating flow rate from them on the assumption of fully developed and axis-symmetric flow. The principle formula is given by

$$Q=(\pi D^2/4)(1/K)\{C/(2\sin\theta)\}\{\Delta T/(T_0-\tau)\} \tag{1}$$

where Q: volumetric flow rate, D: inside diameter, K: conversion factor of average velocity, C: sound velocity of measured liquid, θ: incident angle into liquid, ΔT: transit time difference, T_0: transit time when flow is at rest, τ: transit time in pipe wall and transducers' wedge. The K corresponds to correction coefficient on the assumption of fully developed laminar/turbulent flow.

UVP method utilizes so-called pulsed-Doppler effect, assuming that bubbles and/or particles move with the same velocities as measured liquid. Ultrasonic pulses are transmitted into liquid, echo signals scattered by them are received by the same transducer, the propagation line is divided into small channels, velocity profiles are obtained by connecting Doppler shifts in the channels, and flow rate is calculated by integrating the velocity profiles. The principle formulas are given by

$$Q= \int v(x)dS \tag{2}$$
$$v(x)=\{C/(2\sin\theta)\}\{f_d(x)/f_0\} \tag{3}$$
$$x=(Ct)/2 \tag{4}$$

where v(x): velocity at position x, $f_d(x)$: Doppler shift at position x, f_0: basic excitation frequency, t: round transit time between transducer and position x, others: ditto.

The main specifications of newly developed hybrid type ultrasonic flow meter are shown in table-1

3. CONFIGURATION OF THE FLOW METER

3-1. TRANSMITTER

The hardware block diagram of the transmitter is shown in Fig-2. It consists of a measurement board, a control board, a man-machine interface, and a power supply board.

1) Measurement board: Supplying transmission signals with ultrasonic transducers, amplifying received signals, converting them to digital data, and then calculating flow rate by digital signal processing.
2) Control board: Measuring temperature of transducer's wedge, and controlling key input, DC4-20mA, DOs, serial port for RS-485/RS-232C, and LCD.
3) Man-machine interface: Setting parameters, and indicating flow rate and total.
4) Power supply board: Power supply to the other boards.

Fig-1: Measuring Principle

		UVP METHOD	TRANSIT TIME METHOD
FUNCTIONS	Installation	Clamp-on	
	Number of path	or 4 paths	1 or 2 paths
	Applicable pipe size	φ25 to 1000mm	φ13 to 6000mm
	Pipe material	Metals with / without liner, Plastics	
	Velocity	0 to ± 0.3 ---- 4 m/s (depending on dia.)	0 to ± 0.3 ---- 32 m/s
	Fluid temperature	- 40 to +100 degC	
	Output	DC4 to 20mA (load 1 kΩ) DO: 3 points RS-232C / RS-485	
	Explosion-proof	ATEX EEx m T6	
PERFORMANCE	Accuracy	±0.5% of rate	± 1% of rate
	Straight pipe length	5D(Up), 2D(Down)	10D(Up), 5D(Down)
	Response time	0.1 s	0.5 s
	Permissible air	0.02 to 20 vol.%	0 to 12vol.%
	Undeveloped flow	Applicable	NA

Table-1: Specifications of New Hybrid Ultrasonic Flow Meter

Fig-2: Block diagram of Hybrid Ultrasonic Flow Meter

3-2. DETECTOR

Fig-3 shows the outline of newly developed detector. Composite type piezoelectric oscillator is often used as an ultrasonic transducer for UVP method. However PZT disc is used for the transducers, because the targeting liquid temperature ranges from -40 to +100 deg C, and because of its cost reduction. Optimizing backing structure of PZT disc,

Low-Q transducers were made with almost the same efficiency as ones utilizing composite type piezoelectric devices. For highly accurate measurement over wide temperature range, a temperature sensor is incorporated into the transducer's wedge, automatically compensating its sound velocity change. It also enables diametric measurement of velocity profiles by locating a pair of ultrasonic transducers opposite to each other on a pipe surface. This installation makes it possible to use transit time method as well by adjusting the distance between transducers with the same configuration.

Acoustic absorber units are installed just before sensor units, aimed at decreasing the affect of multiple reflection in pipe wall.
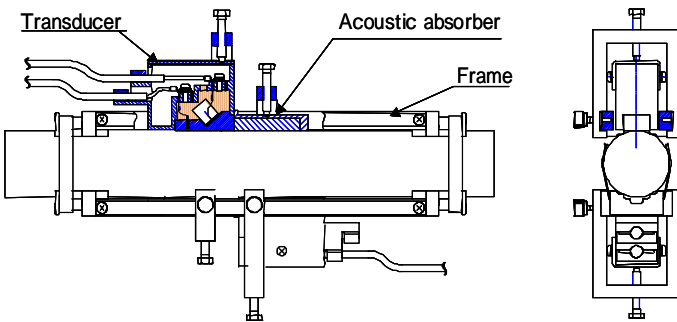
Fig-3: Detector of Hybrid Ultrasonic Flow Meter
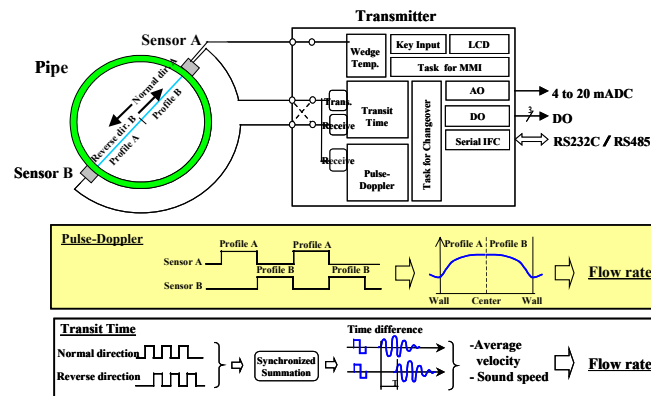
Fig-4: Configuration of Hybrid Ultrasonic Flow Meter

4. SWITCHOVER ALGORIZM

The configuration of hybrid type ultrasonic flow meter is shown in Fig-4, making it possible to use both of UVP method and transit time method. When echo signals are weak due to insufficient existence of reflectors in measured liquid, or when flow velocity exceeds UVP measurable range, transit time method is used. On the contrary, when reflectors increase and then transit time method cannot measure, UVP method is used.

The switchover algorithm is shown in Fig-5. After setting parameters such as pipe material, pipe diameter, wall thickness, kind of liquid, flow range, etc., the maximum velocity will be calculated and checked if it is within UVP measurable range. If the velocity is within the range, the task for UVP method will be performed. And if success rate, which is defined as number of normal channels divided by total channels, is more than for example 70%, it will recover the failed channels, and output

and display flow rate. Without UVP measurable range, or if the success rate is less than 70%, the measuring method will be switched over to transit time method. If neither UVP method nor transit time method can measure normally, it will perform a task for alarm output and display.

In case that conditions of measured liquid change, especially the kind of liquid changes time after time, this switchover function of measuring methods makes it applicable to various kinds of liquids and wider applications than now.
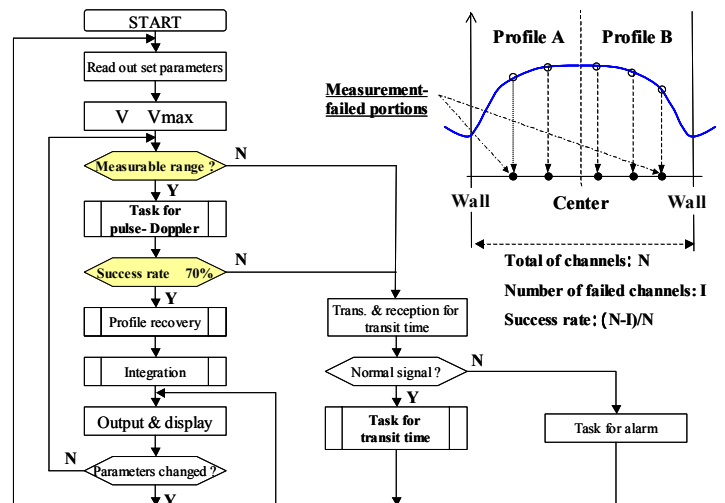
Fig-5: Switchover Algorithm

5. RESULTS OF ACCURACY TESTS

By using the transmitter and the detector, the tests were performed for accuracy evaluation. The tests were done for three kinds of materials, SS (stainless steel), PVC and CS (carbon steel) with ca. 100 mm. The test loop is shown in Fig-6. A flow conditioner, so-called Akashi type, was installed on the upstream side of the pipe. The detector that consists of one transducer only was installed on the pipe surface by 7D downstream from the flow conditioner. The tests were performed by so-called comparison method, where an EMF installed on downstream side was used as the reference meter. The EMF was calibrated within 0.1% by gravimetric method. The liquid was water that contains air bubbles as velocity field tracers. Air was injected into water on the suction side of upstream pump, and broken into small air bubbles by the pump. The mixture ratio was set to ca. 0.02 to 0.2 % in volume owing to flow rate. The excitation frequencies were set to specific values to make the effect of dispersion due to finite pipe thickness at the minimum.
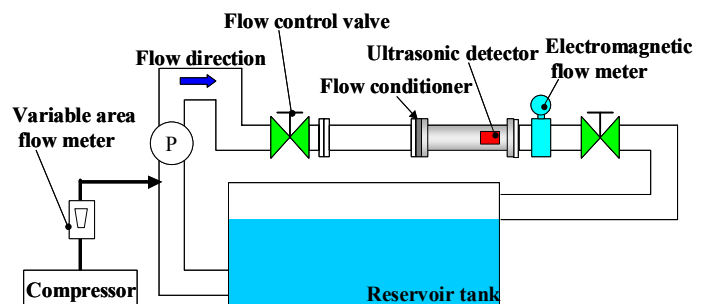
Fig-6: Test Facility for Accuracy Evaluation

The actual flow tests were done at the average velocities from 0.2 to 2 m/sec. The test results are shown in Fig-7 to 9. The examples of velocity profiles at the time of these tests are shown in Fig-10 to 12. For the range of more than 0.4 m/sec, they are within nearly ±1%. For the range of more than 1 m/sec, they are within nearly ±0.5%. It has been confirmed that almost the same accuracy as EMF can be realized.

.
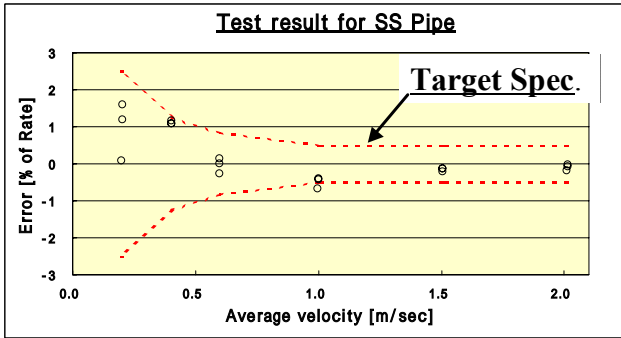
Fig-7: Accuracy Evaluation for SS Pipe
  Inside diameter: 102.2mm,
  Wall thickness: 5.9mm
  Integral range: Far radius
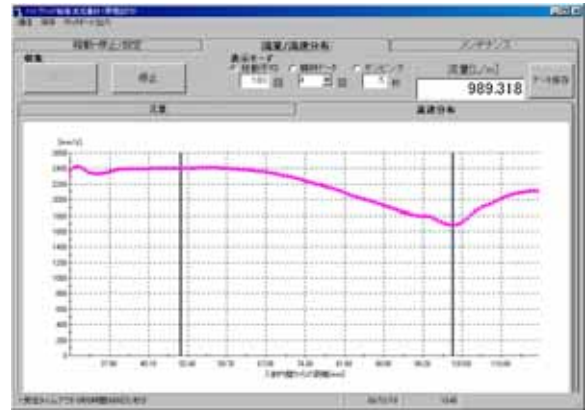
Fig-10   Radius Velocity Profile for SS Pipe (2 m/sec)
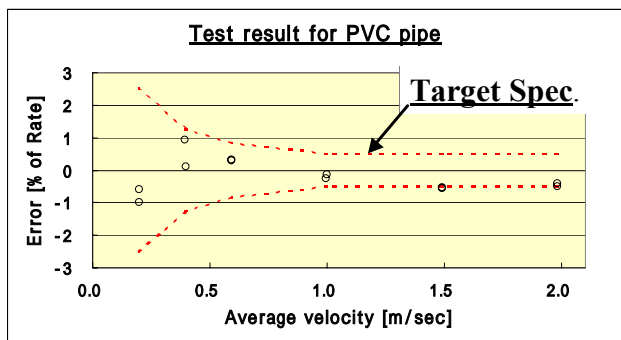
Fig-8: Accuracy Evaluation for PVC Pipe
    Inside diameter: 104.2mm
    Wall thickness: 4.8mm
    Integral range: Far radius
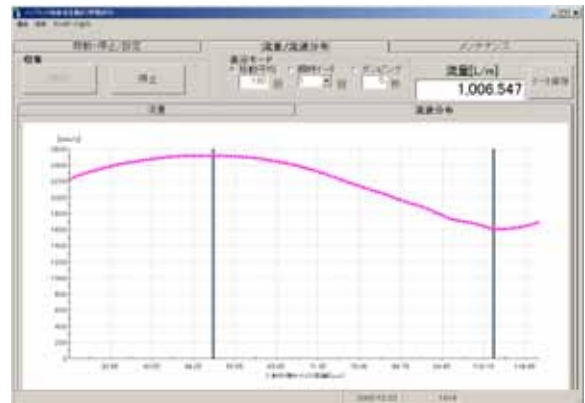
Fig-11: Radius Velocity Profile for PVC Pipe (2m/sec)
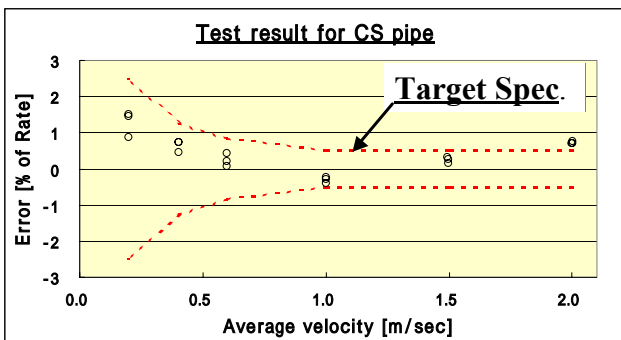
Fig-9: Accuracy Evaluation for CS Pipe
    Inside diameter: 106.0mm
    Wall thickness: 4.3mm
    Integral range: Far radius
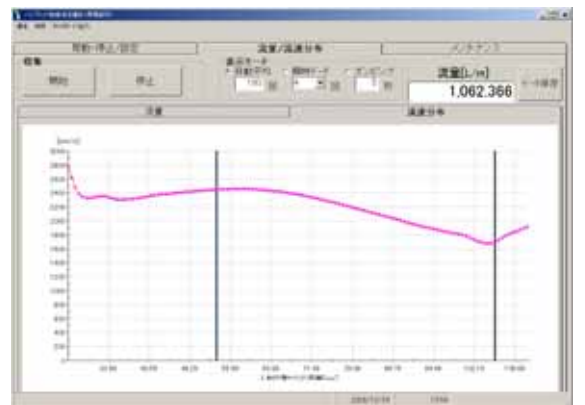
Fig-12: Radius Velocity Profile for SS Pipe (2m/sec)

Next, as shown in Fig-3 and 4, with a pair of transducers installed opposite to each other, accuracy evaluation was performed. The test result is shown in Fig-13. The velocity profiles are shown in Fig-14 and 15 at that time. It was confirmed that two radius flow profiles coincide to each other in the central regions
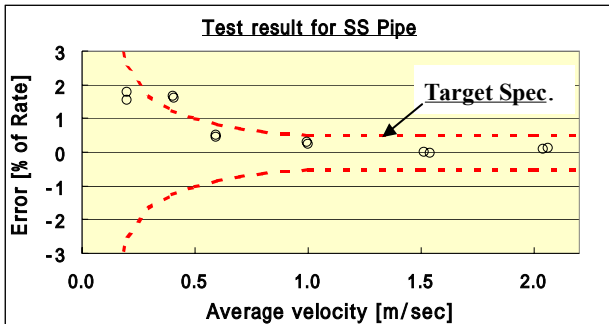
Fig-13: Accuracy Evaluation for SS Pipe
    Inside diameter: 102.2mm
    Wall thickness: 5.9mm
    Integral range: Diameter
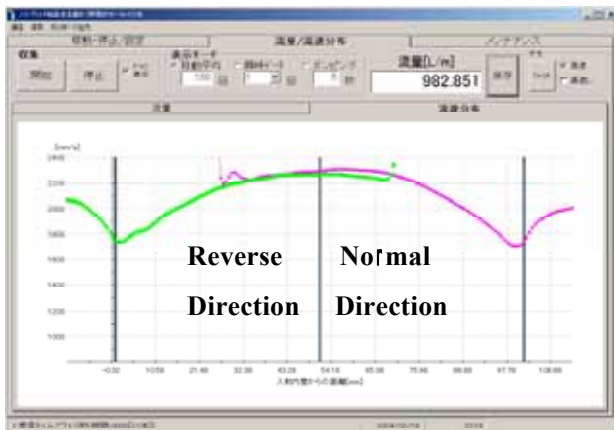
Fig-14: Diametric Velocity Profile for SS Pipe (2 m/s)
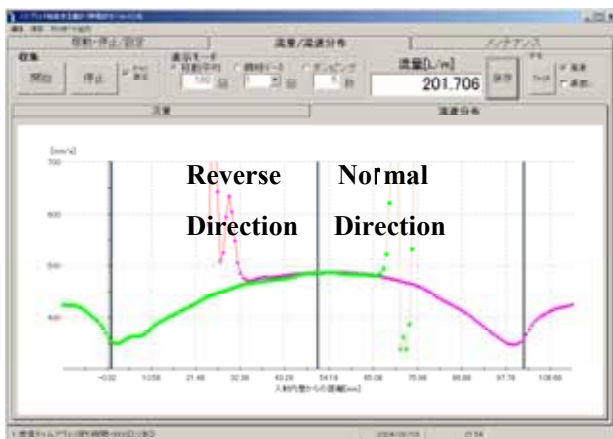
Fig-15: Diametric Velocity Profile for SS Pipe (0.4 m/s)

6. CONCLUSIONS

This time, new hybrid ultrasonic flow meter has been developed, combining UVP method with transit time method. And actual flow tests were performed by using clamp-on detector for three kinds of materials' pipes with diameter of ca. 100 mm. The accuracy was within ±0.5 to ±1.0 % of rate, therefore the authors have got the perspective to be able to achieve the accuracy equivalent to EMF. In addition, it was confirmed that diametric flow profiles can be obtained in real time with a pair of transducers installed opposite to each other on a pipe surface.

In addition, the changeover algorism between UVP method and transit time method was studied.

7. REFERENCES

1. Y. Takeda, Velocity profile measurement by ultrasound Doppler shift method, Int. J. HEAT & Fluid Flow, Vol.17, No.4, pp.313-318 (1986)

2. M. Mori, Y. Takeda, T. Taishi, N. Furuichi, M. Aritomi, H. Kikura, Development of a novel flow metering system using ultrasonic velocity profile measurement, Exp. Fluids, 32, pp.153-160 (2002).

3. K. Tezuka, H. Tezuka, M. Mori, Y. Takeda, H. Kikura, M. Aritomi, N. Furuichi, Development of flow rate and profile measurement using ultrasonic Doppler method (17) Effects of pipe elbows on swirl and Reynolds number changers, Atomic Energy Society of Japan's autumn annual conference in 2003, pp.396

4. S. Wada, H. Kikura, M. Aritomi, Y. Takeda, M. Mori, Development of flow rate and profile measurement using ultrasonic Doppler method (18) Multiline flow rate measurement on inlet flow after pipe elbow, Atomic Energy Society of Japan's autumn annual conference in 2003, pp.397

5. K. Tezuka, H. Tezuka, M. Mori, Application of Ultrasonic Pulse-Doppler Velocity-Profile Flowmeter for Large Pipings, pp.34 (2003)

ANALYSIS OF FREQUENCY CHARACTERISTICS ON NON-INVASIVE ULTRASONIC-DOPPLER FLOW MEASUREMENT FOR METAL PIPES

Masami Kishiro*, Noritomo Hirayama**, Hironobu Yao*, Toshihiro Yamamoto*,Yasushi Takeda***

*Fuji Electric Instruments Co., Ltd. Field Instrument Development Department,
1, Fuji-machi, Hino-city, Tokyo, 191-8502, Japan , E-mail: kishiro-masami@fujielectric.co.jp
**Fuji Electric Advanced Technology Co., Ltd. Electronic Equipment Technology Laboratory,
1, Fuji-machi, Hino-city, Tokyo, 191-8502, Japan
***Div. Mechanical Science Graduate School of Engineering Hokkaido University,
Kita-13, Nishi-8, Sapporo 060-8628, Japan

ABSTRACT

According to the authors' experiments, the accuracy of non-invasive Ultrasonic-Doppler Velocity Profile (UVP) method is influenced by excitation frequency of ultrasonic transducer, especially for metal pipes, depending on their materials, thickness and diameter.

In this paper, it is considered that the frequency characteristics are caused by acoustic dispersion due to Lamb waves. A model for the analysis was made so that L (longitudinal) waves in plastic wedge, which incide obliquely into metal/plastic pipe, would split into L wave, SV (shear vertical) wave, and Lamb waves in different modes with constant frequency secured. Then, the frequency characteristics were calculated based on this multiple-beam model, and it was confirmed that the calculated errors roughly coincide with the measured data.

Lamb waves with angles of refraction near critical angle of 90 degree would cause relatively large errors in case of small diameter pipes. Therefore, as countermeasures, the excitation frequency was set to the average value between two frequencies, where each angle of refraction of Lamb waves reaches the critical angle. It was confirmed that the accuracy is improved approximately within ±1% for metal pipes by taking the countermeasures.

Keywords: UVP, Frequency characteristics, Dispersion, Lamb waves, Critical angle

1. INTRODUCTION

Recently, UVP method has been often reported as a flow mapping technology. Some papers have also shown the performance of UVP flow meter aimed at industrial use, succeeding in highly accurate flow rate measurement mainly as an invasive type flow meter, that is, a flow meter with wetted transducers [1][2].

However, it is the authors' understanding that the study of UVP method as non-invasive flow metering has not been performed in detail so far. The fundamental investigation has been completed at this time on acoustic propagation through metal and plastic pipes in order to develop non-invasive type UVP flow meter. It has been recognized that there are various kinds of acoustic interference waves, of which the influence is remarkable especially for metal pipes.

In this paper, the analysis is described about the frequency characteristics, that is, the accuracy of flow rate measurement is influenced by excitation frequency of ultrasonic transducer. Countermeasures and the effect are also reported so as to improve the accuracy of non-invasive flow measurement by UVP method.

2. PHENOMENA

According to the authors' experiments, the accuracy of non-invasive flow measurement by UVP method is influenced by excitation frequency of ultrasonic transducer.

The effect depends on the material, thickness and diameter, and it is remarkable especially for thin metal and/or small diameter pipes.

Fig-1 shows an example of the frequency characteristics of accuracy, where UVP method was applied to SS (stainless steel) pipe with diameter of 102.2 mm and thickness of 5.9 mm.
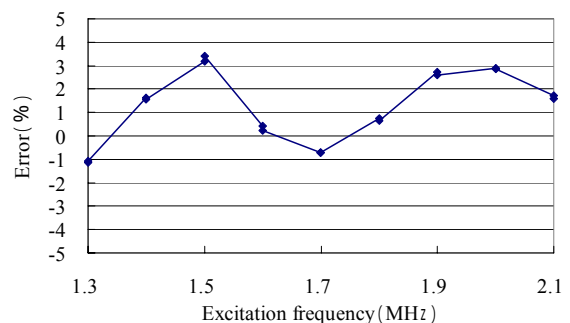
Fig-1: Frequency Characteristics of Accuracy
(SS pipe with 102.2 mm dia., 5.9 mm thick)

It is considered that these phenomena are caused by dispersion of ultrasonic waves in metal or plastic pipes, in which sound velocities (i.e. phase velocity, group velocity) change dependently on the excitation frequency.

3. ACOUSTIC DISPERSION

Table-1 shows the kinds of ultrasonic waves that may cause dispersion. There are three kinds. In this table, SH (shear horizontal) waves are irrelevant, because they would not excite L (longitudinal) waves at the interface between pipe and measured liquid. Rayleigh waves are surface waves that attenuate rapidly in the direction normal to the surface. Therefore, it is concluded that only Lamb waves are relevant to the above-mentioned phenomena.

Table -1: List of Acoustic Dispersion

Mode	Kind of wave	Relation to the phenomena
1)SH waves	Shear wave	Irrelevant
2)Lamb waves	Shear + Longitudinal	Relevant
3)Rayleigh waves	Surface wave	Irrelevant

4. LAMB WAVES

Lamb waves are the combination waves of L (longitudinal) waves and SV (shear vertical) waves, and have both natures. Lamb wave is a kind of plate waves, where the plate with finite thickness makes the wave guide, and only specific ultrasounds can propagate through it. Characteristic equations of Lamb waves specify the wavelengths of ultrasounds, satisfying the boundary conditions and depending on the thickness and sound velocities of the plate.

Lamb waves have two modes, symmetric mode and asymmetric mode, as shown in Fig-2. Characteristic equations of Lamb waves are given by Eq. (1):

$$\beta_1^2=(\omega/V_1)^2-k^2$$
$$\beta_3^2=(\omega/V_s)^2-k^2$$
$$\tan(\beta_1 d/2)/\tan(\beta_3 d/2)=-(k^2-\beta_3^2)^2/(4k^2\beta_1\beta_3)$$
(In case of symmetric mode)
$$\tan(\beta_3 d/2)/\tan(\beta_1 d/2)=-(k^2-\beta_3^2)^2/(4k^2\beta_1\beta_3)$$
(In case of asymmetric mode)

(1)

where d: thickness, ω: angular frequency, V_1: sound velocity of L wave, V_s: sound velocity of SV wave, k: wave number.

Hereafter, each mode of order-number "m" is indicated as Sm and Am (m=0,1,2,) respectively.
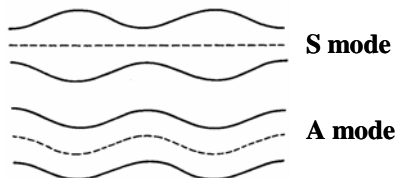
Fig-2: Symmetric Mode and Asymmetric Mode

5. ASSUMPTIONS FOR THE ANALYSIS

For the analysis of the frequency characteristics, the followings are assumed:

1) On phase velocity Vp=ω/k:
Angle of refraction in pipe would be determined by phase velocity in each mode owing to the Snell's law, i.e. k sinθ=const.

2) On group velocity Vg=$\partial\omega/\partial$k:
Transit time in pipe would be determined by group velocity of ultrasonic pulse trains, where Vg$\neq$Vp with dispersion and Vg=Vp without dispersion in general.

3) On acoustic mode conversion at interface:
L wave in plastic wedge, which incides obliquely into pipe, would split into L wave, SV wave and Lamb waves in different modes with constant frequency secured, satisfying the Eq. (1).

The frequency is assumed not to change on the assumption 3), based on the results of the experiment described below.

Fig-3 and Fig-4 show the experimental apparatus for the measurements of waveforms and spectrums of ultrasonic waves penetrated through metal pipe, where the pipe is SS one with diameter of 102.2 mm and thickness of 5.9 mm. The resonance frequency of transducer is 2 MHz. The SS pipe was cut into half, and ultrasonic waves penetrated through it into water were measured by the hydrophone submerged into water. The acoustic absorber made of rubber with tungsten particles was set in front of the ultrasonic transducer for the purpose of absorbing multiple-reflection in SS pipe wall.
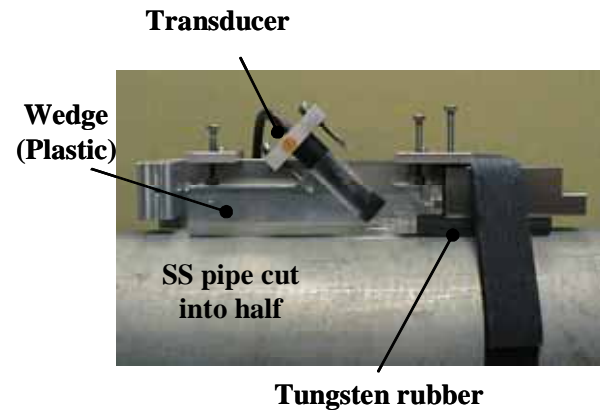
Fig-3: Experimental Apparatus
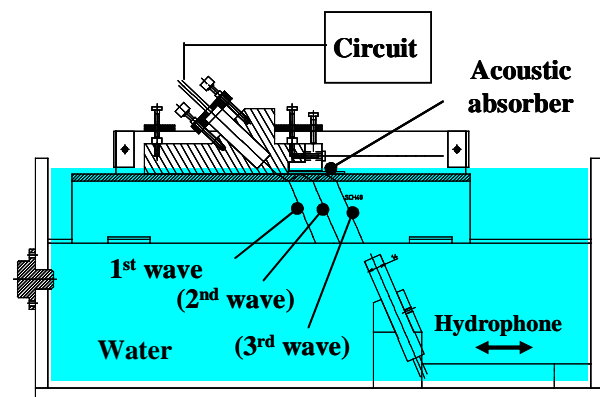
Fig-4: Schematic Diagram of Experimental Apparatus

Fig-5 shows the results of the measurements. The transducer was excited by rectangular 4-pulse waves with basic frequency from 1.5 to 2.0 M Hz. The upper waveforms in Fig-5 are ultrasonic waveforms received by the hydrophone,

and the lower curves are their spectrums obtained by FFT function of oscilloscope.

It was experimentally confirmed that central frequencies of spectrums of ultrasonic waves penetrated through SS pipe are roughly equal to the excitation frequencies.
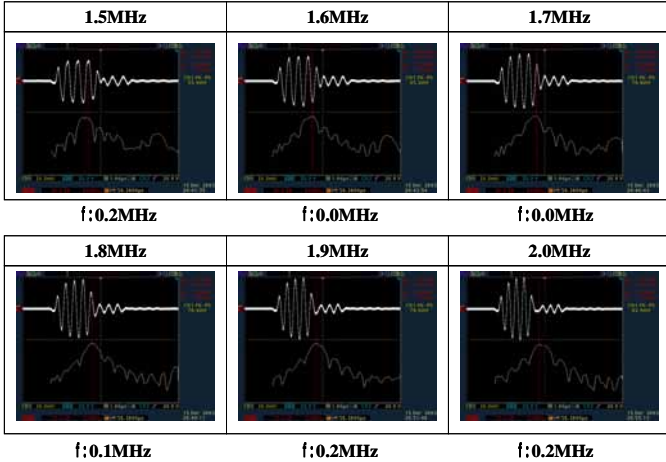
1.5MHz	1.6MHz	1.7MHz
0.2MHz	0.0MHz	0.0MHz
1.8MHz	1.9MHz	2.0MHz
0.1MHz	0.2MHz	0.2MHz

Fig.5: Waveforms and Spectrums of Ultrasonic Waves Penetrated through Metal Pipe (1st wave indicated in Fig-4)

Fig-6 and Fig-7 show the models of split ultrasonic beams at the interface between the plastic wedge and metal/plastic pipe, in accordance with the above-mentioned assumptions 1) to 3). The angles of refraction in pipe θp are different from each other owing to the phase velocities of L wave, SV wave, and each mode of Lamb waves.
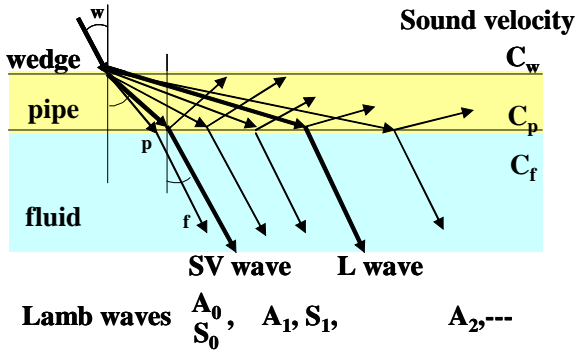
Fig-6: Model of Split Ultrasonic Beams
(Case-1: θw<θc)
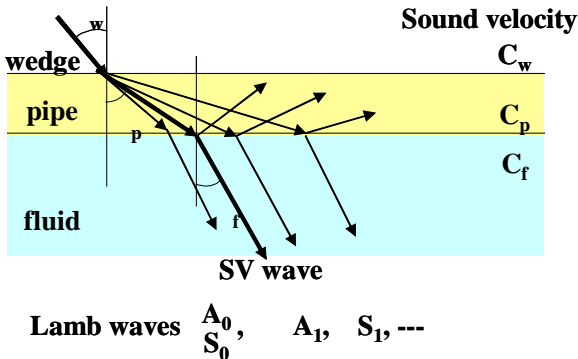
Fig-7: Model of Split Ultrasonic Beams
(Case-2: θw>θc)

Fig-6 shows Case-1, in which incident angle θw is lower than critical angle θc for L wave in the pipe, and Fig-7 shows Case-2, in which θw is oppositely higher than that so that L wave and higher-ordered Lamb waves are not existent.

The analysis hereafter is performed in Case-2, so that it is simplified.

Fig-8 shows an example of dispersion curves of Lamb waves. On the assumption of constant frequency, the intersection points between the dispersion curves and the horizontal bar corresponding to excitation frequency, show the wave numbers "k" of each mode of Lamb waves. But, all the modes do not necessarily occur, and only such modes occur as having the angle of refraction θp of less than 90 degree.
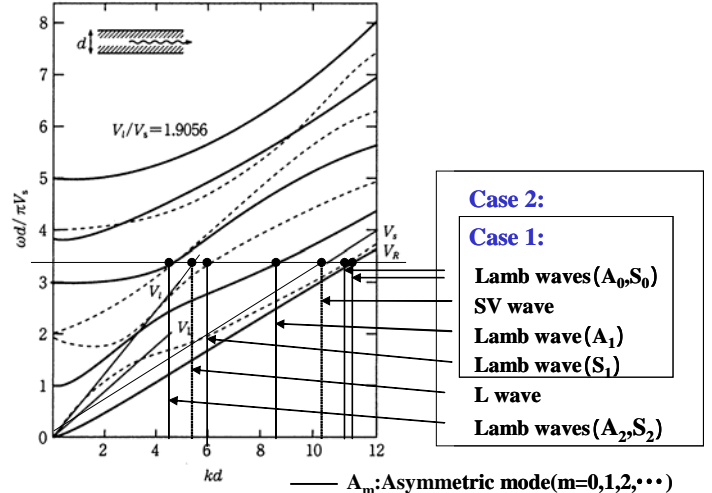
Fig-8: Example of Dispersion Curves of Lamb Wave[3][4]

6. ASYMPTOTIC SOLUSIONS

Phase velocities Vp of Lamb waves are derived from the followings:

$$Vp^{(Am)} = \omega/k^{(Am)}, \quad Vp^{(Sm)} = \omega/k^{(Sm)} \tag{2}$$

In this paper, the superscript $^{(Am)}$ shows asymmetric mode of order number m, and the one $^{(Sm)}$ shows symmetric mode in the same way.

Strictly speaking, $k^{(Am)}$ and $k^{(Sm)}$ in Eq. (2) should be the solutions of Eq. (1).

However, in case that the product of wave number and plate thickness "kd" is large, phase velocities Vp of 0-ordered Lamb waves asymptotically come near sound velocity of Rayleigh wave V_R, and Vp of higher-ordered Lamb waves asymptotically come near sound velocity of SV wave Vs. Asymptotic solutions of phase velocities of Lamb waves Vp are given by the following equations:

- Asymptotic solutions of Vp of 0-ordered Lamb waves:
$$Vp^{(A0)} = Vp^{(S0)} = V_R \tag{3}$$

- Asymptotic solutions of Vp of m-ordered Lamb waves (m=1, 2, ---):
$$\left. \begin{array}{l} Vp^{(Am)} = \omega/\{(\omega/Vs)^2 - (2m\pi/d)^2\}^{1/2} \\ Vp^{(Sm)} = \omega/\{(\omega/Vs)^2 - ((2m+1)\pi/d)^2\}^{1/2} \end{array} \right\} \tag{4}$$

In the case of analysis in this paper, "kd" is nearly 24, where pipe thickness d is 5.9 mm, Vs of SS is 3075 m/s, and transmitted frequency (hereafter excitation frequency is called transmitted frequency) is 2 MHz. Therefore, kd is considered large enough so that the asymptotic solutions of Eq. (3) and (4) are satisfied in following analysis.

Sound velocity of Rayleigh wave V_R is the solution of the following equations:

$$\left.\begin{array}{l} L=\{1-(V_R/V_l)^2\}^{1/2} \\ S=\{1-(V_R/V_s)^2\}^{1/2} \\ 4LS-(1+S^2)^2=0 \end{array}\right\} \quad (5)$$

In the case of SS pipe analyzed in this paper, V_R is calculated to 2854 m/s by Eq. (5), where V_l is 5790 m/s. Therefore, V_R is a little smaller than Vs of above-mentioned 3075 m/s, and has almost no frequency characteristics.

7. FORMULAS FOR THE ANALYSIS

Formulas for the analysis are described below:

1) Angle of refraction: θp

$$\left.\begin{array}{l} \theta p^{(Am)}=\sin^{-1}(Vp^{(Am)}/Cw/\sin\theta w) \\ \theta p^{(Sm)}=\sin^{-1}(Vp^{(Sm)}/Cw/\sin\theta w) \end{array}\right\} \quad (6)$$

where Cw: sound velocity in wedge

2) Group velocity: Vg

$$\left.\begin{array}{l} Vg^{(A0)}=Vg^{(S0)}=V_R \\ Vg^{(Am)}=Vs^2/Vp^{(Am)} \quad (m=1,2,---) \\ Vg^{(Sm)}=Vs^2/Vp^{(Sm)} \quad (m=1,2,---) \end{array}\right\} \quad (7)$$

3) Transit time in pipe: τ

$$\left.\begin{array}{l} \tau^{(Am)}=d/\cos\theta p^{(Am)}/Vg^{(Am)} \\ \tau^{(Sm)}=d/\cos\theta p^{(Sm)}/Vg^{(Sm)} \end{array}\right\} \quad (8)$$

4) Radius shift of velocity profile: r_e

$$\left.\begin{array}{l} r_e^{(Am)}=C_f(\tau^{(Am)}-\tau^{(Vs)})\cos\theta f \\ r_e^{(Sm)}=C_f(\tau^{(Sm)}-\tau^{(Vs)})\cos\theta f \end{array}\right\} \quad (9)$$

where C_f: sound velocity in fluid
θf: refraction angle in fluid
$\tau^{(Vs)}$: transit time of SV wave in pipe

5) Velocity profile of turbulent flow: V(r)

$$\left.\begin{array}{l} V(r)^{(Am)}=V_{max}\{1-(r-r_e^{(Am)})/R\}^{1/n} \\ V(r)^{(Sm)}=V_{max}\{1-(r-r_e^{(Sm)})/R\}^{1/n} \\ n=2.1\log Re -1.9 \end{array}\right\} \quad (10)$$

where R: radius of pipe
V_{max}: maximum velocity of turbulent flow profile
Re: Reynolds number

8. RESULTS OF THE ANALYSIS

Fig-9 to 12 are the results of the analysis based on the assumptions up to here for the case of Fig-1, where the pipe is SS one with inner diameter of 102.2 mm and thickness of 5.9 mm, and resonance frequency of transducer is 2 M Hz, Vs is 3075 m/s, V_l is 5790 m/s, incident angle θw is 46.9 degree, and sound velocity in wedge is 2730 m/s.

Fig-9 shows the results of calculation of Eq. (6). Refraction angle of mode A_2 of Lamb waves reaches critical angle 90 degree around 1.9 MHz of transmitted frequency, and in the same way that of mode S_1 reaches around 1.4 MHz. These two
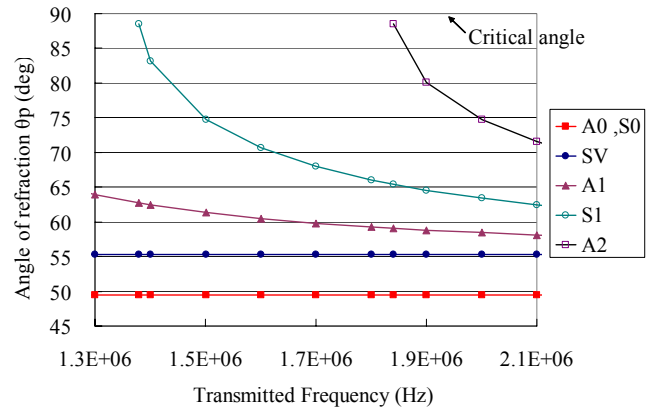
Fig-9: Angle of Refraction vs. Transmitted Frequency (Results of calculation)
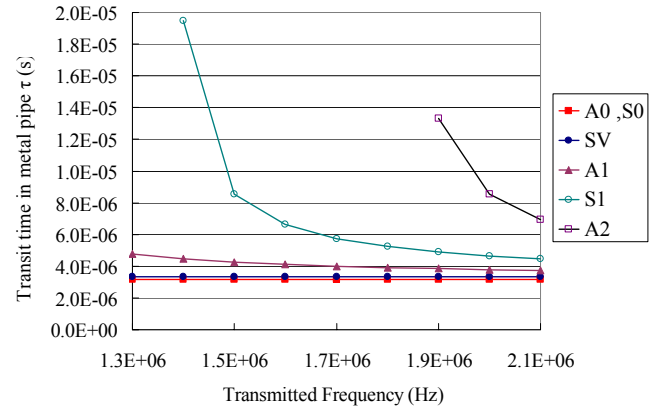
Fig-10: Transit Time vs. Transmitted Frequency (Results of calculation)
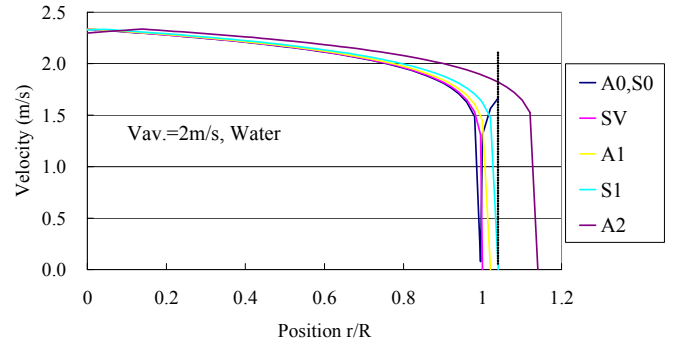
Fig-11: Multiple Velocity Profiles Caused by Differences of Transit Time in SS Pipe (Results of calculation at 2 MHz)

modes are not existent in lower transmitted frequency than them.

Fig-10 shows the results of calculation of transit time by Eq. (8). The SV's straight line shows transit time of SV wave which is originally intended to be used for flow measurement by UVP method. Transit time of the modes A_0 and S_0 of Lamb waves is shorter than that of SV wave, and the transit time of the other higher-ordered modes is longer than that of SV wave. Especially, the modes, whose angles of refraction θp are near critical angle 90 degree, have long transit time in the pipe.

Fig-11 shows the results of calculation on the multiple velocity profiles caused by the differences of transit time between SV wave and each mode of Lamb waves, based on Eq. (10), where transmitted frequency is 2 MHz. Each of split

waves has different transit time in SS pipe, because of differences of group velocities Vg and angles of refraction θp in SS pipe. It is considered that the original velocity profile got by SV wave and interferential velocity profiles caused by Lamb waves, which shift in horizontal axis owing to different transit time in SS pipe, overlap to each other and induce erroneous velocity profile as a result.
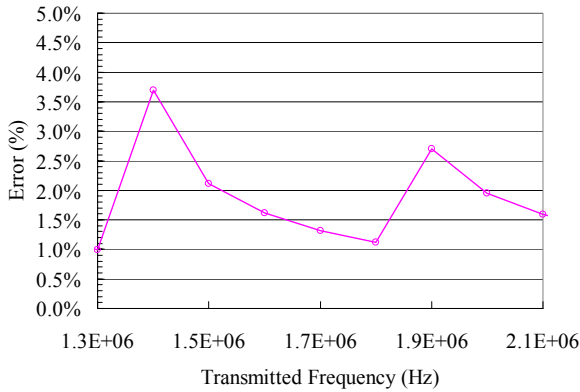
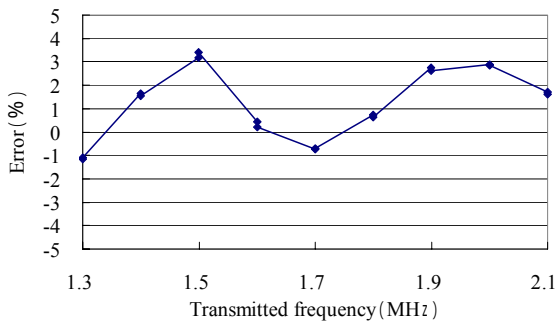

Fig-12: Flow Rate Error vs. Transmitted Frequency
(Results of calculation)

Fig-1: (Re-carried) Flow Rate Error vs. Transmitted Frequency
(Results of measurement)

Fig-12 shows the results of calculation on the flow rate error caused by split ultrasounds according to the assumptions up to here. The flow rate error was calculated by averaging multiple profiles and integrating the averaged profile around the central axis of circular pipe section. The flow rate error becomes at the maximum around 1.4 MHz and 1.9 MHz of transmitted frequency, corresponding to the frequencies where angles of refraction for Lamb waves reach critical angle 90 degree in Fig-9.

Compared with the results of Fig-12, the test data of Fig-1 roughly coincides with Fig-12, therefore it is considered that dispersion due to Lamb waves is surely occurring in metal/plastic pipe and induces the frequency characteristics of accuracy for non-invasive UVP flow measurement.

Furthermore, in Fig-12, it must be commented that all split ultrasounds effect on the accuracy equally. In other words, it is assumed that UVP flow meter has the same measuring resolution for all the modes, regardless of their intensity.

As the pipe diameter becomes bigger, the ratio of transit time in pipe to one in liquid becomes smaller. Therefore, the magnitude of frequency characteristics is inversely proportional to the inside diameter of pipe.

Fig-13 shows the test facility used for the measurement of Fig-1. An ultrasonic detector was located by about 10D downstream from a flow conditioner to make the flow axis-symmetric. Air was injected into water from the suction side of upstream pump and broken into micro bubbles as velocity field tracers. Flow rate error was calculated from the average output value in three minutes of UVP flow meter, in comparison with that of an EMF (electromagnetic flow meter) used as the reference meter. The EMF was calibrated within ±0.1% uncertainty. In this paper, all measurements were performed at average velocity of 2 m/s.
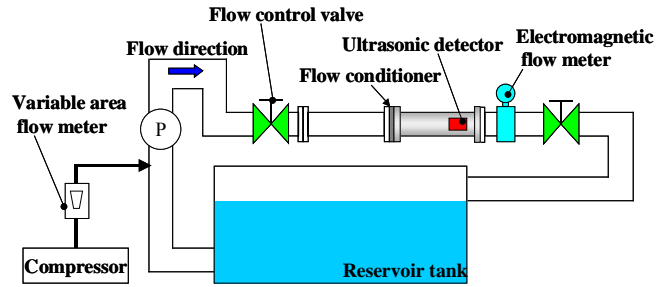
Fig-13: Test Facility of Accuracy Evaluation

9. COUNTERMEASURES AND THE EFFECT

To conquer the frequency characteristics analyzed as above, and to realize high accuracy non-invasive UVP flow meter, countermeasures are taken as below:

1) Specific transmitted frequencies are calculated, where the angles of refraction for all relevant modes of Lamb waves reach critical angle 90 degree. And as shown in Fig-14, the excitation frequency is set to the average value of two of them in the range near resonance frequency of transducer. This is aimed at avoiding the angles of refraction for Lamb waves to become the critical angle, where flow rate error would reach at the maximum.

2) As shown in Fig-14, there is still possibility of occurrence of the offset error even though the excitation frequency is set as described above. Therefore, it is thought that this offset error should be corrected by the actual flow tests, using such standard piping as shown in Fig-13.
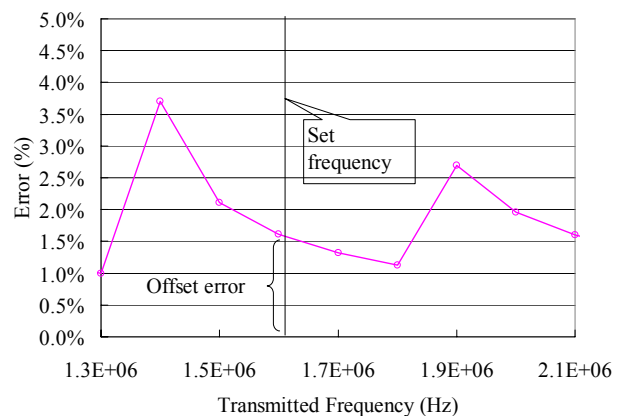

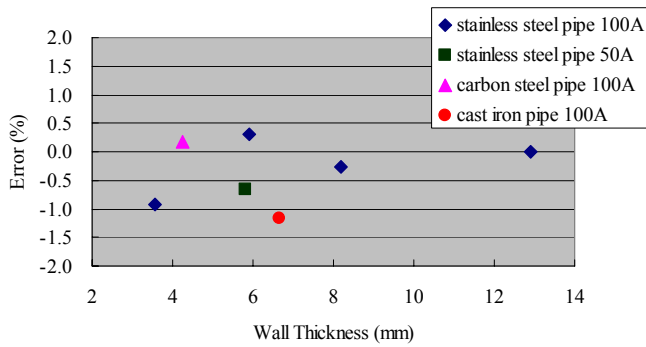Fig-14: Countermeasures for Frequency Characteristics

Fig-15: Effect of Countermeasures (2 m/s)

Fig-15 shows the effect of these countermeasures, where pipes are carbon steel, cast iron, and stainless steel with a few kinds of thickness and diameters. The frequencies corresponding to critical angle 90 degree for these pipes were calculated, the excitation frequencies were set to the specific values, and flow rate errors were measured by using the test facility of Fig-13. It was confirmed that the accuracies are approximately within ±1%.

10. CONCLUSIONS

In terms of non-invasive UVP flow meter, the frequency characteristics of accuracy for SS pipe approximately coincides with the results of the analysis based on the model of dispersion caused by Lamb waves.

It was confirmed that the accuracy was surely improved by setting the excitation frequency at the average value between two frequencies, where angles of refraction of Lamb waves reach the critical angle.

11. ACKNOWLEDGEMENT

12. REFERENCES

1. Y. Takeda, Velocity profile measurement by ultrasound Doppler shift method, Int. J. Heat & Fluid Flow, Vol.7, No.4, pp.313-318 (1986)

2. M. Mori, Y. Takeda, T. Taishi, N. Furuichi, M. Aritomi, H. Kikura, 2002, Development of a novel flow metering system using ultrasonic velocity profile measurement, Exp. Fluids, 32, pp.153-160.

3. Editorial committee of ultrasonic reference book, 1999, Ultrasonic reference book, Maruzen Co., Ltd., pp.62-65.

4. B. A. Auld, Acoustic Fields and Waves in Solids, Vol.2, p.80, John Wiley & Sons (1973)

5. K. Negishi, K. Takagi, 1984, Technology of ultrasonic waves, University of Tokyo Press, pp.173-174

ACCURACY IMPROVEMENT ON NON-INVASIVE ULTRASONIC-DOPPLER FLOW MEASUREMENT BY UTILZING SHEAR WAVES IN METAL PIPE

Noritomo Hirayama*, Takuya Onodera*, Osamu Kashimura*, Sousuke Suzuki**, Hironobu Yao***, Gunji Ohgawara***, Toshihiro Yamamoto***, Yasushi Takeda****

*Fuji Electric Advanced Technology Co., Ltd. Electronic Equipment Technology Laboratory, 1,Fuji-machi Hino-city, Tokyo,191-8502, Japan, e-mail: hirayama-noritomo@fujielectric.co.jp
** Fuji Electric Advanced Technology Co., Ltd. Information & Control Technology Department
*** Fuji Electric Instruments Co., Ltd. Field Instrument Development Department
****Div. Mechanical Science Graduate School of Engineering Hokkaido University, kita-13, Nishi-8 Sapporo 060-8628,Japan

ABSTRACT

In this paper, the essential effect by utilizing shear waves in metal pipes is described in order to improve the accuracy of non-invasive UVP (Ultrasonic-Doppler Velocity Profile) flow measurement along with the transmission/reception efficiency through metal pipe. If the incident angle of ultrasonic transducer from wedge onto metal pipe is set to an angle so as to generate L (longitudinal) waves in metal pipe, SV (shear vertical) waves will be also excited in metal pipe and the ultrasonic transducer will receive two echo signals that correspond to the L wave and the SV wave in metal pipe.

To avoid this double-beam effect, the incident angle of ultrasonic transducer is selected so that the angle of refraction in metal pipe is larger than critical angle of 90 degree for L wave and smaller than that of SV wave, then exciting only SV waves in metal pipe. The authors have got the perspective to be able to achieve high accuracy of ±0.5% for the velocity range of more than 1 m/s ,by optimizing incident angle, reducing multiple reflection and adjusting excitaion frequency of ultrasonic transducer.

Keywords: Shear wave, Incident angle, Multiple reflection, Acoustic noise, Accuracy, Efficiency

1. INTRODUCTION

Recently, UVP method has been often reported as a flow mapping technology. Some papers have also shown the performance of UVP flow meter aimed at industrial use, succeeding in highly accurate flow rate measurement mainly as an invasive type flow meter, that is, a flow meter with wetted transducers [1][2]. However, it is the authors' understanding that the study of UVP method as non-invasive flow metering has not been performed in detail so far. At this time, the fundamental investigation was performed on acoustic propagation through metal/plastic pipes in order to develop non-invasive type UVP flow meter, and it has been recognized that there are various kinds of acoustic interference waves, of which the influence is remarkable especially for metal pipes.

In this paper, the essential effect by utilizing shear waves in metal pipes is described so as to improve the accuracy of non-invasive UVP flow measurement along with the transmission/reception efficiency through metal pipes.

2. CONSIDERATION ON ACOUSTIC NOISES

UVP method receives ultrasonic echo signals reflected by bubbles and/or particles in measured liquid, and calculates velocity profiles by measuring and connecting the Doppler shift frequencies in all channels of the echo signals. Unlike ultrasonic flow meter utilizing transit time method, the transmission of ultrasounds and reception of echo signals are performed by the same transducer.

For highly accurate measurement, it is essential to reduce acoustic interference, which is mainly induced by non-invasive measurement. The would-be acoustic interference is divided into 3 categories as below:

1) Double beam effect:
L (longitudinal) wave and SV (shear vertical) wave are generated in pipes as fundamental waves in case of non-invasive measurement.
2) Multiple reflection:
Acoustic interference waves are excited at the interface between two mediums with different acoustic impedances. The authors especially raise multiple reflection in metal pipes.
3) Dispersion effect:
Lamb waves are generated due to finite pipe thickness, causing split beams in different modes in pipes and then producing frequency characteristics of accuracy.

In this paper, the influence of categories 1) and 2) is described along with their countermeasures. As for dispersion effect, it is reported by the authors' other paper in detail, and only the test data on accuracy are introduced.

3. DOUBLE BEAM EFFECT

3-1. MECHANISM OF DOUBLE BEAM EFFECT

Generally speaking, there are three kinds of acoustic propagation modes in a solid medium with infinite dimensions, L (longitudinal) wave, SH (shear horizontal) wave and SV (shear vertical) wave. L wave is a wave that moves in parallel to particle displacement, and shear waves such as SH and SV waves are ones that move normal to particle displacement.

The sound velocity of L wave is approximately twice larger than that of shear waves in general.

When ultrasounds propagate from medium-1 to medium-2, angle of refraction in medium-2 is determined by the two sound velocities and incident angle into medium-2, yielding to the Snell's law. Therefore, the maximum value of incident angle is limited to the one calculated by the following equation:

$$\theta_c = \sin^{-1}(\frac{c_1}{c_2}) \qquad c_{-1-} \quad c_{-2-} \qquad (1)$$

where c_{-1-}: sound velocity in medium-1, c_{-2-}: sound velocity in medium-2 .

If incident angle of ultrasonic transducer from wedge onto pipe is set to an angle so as to generate L waves in the pipe, SV waves will be also excited in the pipe as shown in Fig-1(a), and the ultrasonic transducer will receive two echo signals that correspond to the L wave and the SV wave in the pipe as shown in Fig-1(b).

The echo signals include the same velocity profile information, though they are superposed on each other with different transit time in the pipe.

Therefore the measured velocity profile will be erroneous without measures against this double-beam effect as shown in Fig-2. This effect is remarkable for metal pipes, and is inversely proportional to the inside diameter.

(a) Transmission process   (b)Reception process
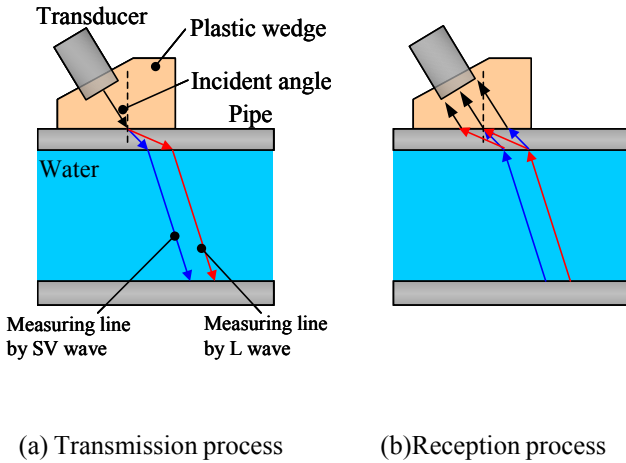
Fig-1: Acoustic Propagation below Critical Angle of L (Longitudinal) Wave (Double beam effect)
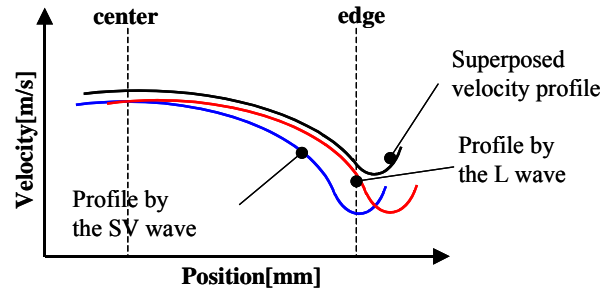
Fig.2: Velocity Profile by Double Beam Effect

For example, the critical angles in SS (stainless steel) pipe are calculated as 28.1degree for L wave and 61.7 degree for SV wave by the Eq. (1), since sound velocities are 5790 m/s for L wave in SS, 3100 m/s for SV wave in SS, and 2730 m/s for L wave in the plastic wedge

When calculating these critical angles at the interface between water and SS pipe, they are 14.9 and 28.8 degree in water for L wave and SV wave in the pipe respectively.

3-2. COUNTERMEASURES AND SIDE EFFECT

(1) IMPROVEMENT OF WAVEFORM

As mentioned above, two kinds of ultrasonic waves will be excited in the pipe if the incident angle is lower than the critical angle for L wave in the pipe. It is considered that the transmitted waveforms from the pipe into liquid would be superposed to each other by this double beam effect. The relation between the incident angle of ultrasonic transducer and the transmitted waveform was experimentally investigated by using the setup as shown in Fig-3.

An ultrasonic transducer with resonance frequency of 2 MHz and diameter of φ13mm was used as the transmitter, and a hydrophone was used as the receiver. These were set into a water tank so as to be in parallel to each other, locating the circular disc that can be tilted between them.

The transducer can widely transmit ultrasounds in the frequency region of 1.5 to 2.5 MHz because of low-Q. The transducer was excited by sinusoidal 4-pulse waves with 2 MHz. The hydrophone has a wide measurable range from 0.5 to 5 MHz, and was connected to the oscilloscope with FFT (fast Fourier transform) function.

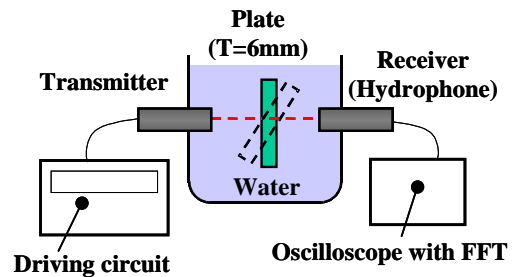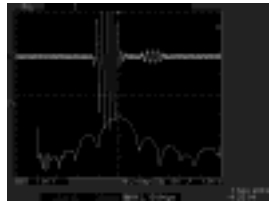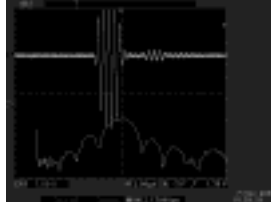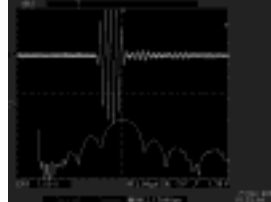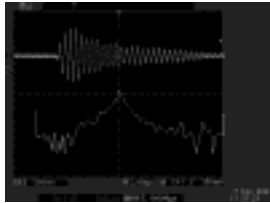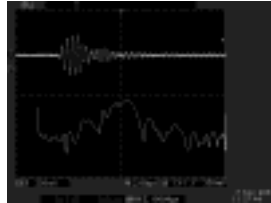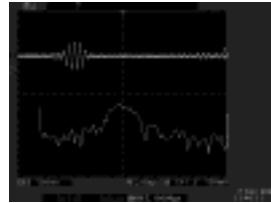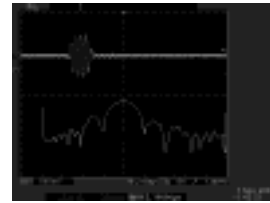The plates were PVC and SS ones 6mm thick.
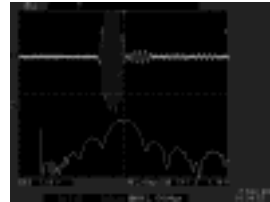
Fig-3: Setup for Investigation of Waveforms

Table-1: Transmitted Waveforms through PVC/SS Plates

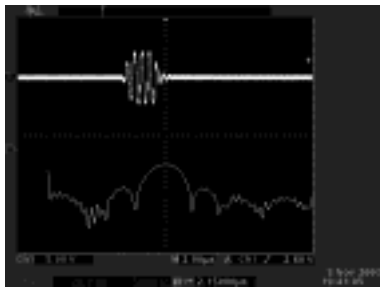|	Tilted angle of plate (equal to the incident angle against the plate)			
	0 deg	8 deg	16 deg	23 deg
PVC plate				
SS plate				

Fig-4: Reference Waveform without Plate

Table-1 shows the test results of transmitted waveforms through PVC/SS plates by changing the tilted angles of the plate. In this table, upper waveforms are ones detected by the hydrophone and lower curves are their frequency spectrums analyzed by the FFT.

Fig-4 shows the reference waveform and spectrum without the plate. In case of PVC plate, the transmitted waveforms were similar to the reference one, and the central frequencies of the spectrums remained at ca. 2 MHz, independent of the tilted angles.

The sound velocity of SV wave in PVC is lower than that of water. Therefore the critical angle does not exist for SV wave, because of not satisfying the condition for Eq. (1). On the other hand, the critical angle is driven to 33.3 degree for L wave, therefore only L waves exist in PVC plate, and there is no double beam effect.

In case of SS plate, the critical angle is calculated as 14.4 degree for L wave. The transmitted waveforms of the tilted angle 0 or 8 degree were distorted compared to the reference waveform. Especially, it was confirmed that resonance phenomenon is occurring at 0 degree. In the spectrums, the central frequencies shift to lower frequency region than 2 MHz.

When the tilted angles were set to 16 or 23 degree of more than the critical angle for L wave, the waveforms were similar to the reference one, and also the spectrums remained almost the same as the reference one.

The double-beam effect was confirmed directly by investigating the transmitted waveforms and spectrums of ultrasounds penetrated though metal/plastic pipes.

(2) IMPROVEMENT OF TRANSMISSION INTENSITY

Furthermore, the relation between transmission intensity through SS plate into water and refraction angle in water (equivalent to incident angle) was investigated by using the same setup as shown in Fig-3. Fig-5 shows the result, in which the vertical scale indicates the ratio of acoustic pressures measured by the hydrophone with/without the SS plate.

Based on this test result, the refraction angle in water has been set to 23.5 degree for the detector of non-invasive UVP flow meter, taking into account the followings:

1) The incident angle of ultrasonic transducer onto pipe should be larger than the critical angle for L wave in metal pipe, and smaller than that of SV wave to avoid the double beam effect.
2) The incident angle of ultrasonic transducer onto pipe should be set to near the peak of transmission intensity into water
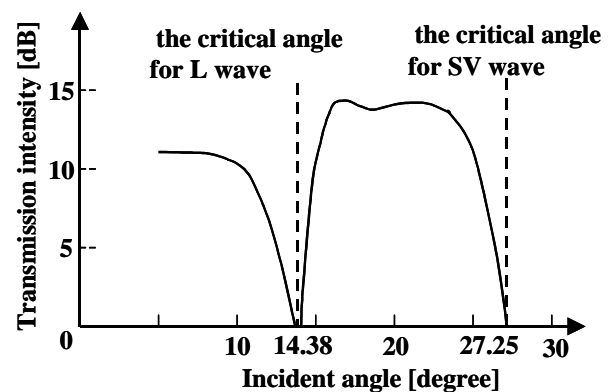

Fig 5: Transmission Intensity vs. Incident Angle

If only shear waves are utilized in metal pipes, the transmission intensity into liquid will be also improved, because penetration rate of ultrasounds will increase at the interface between metals and liquid. However, it will cause a side effect in the next.

(3) LIMITATION OF MAXIMUM VELOCITY

If utilizing SV wave in metal pipes, the maximum velocity of UVP method will be limited to lower value than that in case of L wave. The Doppler shift f_D is expressed by

$$f_D = \left(\frac{2V}{C_f}\sin\alpha\right)f_0 \qquad (2)$$

where V: velocity, C_f: sound velocity of liquid, α: refraction angle in liquid, f_0: basic excitation frequency of ultrasonic transducer.

Because pulse repetition frequency (PRF) corresponds to a frequency of the sampling theorem, the PRF needs to be set to more than twice the maximum Doppler shift.
Besides, PRF needs to be adjusted so that twice of transit time from transducer to opposite wall is smaller than that of PRF. Therefore, PRF is restricted by the following:

$$2f_D \quad PRF \quad 1/(\text{twice of transit time}) \qquad (3)$$

Then, the maximum velocity V_{max} is given by

$$V_{max} \leq \frac{C_f^{\,2}}{8Df_0\tan\alpha} \qquad (4)$$

where D: inside pipe diameter.

Table-2 shows the comparison between refraction angle in water of 8 and 23.5 degree. The maximum velocity is limited to one-third or so by the adoption of only SV waves in metal pipes. However, it is possible to incrase the maximum velocity by lowering resonance frequency of ultrasonic transducer.

Table-2: Comparison between Different Refraction Angles

Refraction angle in water	8deg	23.5deg
Inside diameter	100 mm	
Frequency	2 MHz	
Propagation mode	L wave + SV wave	SV wave
Maximum velocity	19.9 m/s	6.4 m/s

4. MULTIPLE REFLECTION

As for acoustic interference, there would be various types such as below (refer to Fig-6):
  a) Multiple reflection in pipe wall
  b) Multiple reflection between inside wall surfaces
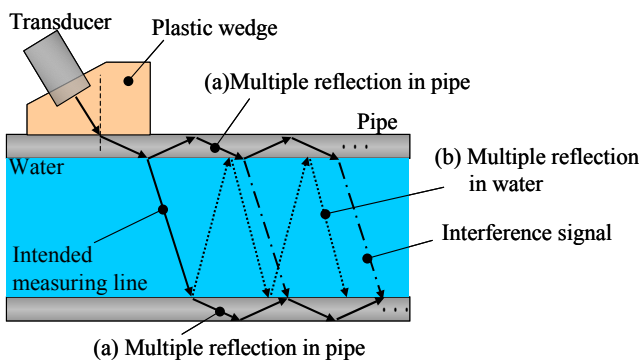 c) Combination of a) and b)

Fig-6: Multiple Reflection

It is of crucial importance for non-invasive UVP measurement to reduce the above-mentioned interference that might cause the similar effects same as double beam effect. That is because many of transmitted ultrasounds come back to the transducer after scattered by reflectors in liquid or reflected by piping devices.

To avoid the interference, acoustic absorber made of material with high acoustic impedance, such as rubber with tungsten particles, should be installed in front of transducer so as to absorb the interference waves of type a), and then type c). Fig.7 shows the detector's configuration for non-invasive UVP flow meter.

On this matter, the authors think that more detailed and comprehensive studies will be needed in the future.
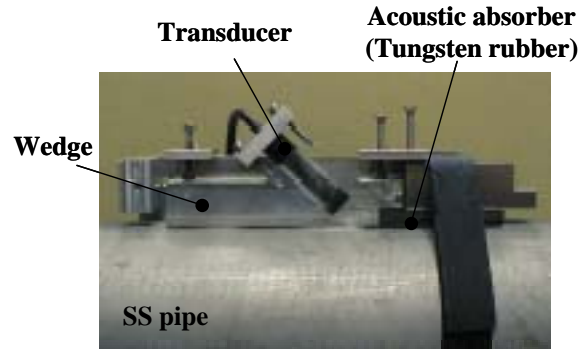

Fig.7: Configuration of Detector

5. EVALUATION OF ACCURACY

5-1. EXPERIMENTAL SETUP

Based on the fundamental analysis and tests as mentioned above, the accuracy tests were performed by using the test facility as shown in Fig-8.

The tests were done for PVC pipe and SS pipe with nominal diameter of 100 mm and thickness of 4.8 mm and 5.9 mm respectively. The detector was installed on the pipe surface by 10D downstream from a flow conditioner. The accuracy evaluation was performed by so-called the comparison method with an EMF (electromagnetic flow meter). The EMF was calibrated within ±0/1% by gravimetric method. The liquid was water that contains air bubbles as velocity field tracers. Air was injected into water on the suction side of upstream pump, and was broken into micro bubbles by the pump.

In case of PVC piping, the acoustic absorber was not used because the effect of the acoustic interference is small.
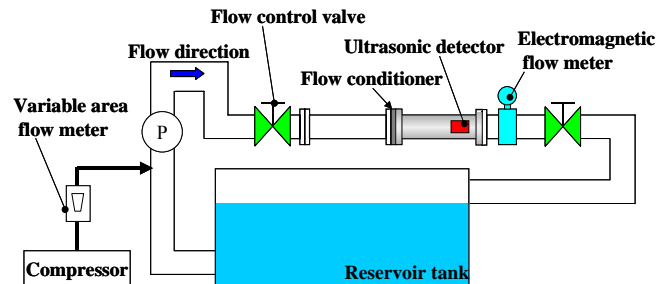

Fig-8: Test Facility for Accuracy Evaluation

5-2. EFFECT OF SHEAR WAVES

In order to confirm the effect of shear waves, the accuracy tests were performed, using two types of wedges made of Plexiglas to cause two different refraction angles in water of 8 degree and 23degree, and comparing those flow profiles. As to the excitation frequency of ultrasonic transducer, it was set to 2 MHz that corresponds to the resonance frequency of piezoelectric device.

Table-3 shows the velocity profiles and accuracy at that time.

As for the velocity profiles, it was confirmed that those of 23 degree are smoother than those of 8 degree for both cases of PVC pipe and SS pipe.

As for the accuracy, it was confirmed that the accuracy in case of 8 degree is less than 7 % of rate for PVC pipe and ca. 20% of rate for SS pipe. On the contrary, it was confirmed that the accuracy in case of 23 degree is ca. 2% of rate for PVC pipe and ca. 4% of rate for SS pipe.

From these results, it was concluded that the adoption of only SV waves in metal pipes has take advantage over that of L waves and then SV waves in addition.

5-3. FREQUENCY CHARACTERISTICS

Additionally, the authors have got the fact that the excitation frequency effects on the accuracy of non-invasive UVP measurement. The mechanism and analysis is shown in authors' other paper in detail. Therefore, in this paper, were shown the test results of the frequency characteristics and the effect after tuning the excitation frequency.

Fig-9 shows one example of the frequency characteristics. Fig-10(a) and (b) show the test results on the accuracy applied to SS pipe and CS pipe.
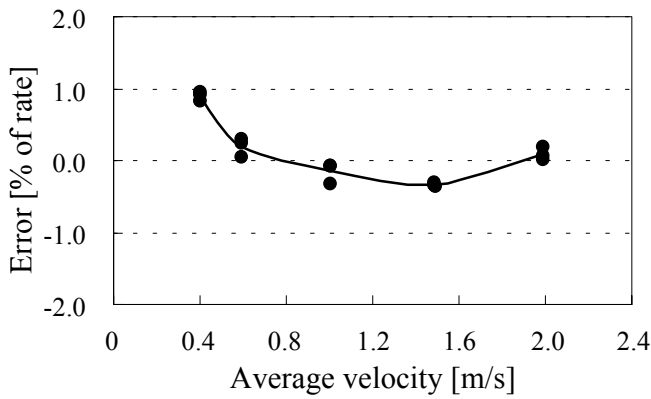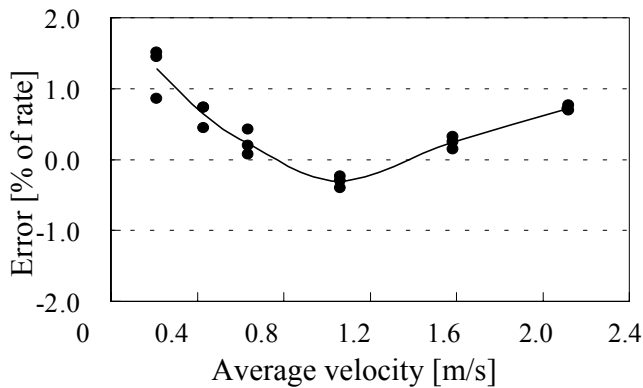
Table-3: Comparison of Velocity Profile and Accuracy
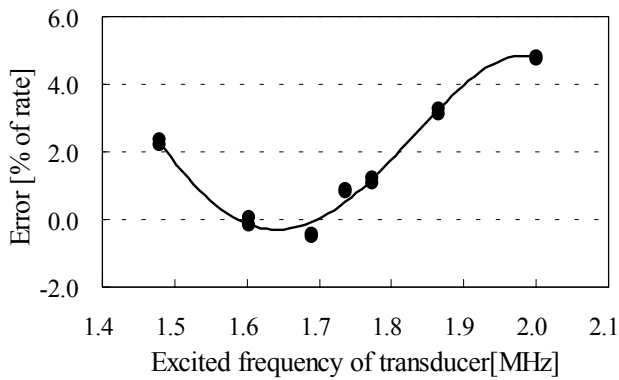
Inside diameter/thickness: 102.1 mm/5.9 mm
Resonance frequency of transducer: 2 MHz
Average velocity: ca. 2 m/s

Fig-9: Frequency Charactristics for SS Pipe

Inside diameter/thickness: 102.1 mm/5.9 mm
Excitation frequency: 1.6 MHz

Fig.10(a): Accuracy in Case of SS Pipe

Inside diameter/thickness: 106.0 mm/4.39 mm
Excitation frequency: 2.0 MHz

Fig-10(b): Accuracy in Case of Carbon Steel Pipe

6. CONCLUSIONS

The accuracy of non-invasive type UVP flow meter was improved by avoiding double-beam effect and reducing multiple reflection. It was also commented that the accuracy was improved by tuning the excitaion frequency.

The wedge angle of ultrasonic transducer was selected so that incident angle onto metal pipe is larger than the critical angle for L wave in the pipe and smaller than that of SV wave, then exciting only SV waves in the pipe. Furthermore the acoustic absorber was installed in front of ultrasonic transducer for the sake of absorbing the multiple reflection in the pipe.

As a result, it was confirmed that the accuracy would be ±0.5% for the average velocity of 1 to 2m/s even if UVP method is applied to non-invasive flow meseasurement.

7. REFERENCES

1. Y. Takeda, "Velocity profile measurement by ultrasound Doppler shift method", Int. J. HEAT & Fluid Flow, Vol.7, No.4, pp.313-318(1986).

2. M. Mori, Y. Takeda, T. Taishi, N. Furuichi, M. Aritomi, H. Kikura, "Development of a novel flow metering system using ultrasonic velocity profile measurement, Exp. Fluids", 32, pp.153-160 (2002).

SURFACE DECORATION OF STAINLESS STEEL FOR LBE FLOW MEASUREMENT BY ULTRASONIC TECHNIQUES

Kenji Kikuchi*, Masao Tezuka**, Shigeru Saito*, Hiroyuki Oigawa*, Yasushi Takeda***

* Japan Atomic Energy Research Institute, Tokai-mura, Ibaraki-ken 319-1195 Japan, E-mail:
kikuchi@popsvr.tokai.jaeri.go.jp
** Sukegawa Electric Co., Ltd., Hitachi-shi, Ibaraki-ken, 317-0051, Japan
*** Hokkaido University, Sapporo-shi, Hokkaido, 060-8628, Japan

ABSTRACT

Ultrasonic techniques were applied to lead bismuth eutectic (LBE). LBE melts at 124.5ºC. Below 400ºC the austenitic stainless steel is not easily corroded in a saturated oxygen content and LBE often adheres on the steel. However, adhered LBE can be removed by blushing easily. So LBE was not bonded strongly to the steel. When the steel is submerged into LBE, LBE will contact with the steel except for the interface among LBE, gas and metal where the surface energy controls the shape of the free surface in LBE. It is supposed that LBE will transmit ultrasonic wave into LBE through the contacting area. However, the ultrasonic echo was too low to detect from the steel container filled with LBE. The measurement was improved by coating the interface between the steel and LBE with the SnPb solder. After an immersion test the steel surface was covered with thin LBE layer. The thickness of the layer is only 10 to 20 µm. So it will not disturb the flow pattern where UVP is applied. Sn was not detected by X ray analyses. This is an evidence how the steel was wetted in LBE and how the ultrasonic wave transmitted though the interface of LBE and the steel.

Keywords: LBE, Ultrasonic wave, Wetting, Austenitic stainless steel, Solder, X ray analyses

INTRODUCTION

Lead bismuth eutectic (LBE) is a potential target for spallation neutron source as well as a coolant material of the sub-critical fast reactor in the concept of the nuclear transmutation system driven by the high-energy proton accelerator.[1] In the R&D of the target system it has been found that a local flow affects the corrosion-erosion rate of the materials and the thermo-mechanical design of the target window where the incident protons bombard. For example, the projected electrode of electro-magnetic flow meter in the flow channel was eroded under the flowing LBE. Material samples for corrosion test were eroded locally. Dissolved elements of the structural material into LBE at the hot leg deposit in the form of polycrystals at the cold leg as a result of mass transfer mechanism in the closed channel.[2] The target window disturbs LBE flow and heat transfer is deteriorated. Ultrasonic method is expected to be a powerful tool to visualize a flow pattern in the particular area of LBE components in order to optimize the flow distributions. It can reveal the flow pattern in the other application such as the liquid mercury.[3] So we applied this technique to LBE.

There are technical issues to be considered the ultrasonic method techniques applied to LBE. It is a boundary property on the ultrasonic wave penetration between the vessel and LBE. Firstly, working temperature should be higher than 124.5ºC, melting point of 45Pb-55Bi(w%) eutectic alloy. Oxygen has a very important role for handling LBE at high temperature. Oxygen dissolves into LBE. Dissolved oxygen makes Fe oxide on the surface of the steel. Saturated oxide in LBE reacts with Pb and makes PbO.[4] It is inevitable that Pb will be oxidized at high temperature without control of the oxygen content in LBE. Though the corrosion test of the austenitic stainless steel the oxide is too small to detect under 400ºC. But over 450ºC the stainless steel was corrosion-eroded and the oxide layer was made.[5] The surface of stainless steel was covered with solidified LBE even after draining out of the container over 450ºC. Secondly, wetting property may affect the measuring efficiency by the ultrasonic method. If the LBE container is not wet, supersonic sound will be reflected at the boundary between the metal container and LBE. Then the echo signal from the LBE will not be given.

EXPERIMENTAL METHOD

Fig.1 illustrates the ultrasonic echo measurement in order to know the intensity of the reflected ultrasonic wave at the interface of the vessel and materials and/or reflector in LBE. Materials used are water and LBE. Test temperatures are RT for water and 140ºC for LBE, respectively, both in air. The reputation frequency of ultrasonic probe used is 4MHz, type TH4-5-8 [6]. The ultrasonic probe is attached to the cylindrical container with 80mm diameter made of the austenitic stainless steel or acrylic resin with using a matching medium. A reflector plate made of stainless steel is set up in LBE in order to reflect the ultrasonic waves. Several types of the vessel are used. The vessel surface is round because of a part of cylinder

and an edge surface of the ultrasonic probe is flat. In order to avoid mismatching of the face-to-face contact, one vessel surface is flattened by machine process at the outer side surface in order to examine the contacting quality. But the internal surface is still round. Ni coated the internal surface of one vessel. Ni is expected to cover the surface roughness after the machining of manufacturing process and to avoid the surface from the oxidation. The internal surface of another vessel was coated by Sn-Pb solder.
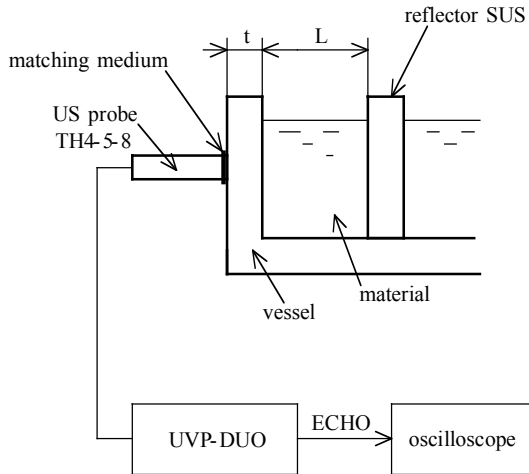
Fig.1 Illustration of ultrasonic echo measurement.
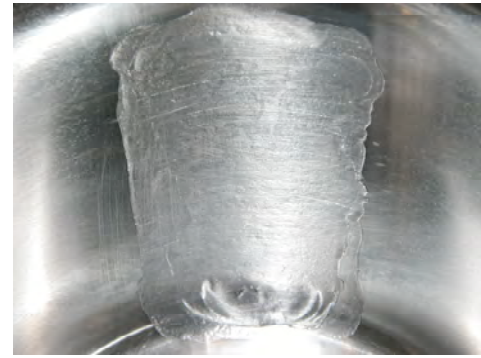
(a)
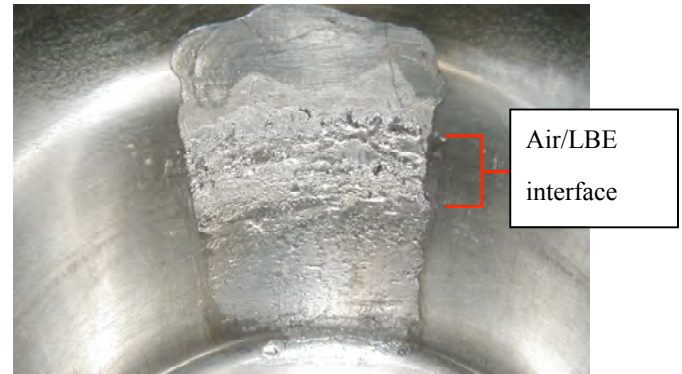
(b)   20 mm

Fig. 2 Optical microscope of internal surface of the vessel (ID8). The vessel diameter is 8 cm. (a): Image before est, (b): Image after test.

RESULTS

Table 1 summarizes the results of the echo intensity measurement. The echo intensity $E(x)$ for IDX (X=2 to 8) is defined by the relative value to the reflected wave height at ID1. In the definition it is also considered that the wave height is proportional to the input voltage.

$$E(x)=20Log[\text{wave height at IDX / wave height at ID1}]$$

The echo intensity from the vessel without any treatment and the reflector plate in LBE was too low to measure (ID5). On the other hand, when the supersonic probe was directly submerged into LBE from the top free surface (ID4) in Fig. 1, the high intensity of the echo signal was detected from the bottom plate. Then the probe was attached to the flattened part of the vessel, but the echo signal was still too low to detect

(ID6). Ni coated vessel also did not help obtain the echo signal (ID7). The echo signal was high enough to measure only in the solder coated vessel (ID8). At a time of sixty hours melting LBE in the vessel the echo signal was measured sufficiently. In the process there are twelve cycles of LBE processing. LBE was melted, kept 140oC during five hours and then solidified. For water the echo intensity was the highest among the measurements when it directly submerged into water(ID1). When the measurement was done from outside the acrylic resin (ID2), the echo intensity is still very high. However, the wave height became small from the outside of stainless steel (ID3).

Table 1 Echo intensity of ultrasonic waves

ID	Vessel	Material	Echo intensity, dB	Wave height	Input voltage,V	Temperature,℃	Echo detection
1	None	Water	0	1.8	30	RT	Good
2	Acrylic resin	Water	-3.5	1.2	30	RT	Good
3	SUS	Water	-23.5	0.12	30	RT	Bad
4	None	LBE	-8.5	0.7	30	140	Good
5	SUS	LBE	-	0	150	140	Bad
6	SUS (flattened)	LBE	-39.1	0.1	150	140	Bad
7	SUS(Ni coating)	LBE	-39.1	0.1	150	140	Bad
8	SUS(Solver coating)	LBE	-25.1	0.5	150	140	Good

Note: Wave height is proportional to input voltage.

Fig.2 shows the optical microscope images of the internal surface of the vessel (ID8) before and after 60 hrs exposures to the melting LBE. SnPb solver was coated partly in the vessel (a). Coated material still existed. Geometrical feature of coated area looks same in both images. The surface became rough, especially, at the interface of air and LBE. It should be noted that the echo intensity was high at the coated area but too low to detect at the uncoated area as experienced inID5. Uncoated area was not wetted by LBE.

DISCUSSION

At relatively low temperatures where the austenitic stainless steel is not corroded, ultrasonic method cannot be applied for measurement of LBF flow because the echo intensity will be too low to measure. However, the surface of the vessel is decorated by SnPb solver, this techniques will be applied. Question is why? Key issue is the wetting property between LBE and the vessel material. The wetting property is related to the surface energies at the contacting area ob LBE. If the steel surface is not wetted, the gaseous layer may exist between LBE and the steel where ultrasonic waves will not transmit to LBE because of the different impedance of the material. Although after the test (ID8) there was material remained on the wall as shown in Fig.2 (b) there was no evidence with regards to the wetting property in LBE.

So we did test to examine a change of surface state of coated solver and LBE by submerging the reflector plates into LBE for sixty hours. Three plates made of SUS316 were prepared. One is a standard sample without any use in LBE. The other two specimens were submerged into LBE during 10 and 60 hrs, respectively. Fi.3 shows the optical microscope images of three plates. Figs.3 (a), (b) and (c) show the plates coated with the SnPb solver. SnPb solver was coated on the three plates in the same manner. Fig.3 (d) shows the plate (b) submerged into LBE during 10 hours. Fig 3(e) shows the plate (c) submerged into LBE during 60 hours. Surface morphologies of (d) and (e) look different from their originated images of (b) and (c), respectively. The cross sections of the plates were examined by the X-ray analyzer. It was found that Sn disappeared in the plates of (d) and (e) but Bi was detected in the remained materials on the plates as shown in Fig.4. The melting point of Sn Pb eutectic and LBE are 183°C and 124.5 °C, respectively. It is, however, thought that bismuth diffuses into coated SnPb and makes LBE in the solidified material on the plates. Optical microscope observation of the plate cross-section showed that thickness of coated layer was 500mm but reduced to 10 to 20 μm after immersion in LBE. Fig.5 showed the photos of the cross section. The thickness of the coated materials on the plates was 500 mm. After immersion in LBE it reduced to 10mm by 60 hrs. Conclusively the coated material is so wetted that the supersonic sound can be transmitted at the interface of the steel and LBE.
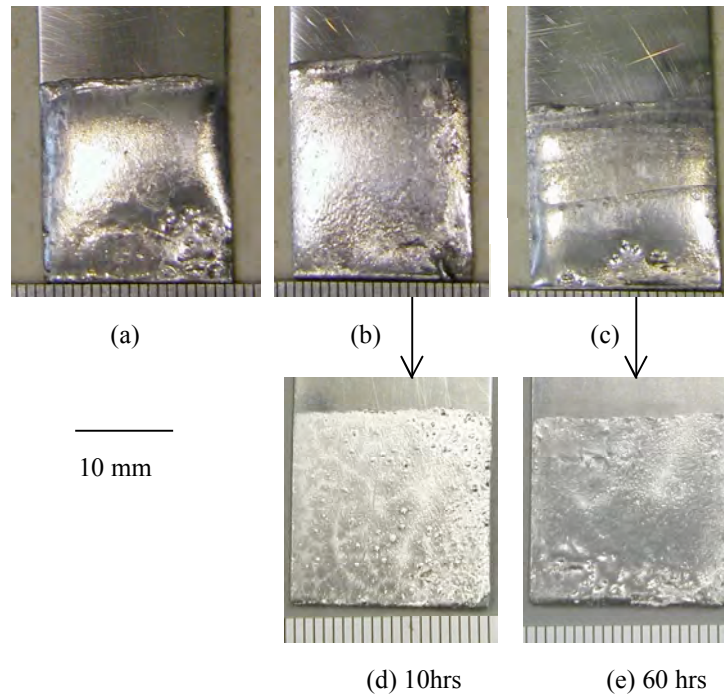

(a) (b) (c)

10 mm

(d) 10hrs (e) 60 hrs

Fig.3 Submerged test of coated plates into LBE.

SEM Pb Sn
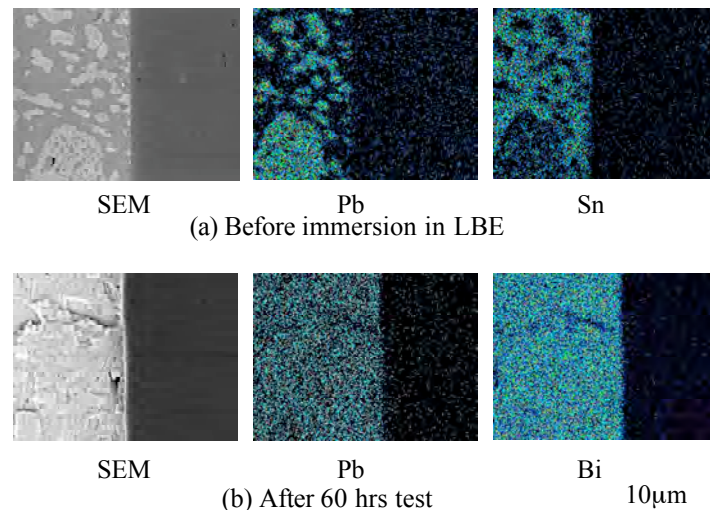(a) Before immersion in LBE

SEM Pb Bi 10μm
(b) After 60 hrs test

Fig.4 X-ray analyses of cross-section of coated SUS 316.

CONCLUDING REMARKS

The ultrasonic wave property in the steeland LBE was examined at 140ºC in air. SnPb solder makes possible to detect the sonic wave by enhancing wetting property of the steel. SnPb eutectic disappeared from the plate surface and PbBi eutectic covered the materials on the SUS316 plate. The thickness of the covered PbBi layer was 10 to 20μm.

REFERENCES

1. K. Tsujimot, T. Sasa, K. Nishihara, T. Takizuka, H. Takano,, Study of Accelerator-driven System for Transmurtation of High-Level Waste from LWR, ICONE-7, Tokyo, 1999.

2. K. Kikuchi, S. Saito, Y. Kurata, M. Futakawa, T. Sasa, H. Oigawa, E. Wakai, M. Umeno, H. Mizubayashi, K. Miura., Lead-Bismuth Eutectic Compatibility with Materials in the Concept of Spallation Target for ADS, JSME Int. J.B Vol.47, No.2 pp.332-339, 2004.

3. Y. Takeda, H. Kikura, G. Bauer, Flow measurement in a SINQ mockup target using mercury, ICANS XIV, pp.321-328, 1998.

4. P. Martynov, Yu. Orlov, A. Efanov, V. Troiynov, A. Resanov and O. Lavrova, Technology of lead-bismuth coolants for nuclear reactors, proc. ISTC-TITech Japan Workshop on Nuclear Reactor Technologies in Russia/CIS, pp.80-105, 2001.

5. K. Kikuchi, Y. Kurata, S. Saito, M. Futakawa, T. Sasa, H. Oigawa, E. Wakai, K. Miura, Corrosion-erosion test of SS316 in flowing Pb-Bi, J. Nucl. Mater., 318, pp. 348-354, 2003.

6. User's Guide of UVP Monitor Model UVP-DUO, 2002.
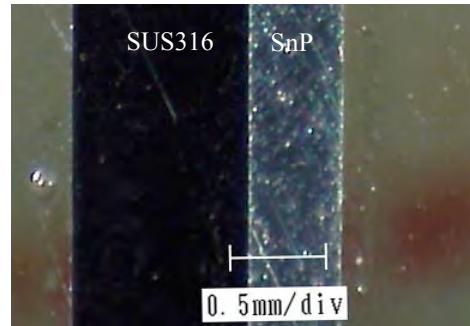
(a) Before immersion
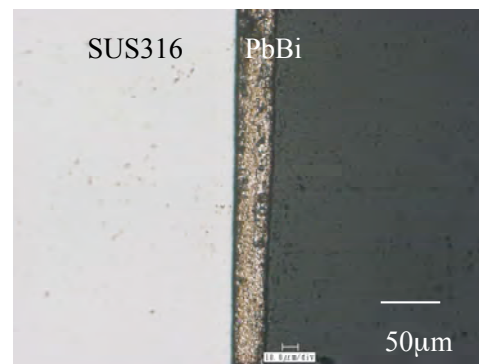
(b) After 60 hrs test.

Fig.5 the cross-section of the plates.

APPLICATION OF MULTI-WAVE TDX FOR MULTI-PHASE FLOW MEASUREMENT

Hideki Murakawa*, Hiroshige Kikura, Masanori Aritomi

*Research Laboratory for Nuclear Reactors, Tokyo Institute of Technology, 2-12-1 O-okayama, Meguro-ku, Tokyo, 152-8550 Japan, E-mail: murakawa@2phase.nr.titech.ac.jp

ABSTRACT

This paper proposes a new measurement technique for multi-phase flow. To measure two kinds of phases at the same place and the time, Multi-wave TDX was newly developed. This TDX includes the two different ultrasonic elements. At first, this TDX was applied for ultrasonic Doppler method (UDM). As changing of the measuring volume of the ultrasonic, the measured data using the UDM change. Applying the effects of measuring volume, the liquid velocity and the bubbles' rising velocity are obtained using the UDM in two-phase bubbly flow. Furthermore, applying ultrasound correlation method (UTDC) for the Multi-wave TDX, the bubbles' rising velocity can be obtained at more accurately. With emitting two kinds of ultrasonic at the same time, two different signals can be obtained. Comparing with the each signal, the bubbles' velocity information can be eliminated from the other signal. Using the UTDC and the signal comparison method, the velocity distribution can be obtained at the same time and the position. This method does not need the velocity difference between two objects, such as the bubbles and the liquid. Hence, this method can be applied for other multi-phase flow.

Keywords: Multi-wave TDX, UDM, UTDC, and Multi-phase flow

INTRODUCTION

This paper proposes a new measurement technique for multi-phase flow using Multi-wave TDX and ultrasonic method.

Zhou *et al.* [1] developed a system to measure the velocity fields in bubbly flows by means of ultrasonic Doppler method (UDM). When the UDM is applied to two-phase bubbly flow, ultrasonic pulses are reflected on both seeding micro-particles in liquid-phase and gas-liquid interfaces. Hence, the velocity data measured by the UVP monitor will include velocity information of both phases.

To apply the statistical method to the UDM, the relation between flow condition and ultrasonic beam diameter is an important factor. With the increase of void fraction, the possibility of bubbles' crossing the measuring line increases. Furthermore, the relation between bubbles' size and TDX's beam diameter is important as well. On the other hand, if an adequate diameter of TDX is applied for multi-phase flow, each phase velocity can be measured using these relations.

To measure liquid velocity distribution at higher sampling frequency and better spatial resolution, ultrasound correlation method (UTDC) was developed [2]. This method is based on cross-correlation between two consecutive echoes of ultrasonic pulses to detect the velocity. Yamanaka *et al.* [3] tried to apply this method for two-phase bubbly flow measurement.

In this paper, a new measurement method for multi-phase flow is proposed using the Multi-wave TDX and ultrasonic methods. The Multi-wave TDX is composed of two different ultrasonic elements and can emit two kinds of ultrasonic independently. This new method employs several kinds of particles whose sizes are greatly different. For each particle, if

the TDX of an appropriate size can be selected, the measured velocity PDF mainly includes a particles' velocity suitable for the TDX's diameter. As the measurement volume changes, the majority of the recorded velocity also changes for each particles size. At first, measurements of bubbly flow using the UDM and the Multi-wave TDX are conducted. Using these methods, the bubbles' rising velocity and liquid velocity distributions are obtained at the same time. Furthermore, to clarify the accuracy of the measuring multi-phase flow, ultrasound time-domain correlation method is applied.

EFFECT OF MEASUREMENT VOLUME

Measurement system of the UDM consists of Ultrasonic Velocity Profiles monitor (UVP-monitor) and TDX. Ultrasonic pulses reflect on liquid-gas interfaces, so the measured velocity profiles must be divided into gas and liquid velocity information. By adopting the UDM to bubbly-flow measurements, the liquid velocity information can be calculated using statistical method [4]. The first step in dividing the velocity information is to obtain the probability density function (PDF) of all measured instantaneous velocities at each measuring position. Bubbles rising velocity is faster than liquid velocity in the case of upward bubbly-flow. Hence, an instantaneous velocity profile has a typical peak if a bubble crosses the measuring line.

Fig. 1 shows an example of velocity PDF at a channel position for each TDX [5]. The velocity was measured in co-current upward bubbly flow in a rectangular channel (20 x 100 mm^2). Because the bubble rising velocity is higher than the liquid velocity, the velocity PDF of the bubbles is higher than that of the liquid at each channel. As a result, velocity PDF can
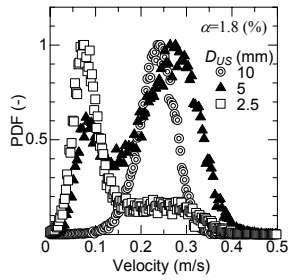
Fig. 1 Velocity PDF depending on the measuring volume [5]

Fig. 2 Multi-wave TDX

Fig. 3 Concept of the UTDC [2]

Fig. 4 UTDC system using the Multi-wave TDX

be calculated as shown Fig. 1. The probability of bubbles' crossing the measuring line becomes higher with the increase of TDX's diameter (D_{us}). At D_{us}=2.5mm, the velocity PDF has a peak value at the mean liquid velocity. However, at the condition of D_{us}=5mm, the maximum value of the PDF becomes higher to the velocity around bubbles' rising velocity and has two peaks. Furthermore, the PDF has one maximum and peak value at D_{us}=10mm. If the void fraction (α) becomes low, these PDF also change. Taking into account these characteristics, TDX must be selected as related to the relative diameters between bubbles and D_{us}, and void fraction. The bubble diameter of this condition was about 3-4mm and void fraction was 1.8%. From these results, about D_{us}=2.5mm must be selected to measure the liquid velocity under this condition. On the other hand, about D_{us}=10mm, the measured data mainly include the bubble rising velocity. This is the reason why that if the D_{us} increases, ultrasonic reflection on the particle relatively decreases for its element diameter.

MULTI-WAVE TDX

The attempt to measure the velocity of each phase was performed by changing the TDX's diameter. From the result shown in Fig.1, D_{us}=10mm and 3mm were selected to measure the bubble and liquid velocity, respectively.

To emit different sizes of ultrasonic beam at the same time and the same position, the Multi-wave TDX is newly developed (Fig. 2). The new TDX consists of special ultrasonic element. The ultrasonic element has two basic frequencies. The central 3mm-diameter area has 8MHz basic frequency and the outer area has 2MHz frequency. Generally, the size of element corresponds to its basic frequency. The Multi-wave TDX can emit ultrasonic independently for 2MHz and 8MHz basic frequencies.

UDM MEASUREMENTS AND METHOD

In this study, two kinds of experiments were performed using the Multi-wave TDX. First experiments were measuring two-phase flow using the UDM. Changing of the ultrasonic measurement volume, the velocity probability density function (PDF) also changes. Using the property, both of the bubbles' rising velocity and the liquid including nylon tracer particles were measured. The 2MHz(φ10) ultrasonic pulses mainly reflected on the liquid-gas interfaces. Because the ultrasonic

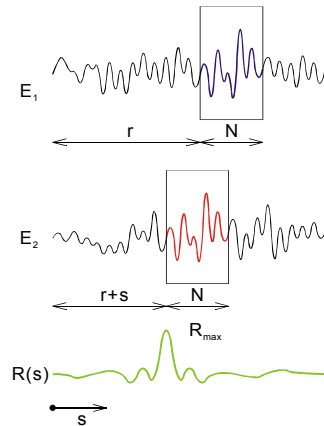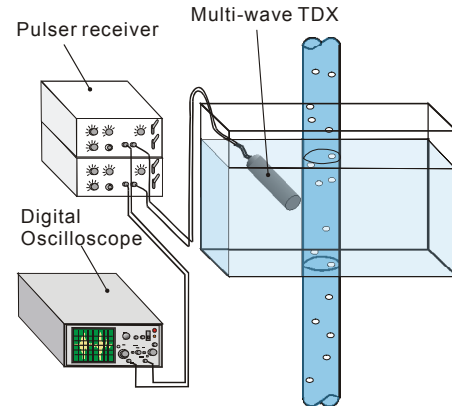pulses strongly reflect at the bubbles' surface, and the possibility of bubbles' crossing the measuring line becomes high. Furthermore, the 2MHz ultrasonic element of Multi-wave TDX is more difficult to detect particles comparing with normal 2MHz TDX because of its central holes, i.e. 8MHz element. On the other hand, the 8MHz(φ10) ultrasonic element can easily receive the ultrasonic pulses reflected on both of the particle and the liquid–gas interfaces.

The velocity distributions were measured using X-3 PS-I model UVP monitor (Met Flow AG). The velocity PDFs were calculated from measured data at the two-phase bubbly flow. The 2MHz ultrasonic element is larger than that of 8MHz. Hence, the measured data mainly include the bubbles' rising velocity. However, the measured data using the 8MHz element includes both of the liquid including tracer particles and bubbles' rising velocity even if the condition is constant. From the velocity PDF, the time-averaged velocity is calculated from 2MHz data. On the other hand, the measured data using 8MHz ultrasonic element include both of the liquid and bubbles' rising velocity information. From these data, the bubbles' rising velocities were eliminated from all of the measured data using statistical methods [4]. From these calculation methods, the time-averaged velocity distributions for liquid and gas are calculated using the Multi-wave TDX.

UTDC MEASUREMENTS

The UTDC is based on cross-correlation between two consecutive echoes of ultrasonic pulses to detect the velocity (Fig. 3). In this study, the UTDC was applied for bubbly flow measurement. Using a normal TDX, the separation techniques between the liquid and gas velocity information are very
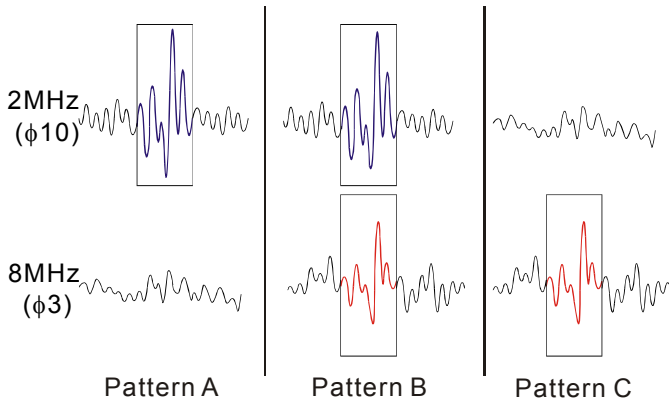
Fig. 5 Signal patterns of the UTDC

(a) Velocity PDF (UDM)   (b) Velocity distribution (UDM vs. UTDC)

Fig. 6 Liquid velocity distribution (single-phase flow)

(a) Velocity PDF (UDM)   (b) Velocity distribution (UDM vs. UTDC)

Fig. 7 Bubbles' rising velocity distribution (two-phase flow)

difficult. For this reason, the Multi-wave TDX was used for measuring of two-phase bubbly flow. Fig. 4 shows the schematic of the UTDC. The each element of the Multi-wave TDX was connected with each pulser-receiver (DPR300 and DPR35+, JSR Co. Ltd.) respectively. Hence, the ultrasonic pulses and their echo signals were received independently by a digital oscilloscope (LC-574A, Lecroy Co. Ltd.). The pulses were triggered with each pulser-receiver and the digital oscilloscope. The digital oscilloscope has the 8-bit A/D converter. The each signal can be recorded at a sampling of 100MS/s. The echo signals can be compared with the 8MHz and 2MHz at the same time using the system. The 2MHz echo signal was adjusted to detect only the bubbles. On the other hand, the 8MHz signal was adjusted to detect both the particles and bubbles. It was confirmed that the signal of 2MHz could not detect the particles in this adjustment.

Signal processing

The digital oscilloscope can record both the 2MHz and 8Mhz echo signals. Comparing with each signals at the same time and same position, the authors tried to divide into three patterns as shown in Fig. 5.

Pattern A :   2MHz signal include reflected pulse
              8MHz signal not include reflected pulse

In the case of Pattern A, the pulse reflected on a bubble. Because the measurement volume of 2MHz is larger than that of 8MHz. Hence, the bubble is estimated to cross the only 2MHz measuring line.

Pattern B :   2MHz and 8MHz signal include reflected pulse

In the case of Pattern B, the signal is apparently reflected pulse on a bubble's surface.

Pattern C :   2MHz signal include reflected pulse
              8MHz signal not include reflected pulse

In this case, the signal pattern is opposite to Pattern A. The signal can be regard as the particle reflection, because the 2MHz ultrasonic was adjusted as not to detect the particles.

RESULTS AND DISCUSSION

All of the experiments were performed at vertical pipe (i.d.=50mm) and z/d=23 from a bubble generator. The experimental condition was set at constant values of mean Re_m=8000, superficial liquid velocity J_G=0.00310m/s.

To compare the UDM and the UTDC, a measurement of single-phase flow was conducted. Fig. 6(a) shows the color

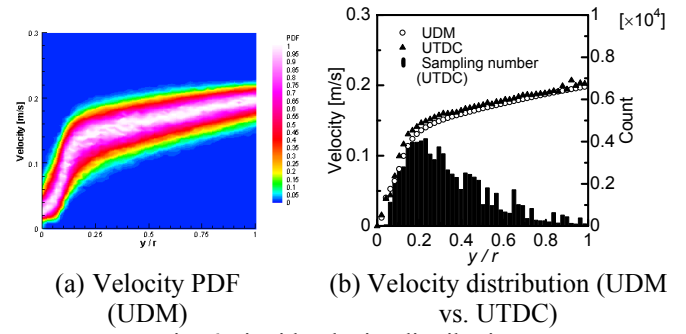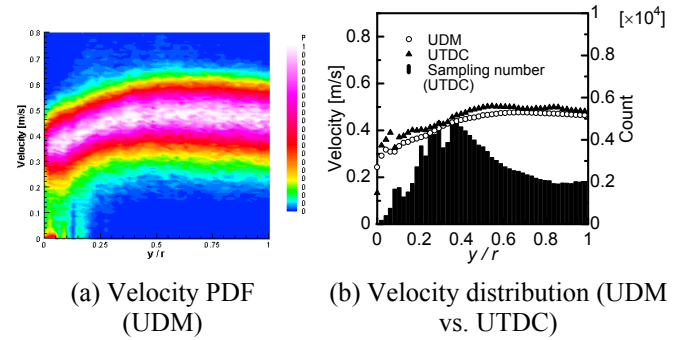map of velocity PDF for each position measured using the UVP monitor. From the velocity PDF, time-averaged velocity distribution using the UDM is calculated as shown in Fig. 6(b). Furthermore, the UTDC measurement was performed at the same condition. Comparing with each other, the velocity distributions are almost the same. However, error of the velocity increases with increase of the distance from the wall because of the signal intensity decreasing. Furthermore, to compare the bubbles' rising velocity distribution, bubbles' velocity were measured (Fig. 7). In this condition, there were few particles in the liquid. Hence, the velocity data measured using the UDM mainly include the bubbles' rising velocity. The reason there are small differences between the results might be the effect of the small number of the including particles.

Two-phase flow measurement

To obtain the bubbles' rising velocity and liquid velocity in two-phase bubbly flow simultaneously, the UDM were conducted using the Multi-wave TDX. The measured velocity PDFs using each element at the same condition were shown in Fig. 8. From these color maps, it can be clarified that the possibility of measuring the bubbles' rising velocity is strongly different. In the case of the 2MHz ultrasonic element, the bubbles' velocity information is dominant. On the other hand, it is clarified that the many of bubbles rise at the near wall region from the data measured using the 8MHz element. From these velocity PDFs, the bubbles' rising velocity and liquid velocity distributions are calculated. The measured data by the 2MHz element is considered as the bubbles' rising velocity distribution because the ratio of measured particles is too small. On the other hands, the raw data measured using 8MHz-element include both of the liquid and gas velocity. Hence, the bubbles' rising velocity information was eliminated from all of the data [4].
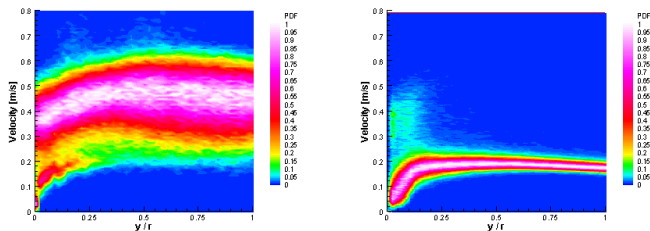
(a) 2MHz element (φ10)   (b) 8MHz element (φ3)
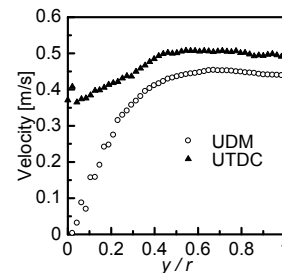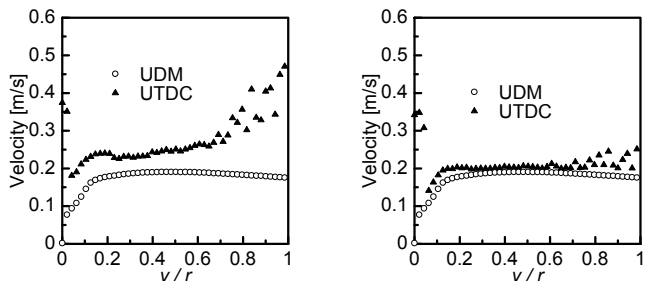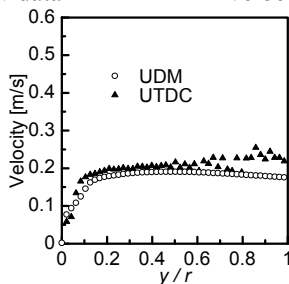Fig. 8 Velocity PDF in two-phase bubbly flow

(a) No elimination from the   (b) Considering of the
     UTDC raw data   velocity difference

(c) Signal comparison method between 2MHz and 8MHz
Fig. 9 Liquid velocity distribution
(8MHz, UDM vs. UTDC)

Liquid velocity distribution measured using UTDC

Fig. 9(a)-(c) show the liquid velocity distribution measured using UTDC and 8MHz ultrasonic element as changing of the data processing. The 8MHz ultrasonic reflect on the both of the particles and the liquid-gas interface. Hence, calculated date by the UTDC includes the liquid and gas velocity information. Fig. 9(a) shows the ensemble averaged velocity distribution by all of the UTDC data. This data is apparent different from the UDM measured data. To eliminate the bubbles' rising velocity, following two methods were adopted.

As same as the UDM data processing, the information of the velocity difference between the liquid and the bubbles are considered to calculate the liquid velocity. If the velocity is higher than the threshold velocity, the data regarded as the bubble's velocity. Following the process, the liquid velocity distribution was calculated as shown in Fig. 9(b) using UTDC. The velocity distribution is almost the same with the data measured using UDM. However, this method is limited to adaptability for multi-phase flow, i.e. the two objectives must have different velocity.

To eliminate the bubbles' information, signal comparison method was applied for the 2MHz and 8MHz ultrasonic signals. 8MHz ultrasonic signals include the Pattern B and Pattern C (Fig. 5). From the 8MHz signals, comparing with 2MHz and 8MHz signals, the Pattern B signals are eliminated. Using the Pattern C data, the velocity distribution was calculated as shown in Fig. 9(c).

Fig. 10 Bubbles' rising velocity distribution
(2MHz, UDM vs. UTDC)

Bubbles' rising velocity distribution

Fig. 10 shows the bubbles' rising velocity measured using UTDC and UDM at 2MHz ultrasonic. Comparing the measured data, the UDM velocity data is smaller than that of the UTDC. Taking into account the results of Fig. 1 and Fig. 7(b), existence of tracer particles decrease the bubbles' rising velocity. This is why the UVP monitor measures the volume-averaged velocity. Hence, with decrease of the ratio of the particles, the bubbles' rising velocity distribution becomes the same values with the result of the UTDC.

CONCLUSIONS

New measurement technique for multi-phase flow using the Multi-wave TDX is proposed. This method can be applied for the both of the UDM and the UTDC. Using the UDM, the liquid velocity distribution can be easily obtained. Furthermore, it is shown that the possibility of measuring several phases simultaneously using the UTDC and the Multi-wave TDX.

REFERENCES

1. S.Zhou, Y.Suzuki, M.Aritomi, M.Matsuzaki, Y.Takeda, M.Mori, 1998, Measurement system of bubbly flow using Ultrasonic Velocity Profile Monitor and Video Data Processing Unit, (III). Comparison of flow characteristics between bubbly cocurrent and countercurrent flows, *J. Nucl. Sci. Technol.,* 35, pp 335-343

2. G.Yamanaka, H.Kikura, M.Aritomi, 2002, Study on the development of novel velocity profiles measurement method using ultrasonic time-domain cross-correlation, *In Proc. 3rd Symposium on Ultrasonic Doppler Methods for Fluid Mechanics and Fluid Engineering*, Lausanne, Switzerland, pp.109-114

3. G.Yamanaka, H.Murakawa, H.Kikura, M.Aritomi, 2003, The Novel velocity profile measuring method in bubbly flows using ultrasound pulses, *In Proc. 7th Int. Symp. on Fluid Control, Measurement and Visualization*, Sorrento, Italy, 214(CD-ROM)

4. H. Murakawa, H. Kikura and M. Aritomi, Measurement of liquid turbulent structure in bubbly flow at low void fraction using Ultrasonic Doppler Method, *J. Nucl. Sci. Technol.*, Vol. 49, pp. 644-654,2003

5. H.Murakawa, H.Kikura, M.Aritomi, Y.Suzuki, M.Mori, 2001, Effect of measuring volume on measurement of bubbly flow using the UVP, *In Proc. JSMF Annual Meeting 2001*, Kitakyusyu, Japan, A7.

SPECTRAL RECONSTRUCTION METHOD
FOR LIQUID VELOCITY MEASUREMENT
BEYOND THE NYQUIST LIMIT

Stéphane FISCHER*, Philippe SCHMITT**, Benoît SCHWALLER***

IMFS, UMR 7507 ULP-CNRS
IUT Louis Pasteur
allée d'Athènes
67300 SCHILTIGHEIM
* stephane.fischer@convergence.u-strasbg.fr,
** schmitt@convergence.u-strasbg.fr,
*** brs@convergence.u-strasbg.fr

ABSTRACT

In pulsed Doppler velocimetry, one of the main constraints is the opposite relation binding the exploration depth and the maximum measurable velocity (Nyquist velocity). Thus for a value higher than the Nyquist limit, the Doppler spectrum is aliased (Shannon Theorem) and the estimated velocity is false. In some applications, this limit is penalizing. Especially, the ultrasonic velocity profiles measurement in sewerage is compromised.

A method allowing velocity measurements beyond the Nyquist limit is proposed. It is based on a technique from weather radars using multiple pulse repetition frequency (PRF). Each folding up, which is different for each PRF, adds information in order to resolve the velocity ambiguity. The proposed algorithm recombines the aliased spectra obtained for each PRF in order to reproduce the original Doppler spectrum. Velocity can thus be calculated on a spectrum not splited by folding up.

With this new method, the limit is not given any more for the maximum frequency in the Doppler spectrum but for the maximum width of this spectrum. Indeed, the only constraint is that the periodisation of the spectrum, which is related to the sampling, does not cause any overlapping of the copies of the original spectrum.

Keywords: range-velocity ambiguity, pulsed ultrasonic Doppler velocimetry, multiple pulse repetition frequency, power spectrum density (PSD)

INTRODUCTION

With the use of ultrasonic Doppler Method for velocity measurements, the pulse repetition frequency (PRF) gives both the exploration depth and the sample rate of the Doppler wave. This results in a bond between the maximum detectable velocity and the exploration depth, also known as range-velocity ambiguity.

The maximum velocity, noted Nyquist velocity v_{Ny}, is given, for the situation given figure 1, by equation:

$$v_{Ny} = \frac{c^2 \tan \beta}{8 f_0 h} \qquad (1)$$

with:

h : water height
β : angle between flow and transducer axis
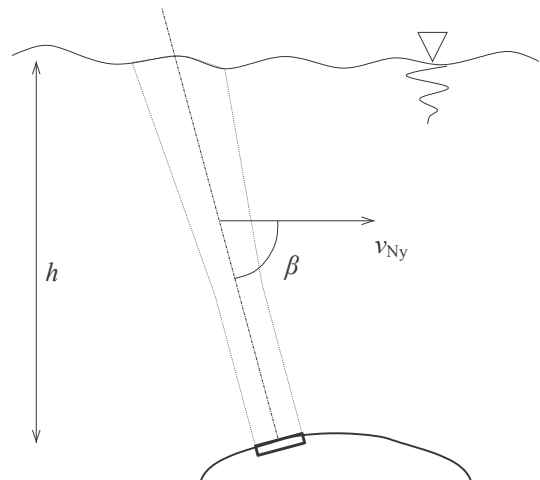c : acoustic velocity
f_0 : ultrasound frequency.

Fig. 1 Principle of flow scan. The transducer sends an ultrasonic burst into the pipe (height h) with an angle β compared to the flow direction (represented by velocity vector v_{Ny}).

The fixed goal is the development of a fluxmeter able to deliver velocity information up to 3 m/s in a 1m depth pipe. These limits include a majority of situations for most pipes present in sewer networks.

In these hydraulic flows, the particles with a higher radius than 750μm move by saltation, and thus be inappropriate ultrasound tracers.

Moreover, reflection on a particle target implies that ultrasound wavelengths are small compared to the particle size [2]. Thus, an emission frequency of 1MHz is an adequate solution. According to equation (1), and with a angle of β= 75°, the Nyquist limit is about 1 m/s, value three times smaller than the desired value.

In order to solve the range-velocity ambiguity, the use of different repetition frequencies has been proposed in the Doppler weather radar domain [3, 4].

This technique, also named *staggered PRT*, *MPDA* (*Multi PRF Dealiasing Algorithm*) or *Dual PRF* is used in addition to *pulse-pair* algorithms. It is based on the calculation of the mean velocity for every PRF, than combine these velocities in order to retrieve the true velocity in the considered spatial volume.

Spectrum mean frequency estimated by the *pulse-pair* method is given, for one given PRF, in the [-PRF/4; PRF/4] interval. Thus, a disadvantage of this method is the biasing of the velocity estimation to a value of PRF/2 for frequencies near on the values $\left(k+\dfrac{1}{2}\right)\dfrac{PRF}{2}$ (k integer). The probability to observe this bias increases for large spectrums and small signal to noise ratios.

This paper focuses on velocity estimation by spectral analysis. The true Doppler spectrum is extrapolated from a batch of folded up spectrums obtained by undersampling the Doppler signal at different PRF. First results obtained with simulation are discussed.

PRINCIPLE

Signal characteristics

The Doppler signal resulting from the echo demodulation in phase and quadrature from particles present in the fluid is noted s(t). It is a complex signal with random phase, available only in its sampled form s*(t) at the sampling frequency:

$$f_e = \frac{1}{T_e} = \frac{\omega_e}{2\pi} \qquad (2)$$

$G(\omega)$ is the power spectral density (PSD) of the continuous signal s(t). The PSD of the sampled signal (Figure 2) can be written as:

$$G*(\omega) = \frac{1}{T_e^2} \sum_{k=-\infty}^{+\infty} G(\omega - k\omega_e) \qquad (3)$$

This density has a limited bandwidth $\Delta\omega$, centered on the Doppler pulsation ω_{Dmed}, proportional to the fluid velocity according to the Doppler effect [9]:

$$G(\omega) = 0 \qquad \forall\, \omega \notin \left]\omega_{Dmed} - \frac{\Delta\omega}{2}; \omega_{Dmed} + \frac{\Delta\omega}{2}\right[\qquad (4)$$

Moreover, the velocity of the fluid is considered to be contained in a specific range, corresponding to a spectral band of $2\omega_M$. We consider:

$$G(\omega) = 0 \qquad \forall\, \omega \notin \left]-\omega_M; \omega_M\right[\qquad (5)$$

General description of the method

Within the traditional framework of the Shannon theorem, the sampling frequency is choose such as :

$$\omega_e > 2\omega_M \qquad (6)$$

Thus, in figure 2, the middle graph present the PSD of the signal sampled at a frequency f_e respecting this theorem. The PSD of the continuous signal (in the upper graph) can be obtained when considering the interval $\left]-\omega_M; \omega_M\right[$.

On the other hand, when using smaller sampling rates, the signal is undersampled and its spectrum is aliased. When considering the interval $\left]-\omega_M; \omega_M\right[$ (interval $\left]-1; +1\right[$ in the lower graph, figure 2), there is an ambiguity on which spectrum is the truth.
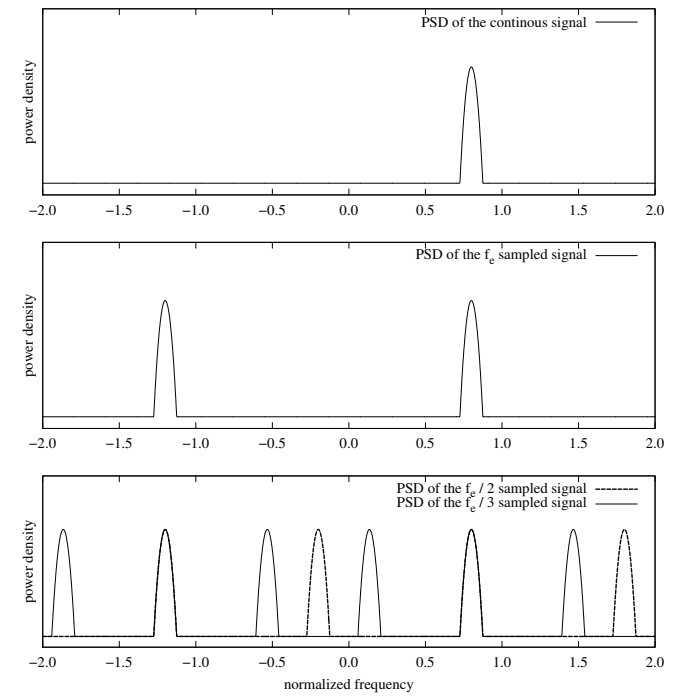

Fig. 2 Effect of folding up according to various sampling rates. The frequency is normalized by f_M, the undersampling factors are 2 and 3.

Undersampling induces a loss of information. Nevertheless, in the case of a signal with limited bandwidth, this loss can be compensated by the use of several spectral densities of the same signal resulting from a sampling at different frequencies. $M(\omega)$ is a combination of the spectral densities of the undersampled signal at various frequencies. An expression of $M(\omega)$ is searched, as well as a criterion on $M(\omega)$ indicating the spectral origin of the energy.

As shown in equation (3), the PSD of the sampled signal can be described as the sum between the spectrum of the continuous signal and infinity of images of this spectrum shifted in frequency (copies). This spectral shift depends only on the sampling frequency. Thus for several different sample frequencies, only the copies will have been moved, whereas

the part of the spectrum corresponding to the continuous signal is always at the same position. When considering the multiplication of the spectra, it is clear that the resulting spectral function has its maximum value where the maxima of the different PSD coincide. This coincidence is systematic at the position of the original spectrum. Elsewhere, the spectrum coincidence will depend on the position(s) of the maximum(s) in the original spectrum and on the sampling rates used.

We consider two sampling rates as well as their associated PSD of the undersampled signal:

$$\begin{cases} f_{e1} = \dfrac{\omega_{e1}}{2\pi}, & G_1^*(\omega) \\ f_{e2} = \dfrac{\omega_{e2}}{2\pi}, & G_2^*(\omega) \end{cases} \tag{7}$$

$M(\omega)$ is the product of these densities:

$$\begin{aligned} M(\omega) &= G_1^*(\omega) \cdot G_2^*(\omega) \\ &= \frac{1}{T_{e1}^2 T_{e2}^2} \sum_{k1=-\infty}^{+\infty} \sum_{k2=-\infty}^{+\infty} G(\omega - k_1\omega_{e1}) \cdot G(\omega - k_2\omega_{e2}) \end{aligned} \tag{8}$$

The conditions on the sampling rates have to be determined so that only the parts corresponding to the original power density in the densities obtained by undersampling have their maxima which coincide. So, the maximum of energy takes place at the noted pulsation $\omega_{D\max}$ defined by:

$$\omega_{D\max} = \underset{\omega}{\arg\max}(M(\omega)) = \underset{\omega}{\arg\max}(G(\omega)) \tag{9}$$

with $\underset{\omega}{\arg\max}$ the function that gives the spectral position of the maximum of power.

By identifying the maximum of the multiplication of the densities from the signal, sampled at various frequencies, and by considering the conditions carried out, one has an indication on the spectral localization of the maximum of energy in the continuous signal.

The subtraction of a portion of energy (represented by a Dirac impulse δ) at this frequency is considered. This implies that the maximum is moved. By recomputing the product and by locating the position of the new maximum, one can locate the presence of energy at another frequency than that of the initial maximum. It is then possible to apply this property in a recursive way in order to rebuild the original power spectral density.

Because this treatment is numerical, the subtraction cannot be applied directly to the spectrum of the continuous signal; on the other hand this one can result in the subtraction of a Dirac comb, defined by $sha_{\omega_e} = \sum_{k=-\infty}^{+\infty} \delta(\omega - k\omega_e)$, to the spectrum of the sampled signal. Thus, the operation of subtraction:

$$G(\omega) - \varepsilon\delta(\omega - \omega_{D\max}) \tag{10}$$

results in:

$$\begin{aligned} & \frac{1}{T_e^2} \sum_{k=-\infty}^{+\infty} G(\omega - k\omega_e) - \varepsilon\delta(\omega - k\omega_e - \omega_{D\max}) \\ =\ & G^*(\omega) - \frac{\varepsilon}{T_e^2} \sum_{k=-\infty}^{+\infty} \delta(\omega - k\omega_e - \omega_{D\max}) \\ =\ & G^*(\omega) - \frac{\varepsilon}{T_e^2} sha_{\omega_e}(\omega - \omega_{D\max}) \end{aligned} \tag{11}$$

The rebuilding of the power spectral density of the continuous signal is carried out by starting with a null density,

then by accumulating at each stage of the recurrence a portion of the energy identified at the frequency of the detected maximum. Conversely, the densities of the undersampled signal are gradually cut down by the algorithm. The iteration is stopped when the remaining energy in these densities is close to zero.

Sampling frequency determination

The depth of exploration is the first constraint on the choice of the sampling rates. This constraint acts through the time of flight of the wave. Thus, whatever the $\omega_{e\{i\}}$, it is necessary to respect:

$$\frac{cT_{e\{i\}}}{2} > \frac{h}{\sin\beta} \tag{12}$$

The condition imposed by the algorithm is deduced from the equations (8) and (9) by introducing the conditions (4) and (5) and by stipulating that the copies should not be superimposed:

$$|k_1\omega_{e1} - k_2\omega_{e2}| > \Delta\omega \tag{13}$$

for all k_1 and k_2 integers such as : $\begin{cases} |k_1\omega_{e1}| < \omega_M \\ |k_2\omega_{e2}| < \omega_M \end{cases}$

An undersampling factor $k_{se\{i\}}$ (real number) is defined for each sampling frequency, such as:

$$2\omega_M = k_{se\{i\}}\omega_{e\{i\}} \tag{14}$$

This factor link the sampling frequency that would be necessary to respect the Shannon theorem ($2\omega_M$) and the effective sampling frequency ($\omega_{e\{i\}}$), respecting the depth constraint described by equation (12).

As the spectrum width $\Delta\omega$ is *a priori* unknown, the distance between the various components (copies) of the folded up spectra have to be maximized. By imposing k_{se1} such as the constraint of depth is respected, $k_{se2} > k_{se1}$ is determined such as (by introducing equation (14) in condition (13)):

$$\underset{k_{se2}}{\arg\max}\left(\underset{k_1,k_2}{\min}\left(\left| \frac{k_1}{k_{se1}} - \frac{k_2}{k_{se2}} \right| \right) \right) \tag{15}$$

for all k_1 and k_2 integers such as : $\begin{cases} |2k_1| < k_{se1} \\ |2k_2| < k_{se2} \end{cases}$

Thus, taking an undersampling factor $k_{se1} = 2$, induces $k_{se2} = 3$ and the limiting spectrum width $\Delta\omega = \dfrac{\omega_M}{3}$.

Spectral density computing

In practice, the spectra are computed with the numerical algorithm of Fast Fourier Transform (FFT). Since algebraic operations have to be carried out between spectra obtained from different sampling frequencies ($f_{e\{i\}}$), it is necessary to choose for each sampling rate the suitable sample numbers $N_{e\{i\}}$ in order to obtain, in each case, the same spectral resolution δf_e. This implies:

$$\delta f_e = \frac{f_{e\{i\}}}{N_{e\{i\}}} \tag{16}$$

The standard algorithm of the Fast Fourier Transform (FFT), initially proposed by Cooley and Tuckey, requires a sample number which is a power of two. This induce that the sampling rates are multiples, and the undersampling factors too, which is in disagreement with the condition (15). Within this framework, the sample numbers imposed by the standard Fast Fourier Transform do not satisfy the conditions. It is thus necessary to use an improved version of the FFT algorithm called mixed radix Fast Fourier Transform, making it possible to work with an unspecified number of samples.

In addition, the FFT computation gives the values of the Fourier transform of the sampled signal on the interval $\left[0; \omega_{e\{i\}}\right[$. Because the interval of interest is $\left]-\omega_M; \omega_M\right[$, the result of the FFT has to be duplicate on it, in order to obtain, for each undersampled spectrum, the same block dimension.

Reconstruction algorithm description

As the algorithm is recurrent, an index of iteration l is defined. The computing starts with several versions of the sampled signal at different frequencies $\omega_{e\{i\}}$. For each version, the power spectral density $G_{\{i,l=0\}}^{*}(\omega)$ is calculated, by Fast Fourier Transform, followed by the duplication on the interval $\left]-\omega_M; \omega_M\right[$.

The next step consists in the multiplication between the several duplicated power spectral densities and in searching the position of the maximum $\omega_{D\max\{l\}}$ in the product. A tiny part ε (a few ten percent) of the identified energy is added to the power spectrum $\hat{G}_{\{l\}}(\omega)$, which has a null initial density and will become the reconstructed PSD:

$$\hat{G}_{\{l+1\}}(\omega) = \hat{G}_{\{l\}}(\omega) + \varepsilon\delta(\omega - \omega_{D\max}) \qquad (17)$$

The duplication, due to the sampling, is then applied to this part of energy, which results in a Dirac comb (see equation (11)). The subtraction of this comb to the PSD obtained at the same sampling rate is then computed:

$$G_{\{i,l+1\}}^{*}(\omega) = G_{\{i,l\}}^{*}(\omega) - \frac{\varepsilon}{T_{e\{i\}}^{2}} sha_{\omega_{e\{i\}}}\left(\omega - \omega_{D\max\{l\}}\right) \qquad (18)$$

This sequence, described by figure (3), is repeated until obtaining folded up spectra of energy lower than a threshold. One will take, for example, the electronic noise level of which the density, for a given system, is known.

Thus, as the folded up spectra are cut down by the algorithm, the spectrum of the Doppler signal is gradually rebuilt.
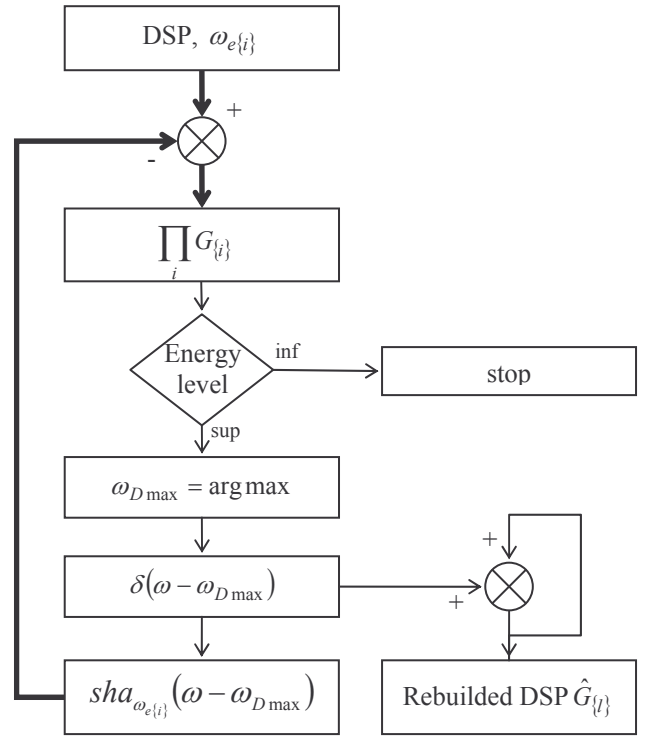

Fig. 3 Synoptic of the reconstruction algorithm. The thick lines represent the parallel processing on each spectral density of index $\{i\}$.

Simulation

In order to validate the functionality of the method, a Doppler signal is simulated on a computer. Various undersampling frequencies are used in order to apply the algorithm and rebuild the power spectral density of the generated signal.

The parameters needed for the signal generation are the central frequency of the spectrum, the bandwidth as well as the signal to noise ratio. The power spectral density is considered to be a Gaussian function of standard deviation taken equal to $\Delta\omega / 6$.

The temporal signal is generated starting from the sum of many particle echoes. Each echo consist in a random phase sinusoid with the desired frequency, multiplied by a Gaussian function of standard deviation equal to the inverse of that of the spectrum. Once the individual echoes are summed, the whole energy is calculated in order to define the density of noise according to the desired signal to noise ratio. This noise is then added to the whole particle echoes.

The signal thus generated is used to calculate the reference spectrum (or original spectrum). This same signal is undersampled with various factors $k_{se\{i\}}$ by taking, in the temporal signal, a sample each $k_{se\{i\}}$ in order to obtain the various undersampled signals. The reconstruction algorithm, presented in the preceding section, is then applied to the batch of undersampled signals.

RESULTS AND DISCUSSION

The spectral reconstruction algorithm allows the proper restitution of the original PSD. Figures (4) to (6) presents several examples of spectral rebuilding in different noise and

signal bandwidth situations. Velocity is identical for all curves because the reconstruction only depends on the spectrum's shape, and not on the velocity value.
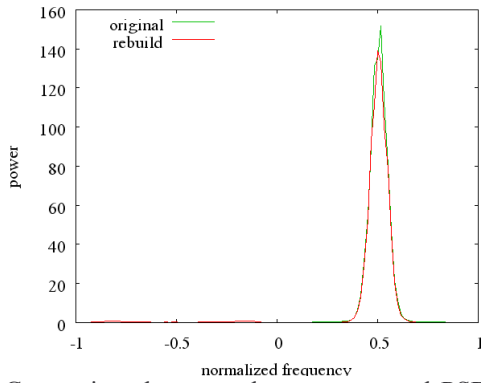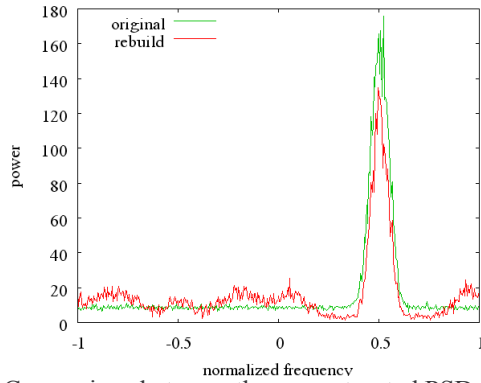

Fig. 4 Comparison between the reconstructed PSD and the one obtained with respect to Shannon theorem for a narrow simulated input spectrum with a signal to noise ration of 100. Frequency is normalized with respect to f_M, and undersampling factors are 2 and 3.
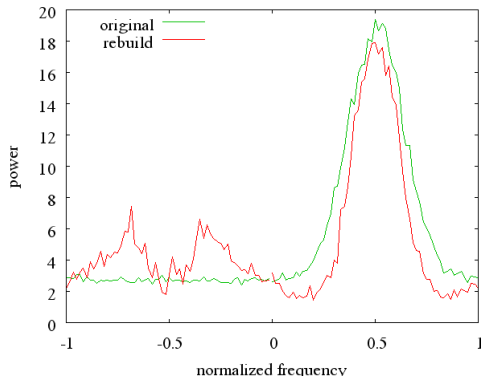

Fig. 5 Comparison between the reconstructed PSD and the one obtained with respect to Shannon theorem for a narrow simulated input spectrum with a signal to noise ratio of 1. Frequency is normalized with respect to f_M, and undersampling factors are 2 and 3.

Fig. 6 Comparison between the reconstructed PSD and the PSD obtained with respect to Shannon theorem for a broad simulated input spectrum (condition (11) not respected) with a signal to noise ration of 1. Frequency is normalized with respect to f_M, and undersampling factors are 2 and 3.

Quality level of reconstructed spectrum depends strongly on signal to noise ratio and on spectrum broadness.

In the case of combination of two spectrum dropped down afterwards to 420 samples, the computing duration (*pentium IV* platform at 2.4 GHz with 512 Mo of RAM) is near on 20ms.

This time equals 0.8ms when 48 samples are needed. According to these values, real time processing is possible.

Theory has demonstrated that the boundary factor of this method is the spectrum broadness. Thereby, figure (4) to (6) shows that the quality of the reconstructed PSD depends strongly on signal to noise ratio and on spectrum fitness. Indeed, without respect to this criterion, parts of the spectrum images grow up in different frequency bands where normally no energy exists (presence of parasitic peaks). This phenomenon is generated during spectral products, and come first from white noise, and second from the overlapping of the spectrum copies, issued from the different undersamplings. Additional sampling frequencies can increase the quality of the reconstructed spectrum.

Another way to extract the original PSD is to use the position of the rebuild density as indicator of the position of the original density, and use it for extracting the original PSD from the folded one.

This can be done in observing a window of width ω_{e1}, centered on this position indicator, in the density obtained from the signal undersampled with the factor k_{se1}.

Indeed, although the rebuilt spectrum is denatured beyond the limit given by the condition (13), its position ω_{Dmed} is available until the surrounding of:

$$\Delta\omega < \omega_{e1} \tag{19}$$

with:

ω_{e1} : highest sampling frequency used.

Moreover, the position of the reconstructed Spectral density is much more consistent than the maximum of the product of the PSD obtained by undersampling. Indeed, unlike the maximum, it is based on the whole spectral information.

Thus, in the case of undersampling factors of 2 and 3, this method would make it possible to pass from a limiting spectrum width of $\omega_M / 3$ to ω_M.

CONCLUDING REMARKS

In order to measure velocities beyond the Nyquist limit, a technique based on the use of multiple PRF was proposed. It uses an original algorithm of spectral reconstruction by combination of the information obtained for each sampling rate. Simulations show the applicability of this method in a large variety of situations. However one notes the appearance of a new limit connecting the width of the Doppler spectrum (instead of the maximum frequency) with the exploration depth.

REFERENCES

1. P. Atkinson and J. P. Woodcock, 1982, Doppler ultrasound and its use in clinical measurement, 2nd edition, *Academic Press*.

2. S. Weidong, 1997, An acoustic instantaneous sediment flux profiler for turbulent flow, Phd thesis, *Ecole Polytechnique fédérale de Lausanne*.

3. Sirmans, D. and D. Zrnic and B. Bumgarner, 1976, Extension of Maximum Unambiguous Doppler Velocity by Use of Two Sampling Rates, 17th conference on Radar Meteorology, *Amer. Meteor. Soc.*, Seattle, WA, pp. 23-28.

4. T. Dazhang, S. G. Geotis, R. E. Passarelli Jr., A. L.

Hansen and C. L. Frush, 1984, Evaluation of an Alternating-PRF Method for Extending the Range of Unambiguous Doppler Velocity., 22nd conference on Radar Meteorology, *Amer. Meteor. Soc.*, Zürich, Switzerland, pp.523-527

5. I. Holleman and H. Beekhuis, 2003, Analysis and Correction of Dual-PRF Velocity Data, *Journal of Atmospheric and Oceanic Technology*, 20, pp.443-453.

6. P. Tabary and G. Scialom and U. Germann, 2001, Real-time retrieval of the wind from aliased velocities measured by Doppler radars, *J. Atmos. Oceanic Technol.*, 18, pp. 875-882.

7. S. Liu, H. Wang and Z. Tao, 2003, A simple algorithm for eliminating Doppler velocity aliasing, 31st International Conference on Radar Meteorology, *Amer. Meteor. Soc.*, Seattle, WA

8. C. N. James and R. A. Houze, Jr., 2001, A real-time four-dimensional Doppler dealiasing scheme, *J. Atmos. Oceanic Technol.*, 18, pp. 1674-1683.

9. G. Cloutier, K. K. Shung and L.-G. Durand, 1993, Experimental Evaluation of Intrinsic and Nonstationary Ultrasonic Doppler Spectral Broadening in Steady and Pulsatile Flow Loop Models, *IEEE Transactions on Ultrasonics, Ferroelectrics, and Frequency Control*, 40, pp. 786-795.

ACKNOWLEDGEMENT

A NEW ALGORITHM FOR LOW VELOCITY MEASUREMENT BY UVP

Hidekazu KITAURA*, Norihiko TADATA*, Yuji TASAKA* and Yasushi TAKEDA*

*Graduate school of engineering, Hokkaido University, Sapporo, Hokkaido, Japan.
E-mail: hideo@ring-me.eng.hokudai.ac.jp

ABSTRACT

UVP (Ultrasonic Velocity Profiler) is a great tool in the experimental fluid dynamics because it can measure an instantaneous velocity profile. In this study, we suggest a new UVP algorithm, which is called as "Phase difference method", for low velocity measurement and compare it with two exiting algorithms. Furthermore, we perform the two verification experiments with a measurement system based on the new algorithm, in order to confirm the validity and the utility of the algorithm.

Keywords: UVP, Algorithm, Velocity profile measurement, low velocity measurement

INTRODUCTION

UVP (Ultrasonic Velocity Profiler), which uses ultrasonic pulses, is available to opaque fluids and measures instantaneous velocity profile along a measurement line. These are great advantages to HWA and optical methods such as PIV. There are two fundamental algorithms for UVP. The conventional one is "Pulse Doppler method". This algorithm is versatile and used widely now. The other one is "Correlation method", which has been devised in order to measure high-speed flow. These method, however, have threshold for low velocity. In this study, we suggest a new algorithm for low speed flow measurement, mm/s order, such as in a natural convection, and investigate performance of the algorithm.

COMMON PRINCIPLE OF UVP

An ultrasonic pulse emitted from an ultrasonic transducer is reflected by the particles suspended in fluid and is received by the same transducer. Positional information is given by the time of flight from emission to reception of the ultrasonic pulse, and velocity information is obtained by analyzing received echo signal. If a number of the particles is enough, ultrasonic pulse are reflected everywhere on the passing line of the pulse. Thus, UVP can measure an instantaneous velocity profile along the line.

EXITING ALGORITHMS OF UVP

A resolution of measurable velocity is a critical factor for the low velocity measurement. This section describes exiting UVP algorithms and how to be determined the resolution in both algorithms.

1. Pulse Doppler method

Fig.1 shows the sampling process of ultrasonic echo in Pulse Doppler method, where the black squares and the black circles express the transducer and particles respectively. The sampling

process is expressed as follows; [1] an ultrasonic pulse is emitted from the transducer, [2] a part of pulse reflects at a particle and the other passes through, [3] the "echo" from the particle reaches the transducer, and is translated into the electric signal, [4] it is sampled with index i, that is d_i, where i means temporal index. If sound speed is known, i can be translated into positional index because positional information is given by time of flight of ultrasonic pulse. This sampling is repeated plural times. In this way, the data set to calculate an instantaneous velocity profile is d_{ij}, where j is pulse repetitional index. Fig.2 shows two examples of sampled data, d_{ij}. If the particle is moving faster, the echo wave becomes shorter
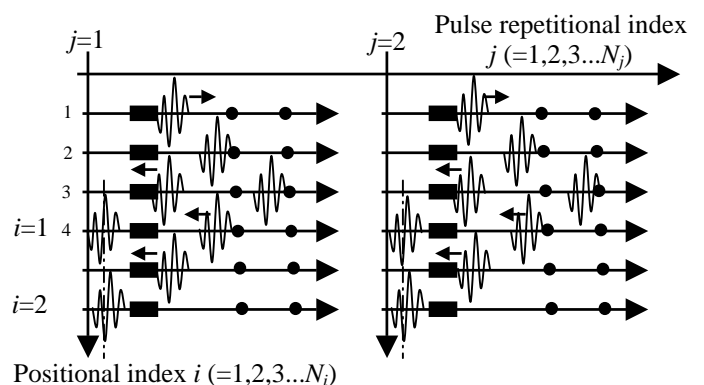

Fig.1 Sampling process for Pulse Doppler method
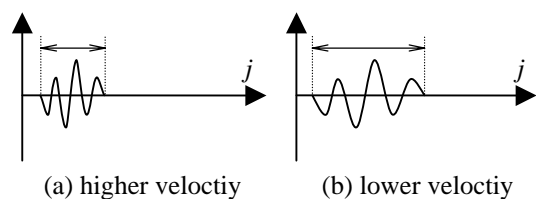

(a) higher veloctiy　　(b) lower veloctiy

Fig.2 Examples of sampled data

(Fig.2(a)), and if later, it becomes longer (Fig.2(b)). That is, velocity corresponds to the frequency of the echo. Velocity is determined from the frequency whose power is the largest in the frequency spectrum. On digital process, the frequency is selected as a discrete value. Therefore, the minimum measurable velocity is determined by the frequency resolution.

2. Correlation method

Fig.3 shows the sampling process of ultrasonic echo for Correlation method. The sampling process is described as follows; ① an ultrasonic pulse is emitted from the transducer, ② a part of ultrasonic pulse reflects and the other passes through, ③ the echo from the transducer reaches the transducer, and is translated into the electric signal, ④ it is sampled with positional index i, and additionally sampled with index k between each i, where k is sampling index. Thus, the Correlation method needs higher sampling rate than Pulse Doppler method. This sampling is repeated at least two or generally more times. There is a time delay between two waves, which has the same positional index i. It corresponds to moving distance of the particle, and then, the velocity can be obtained by calculating the time delay. In other words, the velocity is determined from the time delay at which correlation coefficient is the largest in correlation function. As well as Pulse Doppler method, the minimum measurable velocity is limited because of discrete value, in this method time delay.
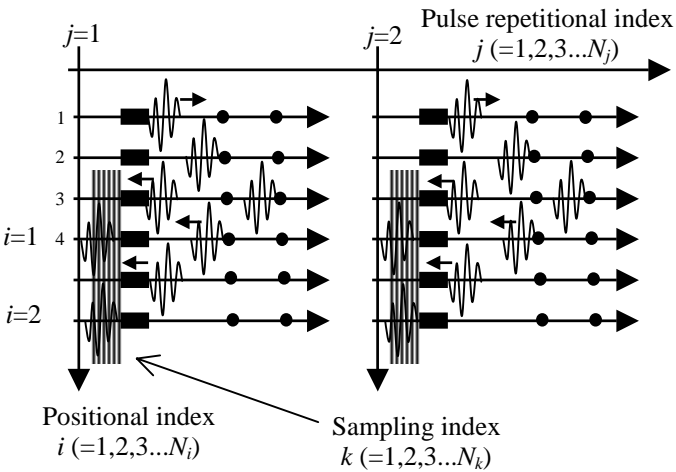
Fig.3 Sampling process for Correlation method

NEW ALGORITHM FOR LOW VELOCITY

1. Theoretical concept of new algorithm

A primal concept is similar to Correlation method. Namely, measurement data set of echo is described as $d_{ij}(k)$ as shown in Fig3. In the new algorithm, however, velocity is not obtained from time delay, but from phase difference between two waves. The theoretical calculating process is described as following. First, echo data $d_{ij}(k)$ is decomposed by using Fourier Transform,

$$C_{ij}(s) = \mathbf{Re}\left[\frac{1}{N_k} \sum_{k=0}^{N_k-1} d_{ij}(k)(W_{N_k})^{kS} \right] \qquad (1)$$

$$S_{ij}(s) = \mathbf{Im}\left[\frac{1}{N_k} \sum_{k=0}^{N_k-1} d_{ij}(k)(W_{N_k})^{kS} \right] \qquad (2)$$

where N_k is sampling number about index k and s is the Fourier index, defined as,

$$f_s = sf_1, \qquad f_1 = \frac{1}{N_k t_{sa}}$$

where t_{sa} is sampling time interval about k. $C_{ij}(s)$ is the cosine component and $S_{ij}(s)$ is the sin component of the original echo signal. $\theta_{ij}(s)$, an initial phase of the decomposed wave with frequency f_s, is obtained as the ratio of $C_{ij}(s)$ and $S_{ij}(s)$ as,

$$\theta_{ij}(s) = \tan\frac{S_{ij}(s)}{C_{ij}(s)}. \qquad (3)$$

$\theta_{ij}(s)$ gives initial position of the decomposed wave as,

$$x_{ij}(s) = \frac{\theta_{ij}(s)}{2\pi}\lambda(s) \qquad (4)$$

where $\lambda(s)$ is wavelength of decomposed wave with frequency f_s, and is determined as follows.

$$\lambda(s) = \frac{c}{f_s} = \frac{N_k t_{sa} c}{s} \qquad (5)$$

The moving distance $dx_{ij}(s)$ is defined as positional difference between j-1 and j as follows.

$$dx_{ij}(s) \equiv x_{ij}(s) - x_{ij-1}(s)$$
$$= \frac{\theta_{ij}(s) - \theta_{ij-1}(s)}{2\pi}\lambda(s) \qquad (6)$$

If form of two waves, j-1 and j, is quite same, the positional difference of all decomposed waves must be constant. Namely, $dx_{ij}(s)$ does not depend on s, and becomes constant.

$$dx_{ij}(s) = \text{const.} \equiv dx_{ij} \qquad (7)$$

dx_{ij} corresponds to the moving distance of particle. The velocity is calculated as following equation,

$$u_{ij} = \frac{1}{2}\frac{dx_{ij}}{t_j}$$

where t_j is time interval of ultrasonic emitting. We call this new algorithm "Phase difference method". In ideal system, u_{ij} does not depend on s, and then velocity can be calculated from just representative frequency f_r. Thus, Fourier index s is rewritten as s_r in Eq.(1)-(7). Namely, if f_r is determined at the beginning of the calculating process, the computational amount can be reduced drastically. The base frequency of an ultrasonic pulse should be selected as f_r because it is less sensitive to noise than any other frequency components.

The phase range determines theoretical maximum limit of measurable velocity. This method cannot give the correct result when the componental wave moves beyond its wavelength $\lambda(s)$. Following equation must be fulfilled,

$$dx_{ij} < \lambda(s)$$

as assigning Eq.(2) and Eq(1) to this equation,

$$\Rightarrow 2u_{ij}t_j < \lambda(s)$$

$$\Rightarrow u_{ij}f_s < \frac{c}{2t_j}. \qquad (8)$$

Because representative frequency f_r is used to calculate the velocity, f_r substitutes for f_s in Eq.(8). Ultimately, maximum limit of measurable velocity is determined as follows.

$$u_{ij}f_r < \frac{c}{2t_j}.$$

On the other hand, the minimum limit of measurable velocity is not determined theoretically. As refers to above, in Pulse Doppler method and Correlation method, it is

determined by discrete value f_D and τ_p whose value is largest in frequency spectrum and correlation function respectively, as shown in Fig.4(a) and (b). In this new algorithm, however, discrete value is not used. dx_{ij} is calculated from $\theta_{ij}(s_r)$, a ratio of cosine and sin component, and it does not depend on frequency index and varies continuously, as shown in Fig.4(c). If we determine the minimum limit forcedly, it becomes resolution of quantization in a system. For instance, when we use 8-bit double–precision floating point variables, this limit becomes $4.9*10^{-324}$. In actual measurement, the measurement deviation is far larger. Because Phase difference method has no theoretical limit of measurable minimum velocity unlike exiting algorithm, it is available and suitable for low velocity measurement.

(a) Pulse Doppler method   (b) Correlation method   (c) Phase difference method
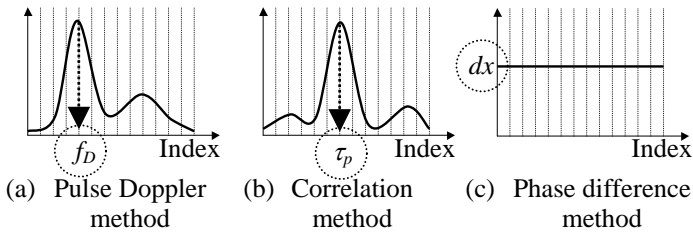
Fig.4 Value of determining velocity in each algorithms

2. Setup of UVP system

The setup of UVP system that we specify in this study and its measurement conditions are shown in Table 1. A basic frequency of pulse emitted from a transducer is 4 MHz, and then a representative frequency f_r in calculating process is 4 MHz as well. A sampling interval t_{sa} is 2 ns and a burst repetition interval t_j is 75 μs. When the analog signal of an echo is quantized into the digital signal, $d_{ij}(k)$, a quantization error is caused. As using this parameter, it becomes about 0.12 mm/s. this error depends on the sampling resolution of ADC, and it can be reduced by using higher-performance one. Numbers of each index N_i, N_j and N_k are 67, 5 and 550 respectively. Namely, 67 measurement points are on the measurement line, the velocity is calculated from 550-sampled echo, and the average of repeating 5 times gives an instantaneous velocity profile. By these parameters, the measurement conditions are determined as described in Table 1. These depend on sound speed c, and Table 1 show the case of water, $c = 1480$ m/s.

Table 1 The specification an performance of UVP built on new algorithm

Setup parameters	
Base frequency of pulse	4 [MHz]
Number of positional index $i : N_i$	67
Number of pulse repetitional index $j : N_j$	5
Number of sampling index $k : N_k$	550
Sampling interval: t_{sa}	2 [ns]
Burst repetition interval: t_j	75 [μs]
Measurement conditions*	
Start of the measurement section	0 [mm]
End of the measurement section	53.80 [mm]
Positional resolution	0.803 [mm]
Temporal resolution	0.2 [s]
Measurable maxmum velocity	2713 [mm/s]

* in the case of using water, c = 1480 [m/s]

VERIFICATION EXPERIMENTS

As discussed above, a possibility of the low velocity measurement with a new algorithm is indicated theoretically. But, there is no guarantee that the algorithm can apply to the realistic low velocity measurement, because of various error factors. It is necessary to confirm validity and the utility of the algorithm for low velocity measurement, to bring out the problem of measurement and to improve the measurement accuracy through realistic experiments. In this section, two verification experiments are performed.

1. Measurement of the pseudo-flow model

The model assumed a low velocity flow is constructed, in order to confirm that new algorithm can really measure low velocity with a few mm/s order. Fig.5 shows the experimental setup. In water, six strings as reflectors of the ultrasonic pulse are fixed perpendicularly on the measurement line of an ultrasonic transducer. The transducer is moved by stepping motor controlled by PC. The speed of transducer toward strings is 1 mm/s and away is 4 mm/s. Fig.6 shows the velocity profile, where the horizontal axis is time, the vertical axis is distance from the transducer and gray scale expresses velocity.
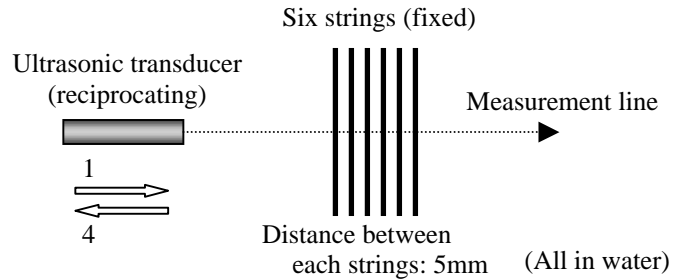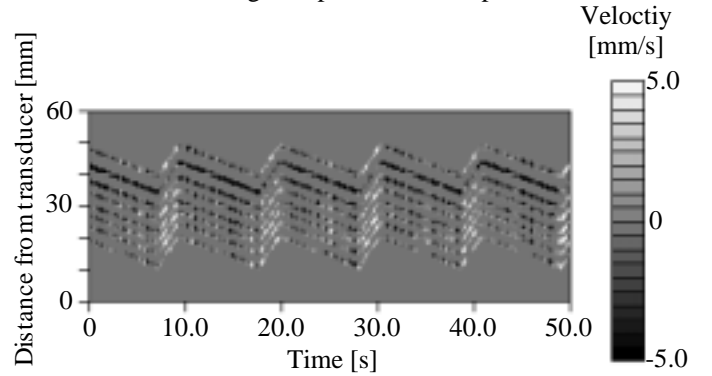

Fig.5 Experimental setup
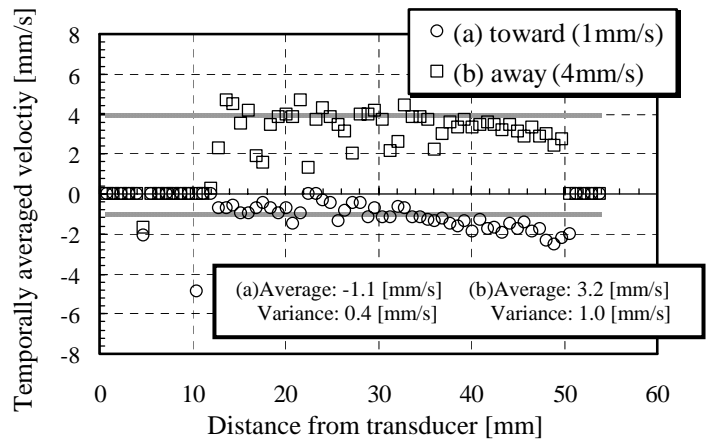

Fig.6 Veloity color map

Fig.7 Temporally averaged velocity profile and its positional average and variance

When the transducer moves toward strings, velocity is positive, otherwise negative. In Fig.6, six lines drawn zigzag are identified with six strings. This proves that UVP with new algorithm measure velocity at correct position. Fig.7 shows the averaged velocity, where the horizontal axis is distance from the transducer and the vertical axis is velocity. It is found that measured velocity corresponds to setting value. Consequently, it is confirmed that this new algorithm can measure low velocity.

2. Measurement of the flow in the rotating cylinder

As a measurement of a realistic flow, we use the flow in a rotation cylinder with 150 mm diameter. This system has theoretical solution of the flow and then often used as a verifier for UVP. Fig.8 shows the experimental setup as looking downward. The cylinder filled with water suspended tracer particles is rotating with stationary angular velocity ω. Just after the beginning of rotating, water starts to move by being pulled, and as time goes by enough, water rotates as rigid body. In this time, velocity measured by UVP should be spatially and temporally constant. This is described as follows. A distance between the measurement line and the central axis on the horizontal section of the cylinder is a, now $a = 22$ mm. A circumferential velocity v_θ at a certain position on the measurement line is described by using a and θ as shown in Fig.8 and as following equation.

$$v_\theta = \frac{a\omega}{\cos\theta}$$

Because the velocity measured by UVP is the component of the measurement line, theoretically expected velocity u_m becomes,

$$u_m = v_\theta \cos\theta$$
$$= a\omega$$

u_m is constant at any positions on the measurement line.

Table 2 shows ω and u_m in each cases, where negative ω means reverse rotation. Fig.9 shows the results of temporally averaged velocity profile with each condition, where the horizontal axis is the distance from transducer and the vertical axis is averaged velocity with 2000 time steps. It is found that velocity value well corresponds to u_m.

Table 2 Angular velocity ω and expected velocity u_m

	(a)	(b)	(c)	(d)
ω [rad/s]	3.9	-3.9	1.1	-1.1
u_m [mm/s]	86	-86	24	-24

These two averaged velocity profile shown in Fig.7 and Fig.9 indicates possibility for low velocity measurement. But, there is a fluctuation in instantaneous velocity profile. It is thought that this error of measurement is caused by poverty of particles in measurement volume. It is a common problem for any UVP algorithm. Particularly, it is a serious problem for this new algorithm. Because it requires that form of two waves of echo correspond, the deformation of the echo may affect the deformation of velocity directly. So, seeding particles needs to be paid close attention. And there is still room for improvement in the algorithm.

CONCLUDING REMARKS

The new UVP algorithm, Phase different method, is suggested in this study. It has no theoretical limit of measurable minimum velocity unlike exiting algorithm. By this reason, it is available and suitable for low velocity measurement. Two verification experiments confirm its possibility. And these also expose its problem. It is essential that the precision is improved, in order to measure low velocity.

REFERENCES

1. Y.Takeda, 1995, Instantaneous Velocity Profile Measurement by Ultrasonic Doppler Method, *JSME International Journal*, *series B*, Vol. 38, No.1, pp.8-16.

2. Y.Ozaki, T.Kawaguchi, Y.Takeda, K.Hishida and M.Maeda, 2001, High Time Resolution Ultrasonic Velocity Profiler, *Experimental Heat Transfer, Fluid Mechanics, and Thermodynamics*, pp.1177-1182.

3. Y.Sato, M.Mori, Y.Takeda, K.Hishida and M.Maeda, 2002, Signal Processing for Advanced Correlation Ultrasonic Velocity Profiler, Third International Symposium on Ultrasonic Doppler Methods for Fluid Mechanics and Fluid Engineering, pp.1-7.
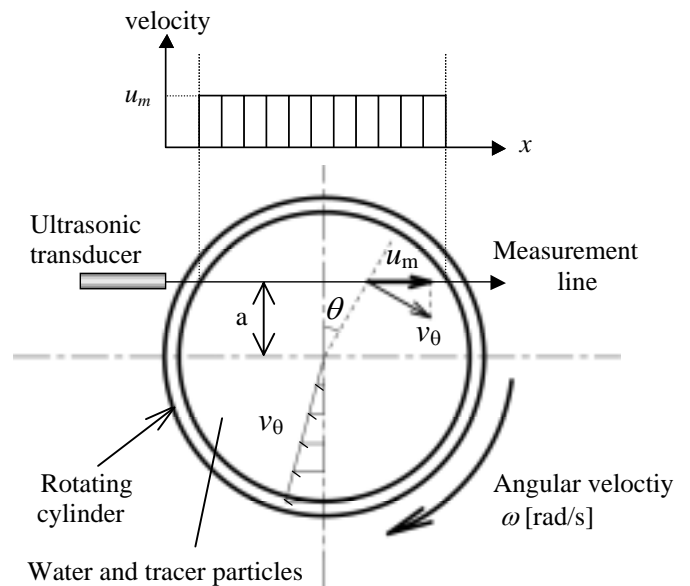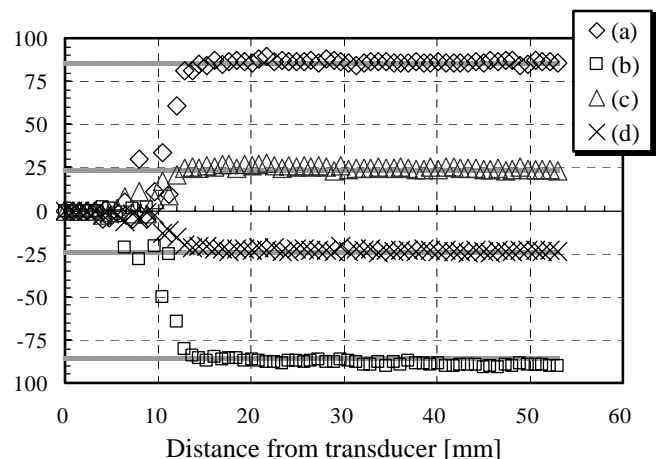
Fig.8 Experimental setup

Fig.9 Temporally averaged velocity proifle at four diffrent conditions as shown in Table 2

FUNDAMENTAL STUDY FOR DEVELOPMENT OF VECTOR-UVP
ー (1) CONCEPT AND TIME INFOMATION ー

Hironari Ohbayashi, Yasushi Takeda, Kouhei Yamaguchi

Laboratory of Flow Control, Division of Mechanical Science, Hokkaido University
Kita-13, Nishi-8, Kita-ku, Sapporo,
E-mail oobayashi@ring-me.eng.hokudai.ac.jp

ABSTRACT

The velocity vector of fluid is expressed by functions for three velocity components to three directions of space and time. Therefore, in order to investigate the flow structure, it is essential to measure these components. We propose the new system that enables us to measure three-dimensional velocity vector measurement of the flow field; named Vector-UVP. It consists of a central emitter, symmetrically surrounded by three receivers. If the plane transducer is used for the emitter, the ultrasonic beam will diverge in the practical range, and consequently a measurement volume will become too large. For the solution of this problem, and in order to simplify our system, we use a commercial focusing transducer for the emitter. Thus, the characteristic of the ultrasonic beam from the emitter has strong influence on the performance of Vector-UVP. As an initial stage of developing this system, we investigated this ultrasonic beam characteristic of the transducer to be used and the synchronous state between the emitter and the receiver by experiment. From these experimental results, it is expected that the spatial resolution of our equipment becomes very high compared with other conventional system. Additionally, the anticipative specification of Vector-UVP was presented.

Keywords: UVP, velocity vector measurement, spatio-temporal

Introduction

Ultrasonic Velocity Profiler (UVP) has been established in experimental study in fluid dynamics and engineering applications of flow measurement. The objective of this study is development of advanced UVP system;vector-UVP.It enables us to obtain vector field of the fluid flow on a line.

As is shown in the Eq.(1), the velocity vector field of fluid is expressed by three functions of the velocity components (u,v,w) as a function of space and time (t).

$$\boldsymbol{u} = \boldsymbol{u}(\boldsymbol{x}, \ t) \qquad (1)$$

Therefore, in order to investigate the flow structure, it is essential to measure these components in space and time. UVP is the method that enables us to obtain spatio-temporal information on the flow field; the first time on such a type of data format for experimental fluid flow investigations. It is, however, one-dimensional in spatial coordinate. On the other hand, PIV and PTV give two or three dimensional vector velocity information, but acquisition of time series data is difficult for PIV because of the performance which equipment has. On the other hand, acquisition of time series data is still difficult. (see. Table1.) The purpose of the present development is to overcome this disadvantage of the conventional UVP by expanding the dimension velocity vector to be measured.

An idea and concept of vector-UVP has been attempted earlier by U.Lemmin [1-4] for civil engineering study. Its concept is illustrated in Fig.1 and 2.

Table.1 The measurable dimension

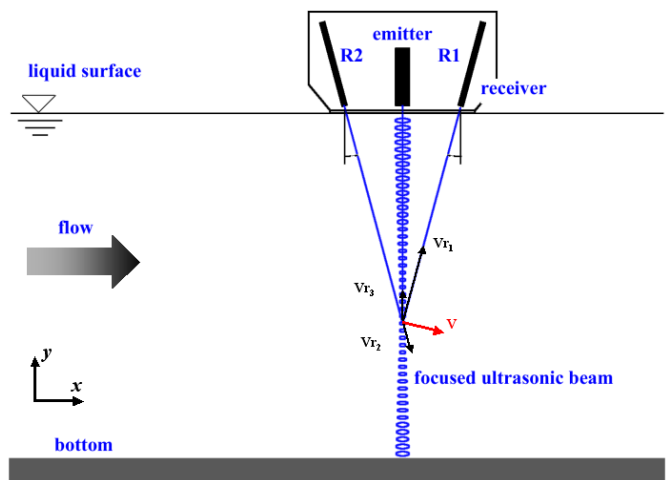|	*u*	*x*	time series
UVP	1	1	○
Vector-UVP	3	1	○
PIV / PTV	2	2	△
Stereo PIV / PTV	3	2	△

Fig.1 Illustration of Vector-UVP

It consists of a central emitter, symmetrically surrounded by three receivers, R1 to R3. (only two are visible in Fig.1) An ultrasonic pulse is emitted into fluid from the emitter, and the

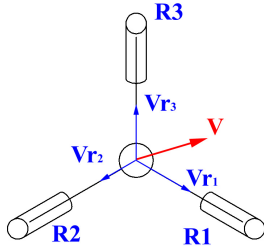surrounding receiver receives the echo reflected from tracer particles.

Fig.2 Upper surface of Vector-UVP

As illustrated, a position information to be obtained is from a flight path $x + x'$. (see. Fig.3) By analyzing these received echo waves, three directional velocity components can be obtained in the same manner as in the conventional UVP for each receivers and three-dimensional velocity vector can be formed. Since these receivers have a certain spatial range of receivable area, it can receive the echo from each point on the ultrasonic beam in this range. Therefore, this system can obtain the profile of the three-dimensional velocity vector on the ultrasonic beam.
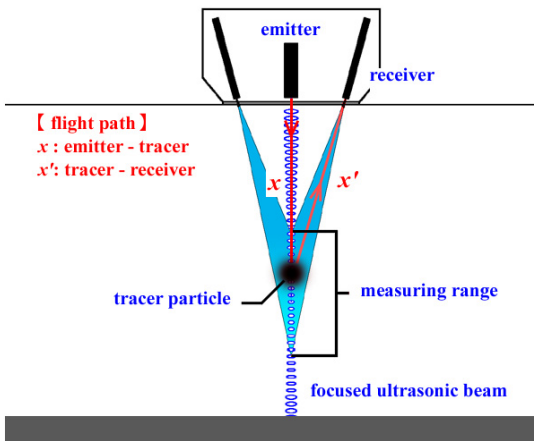
Fig.3 flight path of Vector-UVP

Divergence of the ultrasonic beam

Since ultrasonic beam does not have high coherency like the laser beam, the beam cannot avoid having a significant divergence in the practical range. The divergence of ultrasonic beam is shown in Fig.4
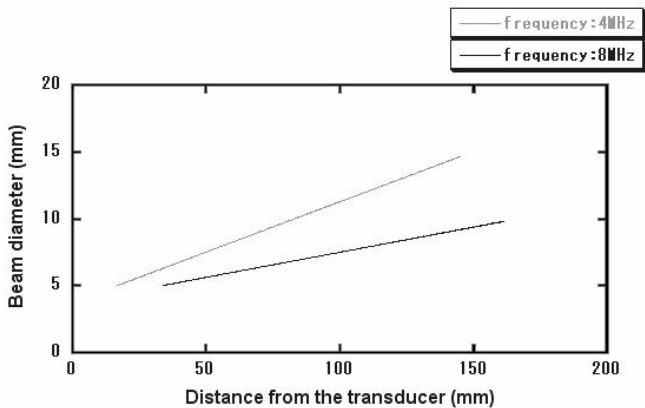
Fig.4 Divergence of the ultrasonic beam
;underwater, active diameter:5[mm]

For instance, a standard transducer for the conventional UVP (basic frequency: 4 [MHz]) has a beam divergence of 4°. Consequently, the diameter of ultrasonic beam is 10.2 [mm] in the position that distance from a transducer is 100 [mm]. This means that the measurement volume is too large for general fluid dynamical investigation. For solving this problem, Lemmin and others used "phased-array transducer system" in their equipment [1] to narrow the beam. However, this system is very complex and too expensive. Furthermore, the spatial resolution of their equipment is not high enough when turbulent flow is to be measured.

In order to simplify our system, we use a commercial focusing transducer for the emitter. This transducer can focus the ultrasonic beam by setting a concave lens on the transmitter front surface as shown in Fig.5. (r = curvature radius, Zt = focal length)
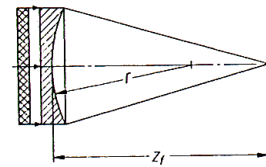
Fig.5 Focusing technique (with the spherically curved lens)

The ultrasonic beam emitted from the plane radiator is focused by being refracted with the spherical lens attached at the tip of the radiator. Vector-UVP uses only the optimal range near the focal point of the ultrasonic beam. By this method, it is expected that spatial resolution of our system is fully applicable to measurement of turbulent flow.

Measurement of the ultrasonic beam characteristic

The characteristic of the ultrasonic beam from the emitter has an essential influence on the performance of Vector-UVP. In the initial stage of development of our system, the characteristic of the ultrasonic beam from the emitter was checked by experiment. The specification of the focusing transducer used for the experiment is shown in Table 2. The experimental set-up is shown in Fig.6. Under a continuous beam operation, the sound field was measured using a needle hydrophone (Toray engineering, NH8028, active diameter 0.5 [mm]). The received signal was observed using a spectrum analyzer to record a sound pressure. The measured field spans from 0.5 to 40 [mm] to x-direction and −10 to +10 [mm] to y-direction. The interval of each grid was set to dx = 0.5 [mm] and dy = 0.5 [mm].
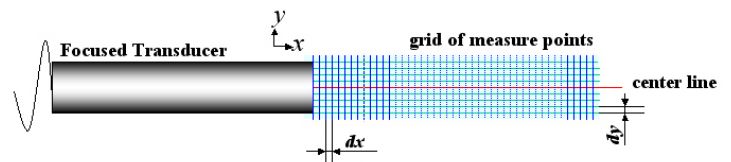

Fig.6 Experimental set-up for ultrasonic beam measurement

Table.2 Specification of the focused transducer
; Imasonic : TF8-7-10

frequency[MHz]	active diameter[mm]	curvature[mm]
8	7	30

The result of the acoustic field of the focusing transducer is shown in Fig. 7. The horizontal axis of this figure shows the

distance from the transducer, and a vertical axis is a transversal distance (y) normalized by the active diameter of the transducer (D). The color map shows the measured sound pressure. This figure shows that an ultrasonic beam is focused in the range of x =20.0 to 30.0 [mm]. The crack of the spherical lens has caused the deficit of an ultrasonic beam in the range of x = 26.0 to 28.5 [mm].
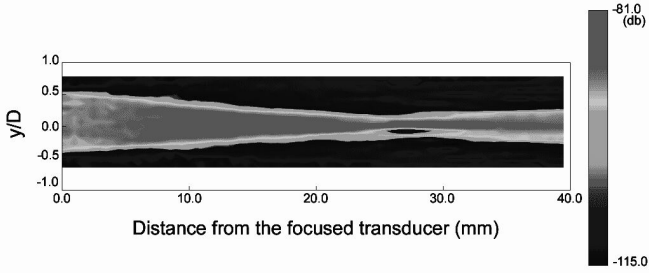

Fig.7 Ultrasonic beam of the focused transducer

In order to determine the range of the ultrasonic beam used for measurement the diameter of the beam is determined by following method. Fig. 8 is one data in the section of x = 12.5 [mm]. Each circle shows the intensity of the ultrasound beam measured in this experiment. The solid curve was drawn with the gauss function fitted to these data, and the diameter of the beam was determined as a FWHM of the peak. This result is shown in Fig. 9. The ultrasonic beam is focused to the minimum in the section of x = 25 [mm]. For realization of high special resolution, we determine the measurement range based on the diameter of the ultrasonic beam. When the diameter of the beam is set as less than 1 [mm], the range of x = 19.5 to 32.5 [mm] could be used for measurement. For 1.5 [mm] or less, x = 14.5 to 36.0 [mm] could be used. This measurable range is one example and it is also possible to measure a range larger than this value.
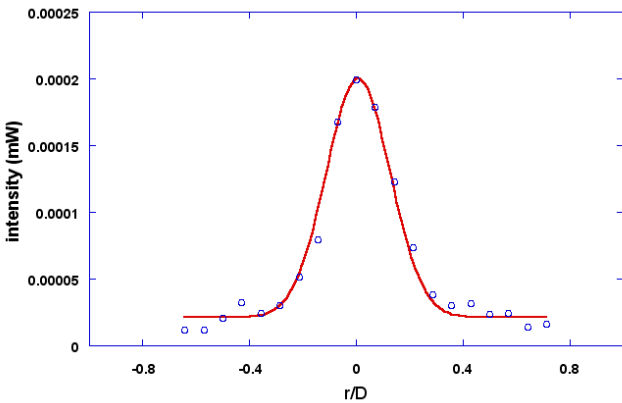
Fig.8 Determination of the ultrasonic beam diameter
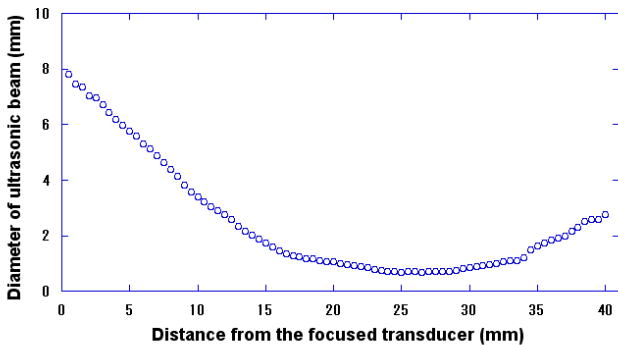
Fig.9 Ultrasonic beam diameter of the focused transducer

Synchronization and Time information

In Vector-UVP, for realization of the vector measurement that used single emitter and three receivers, it is necessary to obtain time synchronization among them. The synchronization was verified by the experiment shown in Fig.8. For simplification, single receiver is used in this experiment.
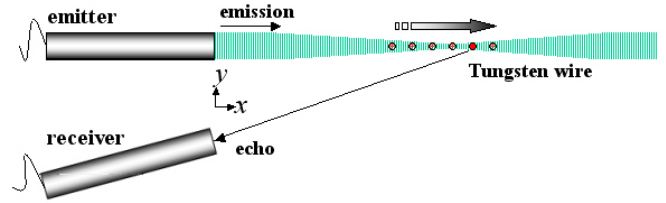

Fig.10 The experimental set up for verification of Synchronization

The emitter and the receiver have been arranged as shown in Fig. 10, and the tungsten wire as a reflector was installed near the focusing point of the ultrasonic beam. The receiver was leaned is set with opening angle of 41˚. The wire is moved only in the direction of x. The emitter emits an ultrasonic pulse, and the digital oscilloscope measures the flight time (t) that the receiver receives the echo from a wire. The flight time of the echo in each measurement points on the focusing ultrasonic beam are measured.
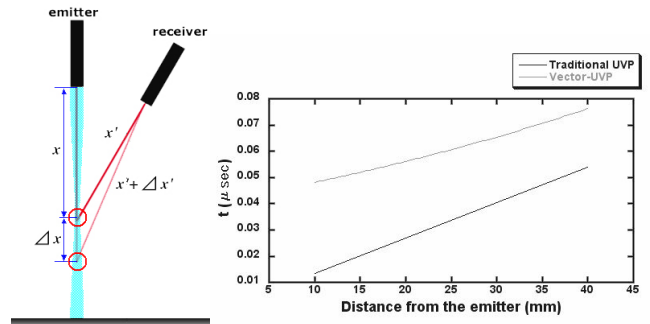

Fig.11 The configuration and flight time of ultrasonic pulse

In the Conventional UVP single transducer performs emission and reception of an ultrasonic pulse, and the flight time of an ultrasonic pulse (t_1) increases linearly in proportion to the distance from the transducer (x). When a measuring point is installed on a measurement line at equal intervals, the gap of the flight time ($\triangle t_1$) between a measuring point and the next point is constant. (c is ultrasonic speed.)

$$2x = ct_1 \qquad (2)$$

$$t_1 = const \qquad (3)$$

However in Vector-UVP, as its configuration is shown in Fig. 11, the relation between the flight time (t_2) and the distance from the transducer to a measuring point is expressed by Eq.(4).

$$x + x' = ct_2 \qquad (4)$$

$$t_2 \neq const \qquad (5)$$

As shown in Fig. 12, x' increases gradually even if $\triangle x$ is fixed, the gap of the flight time increases. Therefore, when analyzing the received signals, it is necessary to take this time information into consideration.
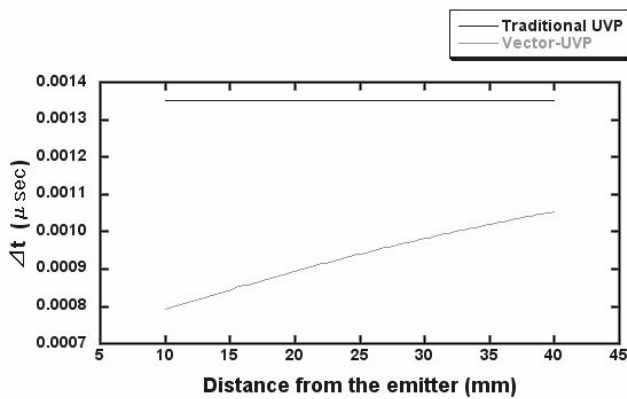
Fig.12 The gap of the flight time

This experiment gives us the theoretical and the measured value. The result could estimate the synchronous state of our system, and the reliability of the received echo. The result of this experiment is shown in Fig. 13.
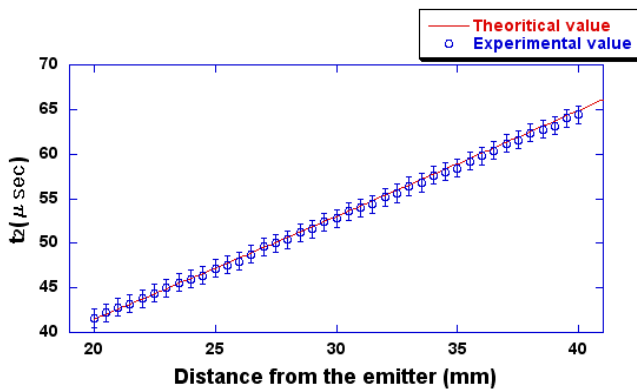

Fig.13 Result of the flight time measurement

The measured flight time agrees well with theoretical values. Time difference of these data is 0.23 [μ sec] at the maximum. It is 0.34 [mm] when it converts into distance. This value is within the range of special resolution that Vector-UVP will have in future.

In Pulse Doppler method, if channel distance and measuring depth are decided, a certain specification can be determined. The length of an ultrasonic pulse determines the spatial resolution of the direction of an x-axis. In our system, it is estimated that pulse length and the diameter of ultrasonic beam is equal. Finally, the anticipative specification of the vector-UVP based on these experiments is shown in Table.3. The algorithm for velocity calculation uses Pulse Doppler method and Number of profile measurement repetitions is 32. Inspection fluid is water and the basic frequency of emitter is 8 [MHz].

Conclusion

In this report, we introduced about the initial stage of development of Vector-UVP. The following points have been verified in this investigation.

- The optimal range of the focused ultrasonic beam that can be used.
- Reliability of the flight time of the received echo.
- The synchronization of our system.

Table. 3 Anticipative specification of Vector-UVP

Ultrasonic beam diameter [mm]	$\leqq 1.0$	$\leqq 1.5$
Optimal range [mm]	13	21.5
Number of cycle per pulse	4	8
Number of channels	17	14
Pulse repetition frequency [kHz]	18	17
Maximum measurable depth [mm]	52.5	100
Maximum measurable velocity [mm/sec]	825	770
Scanning time [μ sec]	74	134
Spatial resolution [mm]	0.74	1.48
Velocity resolution [mm/sec]	4.92	2.72
Time resolution [msec]	2.37	4.28

REFERENCES

1. D. Hurther, U. Lemmin, 1998, "A constant-beam-width transducer for 3D Acoustic Doppler Profile measurements in open-channel flows", Meas. Sci. technol 9, pp.1706-1714.

2. C. Shen, U.Lemmin, 1997, "A two-dimensional acoustic sediment flux profiler", Meas. Sci. technol 8, pp.880-884.

3. U.Lemmin, 2002, "Keynote lecture high resolution 3-D Acoustic Doppler Velocity and sediment flux profiling in laboratory and environment studies: potential and limits", Third ISUD for fluid mechanics and fluid engineering (EPFL), pp.145.

4. K.Blanckaert, 2002, "Analysis of coherent flow structures in a bend based on instantaneous-velocity profiling", Third ISUD for fluid mechanics and fluid engineering (EPFL), pp.51-58.

5. A.Kurniawan, Mustafa S. Altinakar, 2002, "Velocity and turbulence measurements in a scour hole using an Acoustic Doppler Velocity Profiler", Third ISUD for fluid mechanics and fluid engineering (EPFL), pp.51-58.

6. Y.Takeda, 1995, "Instantaneous Velocity Profiler Measurement by Ultrasonic Doppler Method", JSME International Journal, Series B, Vol.38, No.1, pp8-16.]-

7. Y.Sato, M.Mori, T.Takeda, K.Hishida, M.Maeda, 2002, "Signal processing for advanced correlation Ultrasonic velocity profiler", Third ISUD for fluid mechanics and fluid engineering (EPFL), pp.5-11.

INFLUENCE OF CHAIN-LIKE CLUSTERS ON OSCILLATING PIPE FLOW OF A MAGNETIC FLUID

Takashi In-nami*, Yuki Oshikawa**, Ryo Hasegawa*, Tatsuo Sawada*

*Dept. of Mech. Eng., Keio University, 3-14-1 Hiyoshi, Kohoku-ku, Yokohama 223-8522, Japan
E-mail: sawada@mech.keio.ac.jp
** Imaging System Division, Ricoh Corporation, 1-3-6 Nakabakomi, Ota-ku, Tokyo 143-8555, Japan

ABSTRACT

The Ultrasonic Velocity Profile (UVP) method is used to sense velocity information using ultrasonic waves, and, as such, is very suitable for measuring the velocity profile of opaque fluids. In this experiment, the UVP method is used to investigate oscillating pipe flow of a magnetic fluid subject to a magnetic fluid. The test liquid is a diluted water-based magnetic fluid and the magnetic field is applied by two permanent magnets. When the magnetic field is applied for some period before measurement, interesting velocity profiles are obtained and are suggested to be caused by the growth of chain-like clusters in the magnetic fluid. The influence of the amount of time of pre-applying the magnetic field and magnetic field intensity on flow behaviors are discussed. The apparent flow rate is introduced to aid in evaluating the correlation between the velocity profile and the growth of chain-like clusters. It is found that the rate of change of the apparent flow rate increases with both magnetic field the pre-application time and magnetic field intensity.

Keywords: Magnetic Fluid, Oscillating Pipe Flow, UVP, Clusters

INTRODUCTION

A magnetic fluid is a stable colloidal suspension of uniformly dispersed ferromagnetic particles in solvents such as water and kerosene. The ferromagnetic particles remain suspended because of their Brownian motion. When a magnetic field is applied to a magnetic fluid, several interesting phenomena, which do not occur in a Newtonian fluid, are observed because of the combination of strong magnetism and liquidity. Several unusual flow behaviors of a magnetic fluid have been observed and they are considered to be caused by the formation of chain-like clusters. To date there have been few experimental studies directed to clarifying the influence of these clusters on magnetic fluid flow behavior. In order to use magnetic fluids in fluid mechanical systems, for example as a magnetic fluid damper, a magnetic fluid actuator, etc., a more-detailed measurement of internal velocity profiles is necessary. It is expected that further applications will be developed by further examining these phenomena in a magnetic fluid.

The Ultrasonic Velocity Profile (UVP) method, which was been developed by Takeda[1], is a method of measuring a velocity profile on a line with respect to the velocity component along an ultrasonic beam. This technique has two main advantages in comparison with ordinal methods like LDV or PIV. First, it can be applied to opaque fluids such as liquid metals, chocolate in food processing, and the like, and second, flow mapping is practical because a line measurement is used. Takeda has studied a mercury flow[2] and has developed this method systematically[3]. Kikura, et al.[4] measured velocity profile of the Taylor vortex flow of a magnetic fluid using the UVP method. Sawada, et al.[5]

examined horizontal velocity profiles of a magnetic fluid in a rectangular container which was laterally vibrated. These experimental studies have shown the efficiency of the UVP method for velocity profile measurement of opaque fluids, including magnetic fluid.

In the present paper, we examine the characteristics of the velocity profile of oscillating pipe flow of a magnetic fluid subject to a magnetic field. In particular, the effect of chain-like cluster formation in a magnetic fluid on the velocity profile is experimentally investigated using the UVP method.

EXPERIMENT

Figure 1 shows the experimental apparatus. The test section is an acrylic pipe having inner diameter 30 mm, outer diameter 40 mm and length 3000 mm. One end of the pipe is connected to a tank (300 mm × 300 mm × 300 mm), which is at 540 mm height from the center of the pipe. The water pressure is controlled to fluctuate less than 1 % . The other end of the pipe is provided with a piston which is driven by a crank system to cause oscillating flow. The piston frequency is controlled by an inverter. A water-based magnetic fluid W-40 is used as a test liquid. The ratio of the volume of the magnetic fluid to water is 7 : 3. The kinematic viscosity is $\nu = 4.35$ mm^2/s and the sound velocity in the magnetic fluid is $c = 1420$ m/s at 20 °C.

The UVP monitor is a model XW-PSi manufactured by Met-Flow SA. The basic ulutrasound frequency is 4MHz. In order to obtain an echo, porous SiO_2 particles with a mean diamiter of 0.9 μm (MSF-10M, Liquidgas Co., Ltd.) were added as reflectors. A transducer is fixed on the outer wall of the pipe at an angle of 14° and a measurement line from the transducer is parallel to two magnets (described in Fig.2). The diameter of the transducer is 5 mm, and the measuring volume has a thin-disc shape, $\phi\, 5$ mm $\times\, 0.71$ mm.
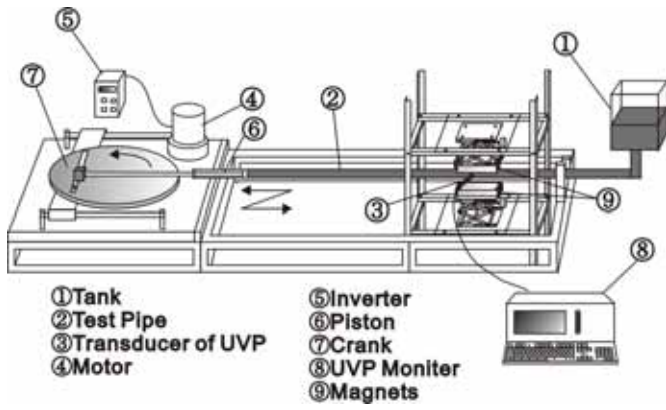
Fig.1 Experimental apparatus

① Tank
② Test Pipe
③ Transducer of UVP
④ Motor
⑤ Inverter
⑥ Piston
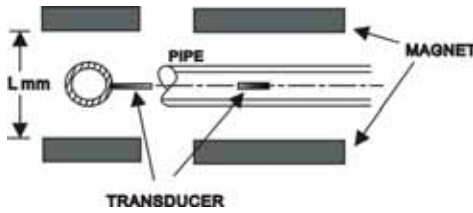⑦ Crank
⑧ UVP Moniter
⑨ Magnets
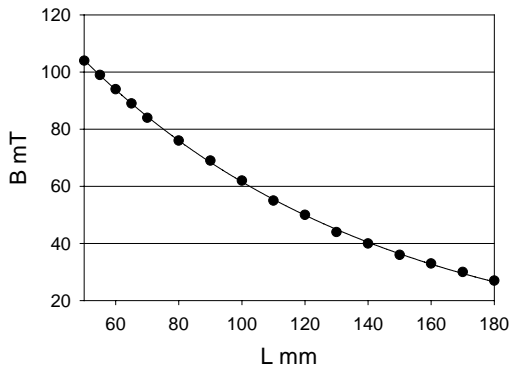

Fig.2 Close-up of permanent magnets

Fig.3 Magnetic flux density vs. interval between magnets

Two permanent magnets (150 mm × 100 mm × 25 mm) are placed on opposite sides of the pipe as shown in Fig. 2. The magnetic field intensity in the pipe can be controlled by the interval between the two magnets. The relation between magnetic flux density and interval L of the magnets is shown in Fig. 3. Here B is the magnitic flux density at the center of the pipe.

The piston frequency is kept at 0.053 Hz and Wormersley number $W = 4.2$ which is defined by

$$W = R\sqrt{\frac{\omega}{\nu}} \qquad (1)$$
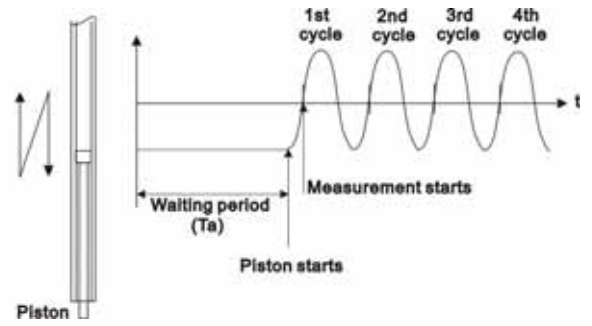
Fig.4 Measurement time chart

where R is radius of the pipe and ω is angelar velocity of the piston. The Wormersley number is an important dimensionless parameter for an oscillating flow and indicates the ratio of unsteady inertia and viscosity forces.

RESULTS AND DISCUSSION

In the experiments, a magnetic field is applied prior to the measurement of velocity profiles as shown in Fig. 4. Since the magnetic field is applied parallel to the pipe for Ta minutes before measurement begins, chain-like clusters have an opportunity to form in the direction of the magnetic field lines. After Ta minutes an oscillating flow is generated by the piston, and changes in velocity profiles are observed. The observed changes were quite remarkable and, can not be explained by an increase of the apparent viscosity owing to the magnetic field.

Figure 5 shows velocity profiles for different times of pre-applying the magnetic field: $Ta = 0$ min, 45 min, 90 min at the same magnetic flux density $B = 62$ mT. Here $v*$ and $r*$ are defined by

$$v* = \frac{v}{r_k\omega}, \qquad r* = \frac{r}{R} \qquad (2)$$

where r_k is the radius of the crank and $r_k = 100$ mm. ϕ corresponds to the phase difference from the middle point of top and bottom dead points. $r* = -1$ indicates the side wall where the transducer is fixed and $r* = 1$ indicates the opposite side wall. Figure 6 shows changes of the velocity profiles for various Ta at each phase. From Figs. 5 and 6, it appears that velocities at each phase approach zero near the center of the pipe with an increase of Ta. We also found that after several cycles, the singular velocity profiles shown in Fig. 5 (b)-(c) become the ordinary velocity profile (of Fig .5 (a)). Figure 7 shows the process of returning to a stable velocity profile for $B = 62$ mT, $Ta = 180$ min and $\phi = \pi$. From these figures, it is suggested that the size of the chain-like clusters grows gradually larger near the pipe wall and spreads in a cross-section of the pipe. This process is illustrated in Fig. 8. If chain-like clusters grow toward the center area of the pipe, the magnetic fluid may be prevented from flowing by the chain-like clusters. These chain-like clusters may then collapse gradually after the beginning of the oscillating flow.
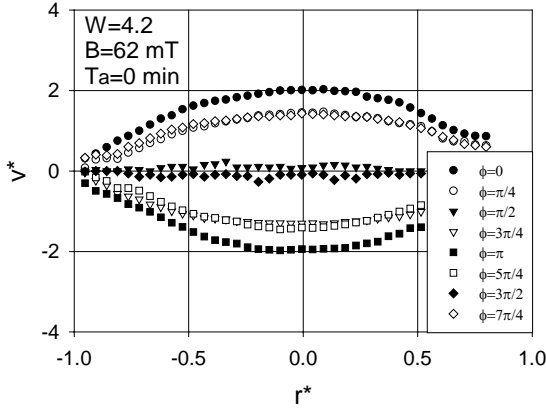
(a)
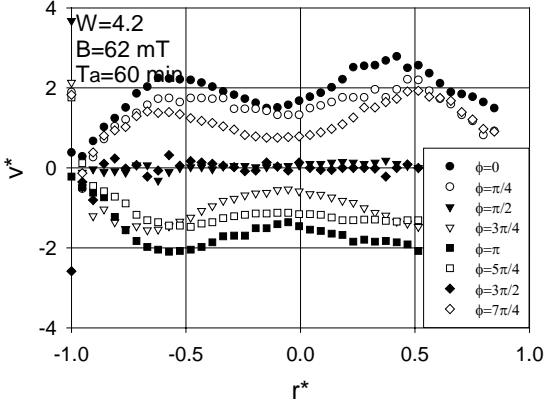
(b)
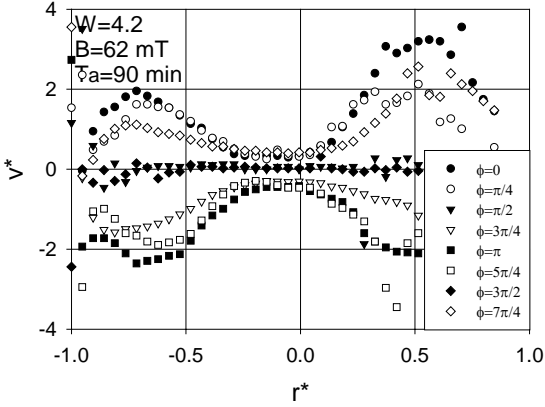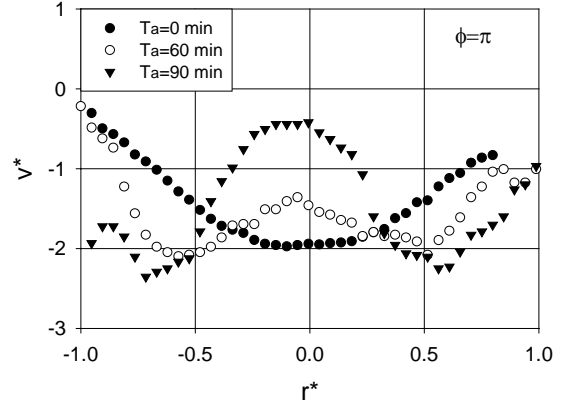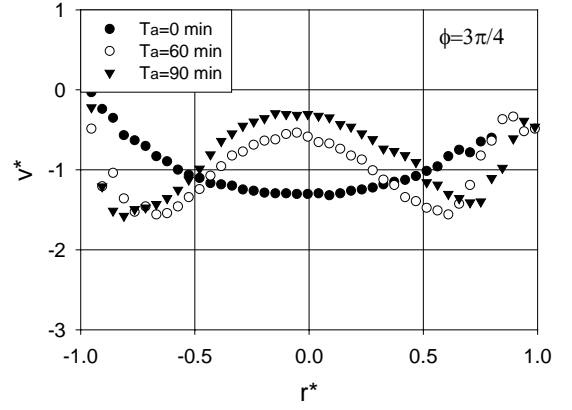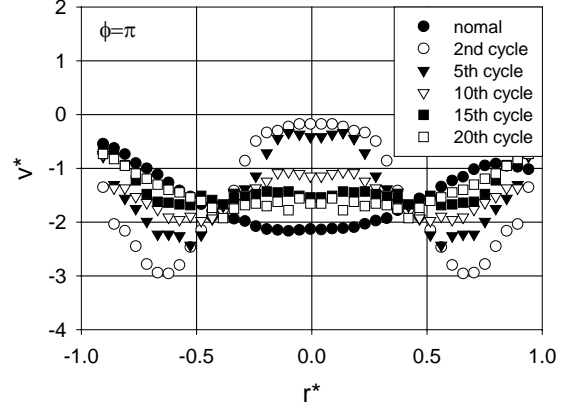

(c)

Fig.5 Velocity profiles with pre-applied magnetic field

Fig.6 Velocity profiles at two phases

Fig.7 Process of returning to stable velocity profile
($W = 4.2$, $B = 62$ mT, $Ta = 180$ min)

In order to examine the influence of the growth of chain-like clusters on the change of velocity profiles, we introduce the chage rate of the apparent flow rate (ΔQ) as follows:

$$Q_\phi{}^* = 2\int_0^1 \left| v_\phi{}^* \right| dr^* \tag{3}$$

$$Q^* = (Q_0{}^* + Q_{\pi/4}{}^* + Q_{3\pi/4}{}^* + Q_\pi{}^* + Q_{5\pi/4}{}^* + Q_{7\pi/4}{}^*) \tag{4}$$

$$\Delta Q^* = (Q^*{}_{B\,\text{mT},\,Ta\,\text{min}} - Q^*{}_{0\,\text{mT},\,0\,\text{min}}) / Q^*{}_{0\,\text{mT},\,0\,\text{min}} \tag{5}$$

Here $Q_\phi{}^*$ is an apparent flow rate at each phase, which is obtained by integrating the absolute velocity along the measuring line, i.e. the horizontal center line in Fig. 8. Q^* is the sum of apparent flow rates. When the magnetic field is applied, Q^* becomes larger in accordance with the growth of chain-like clusters. ΔQ^* is the change rate of Q^* when a magnetic field is pre-applied.

Figures 9 and 10 show the relationsip between ΔQ^* and Ta, and ΔQ^* and B, respectively. From Fig. 9, it can be seen that when Ta increases, ΔQ^* also increases in a linear fashion. Further, ΔQ^* is larger under strong magnetic fields than under
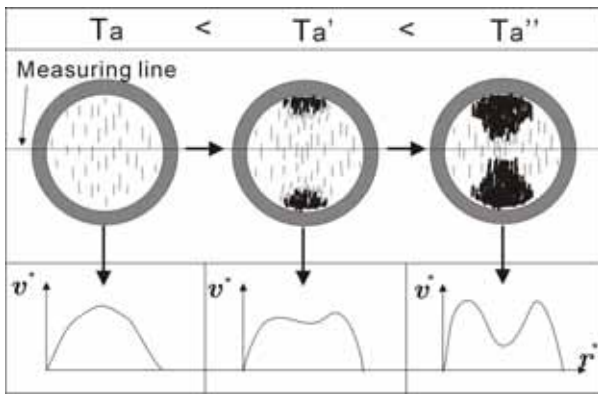
Fig. 8 Growth of the chain-like clusters

Fig. 9 Increase in change rate of the apparent flow rate with *Ta*

weak magnetic fields. From Fig. 10, it can be seen that, when the magnetic field intensity increases, ΔQ^* has a tends to grow larger. Further, ΔQ^* is larger for longer *Ta*. It is suggested that an increase of ΔQ^* has some correlation with the growth of the chain-like clusters, and the growth of the chain-like clusters depends on the amount of the times of pre-applying the magnetic field and the magnetic field intensity.

CONCLUDING REMARKS

Magnetic fluids show more complicated behaviors than ordinary fluids because of the formation of chain-like clusters when the magnetic fluid is subject to a magnetic field. We observed a unique phenomenon of the velocity profile of an oscillating pipe flow subject to pre-application of a magnetic field that might be caused by the chain-like clusters. This lead to a study of the growth of the chain-like clusters by using the velocity profile measured by the UVP method. As a results, we observed that individual velocity profiles had some correlation with the amount of time the magnetic field was pre-applied before taking measurements. These individual velocity profiles appeared to be dependent on the magnetic field intensity as well as the amount of time pre-applying the magnetic field. The apparent flow rate was introduced to evaluate a correlation between changes in the velocity profile and the growth of chain-like clusters. It was clarified that the rate of change of the apparent flow rate increases with increases in the amount of time pre-applying the magnetic field and with the magnetic field intensity.
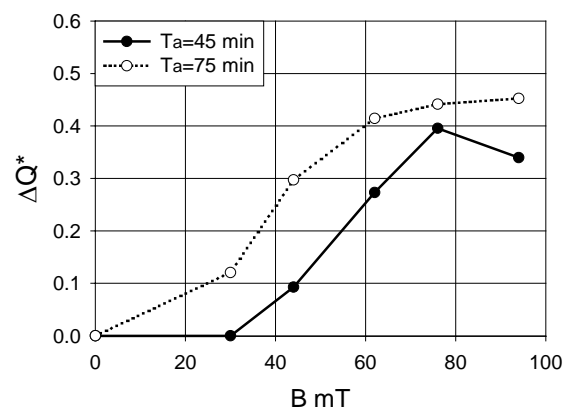

Fig. 10 Increase in change rate of the apparent flow rate with *B*

REFERENCES

1. Takeda, Y., 1986, Velocity Profile Measurement by Ultrasound Doppler Shift Method, *Int. J. Heat Fluid Flow*, 7, pp.313-318.

2. Takeda, Y., 1987, Measurement of Velocity Profile of Mercury Flow by Ultrasound Doppler Shift Method, *Nucl. Technol*, 79, pp.120-124.

3. Takeda, Y., 1995, Velocity Profile Measurement by Ultrasonic Doppler Method, *Exp. Therm. Fluid Sci.*, 10, pp.444-453.

4. Kikura, H., Takeda, Y. and Durst, F., 1999, Velocity Profile Measurement of Taylor Vortex Flow of a Magnetic Fluid Using the Ultrasonic Doppler Method, *Exp. Fluids*, 26, pp.208-214

5. Sawada, T., Kikura, H. and Tanahashi, T., 1999, Kinematic Characteristics of Magnetic Fluid Sloshing in a Rectangular Container subject to Non-Uniform Magnetic Fields, *Exp. Fluids*, 26, pp.215-221.

VELOCITY MEASUREMENT AROUND A LARGE BUBBLE RISING IN STAGNANT WATER IN A ROUND PIPE USING THE UVP

Hisato Minagawa*, Masaya Ibuki**, Satoshi Yamada***, Yoichi Shiomi****

* Department of Mechanical Systems Engineering, The University of Shiga Prefecture,
2500 Hassaka, Hikone, Shiga 522-8533, JAPAN, E-mail: minagawa@mech.usp.ac.jp
** Dainippon Screen MFG Co. Ltd., Tenjinkita-cho 1-1, Teranouchi-agaru
4-chome, Horikawa-dori, Kamigyo-ku, Kyoto 602-8585, JAPAN
***Engineering Graduate School, The University of Shiga Prefecture,
2500 Hassaka, Hikone, Shiga 522-8533, JAPAN, E-mail: satoshi@cont4.mech.usp.ac.jp
**** Department of Mechanical Systems Engineering, Ryukoku University,
1-5 Yokotani, Seta Oe-cho, Otsu, Shiga 520-2194, JAPAN, E-mail: shiomi@rins.ryukoku.ac.jp

ABSTRACT

A UVP measurement was performed to obtain the liquid velocity field in front of, around and behind the large bubble rising in stagnant water in a round pipe of D=54mm in order to get basic information for the gas-liquid two-phase slug flows. It is also useful if we can establish the measuring technique of the subject by a more convenient but precise measuring technique. Two ultrasonic transducers were used simultaneously for the measurement to get velocity vectors. The measured results are presented and compared with some existing studies on the corresponding phenomena. In the liquid film near the bubble nose, velocity profile and acceleration are presented and compared with existing studies. The different in D may affect some features. The parameter z/D is found more dominant than z for this phenomenon. In the liquid phase behind the bubble tail or the wake region, a large ring vortex is recognized without another weaker vortex behind it. The upward velocity near the pipe axis agrees well with the predicted results by an existing prediction.

Keywords: Large Bubble, Multiphase flow, Velocity Vector, Vortex, Wake, Velocity Profile, UVP

INTRODUCTION

Gas-liquid two-phase slug flows in vertical pipes are frequently encountered in industrial pipelines, chemical and nuclear reactors and other fluid machineries. The flow is characterized by a series of bullet-shaped large bubbles or Taylor bubbles, and liquid slugs which contains small bubbles. In order to clarify the characteristics of the flow, a lot of studies have been performed [1]. The characteristics of the void fraction, the frictional pressure drop of the flow and the rising velocity of the large bubbles have been revealed considerably. The precise velocity field around the large bubbles in the slug flow, however, is not clarified so well. It is useful to know the velocity field around a large bubble rising in a stagnant liquid, which is one of the simplified forms of large bubbles in slug flows in vertical pipes. Even for the subject, few studies have been reported: for example, the measurement using photochromic dye activation method by Kawaji et al. [2] and that using PIV by van Hout et al. [3]. Tomiyama et al. [4] performed the measurements using LDV especially to clarify the flow field in the wakes behind the large bubbles.

Kawaji et al. [2] measured the velocity field around a large bubble rising through stagnant kerosene in a 25.6mm I.D. pipe. 0.01% TNSB, a photosensitive substance (photochromic dye) was dissolved beforehand and a periodic laser beam was used to expose the dye. van Hout et al.[3] measured the velocity field around a large bubble rising through stagnant water in a 25mm I.D. pipe. Polystirol particles of 20 to 40 μm diameter containing fluorescent dye were added to the water, and PIV measurements were performed with the help of Laser-Induced-

Fluorescence. Their both studies presented velocity fields around a large bubble rising through stagnant liquid and also those in the liquid lump behind the bubble or the wake region. But the effects of the pipe diameter, the large bubble length, the liquid properties, the wall wettability, the existence of small bubbles in the liquid slug and so on, on the velocity field are not quite clear. So we still need a systematic and precise data base on the flow field. Moreover, we will need the velocity field in the two-phase slug flow in future in order to investigate the flow characteristics of the flow and to model the flow more precisely.

Hence we need a more convenient but precise measuring technique to achieve this purpose. The Ultrasonic Velocity Profile monitor (UVP) is one of the candidates, because it is easy to operate once the measuring technique is fixed, it has effective time and space resolutions, and it obtains velocity vectors on a line in an instant. In this paper, the UVP measurement was performed to measure the velocity field around a large bubble rising in stagnant water filled in a round vertical pipe so as to obtain basic information to establish the measuring technique of the subject.

EXPERIMENTAL METHOD

A schematic of the experimental apparatus is shown in Fig.1. Water filled in the tank was supplied by a Mohno pump to the test section. Polyethylene particles of median diameter 160μm were used for the scattering particles. The temperature of the water was kept at 20±1°C by a regulator. When the test section
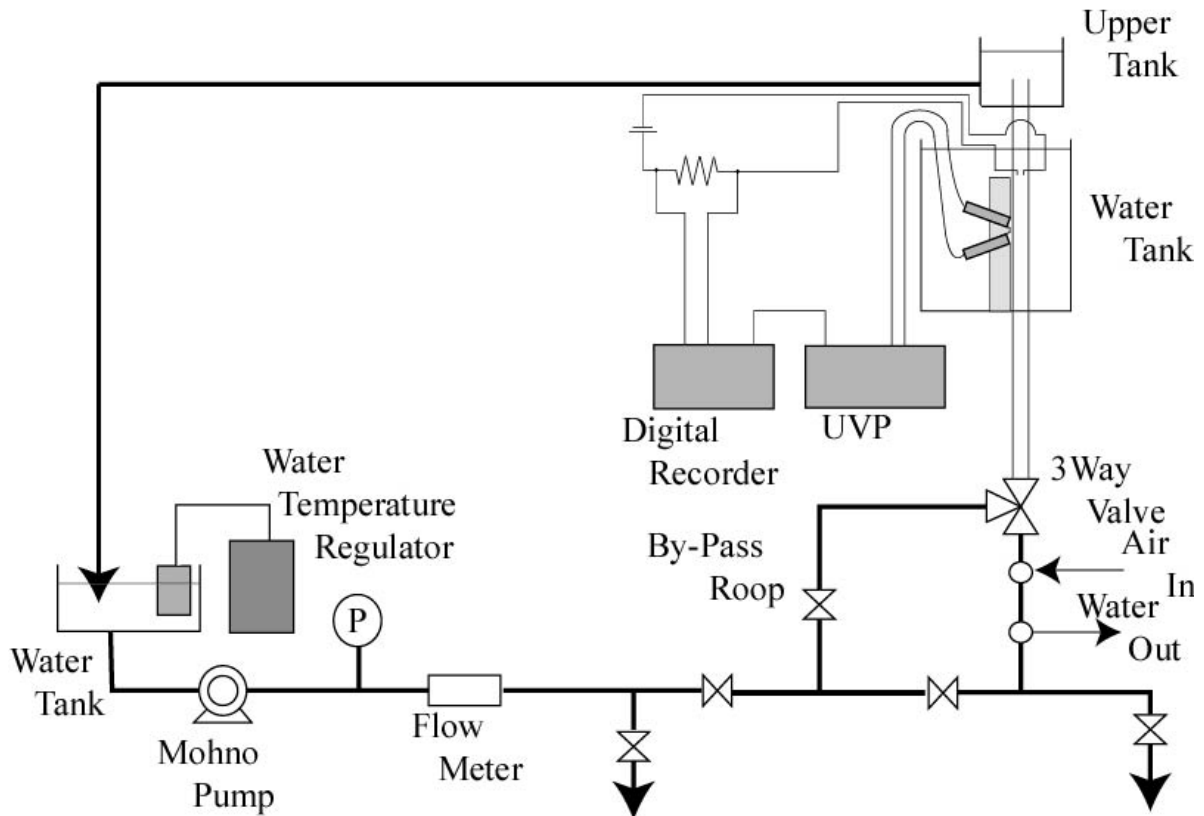
Fig.1 Experimantal Apparatus

was fully filled by the water, the pump was stopped. The valves were once closed, and air was stored in the pipe just under the 3 way valve by draining water from the pipe.

The test section was consisted of a transparent acrylic vertical round pipe of 54mm I.D. and about 3m in length. Two ultrasonic transducers of UVP (frequency: 4MHz) were set at the outside of the test section at 2.3m from the 3 way valve: one +20 degree and the other –20 degree inclined from the horizontal line as shown in Fig.2. They were set in water in a tank, whose water surface was covered with a styrene foam sheet to prevent the noise caused by the shaking water surface. The measuring frequency of UVP was 50Hz. A pair of electrode was installed in the pipe 75mm downstream of the transducers to detect the relation between time and position of the large bubble, which is denoted by the large bubble sensor. Signals from UVP and the large bubble sensor were recorded simultaneously by a digital recorder.

When all the facilities were ready, 3 way valve was quickly opened, and a large bubble rose up into the test section, and signals were recorded. Velocity field for about 30 large bubbles were measured for one air volume in this study. The averaged large bubble length was 0.225m and the averaged terminal rising velocity of the large bubbles, V_{Bt}, was 0.269m/s, which is a reasonable value compared with some predicted values by existing methods for V_{Bt} [1].

After getting data for these 30 large bubbles, we obtained averaged velocity vectors. The velocity data were divided both for longitudinal and radial sections; divided into each 5.2mm for the longitudinal direction (Z axis), and into each 0.695mm for the radial direction (r axis) to make many cells. The Z- and r-components of the velocity were averaged for each cell.

The specification of the pipe wall position was performed using the measured data for the liquid single phase flow. Figure 3 exhibits a velocity profile of a liquid single phase flow by the same setup. Solid and open symbols are for the transducer of an elevation angle ($\theta=+20°$) and for the transducer of a depression angle ($\theta=-20°$), respectively. The solid line is an approximation by the 1/7th power law. Although the data are scattered to a certain degree near the pipe wall at the far side of the transducer ($r/R =1$), we can easily find the wall position at the near side of the transducer ($r/R =-1$).
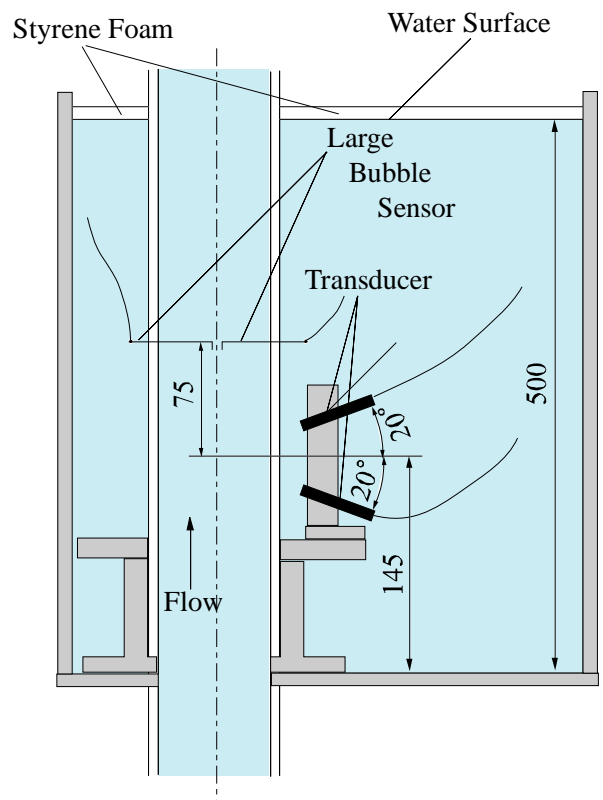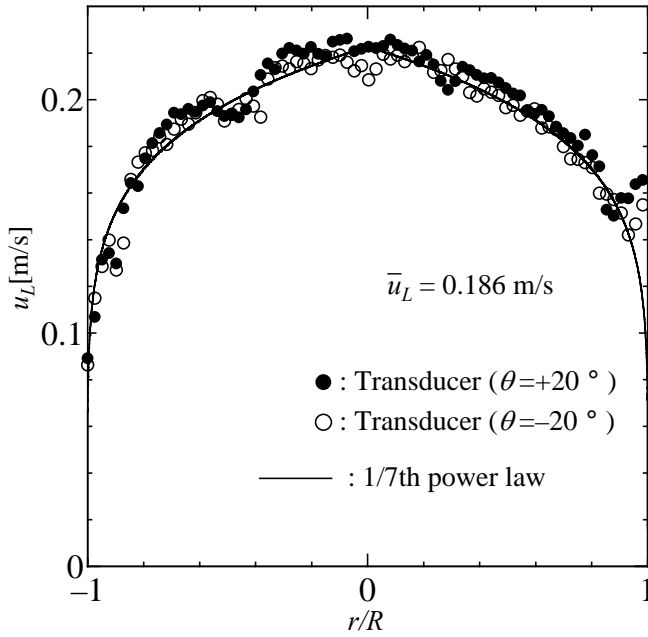

Fig.2 Test Section

Fig.3 Velocity Profile of Liquid Single Phase Flow

RESULTS AND DISCUSSION

The obtained result of the velocity field is presented in Fig.4 (a) and (b). Figure 4 (a) shows the velocity field in the liquid phase in front of the large bubble, and that in the liquid film around the large bubble, whereas (b) shows the velocity field in the liquid phase behind the large bubble. Z denotes the downward distance from the tail of the large bubble and z from the nose. Only the measured data of the near side, i.e. the data from the wall at the near side of the transducer to the pipe center axis, are used in the figures below, and are copied to the other side under the assumption of the axial symmetry. The shape of the large bubble is estimated by the bubble shape function proposed by Nakahara et al. [5].

$$r/R = 0.9 - \left\{ (z/R)^{0.7} + 0.9^{-1/a} \right\}$$
$$a = \begin{cases} -3.26 \times 10^{-4} \, \mathrm{Re} + 2.83 & (\mathrm{Re} \leq 1550) \\ -2.29 \times 10^{-5} \, \mathrm{Re} + 2.36 & (\mathrm{Re} > 1550) \end{cases} \qquad (1)$$

The gas-liquid interface is predicted to be at r in Eq.(1) with Re=0 because of stagnant water. All the velocity vectors in the large bubble were eliminated, although some vectors were obtained in it according to the error supposed to be occurred by the reflection of ultrasonic sound by the interface. Figure 4 is scaled with even intervals on both axes; the shape of large bubble is drawn in the correct aspect ratio.

Liquid Phase in front of Large Bubble

In the liquid phase in front of the large bubble, only very small velocity components are recognized. In order to make the flow field clear, we enlarged the velocity vector display in this region as shown in Fig.5. The effect of the rising large bubble is recognized to approximately $z=-0.025$m from the bubble nose. It corresponds nearly $D/2$ from the nose, where $D=2R$ is the pipe diameter, which is the same result as van Hout et al. [2]. In this effected region, the liquid near the pipe axis is lifted owing to the rising bubble nose, whereas near the pipe wall, the downward flow is recognized, which will flow into the liquid
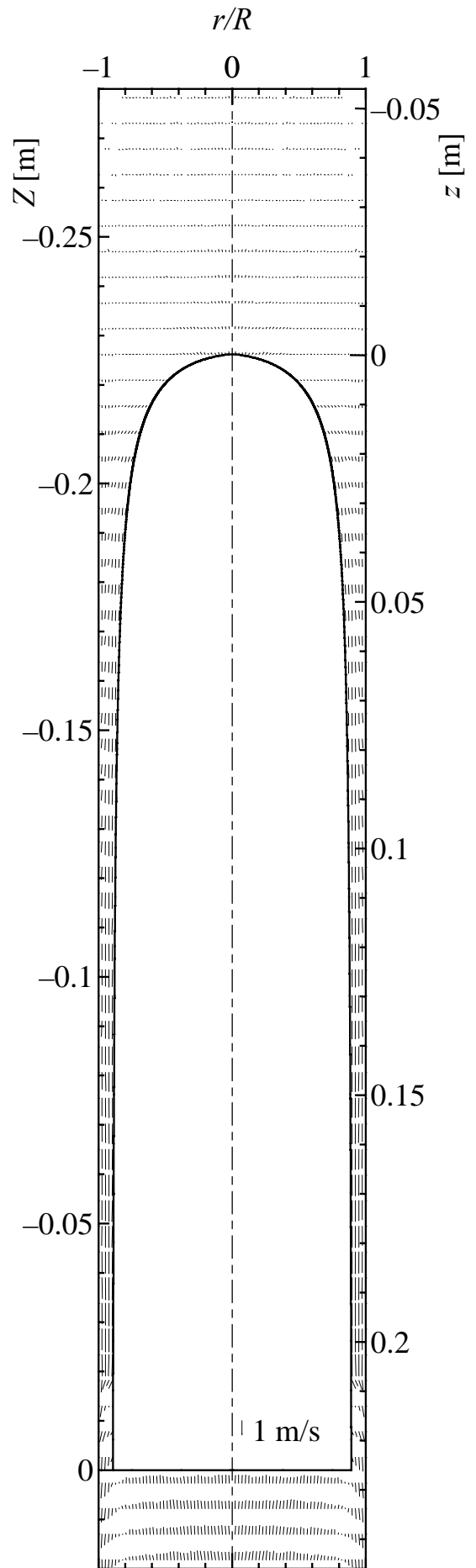

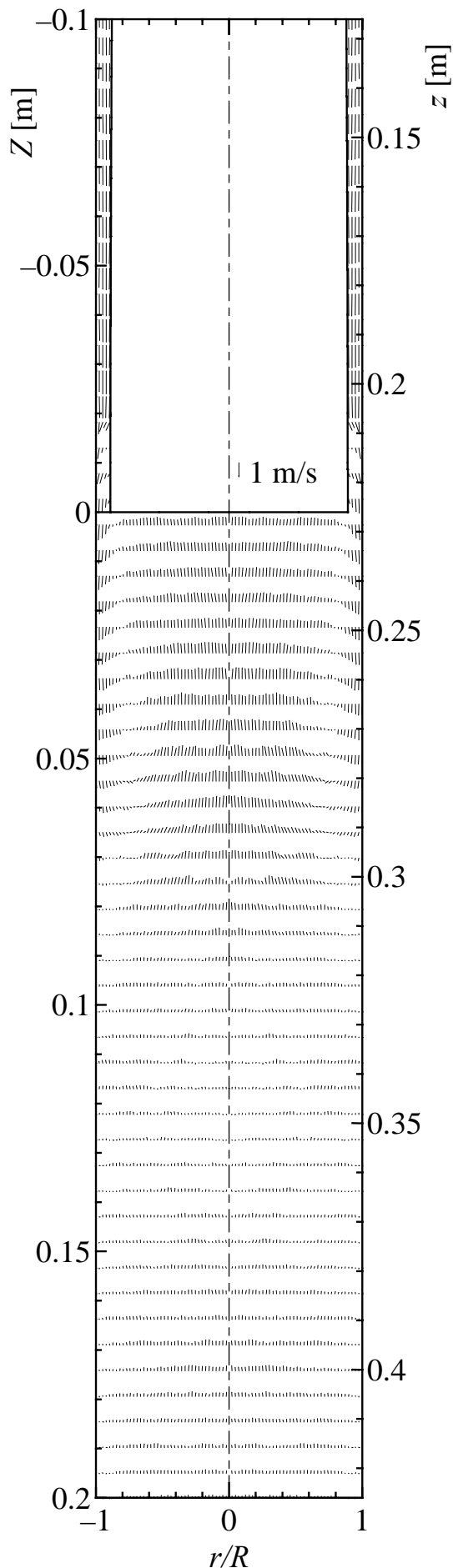Fig.4 (a) Velocity Field (Around Large Bubble)

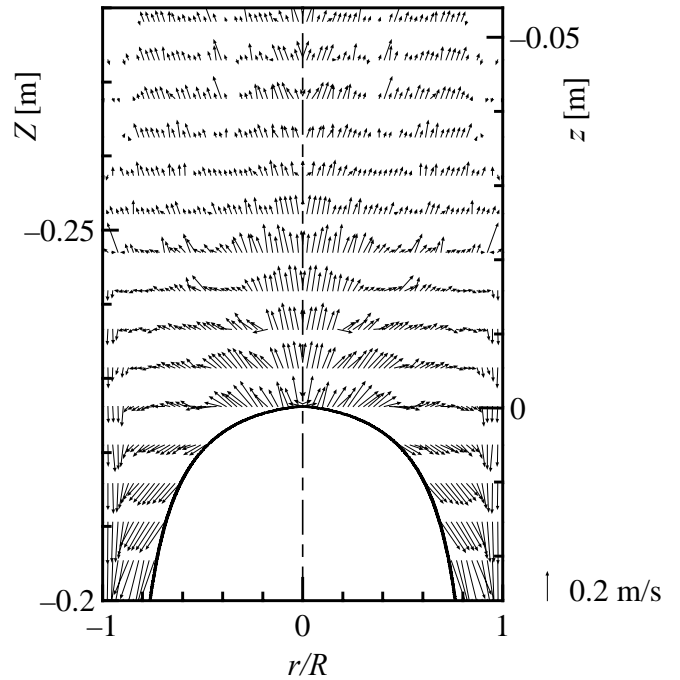Fig.4 (b) Velocity Field (Behind Large Bubble)

Fig.5 Velocity Field in Front of the Large Bubble

film around the large bubble, which also agrees with the findings of van Hout et al.

Liquid Film around Large Bubble

In the liquid film near the bubble nose, the velocity vectors near the pipe wall are almost vertically downward, but those near the gas-liquid interface are toward its tangential direction; they tend to shift the direction to the vertical downward direction as they travel downward. At the midway of the large bubble length, they are fully vertically downward as shown in Fig.6. The downward velocity slightly increases from the pipe wall ($r/R=-1$) to the gas-liquid interface. At the interface, the velocity gradient is, however, negligible so that the shear stress is also negligible. The velocity profiles in the liquid film are shown and are compared with van Hout's and Kawaji's results in Figs.7 & 8. The plotted data, u_L, are obtained as the axial downward component of the velocity vectors. We can recognize the velocity profiles in the liquid film have the maximum values at the interfaces. In Fig.7, the figure parameter is z. In this case, the velocities measured in this study are smaller than van Hout's and Kawaji's data for the same value of z. The difference is more remarkable when z is smaller. Thus, even if the distance from the nose is the same, the liquid velocity in the film falls faster when D is smaller.

Figure 8 is the similar plot with z/D as parameter instead of z in Fig.7. When the value of z/D is smaller than unity, the velocity profiles of this study agree with the two existing studies to a certain degree. When it exceeds unity, the liquid velocities in this study are longer than them. This is probably because of the difference in pipe diameters. Although van Hout's and Kawaji's measurements were based on around D=25mm pipe, our UVP measurement was performed for D=54mm pipe. Thus, the parameter z/D is more dominant than z itself especially when z/D is less than unity.

The maximum downward velocities, $u_{L\,max}$, in the liquid film are plotted against Z and z in Fig.9. The liquid downward velocity of course increases as they travel downward. As the result, the film thickness becomes thin gradually. But the accelerations are somewhat different.
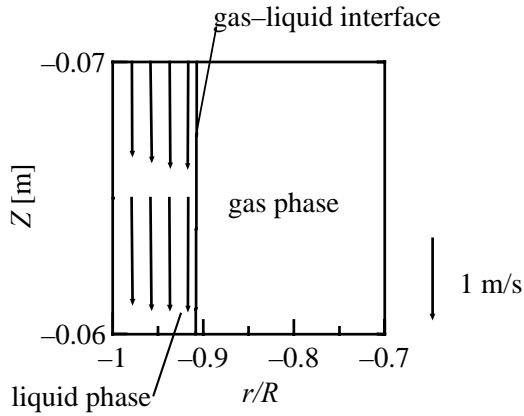
Fig.6 Velocity Vectors in the Liquid Film
around the Large Bubble

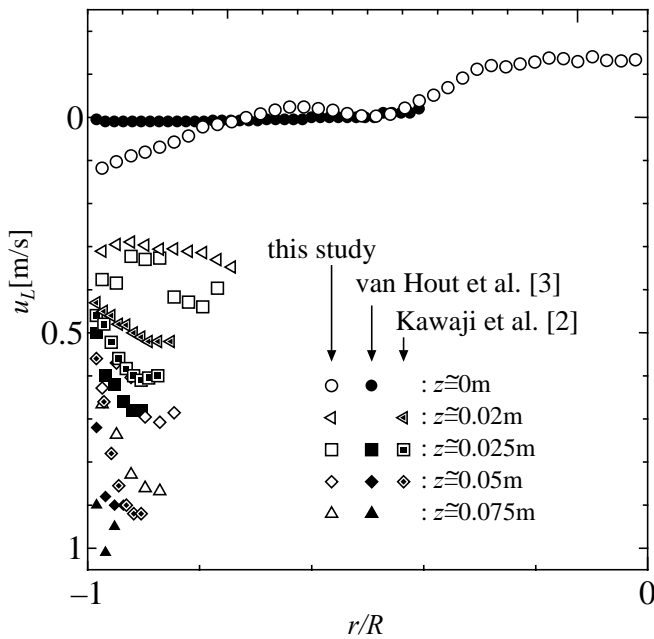
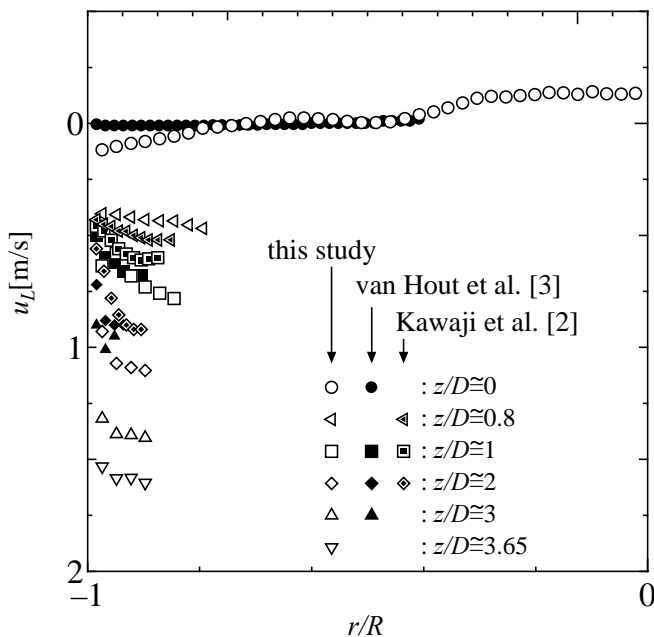Fig. 7 Velocity Profiles in the Liquid Film
with z as Parameter

Fig. 8 Velocity Profiles in the Liquid Film
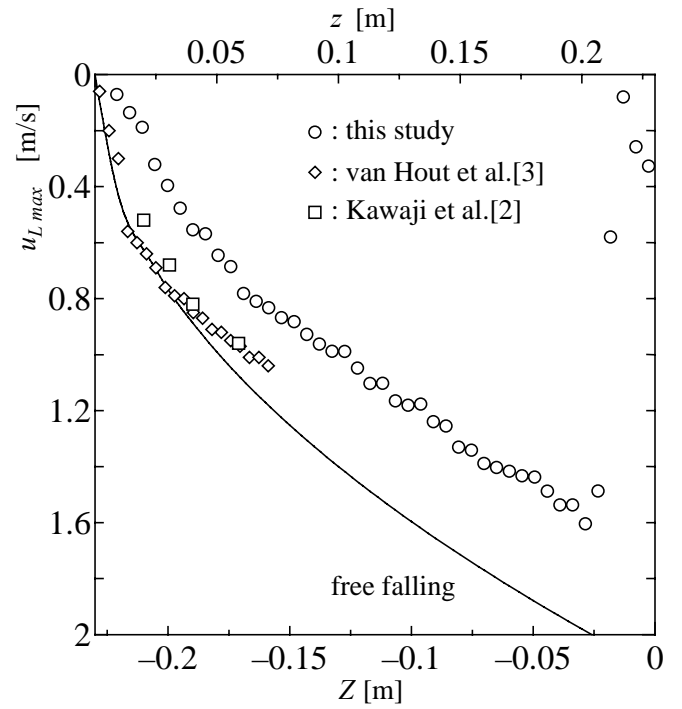with z/D as Parameter

Fig.9 Maximum Downward Velocities in the Liquid Film

For smaller pipe diameters ($D\cong 25$mm), the accelerations are approximately g near the bubble nose (z<2.5cm). But their data soon begin to depart from the free falling curve. The acceleration is repressed probably according to the viscous force. In our data for larger pipe diameter (D=54mm), the effect is more remarkable. The value of acceleration is smaller than g even near the bubble nose. In the region near the bubble tail (z>0.2), the values of $u_{L\,max}$ suddenly decreases. It does not mean the liquid film decelerates; acceleration continues to the bubble tail at least for each large bubble. But due to the vigorous oscillations of bubble tail, the averaged values of u_L in this region decreases drastically. The difficulty in measuring velocity here was also pointed out by van Hout et al. [3].

Liquid Phase behind Large Bubble

The liquid falling down in the film penetrates into liquid phase behind the large bubble to make a wake region as shown in Fig.4 (b). On the other hand, upward velocity is observed near the pipe axis. These flows form a ring vortex whose longitudinal length is about 0.08m or 1.5D. The corresponding value by van Hout et al. [3] was 2D, which is not different so much, whereas we do not find another weaker vortex they identified below the first vortex.

The upward velocity near the pipe axis was studied and related to large bubble length by Tomiyama et al. [4]. Figure 10 illustrates the upward liquid velocity at the pipe axis, $-u_{L\,axis}$, with Tomiyama's predicted curve. They agree well qualitatively. About less than 0.07m from the large bubble tail is the near-wake region, where liquid upward velocity exceeds V_{Bt} or terminal rising velocity of the large bubble. Behind the near-wake region, we recognize the far-wake region where the upward velocity is decaying to zero. Thus, the near-wake region length has a similar value to that of the vortex size, 0.08m. This actual dimension is also close to that of van Hout, 0.10m.
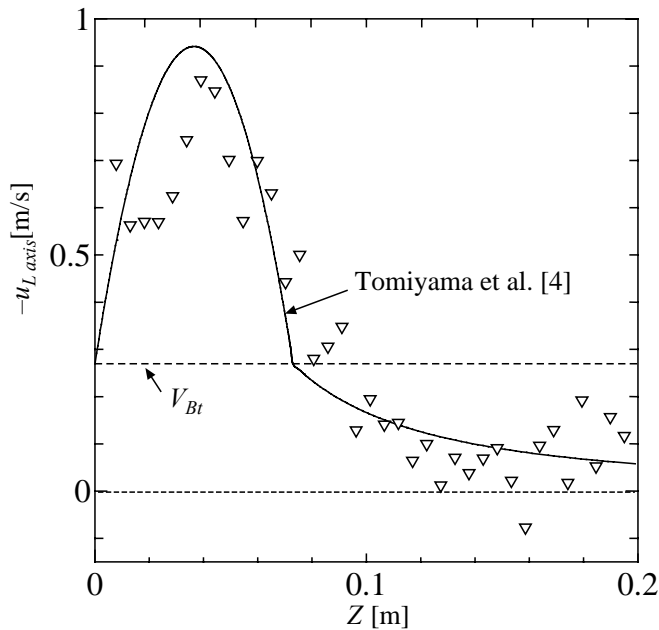
Fig.10 Upward Liquid Velocity at the Pipe Axis in the Wake

CONCLUDING REMARKS

A UVP measurement was performed for the liquid velocity field in front of, around and behind the large bubble rising in stagnant water in a round pipe of D=54mm. The measured results are presented and compared with some existing studies on the corresponding phenomena. In the liquid phase in front of the large bubble, the liquid near the pipe axis is lifted owing to the rising bubble nose, whereas near the pipe wall, the downward flow is recognized which will flow into the liquid film in the region $0.5D$ from the nose. In the liquid film near the bubble nose, velocity profile and acceleration are presented and compared with existing studies. The different in D may affect some features. The parameter z/D is found more dominant than z itself especially when z/D is less than unity. In the liquid phase behind the bubble tail or the wake region, a large ring vortex is recognized without another weaker vortex behind it. The upward velocity near the pipe axis agrees well with Tomiyama's prediction qualitatively. The near-wake region length has a similar value to that of the vortex size.

REFERENCES

1. JSME, 1995, Handbook of gas-liquid two-phase flow technology, Korona-sha, Tokyo (in Japanese).

2. M. Kawaji, J.M. Dejesus, G. Tudose, 1997, Investigation of flow structures in vertical slug flow, *Nuclear Engineering and Design,* 175, pp.37-48.

3. R. van Hout, A. Gulitski, D. Barnea, L. Shemer, 2002, Experimental investigation of the velocity field induced by a Taylor bubble rising in stagnant water, *International Journal of Multiphase Flow*, 28, pp.579-596.

4. A. Tomiyama, H. Tamai, S. Hosokawa, 2001, Velocity and pressure distribution around large bubbles rising through a vertical pipe, *proc. ICMF 2001*, New Orleans, in CD-ROM.

5. Y. Nakahara, G. Morita, A. Tomiyama, 2000, Study on shape and terminal rising velocity of single bubbles moving in a vertical pipe, *proc. annual meeting JSMF 2000*, pp.175-176 (in Japanese).

NOMENCLATURES

D : pipe inner diameter [mm]
g : gravitational acceleration [m/s^2]
r : radial distance from the pipe axis [mm]
R : pipe radius (=$D/2$) [mm]
u_L : axial component of local liquid velocity [m/s]
V_{Bt} : terminal rising velocity of a large bubble [m/s]
z : longitudinal distance from the bubble nose [m]
Z : longitudinal distance from the bubble tail [m]

AN UNSTEADY FLOW STRUCTURE ON THE HEATED ROTATING DISK
UNDER THE MIXED CONVECTION CONDITION

Noriyuki FURUICHI*, Masashige YOSHIDA**, Masaya KUMADA**

*National Institute of Advanced Industrial Science and Technology
Center 3, Umezono1-1-1, Tsukuba 305-8563, Japan, E-mail: furuichi.noriyuki@aist.go.jp
**Gifu Univ. Dep. Mechanical and System Engineering
1-1 Yanagido, 501-1193, Japan, E-mail: kumada@cc.gifu-u.ac.jp

ABSTRACT

The flow field under a mixed convection on the heated rotating disk has been measured using ultrasonic velocity profiler (UVP). The measured velocity field is a spatio-temporal one as a function of a radial coordinate and time. The objective of this paper is to clarify a vortex structure caused by instability between the buoyancy and centrifugal force. The vortex appears under typical Reynolds numbers and Grashof numbers and it moves toward outside of the disk. This behavior can be classified into two patterns. The size of the vortex structure decreases with increase in Reynolds number and increases with Grashof number. The traveling velocity of the vortex increases with Grashof number and decreases with increase in Reynolds number in spite of increase of centrifugal force. According of these results, the region dominated by natural, forced and mixed convection is classified in the relationship between Reynolds and Grashof number.

Key words : Mixed convection, Heated rotating disk, UVP, Buoyancy, Centrifugal force

INTRODUCTION

A heated rotating disk can be seen in many industrial applications such as CVD method for a thin film making and a rotor in a gas-turbine and so on. In this flow field, flow direction induced by rotating of the disk is different with one induced by buoyancy. As the basic flow field to consider a heat transfer mechanism under mixed convection, many investigations have been carried out for time-averageed characteristics[1][2].

On the other hand, the flow field behaves a characteristic unsteady structure due to an instability between a natural and forced convection[3][4]. As concerning with that instability, we make attention to a vortex structure which appears on the disk[5]. This vortex can be observed on the critical Grashof number ($Gr_c \sim Re_\omega^{3/2}$) even if the rotating Reynolds number is small as a laminar condition. From a visualization, it was found as a longitudinal vortex stretching to the azimuthal direction. It was also found that the vortex travels to the azimuthal direction due to Coriolis force and to the outside of the disk due to centrifugal force.

To obtain a knowledge of this vortex structure such as an origin of appearance, deformation and traveling path is very important to clarify the unsteady structure of the mixed convection. However, since an experimental investigation is difficult because of the heating and rotating flow field, these structure have not been clarified well. The objective of this paper is to clarify the basic structure of the vortex and the classification of the natural and forced convection based on the rotating Reynolds number and Grashof number.

EXPERIMENTAL METHOD

Experimental apparatus is shown in Fig.1. A radius of the rotating disk submerged in the water tank (620×720×400mm) is R=85mm. The water has 400mm depth and free surface condition. To avoid natural convection induced by a temperature difference between the water and ambient air, the water tank is covered by insulators. The rotating disk is consisting of a cupper plate with 5mm thickness and an insulator. Heating was carried out by a heater attached to the cupper plate by an adhesives with high thermal conductivity.

Rotating velocity of the disk was varied 5~25[rpm] (Reynolds number is $Re_\omega=R^2\omega/\nu=0.66\times10^4 \sim 3.29\times10^4$). This is laminar condition in un-heating case. A difference of the temperature between the surface of the rotating disk and the water was varied Δt=2.5~55[°C] (Grashof number is $Gr=g\beta(T_w - T_\infty)R^3/\nu = 0.23\times10^8 \sim 5.07\times10^8$). The temperature of the water is set to T_∞=40[°C] to eliminate a change of an ultrasonic velocity. In the temperature range of 40 ~ 95[°C], the change of the ultrasonic velocity is less than 1%.

A detail of the test section on the heated rotating disk is shown in Fig.2. Measurement was carried out using ultrasonic velocity profiler. A transducer directed to the center of the disk was set outside of it, therefore, measuring component is $v_r(r,t)$ in this experiment. A center line of the transducer is set to z=1.5[mm] upside from the surface of the disk. A basic frequency of the transducer is 8[MHz] and a pulse number is 6. A spatial interval for each measuring point is 0.77[mm] and a time interval for each profile is 41[msec]. Nylon powder (density 1.02, diameter 100[μm]) is mixed to the water as a tracer.

RESULTS AND DISCUSSION

Spatio-Temporal Velocity Field

Typical spatio-temporal velocity field $v_r(r,t)$ is shown in Fig.3 to observe a change of a behavior with Grashof number. The horizontal axis is time and the vertical axis is radius position. In figure (a) which is the case of the largest angular velocity, the velocity component increases with radius position toward the outside of the disk. This obviously indicates an increase of the centrifugal force. Any effect of the heating can not be observed in this figure since a effect of the forced convection is lager than the natural convection. On the other hand, in the figure (b) and (c), some instability can be observed like a stripe structure as indicated by the dotted line. These stripe-like structures angled to right-up show a behavior that some eddy is moving to outside of the disk. Ogino et.al[5] indicated that a vortex structure of crurve like shape caused by the instability of buoyancy appears under typical condition between rotating Reynolds number and Grashof number. They also showed that it moves azimuthal direction with slower than the rotating speed of the disk and moves toward outside of the disk. From a visualization of the flow field under same condition, the vortex structure moving toward the outside of the disk can be also observed in this experiment. The vortex shows up-wash flow by the heating. We can conclude that the stripe structure in the figure shows a vortex moving toward outside.

The vortex structure can be also observed under the figure (c) condition, however, there are some difference behavior between in (b) and (c). In the (b), the appearance point of a vortex is roughly rigid; around $r/R=0.5$, on the other hand in the (c), it is unstable as some reaches to the center of the disk. In the (c), a reverse flow directed to the center of the disk can be observed. This flow is considered an appearance of the natural convection. The flow toward the center can be observed more clearly in the figure (d) which is the largest Grashof number case. In the (d), the vortex toward the outside of the disk can not be observed.

Cross Correlation of Reconstructed Velocity Field

We consider a detail structure of the vortex moving toward the outside of the disk by a cross-correlation of velocity fluctuation. However, the cross correlation coefficient obtained by this computation is strongly affected by the flow toward the center of the disk, especially under a condition dominated by the natural convection. To eliminate of this effect, we compute the two-dimensional Fourier transform as a following formula at first.

$$S(f,k) = \int_{-\infty}^{\infty} \int_{-\infty}^{\infty} v_r(r,t) e^{-ift} e^{-ikr} dt dr \qquad (1)$$

Where, f is frequency and k is wave number. The obtained spectrum $S(f,k)$ phase indicates each energy of the velocity fluctuation toward the outside and the center of the disk separately. To obtain only the velocity fluctuation toward the outside, the phase indicating toward the center was cancelled through a filter. After this computation, the velocity field was reconstructed by a inverse Fourier transform. Typical reconstructed velocity field is shown in Fig.4 corresponding to the Fig.3(c). It can be observed that the velocity component toward the outside of the disk is extracted clearly.
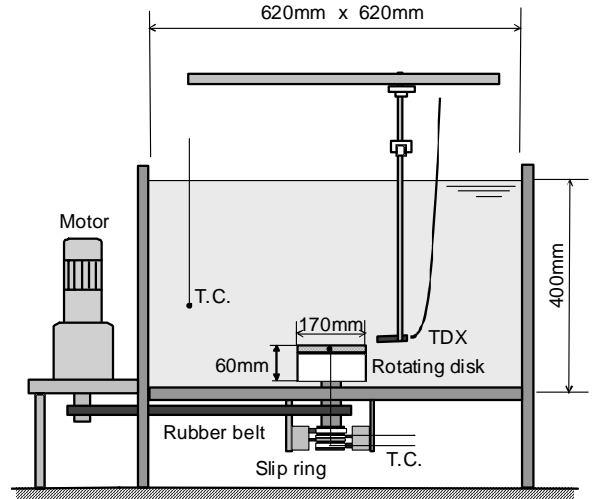

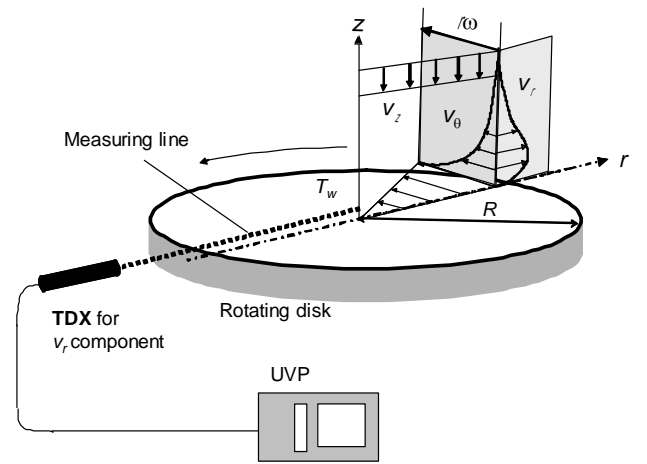Fig.1 Schematic of the experimental apparatus

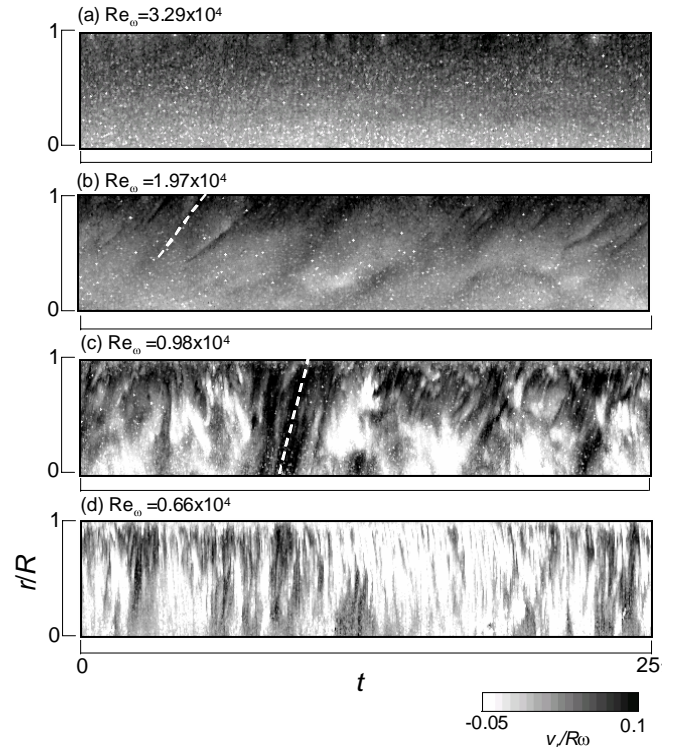Fig.2 Coordinate system and measuring system

Fig.3 Examples of spatio-temporal velocity field $v_r(r,t)$ at Gr=1.84×10^8

The cross correlation coefficient was computed using the reconstructed velocity field as a following formula.

$$R_{vv}(r_1, r, \tau) = \frac{\overline{v_r^{*'}(r_1, t) \cdot v_r^{*'}(r, t+\tau)}}{\sqrt{\overline{v_r^{*'2}(r_1, t)}} \sqrt{\overline{v_r^{*'2}(r, t+\tau)}}} \quad (2)$$

Where, r_1 is a fixed point, v_r^* is the reconstructed velocity field by the two-dimensional Fourier transform.

Example of a lag-time and radius position contour map of the correlation coefficient is shown in Fig.5. The fixed point is $r_1=0.75R$. The horizontal axis is dimensionless lag-time and the real time scale is same between two maps. The bold line is shown for larger correlation coefficient than 0.3 as a high correlation area. The high correlation area around the lag-time 0 and the fixed point r_1 shows right-up shape because the velocity fluctuation caused by vortex moves toward outside. The shape of the high correlation area in the dimensionless axis is almost same between two maps however the size of (a) for the radius direction is smaller than (b).

To quantitative analysis of the size of vortex, a variation of a integral scale (L_r) at $\tau\omega=0$ is shown in Fig.6. It is clearly found that the integral scale becomes smaller with increasing Reynolds number. Considered the conservation of an angular momentum, this result shows that the vortex is stretching to the angular direction with increasing Reynolds number. Moreover, the length scale approaches to the zero with Reynolds number. This shows that there is a limitation for an appearance of the vortex toward higher Reynolds number. On the other hand, it can be also found that the integral scale increases with Grashof number. It is considered that the up-wash flow becomes larger with increasing the temperature of the disk.

Traveling Velocity of Vortex

The dotted line in Fig.5 means the most clear ridge line of the contour map. The angle of it indicates that an averaged traveling velocity of velocity fluctuation; in other words vortex toward the outside of the disk. Ogino et al.[5] shows that the traveling velocity of vortex computed by the temperature correlation is almost uniform and it has no correlation with the radius position and Grashof number. However, our investigation as shown the dotted line in the correlation map of Fig.5 is not agreement with that result.

A radial variation of the traveling velocity (v_t) of vortex estimated by the inclination angle of the dotted line in Fig.5 is shown in Fig.7. Obviously, a large difference can be found between the Reynolds number $Re_\omega=1.34\times10^4$ and 1.97×10^4. At the smaller case, the traveling velocity is uniform till $r/R\approx0.8$. At near of the edge of the disk, it decreases with position because of an interaction between the flow on the disk and of the ambient. On the other hand, the large Reynolds number case, the traveling velocity increases with the radius position.

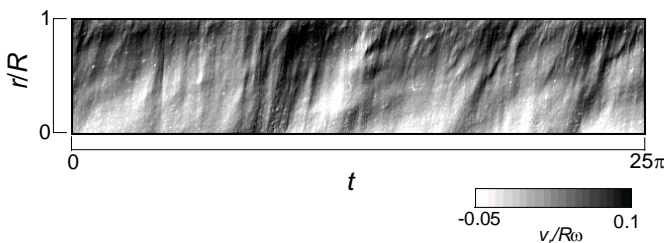In Fig.8, the relationship between the traveling velocity and

the rotating Reynolds number under several Grashof number. This result shows the traveling velocity at $r/R=0.75$. It is found that the traveling velocity increases with Grashof number. This is caused by a change of the density of the working fluid by heating. On the other hand, when Grashof number is same case
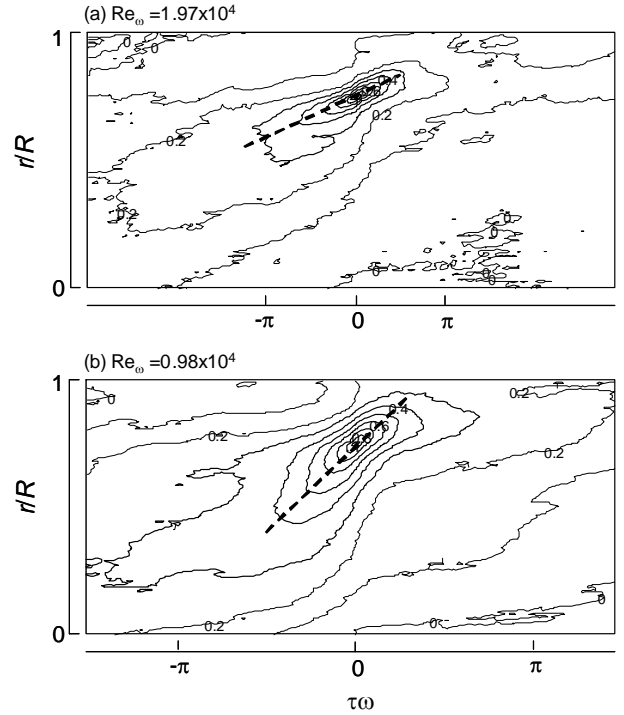

(a) $Re_\omega =1.97\times10^4$

(b) $Re_\omega =0.98\times10^4$

Fig.5 Contour maps of correlation coefficient of the reconstructed velocity fluctuation at Gr=1.84×10^8

Fig.6 Variation of integral scale

Fig.4 Reconstructed velocity field at $Re_\omega=0.98\times10^4$, Gr=1.84×10^8 corresponding to the Fig.3(c)
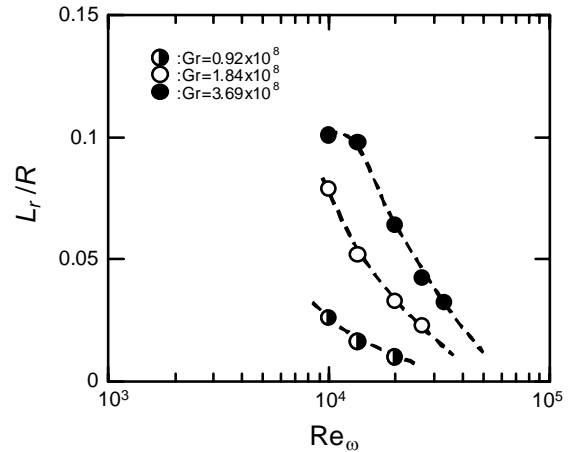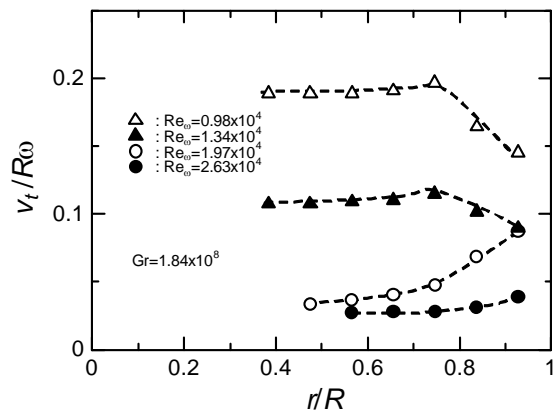

Fig.7 Radial variation of the traveling velocity of vortex

as shown by the dotted line, the traveling velocity decreases with increasing Reynolds number. An increase of the Reynolds number induces an increase of v_r component by the centrifugal force. However, in spite of this matter, the traveling velocity decreases with Reynolds number. This is also concerning with the conservation of the angular momentum.

Classification

To clarify the dominant region of each force from the view point of vortex appearance, we plot symbols in the Reynolds and Grashof number correlation as Fig.9 whether vortex can be observed or not. As shown by the hatching region, steady detection case as which a position of vortex appearance is stable, unsteady detection case as which is unstable and un-detection case is classified. The solid line indicated by Ogino et al.[5] is the critical Grashof number which classifies the dominant region of natural and forced convection. Their result was obtained by the variation of the Nuselt number on the heated rotating disk. They also suggested that the vortex can be observed well around this critical Grashof number. Our result is in good agreement with Ogino's for the steady detection case. The higher limitation as observed in the integral scales of Fig.6 and traveling velocity of Fig.8 is agreement with the critical Grashof number. On the other hand, for the unsteady detection case, the vortex can be observed at $Re_\omega > 0.986 \times 10^4$, $Gr > 0.922 \times 10^8$. The phenomena of these flow structure is typical one investigated under only mixed convection since the vortex can not be observed in other region dominated by the natural or forced convection.

The solid line by Ogino et al. is showing $Gr \sim Re_\omega^{3/2}$. They suggested the agreement with the linearity unsteady analysis by Wu and Cheng[6] in spite of the difference of the flow field. On the other hand, the dotted line is showing $Gr \sim Re_\omega^{5/2}$. When the flow direction between the convection and buoyancy is different, the dominant region by natural and forced convection is separated by this relationship obtained by a dimensional analysis[7]. For the unsteady detection case, the dotted line is in agreement with the limitation for detection of vortex. As concluding of result, the behavior on the heated rotating disk is classified to I to III region in the figure. The I is the region dominated by the forced convection induced by the rotating the disk. The III is by the buoyancy induced by the heating. The IIa and IIb is the mixed convection region which decided by the unstable flow structure on the heated rotating disk.

CONCLUDING REMARKS

The flow field on the heated rotating disk as the mixed convection condition was measured by the UVP. From the spatio-temporal velocity field, it was found that the vortex appears under typical condition and it travels to outside of the disk. The scale of the vortex decreases with Reynolds number and increases with Grashof number. The traveling velocity of the vortex also shows similar variation. According these result, the dominated region by natural, forced and mixed convection were classified.

REFERENCES

1. F. Kreith, J.H. Taylor, J.P.Chong, 1959, Heat and mass transfer form a rotating disk, *Trans. ASME J. of Heat Transfer*, 81, pp-95-105
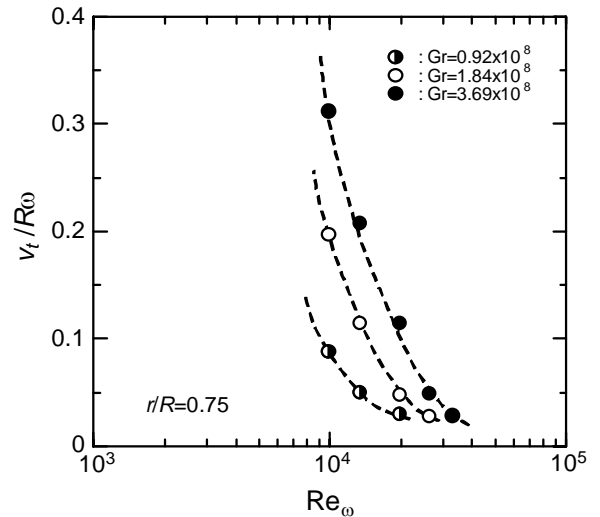
Fig.8 Variation of the traveling velocity of vortex
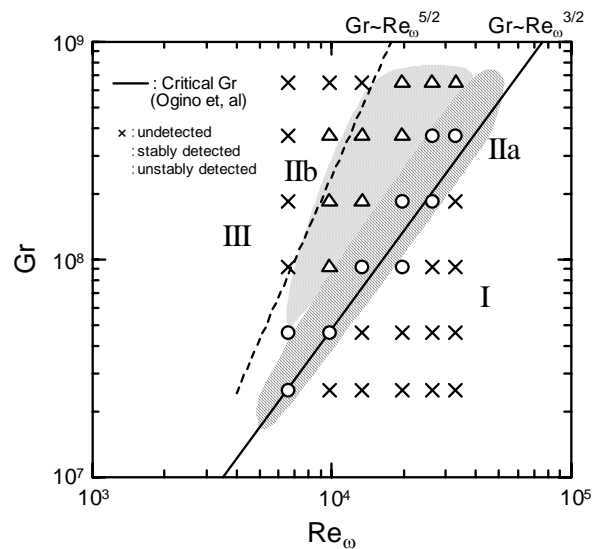

Fig.9 Detection of vortex

2. C.J Elkins, J.K. Eaton, 2000, Turbulent heat and momentum transport on a rotating disk, *J. of Fluid Mech.*, 402, pp.225-253

3. P. Jacobs, G.N. Ivey, 1998, The influence of rotation on shelf convection, *J. of Fluid Mech.*, 369, pp.23-48

4. U.R. Christensen, 2002, Zonal flow driven by strongly supercritical convection in rotating spherical shells, J. of Fluid Mech., 470, pp.115-133

5. F. Ogino, Y, Saitoh, T. Yoshida, K. Masuda, K. Mizuta, 1997, Heat tannsfer and flow characteristics in a rotating disk system, J. of Chemical Engineering of Japan, 23-5, pp.679-686 (in Japanese)

6. R.S. Wu, K.C. Cheng, 1976, Thermal instability of Blasius flow along horizontal plates, *Int. J. Heat Mass Transfer*, 19, pp.907-913

7. G. Wickern, 1991, Mixed convection from an arbitrarily inclined semi-infinite flat plate – I. The influence of the inclination angle, *Int. J. Heat and Mass Transfer*, 34, 8, pp.1935-1945

UVP MEASUREMENTS OF THE FLOW BEHIND A ROTATING CIRCULAR CYLINDER

Yoshihiro Inoue*, Akira Ito** and Shintaro Yamashita*

* Dept. Mathematical & Design Eng., Gifu University, 1-1 Yanagido, Gifu 501-1193, Japan
E-mail: inouey@cc.gifu-u.ac.jp, yamasita@cc.gifu-u.ac.jp

** Graduate School of Eng., Gifu University, 1-1 Yanagido, Gifu 501-1193, Japan
E-mail: i3132005@guedu.cc.gifu-u.ac.jp

ABSTRACT

Separated flow past a rotating circular cylinder has been investigated by flow visualizations and velocity profile measurements using the ultrasonic Doppler method. Experiments were performed in a free-surface water channel with $Re_d = 800$, a Reynolds number larger than the critical Reynolds number of the flow behind a circular cylinder, within a rotational speed ratio range of $U_c^* = 0$ to 6. Flow visualized images were obtained by the dye method and captured with the digital video camera. Fluctuating velocity fields, $v(y, t)$, measured by the UVP monitor were represented in contour maps and analyzed with the POD. Wake patterns are divided into two main categories in terms of the rotational speed ratio; (i) regular vortex street within the lower speed range and (ii) disordered vortex structure within the higher range. There are three subcategories between two main-categories. It is shown that the fluctuation energy within the wake shear layers, and the deflection amount and width of the shear layer are changed with the rotational speed ratio.

Keywords : Cylinder Wake, Centrifugal Instability, Flow Visualization, Shear Layer Oscillation

INTRODUCTION

It is an important engineering issue in relation to the occurrence of flow-induced vibration and/or airborne noise to illuminate a large-scale structure formed behind a bluff body in a uniform flow [1-3]. When a circular cylinder is rotating around its axis, the wake is accompanied by several characteristic phenomena and more complicated in comparison with a case where the circular cylinder is not rotating. One reason for this difference is that the flow separation phenomenon occurs not from the wall surface of the circular cylinder but from the inside of the fluid [4]. Another reason is that the secondary flow is induced by centrifugal instability [5]. These two phenomena exert a considerable influence on the location of the flow separation and the behavior of the separated shear layer, playing a dominant role in the formation process of the flow structure in the entire wake. One of the effectual parameters is the ratio of the rotational speed of the circular cylinder U_c to the uniform flow velocity U_0, which is denoted as $U_c^* = U_c / U_0$. Flow structures in the wakes are expected to vary with U_c^*.

Glauert [6, 7] analyzed the two-dimensional flow passing by a circular cylinder placed in a uniform flow as to a case where separation phenomenon was not seen at a high rotational speed ratio based on the boundary layer theory. Moore [8] also put a flow field at a high rotational speed ratio to theoretical analysis. Moore approached this issue by utilizing small perturbation from exact solution at the infinite rotational speed ratio. On the other hand, Swanson [9] overviewed the studies in Magnus force acting on a rotational body made by 1960. Koromilas and Telionis [10] examined an unsteady laminar separation through the flow visualization and with a laser Doppler velocimeter. In the numerical study, including the discrete vortex simulation by Ingham [11] and Cheng *et al*. [12], a number of research papers have been presented since the latter half of the 1980s.

This study is designed to experimentally treat the flow behind a circular cylinder rotating uniformly in a uniform stream, and identify the wake vortex structures by varying the rotational speed ratio U_c^* and classify them accordingly. Since the dependency of this flow field on Reynolds number is not negligible, care should be directed to the selection of an experimental Reynolds number. In this study, experiment was conducted with $Re_d = 800$, a Reynolds number larger than the critical Reynolds number of the flow behind a circular cylinder, within a rotational speed ratio range of $U_c^* = 0$ to 6. In order to observe and identify the flow patterns, the flow fields were visualized by the dye method, and then the flow velocity pattern visualization was applied by using an ultrasonic velocity profile (UVP) monitor [13]. Furthermore, the feature extraction of the velocity variation pattern was conducted by using the proper orthogonal decomposition, and thereby the variation in the wake vortex structure according to the change of the rotational speed ratio was examined.

EXPERIMENTAL PROCEDURE

Apparatus

The experiment was conducted in a water tunnel with an open channel of 700 mm in width, 500 mm in depth and approx. 2000 mm in length to be used as a measurement part. The test channel was provided with an acrylic resin window on both sides. A uniform flow was driven by an inverter-controlled mixed flow pump and settled by a straightener and screens. On the other hand, the circular cylinder was rotated by an AC motor equipped with reduction gear and a toothed belt, and the rotational speed of the circular cylinder was obtained by counting the number of signals detected by an electromagnetic pickup.

The outline of the flow field and its coordinate system are

shown in Fig. 1. The z-axis is coincided with the circular cylinder axis, the x-axis is coincided with the uniform flow direction, and the y-axis is taken at right angles to both the axes. The circular cylinder is rotated in the direction as shown in the figure. At this time, when $y > 0$, the circular cylinder surface speed is in the direction opposite to the direction of the main stream, and when $y < 0$, the circular cylinder surface speed is in the same direction as the direction of the main stream. The former is called "pressure side" and the latter "suction side" in likening to the air flow around a wing. The diameter of the circular cylinder used in this experiment was $d = 20$ mm, and the reference Reynolds number was $Re_d = U_0\, d\, /\, \nu = 800$ (uniform velocity $U_0 \approx 40$ mm/s). The rotational speed ratio of the circular cylinder $U_c^* = U_c\, /\, U_0 = \omega\,(d\,/\,2)\,/\,U_0$ was varied within a range of 0 to 6 (rotational angular speed $\omega \approx 0$ - 24 rad/s).

Flow visualization technique

For the flow visualization, the electrolytic precipitation method and the dye image method using Uranine were utilized. Both the methods are the same in that the circular cylinder surface is used as a dye source, while the latter enables localized visualization by means of sheet light illumination since Uranine is a fluorescent dye. In fact, since the three-dimensional nature of the flow field, *i.e.*, variation in the z-direction, was not negligible, the laser light sheet technique was utilized in the dye image method to grab images visualized within the x-y plane. The laser used was Ar-ion laser with an output of 500 mW. On the other hand, the electrolytic precipitation method was utilized to observe the three-dimensional nature of the flow in the span direction, and the x-z plane was illuminated with a higher-output straight tube type mercury lamp. However, the images captured by this method were omitted in the present paper.

The visualized images were grabbed with a digital video camera (SONY TRV900) and recorded in a mini DV tape. The captured images were transferred from a DV recorder (Panasonic NV-DM1) to a PC, and processed on the PC. In reconstructing the visualized images based on Taylor's hypothesis, a necessary range of pixels were cut out of 600 images with a frame rate of 30 fps, and connected in chronological order to obtain a single image.

UVP measurement method

Ultrasonic velocity profile (UVP) measurement is conducted in such a way that an ultrasonic beam is emitted into the water and the ultrasonic Doppler-echoes from the seeding particles within the water are detected and analyzed. For Met-Flow Model X3-PS used in this experiment, the same ultrasonic transducer is utilized both to send and to receive an ultrasonic wave, and the instantaneous velocity information $\tilde{v}_\xi$ on the ultrasonic beam is measured as the function of the distance ξ in the beam direction. By repeating this procedure temporally, the time-series data of velocity profile $\tilde{v}_\xi(\xi, t)$ is obtained.

In this experiment, an ultrasonic transducer with the basic frequency of 4 MHz and 5 mm in diameter was used. The ultrasonic beam was directed in parallel with the x-direction and the y-direction, and $\tilde{u}(x, t)$ and $\tilde{v}(y, t)$ were measured, respectively. At this time, as ultrasonic scattering particles, hydrogen bubbles continuously generated from a platinum wire of 80 μm in diameter located in the upstream of the measurement position were used. When it comes to the space and time sampling intervals
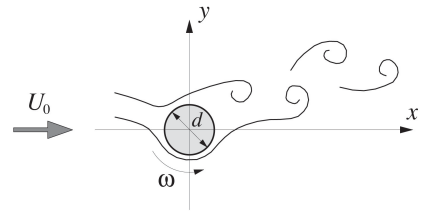

Fig. 1 Flow field and coordinate system.

under the operating conditions of this experiment, the time interval was about 38 ms, and the space intervals was 2.96 mm in the x-direction profile and 2.22 mm in the y-direction profile.

In processing the velocity profile data, the space and time profile $\tilde{v}_\xi(\xi, t)$ of the instantaneous velocity component in the ξ-direction is divided into the mean component and the fluctuating component, and expressed as $\tilde{v}_\xi(\xi, t) = V_\xi\,(\xi) + v_\xi\,(\xi, t)$. Then, the fluctuating component profile is analyzed by using Fourier transform and POD to examine the space and time variable characteristics of the flow field. This procedure should be referred to Inoue *et al*. [14].

RESULTS AND DISCUSSION

Flow visualizations by the dye images

The dye pattern emitted from the Uranine coated over the circular cylinder was illuminated with a laser light sheet positioned in parallel with the x-y plane. The images captured in this method are shown in Fig. 2. The rotational speed ratios of the shown images were $U_c^* = 0$, 1.0, 1.85, 2.0, 3.0, 4.0 and 5.0. As evident from the figure, changes in the wake pattern due to the rotational speed ratio U_c^* are significant. At $U_c^* = 0$, a vortex street subjected to alternative shedding due to the roll-up of the separated shear layer is observed. Also at $U_c^* = 1.0$, the shear layer separated on the pressure side and suction side was rolled up, respectively, composing a vortex street similar to that at $U_c^* = 0$. However, differences from the flow field at $U_c^* = 0$ lie in that the cylindrical vortex formation region is closer to the circular cylinder and that the center axis of the vortex street is deviated upwards from the x-axis.

Here, it should be noted in this visualization method that the dye is emitted from the circular cylinder surface but the flow separation points are not existent on the circular cylinder surface except for the case at $U_c^* = 0$. Since the dye supply to the separated shear layer is not so reliable as seen at $U_c^* = 0$, there is no choice but to reply on other dye transport mechanism. That is, the dye is carried out of the surface through the boundary layer adhered to the circular cylinder surface and rotating together, and carried away to the downstream by the flow in the outer layer. In the photo of the case at $U_c^* = 1.0$, the separated shear layer from the pressure side is visualized as a layer with a high dye concentration, while no such layer is seen on the suction side. At $U_c^* = 1.85$ and 2.0, the layer with a high dye concentration is not observed on the pressure side or the suction side, and a very narrow dead water area is seen behind the circular cylinder. There is little dye pattern appeared showing the vortex street in the wake, but only dye streaks have feebly ordered features.

When the rotational speed is faster, the flow in the boundary layer is under a strong centrifugal instability, and a vortex structure similar to Taylor vortex around the circular cylinder [13].

This vortex receives a supply of dye from the circular cylinder surface, forming a banded area with a high dye concentration. This vortex area breaks away from the circular cylinder under the influence of the flow in the outer layer. These behaviors are clearly seen in the photos of $U_c^* = 3.0$ and 4.0. The complicatedly winding dye patterns fill in the broad layer almost disorderly. At a higher rotational speed ratio of $U_c^* = 5.0$, the boundary layer on the circular cylinder appears turbulent, and dye patterns of various scales, like turbulent eddies, can be seen in the wake shear layer.

Contrast with the dye images and velocity contour maps

In this section, the contrast between the dye patterns shown in Fig. 2 and the flow field is considered at a location comparatively near to the circular cylinder, $x / d = 3$. For this purpose, the visualized images are reconstructed based on Taylor's hypothesis and shown in Fig. 3. The flow field is obtained from the y-direction UVP measurement at $x / d = 3$, and shown as a contour map of the fluctuating velocity $v (y, t)$ in Fig. 4. In the figure, the solid line represents the positive fluctuating velocity contour and the broken line the negative fluctuating velocity contour. The results are shown as to the cases with the rotational speed ratios $U_c^* = 0$, 1.0, 1.85, 3.0 and 5.0, respectively.

In contrast of dye patterns between the flow fields with $U_c^* = 0$ and 1.0, there is a difference in dye concentration, there is agreement in the fundamental structure that the cylindrical vortex areas are arranged alternately with the center axis between them and these two areas are connected staggeringly. There is a good agreement in fluctuating velocity contour between these rotational speed ratios, representing the y-direction velocity field induced to the cylindrical vortices of the staggered arrangement. At $U_c^* = 1.85$, there is no dye pattern corresponding to the well-organized cylindrical vortices, but rather the dye pattern like zigzagged lines is dominant. In correspondence with the weakening of the cylindrical vortices, there is no longer the orderliness in the v-fluctuation pattern, and the fluctuation amplitude is considerably weakened in comparison with that at $U_c^* = 0$ and 1.0.

On the other hand, the dye pattern at $U_c^* = 3.0$ forms a widening layer of streaky, high-dye-concentration area originated in Taylor vortex, and its coherence is low. This is also clearly seen in the v-fluctuation contour map. Furthermore, the fluctuation energy within the layer is considerably low. Lastly, in the flow field at $U_c^* = 5.0$, like in the flow field at $U_c^* = 3.0$, the visualized pattern is seen with dye lumps filled in the wide layer. In comparison with these two flow fields, the layer at $U_c^* = 5.0$ is considerably wider, the individual dye lumps are of more complicated shape and of more minute segmentation, and the dye concentration is lower. However, there is an organized velocity fluctuation area seen in the v-fluctuation contour map. This implies the generation of an organized motion whose image is different from that of the flow at $U_c^* \leq 3.0$.

Lateral fluctuating velocity field

In order to quantitatively discuss the variation in the flow structure according to the rotational speed ratio considered until the preceding section, the y-direction UVP measurement data is analyzed statistically. Figure 5 shows the total energy of the v-fluctuation within the wake shear layer, E_v, in relation to the rotational speed ratio. Here, E_v is defined by the following equa-

(a) $U_c^* = 0$

(b) $U_c^* = 1.0$

(c) $U_c^* = 1.85$

(d) $U_c^* = 2.0$

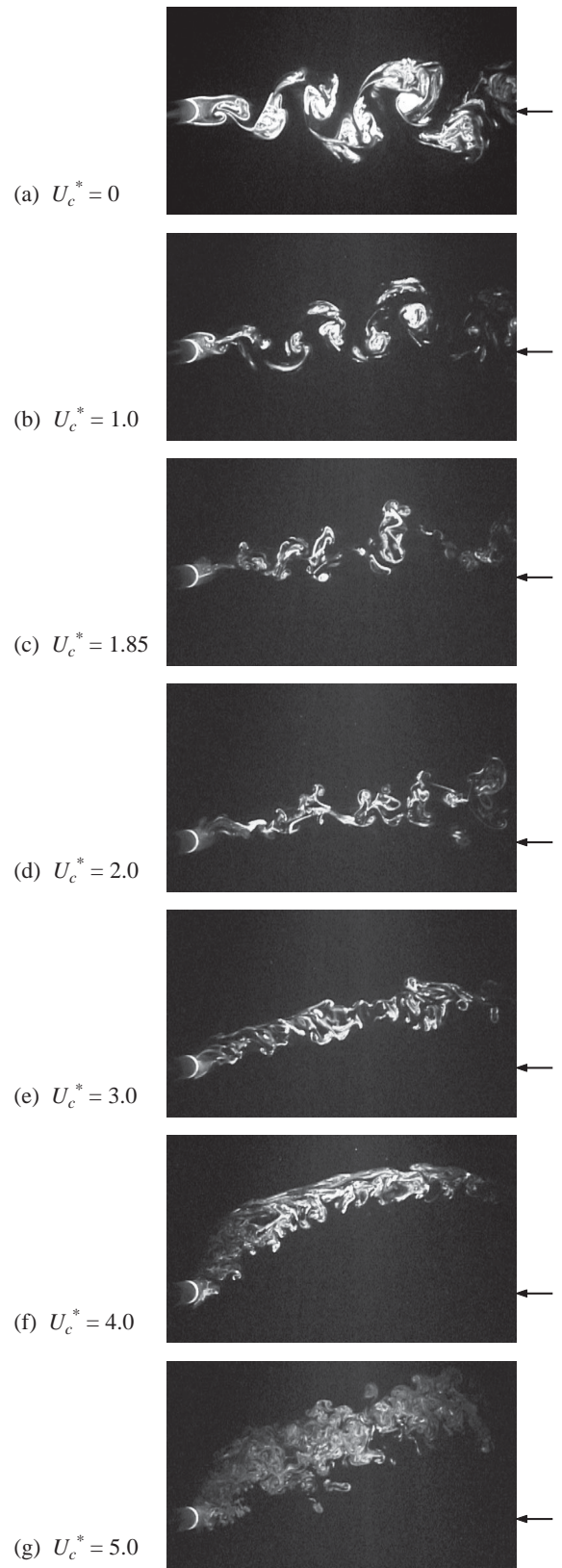(e) $U_c^* = 3.0$

(f) $U_c^* = 4.0$

(g) $U_c^* = 5.0$

Fig. 2   Plan views of wakes behind the rotating circular cylinder visualized with a thin laser light sheet.

tion:

$$E_v = \frac{1}{T} \int_{-T/2}^{T/2} \int v^2(y,t)\,dy\,dt = \int \overline{v^2}(y)\,dy . \qquad (1)$$

It is evident from the figure that the high fluctuation energy held at $U_c^* < 1$ sharply decreases along with the increase in the rotational speed ratio within a range of $1 < U_c^* < 1.7$, and fur-
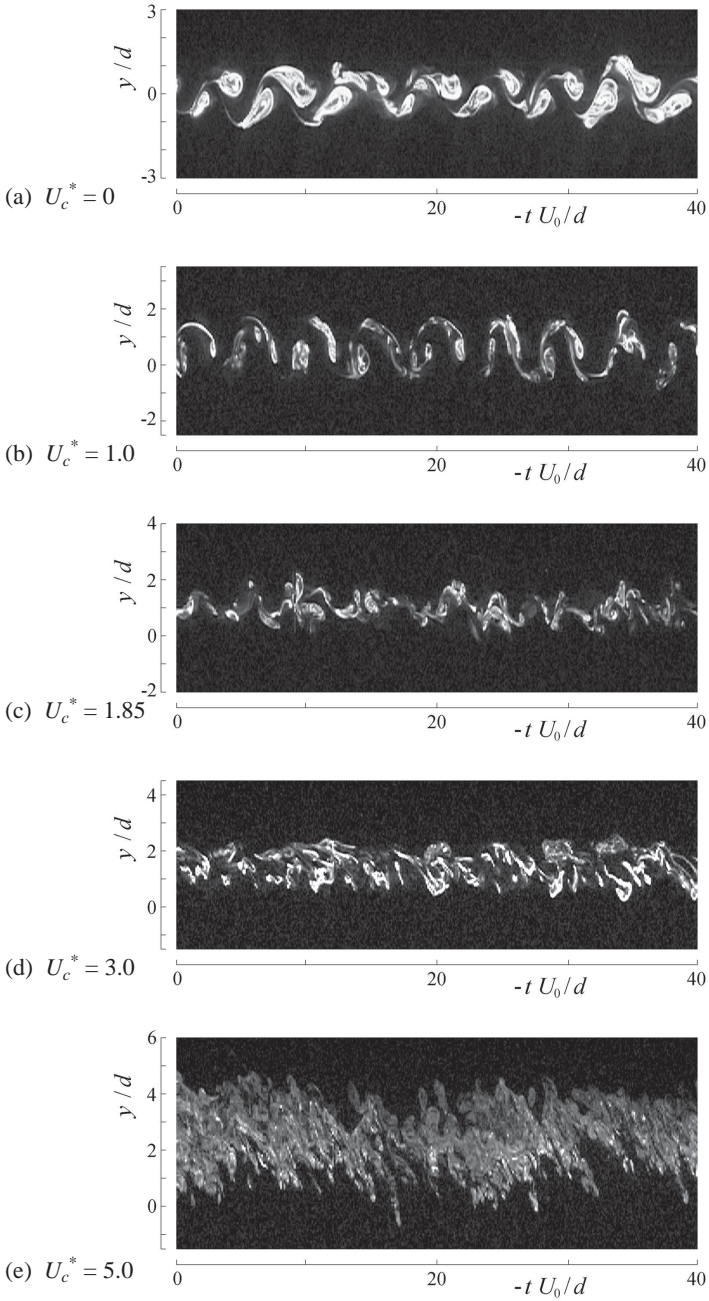
(a) $U_c^* = 0$

(b) $U_c^* = 1.0$

(c) $U_c^* = 1.85$

(d) $U_c^* = 3.0$

(e) $U_c^* = 5.0$

Fig. 3   Dye images based on the Taylor's hypothesis

(a)

(b)

(c)

(d)

(e)

Fig. 4   Contour maps of velocity fluctuation in the y-direction.

ther slowly decreases within a range of $1.7 < U_c^* < 3$. E_v remains little changed within a range of $3 \leq U_c^* \leq 4$, and increases again when $U_c^* \geq 5$.

Next, the lateral-direction fluctuation characteristics of the shear layer are analyzed by the POD method, and the spatial mode of the v-fluctuation profile is identified firstly. The eigenvalues, $\lambda_v^{(n)}$ and the empirical eigenvectors, $\phi_v^{(n)}$ are shown in Figs. 6 and 7, respectively. Here, n is an integer representing the mode, and only the results of $n = 1$ and 2 are shown in these figures. The eigenvalues, i.e., the ratio of contribution from each mode to the total energy, are as high as 75 to 80% at $U_c^* \leq 1.25$ only in the 1st mode. Then, the contribution ratio sharply decreases along with the increase in the rotational speed ratio within a range of $1.25 < U_c^* < 3.5$ down to the minimum ratio of 25% at $U_c^* = 3.5$. The contribution ratio $\lambda_v^{(1)}$ increases along with the rotational speed ratio within a range of $3.5 < U_c^* < 5$ up to over approx. 40% at $U_c^* \geq 5$. On the other hand, the contribu-
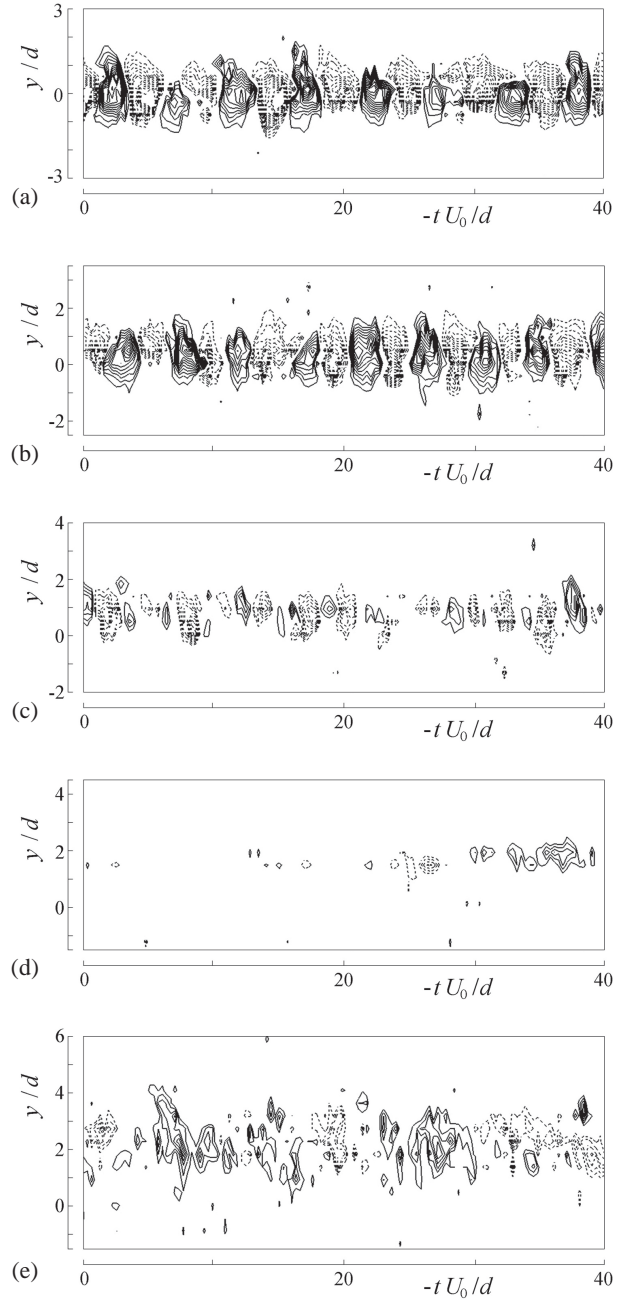
tion ratio $\lambda_v^{(2)}$ remains lower than the contribution ratio $\lambda_v^{(1)}$. It takes the maximum value of 12% at $U_c^* = 2.25$, and shows almost constant value within a range of $3 \leq U_c^* \leq 4$, and reaches approx. 15% at $U_c^* = 5.0$. It is evident from these results that there is a distinguished mode in the v-fluctuation profile of the wake in the vicinity of the rotating circular cylinder, and that, except for the rotational speed ratio range of $3 \leq U_c^* \leq 4$, the spatial fluctuations in the 1st and 2nd modes make the energy contribution of 50 % or more.

In Fig. 7, the eigenvectors of these modes are normalized by using the maximum value of $\phi_v^{(1)}$, and also the y-coordinate is normalized by using the position y_c in which the $\phi_v^{(1)}$ is the maximum value and the half-value width $b_{0.5}$ of the $\phi_v^{(1)}$ profile. From this scaling, the eigenvectors have similar distributions at all rotational speed ratios within the experimental range. It is evident from this that the spatial mode with dominant v-fluctuation receives almost no influence of the rotational speed
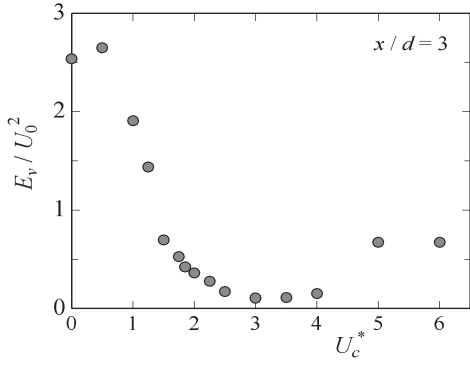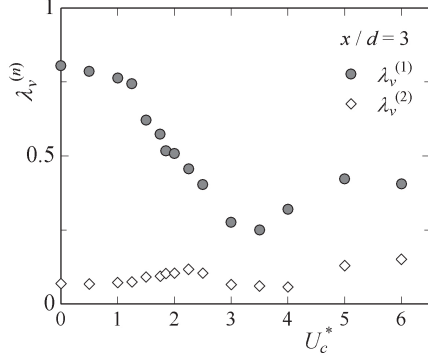
Fig. 5   Energy of v-fluctuation at $x/d = 3$.
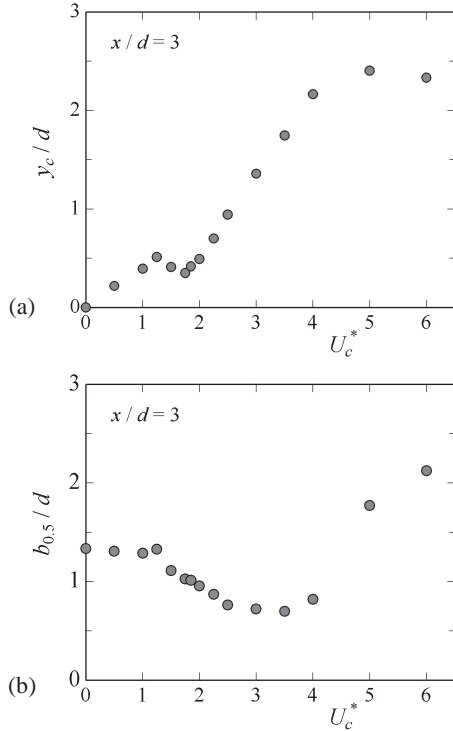

Fig. 6   Eigenvalues in the 1st and 2nd mode.

Fig. 8   Center position and width of the shear layer.

Fig. 7   Distributions of the eigenfunction at the first two POD modes.

Fig. 9   Power spectrum of the random coefficient of v-fluctuation in the first POD mode at $x/d = 3$.

ratio. Furthermore, it is interpreted that the 1st mode representing the bell-shaped distribution shows the y-direction fundamental oscillation of the shear layer and that the 2nd mode, which is an odd function, shows the expansion and compression around the center axis of the shear layer.

The relation of y_c and $b_{0.5}$, which characterize the spatial scale of the wake shear layer, to the rotational speed ratio are shown in Fig. 8. The coordinates, y_c can be interpreted as the
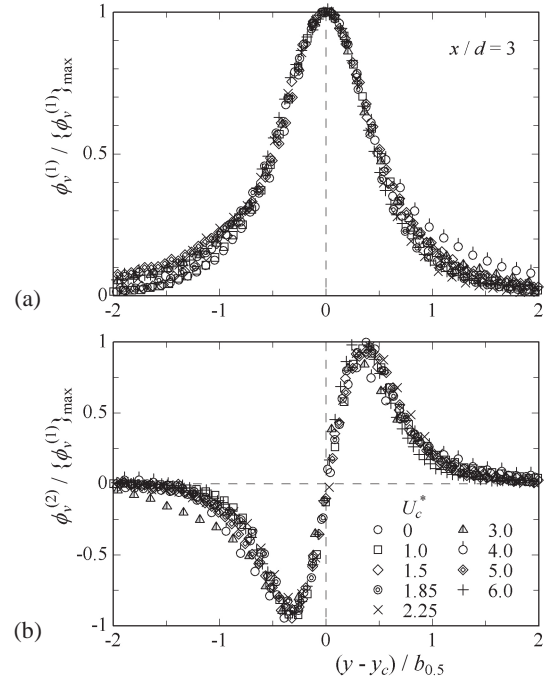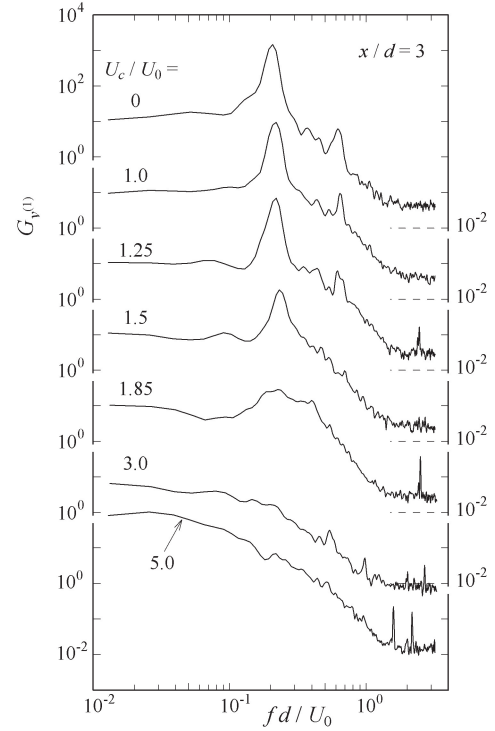
center of the shear layer, that is, the magnitude of the wake deflection due to the rotation of the circular cylinder can be estimated. On the other hand, $b_{0.5}$ indicates the y-direction scale of the shear layer. From Fig. 8(a), it is seen that y_c increases almost linearly at $U_c^* \leq 1.25$. It reaches the relative maximum of 0.51 d at $U_c^* = 1.25$, then increases monotonously from the minimum value of 0.35 d at $U_c^* = 1.75$ up to 2.4 d at $U_c^* = 5.0$, and then almost flattens out at $U_c^* \geq 5$. In contrast, it is seen from Fig. 8(b) that the half-value width $b_{0.5}$ shows almost a constant value of 1.3 d, then, in a range of $1.25 < U_c^* < 3$, de-

creases monotonously along with the increase in the rotational speed ratio, then in a range of $3 \le U_c^* \le 4$, shows approx. 0.7 d with little change, then, at $U_c^* > 4$, increases sharply, and then reaches 2.1 d at $U_c^* = 6.0$.

Spectra of the random coefficient

Lastly, the spectrum obtained as a result of Fourier transform of the velocity fluctuation is described. According to the analysis by the POD method of the v-fluctuation distributions described in the preceding section, the space mode of the fluctuation is identified, and the information in the time direction is obtained by projecting the fluctuation data set to each spatial mode. This is called "random coefficient" and defined by the following equation:

$$v^{(n)}(t) = \int v(y,t)\, \phi_v^{(n)}(y)\, dy \ . \tag{2}$$

By obtaining the spectrum of this coefficient, the occurrence state of each spatial mode can be examined in the frequency space. In this flow field, as shown in Fig. 6, since the fluctuation of the 1st mode is distinguished, the power spectrum of this 1st mode alone is shown in Fig. 9. At $U_c^* \le 1.5$, a spectral peak with the dimensionless frequency $f\,d/U_0 \approx 0.21$ in the center is seen. This peak frequency increases slightly along with the increase in the rotational speed ratio. At $U_c^* = 1.85$, broadband spectrum having high-energy hump is seen in a range of $f\,d/U_0 = 0.2 - 0.4$. At $U_c^* \ge 3$, the spectrum monotonously lowers the energy density toward the high-frequency zone, showing the profile similar to turbulent spectrum.

CONCLUSIONS

Results in the present study are put together, this flow field is classified, and the boundary values of the rotational speed ratios are shown in approximate numerical values as follows:

(i) $0 \le U_c^* \le 1.25$: The flow structure is that the staggered arrangement of the cylindrical vortex is dominant, and the deflection amount of the center coordinates of the vortex street increases linearly along with the rotational steed ratio.

(ii) $1.25 < U_c^* < 1.85$: The width of the wake shear layer is narrower in comparison with the lower rotational speed ratio, and the deflection amount of the wake center coordinates decreases due to the increase in the rotational speed ratio.

(iii) $1.85 < U_c^* < 3$: The width of the shear layer and the fluctuation energy contained in the shear layer decrease, together with the lowering of the coherence of fluid motions, along with the increase in the rotational speed ratio.

(iv) $3 < U_c^* < 4$: The flow in the shear layer is inactive, and the width of the shear layer and the fluctuation energy also take the minimum value, but only the deflection amount of the flow in the shear layer increases.

(v) $U_c^* \ge 5$: The disordered vortex structure like turbulent eddy is dominant, and the width of the shear layer and the fluctuation energy increase again.

REFERENCES

1. S. Taneda, 1977, Visual study of unsteady separated flows around bodies, *Prog. Aerospace Sci.*, 17, pp. 287-348.
2. C.H.K. Williamson, 1996, Vortex dynamics in the cylinder wake, *Annu. Rev. Fluid Mech.*, 28, pp. 477-539.
3. T. Leweke, C.H.K. Williamson, 1998, Three-dimensional instabilities in wake transition, *Euro. J. Mech. B/Fluids*, 17, pp. 571-586.
4. J.C. Williams, III, 1977, Incompressible boundary-layer separation, *Annu. Rev. Fluid Mech.*, 9, pp. 113-144.
5. P.G. Drazin, W.H. Reid, 1981, "Hydrodynamic Stability," Cambridge University Press.
6. M.B. Glauert, 1957, A boundary layer theorem, with applications to rotating cylinders, *J. Fluid Mech.*, 2, pp. 89-99.
7. M.B. Glauert, 1957, The flow past a rapidly rotating circular cylinder, *Proc. Royal Soc. London*, Ser. A, 230, pp. 108-115.
8. D.W. Moore, 1957, The flow past a rapidly rotating circular cylinder in a uniform stream, *J. Fluid Mech.*, 2, pp. 541-550.
9. W.M. Swanson, 1961, The Magnus effect: a summary of investigations to date, *Trans. ASME J. Basic Eng.*, pp. 461-470.
10. C.A. Koromilas, D.P. Telionis, 1980, Unsteady laminar separation: an experimental study, *J. Fluid Mech.*, 97, pp. 347-384.
11. D.B. Ingham, 1983, Steady flow past a rotating cylinder, *Computers and Fluids*, 11, pp. 351-366.
12. M. Cheng, Y.T. Chew, S.C. Luo, 1994, Discrete vortex simulation of the separated flow around a rotating circular cylinder at high Reynolds number, *Finite Elements in Analysis and Design*, 18, pp. 225-236.
13. Y. Takeda, 1995, Velocity profile measurement by ultrasonic Doppler method, *Exp. Thermal Fluid Sci.*, 10, pp. 444-453.
14. Y. Inoue, S. Yamashita, K. Kondo, 2002, The ultrasonic velocity profile measurement of flow structure in the near field of a square free jet, *Exp. Fluids*, 32, pp. 170-178.

UVP MEASUREMENT OF TAYLOR-COUETTE VORTEX FLOW
WITH SMALL ASPECT RATIO

Daisuke Ito*, Shingo Kishikawa**, Hiroshige Kikura*, Hideki Kawai**, Masanori Aritomi*
and Hiroshi Takahashi**

* Reseach Laboratory for Nuclear Reactors, Tokyo Institute of Technology,
2-12-1 Ohokayama, Meguro-ku, Tokyo, 152-8550, Japan, E-mail: ito@2phase.nr.titech.ac.jp
** Muroran Institute of Technology, 27-1 Mizumoto-cho, Muroran-shi, Hokkaido 050-8585, Japan

ABSTRACT

In this study, experiment was carried out for Taylor-Couette vortex flow. Taylor-Couette vortex flow with small aspect ratio can be generated by two concentric rotating cylinders; a rotating inner cylinder and a fixed outer cylinder. Two test section sizes with radial ratio of 0.375 and 0.667 were applied. Aspect ratio and gap between inner and outer cylinder were kept constant 3 and 25 mm respectively. Successive instantaneous and mean velocity profiles were obtained by using an ultrasonic velocity profiler (UVP). The spatiotemporal velocity field was analysed by two dimensional Fourier transform. In this case, the characteristics of Modulated Wavy Vortex Flow (MVF) and Wavy Vortex Flow (WVF) transition are confirmed. Furthermore, the bifurcations between each cell modes namely the N-2Cell, N-4Cell, A-3Cell and A-4Cell modes are clarified.

Keywords: Taylor-couette vortex flow, small aspect ratio, UVP

INTRODUCTION

Taylor-couette flow can be observed usually in between two concentric rotating cylinders and applied intensively for bioindustry and medical field [1]. The study of flow pattern and bifurcation in the finite boundary (end-wall) with small aspect ratio become great interest. Nakamura [2] studies the flow pattern with the variation of aspect ratio (1-8). Benjamin [3] studied the mutation of primary flow at the length of comparatively short annulus was changed. Mullin [4] investigated the evolution of primary flow and the transition from N-cell mode to (N+2)-cell mode by flow visualization. However the dfficulty is to understand the mode bifurcation measuring the spatiotemporal internal flow completely. For this reason, the direct measurement of the internal velocity field is nessesary.

Recently, in a series of research by Takeda using an ultrasonic velocity profiler (UVP), the spatiotemporal velocity field was measured. The flow fields were analysed by using two dimensional Fourier transform and the orthogonal decomposition technique, and intensities of coherent structual modes were quantitatively obtained. The variation of the intensities of various modes with respect to Reynolds number clearly shows a transition behaviour of the quasi-periodic state resulting from the wavy vortex mode and the modulating waves, which is found to disappear suddenly [5].

The purpose of this study is to perform a direct measurement of velocity field in the Taylor-Couette vortex flow structure with small aspect ratio by using an ultrasonic velocity profiler (UVP) and a visualization by laser sheet. Furthermore, the characteristics of the vortex flow such as vortex mode bifurcation, vortex intensity and spectrum transition in each vortex mode are investigated by Fourier transform analysis.

EXPERIMENTAL METHOD

Fig. 1 shows the set up of UVP measurement system, and Fig. 2 shows the test section. Test section consists of concentric cylinders made of Plexiglas. The inner cylinder was rotated, being direct driven by electric motor and the outer cylinder was stationary. To isolate the external vibration transmission, the appliance was held at the special isolator of resonance frequency of 0.5Hz. The length of the cylinder was H=75mm. In this experiment, two sizes of test section were utilized. The first one has R_1=15mm and R_2=40mm corresponding to η=R_1/R_2=0.375. The second one has R_1= 50mm and R_2= 75mm corresponding to η=R_1/R_2=0.667. Both types has the same gap of Δr=R_2-R_1=25mm and the aspect ratio, H/d=3. The working fluid was 68wt% glycerol water. The Reynolds number is given by Re=$\Omega R_1 d/\nu$ (Ω is rotation frequency of the inner cylinder, ν is kinematic viscosity).The number of generated vortex cell can be controlled by acceleration and deboost of motor frequency.

The applied measuring system for velocity profile measurements was UVP (MetFlow, Model X3-PSi) with a personal computer for data analysis. The principle of the ultrasonic Doppler method is based on the echography for position information and Doppler shift relationships for velocity detection. For more details about the UVP measuring system, see Takeda 1995.

Table 1. UVP parameters

Basic frequency	8MHz
Ultrasonic beam diameter	2.5mm
Channel distance	0.87mm
Measurement points	128(82)
Number of profiles	1024
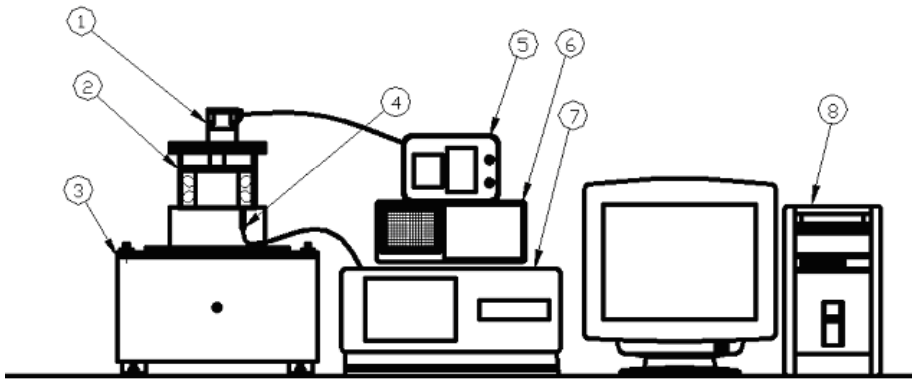
1.Motor, 2.Taylor-Couette Vessel, 3.Isolator, 4.US transducer, 5.Controller, 6.Oscilloscope, 7.UVP monitor, 8.Personal Computer
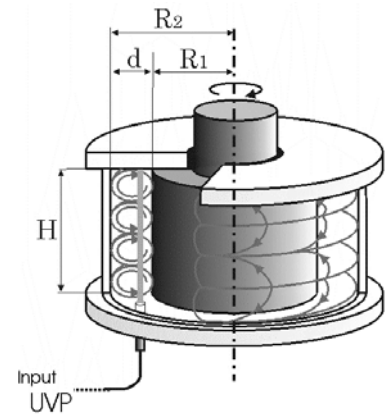
Fig. 1 Setup of UVP measurement


Fig. 2 Test section

In the present investigation, the ultrasound transducer was located at the outer wall of the end plates. The transducer was placed at the upper plate for η=0.667 and lower plate for η=0.375. The axial velocity components were measured in between the gap at the distance of 7 mm from the inner cylinder. The parameters of UVP measurement are shown Table 1. The ultrasound transducer was operated with a basic frequency of 8MHz. Then the sound velocity at 68wt% glycerol water was 1800m/s. In order to obtain the different vortex mode and bifurcation of vortex intensity, the Re was varied in the range of 0-2800.

Fig. 3 shows the set up of visualization. The conditions of each cell modes were visualized by using an Argon laser sheet. Static and moving images were obtained by digital camera and Hi-vision video camera, and edited by the personal computer.

RESULTS AND DISCUSSION

For the lower critical Reynolds numbers, the two-dimensional Couette flow is generated. In this case, the tangential velocity depends only on the radius position, V=$(0, V_\theta(r), 0)$. At the critical Reynolds number, the Couette flow becomes unstable and be transformed to the three dimensional Taylor vortex flow (TVF). In this case, the vortical structure called "counter-rotating toroidal vortices" was generated. In Taylor vortex flow at small aspect ratio, various flow patterns appear.

Fig. 4 shows the flow patterns obtained from visualization at the aspect ratio of 3. At a constant aspect ratio, the flow is classified as a primary mode and secondary modes. For the primary mode flow, the normal-2cell mode (N-2Cell, Fig. 4(a)) is formed smoothly from Couette flow by a gradual increase in Re. For the secondary mode, the normal-4cell mode (N-4Cell, Fig.4(b)) appears when the Re is increased abruptly at a certain value. The number of vortices in the secondary mode is different from those in the primary mode. From the results, normal mode can be observed only for the primary mode, while both normal and anomalous mode are observed for the secondary mode. On each end wall, the flow in the normal mode has a normal cell which gives an inward flow in the region adjacent to the end wall. The flow of the anomalous modes have an anomalous cell, which gives one or two outward flow near the end wall. In this case, the anomalous modes are anomalous-3cell mode (A-3Cell, Fig. 4(c)) and anomalous-4cell mode (A-4Cell, Fig. 4(d)).
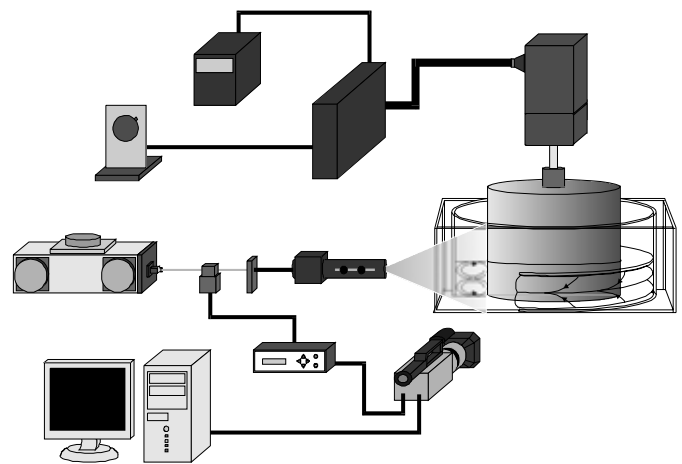
1 Taylor-Couette Vessel 2.Argon laser 3.AOM 4.Cylindrical lens 5.Laser sheet 6.PIV driver 7. Camera 8.PC 9.Motor 10.Controller 11.Tachometer 12.Speed converter

Fig. 3 Setup of visualization
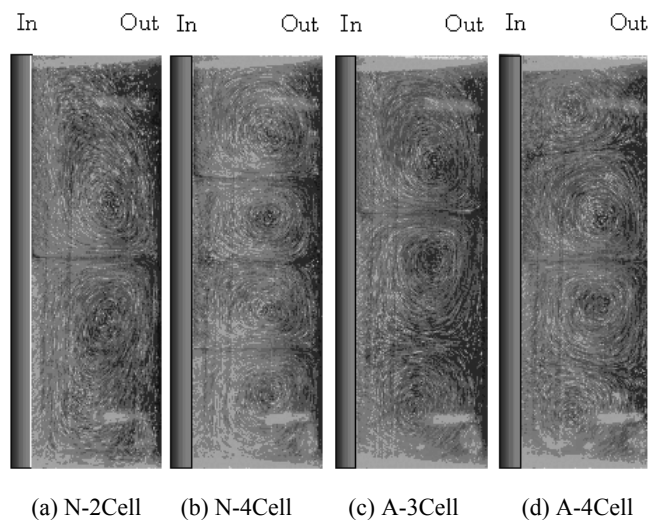
(a) N-2Cell　　(b) N-4Cell　　(c) A-3Cell　　(d) A-4Cell
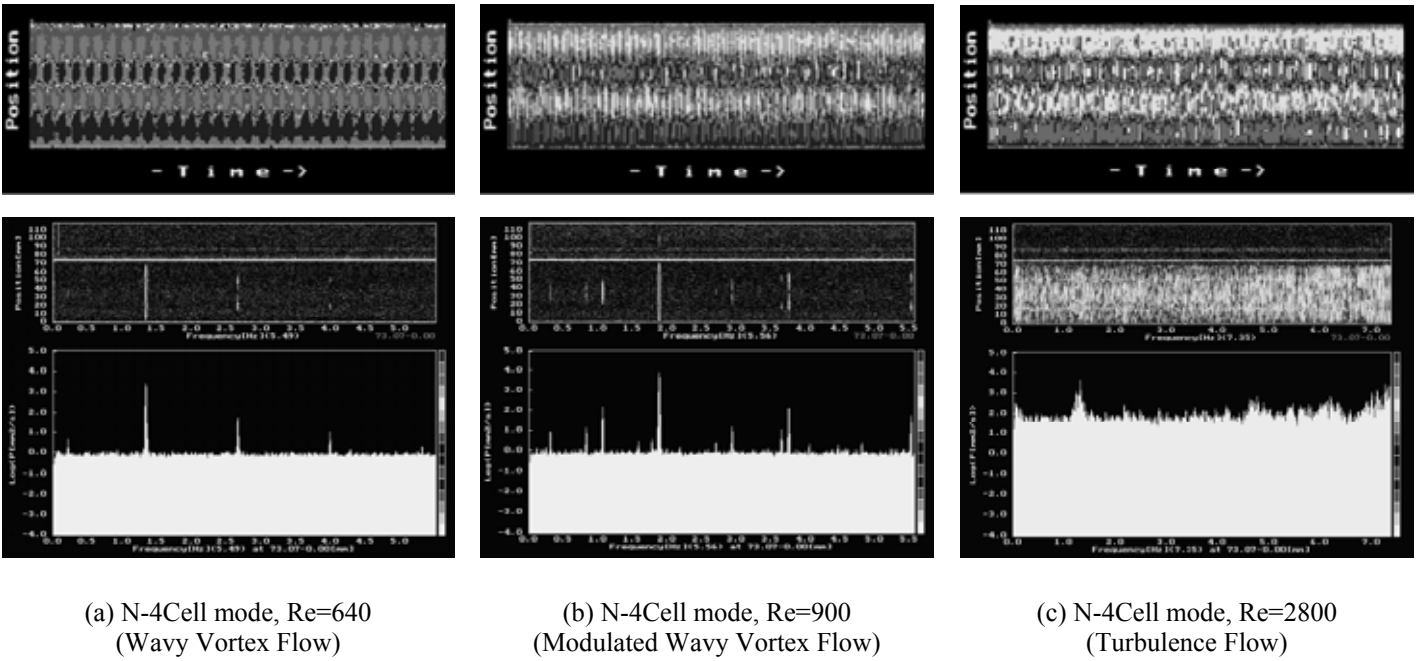
Fig. 4 Vortex mode at η=0.375 (Re=370)

(a) N-4Cell mode, Re=640
(Wavy Vortex Flow)

(b) N-4Cell mode, Re=900
(Modulated Wavy Vortex Flow)

(c) N-4Cell mode, Re=2800
(Turbulence Flow)

Fig. 5 Velocity fields and the corresponding space-averaged power spectra at η=0.667

(a) N-4Cell mode, Re=870
(Wavy Vortex Flow)

(b) N-4Cell mode, Re=1230
(Modulated Wavy Vortex Flow)

(c) N-4Cell mode, Re=2360
(Turbulence Flow)
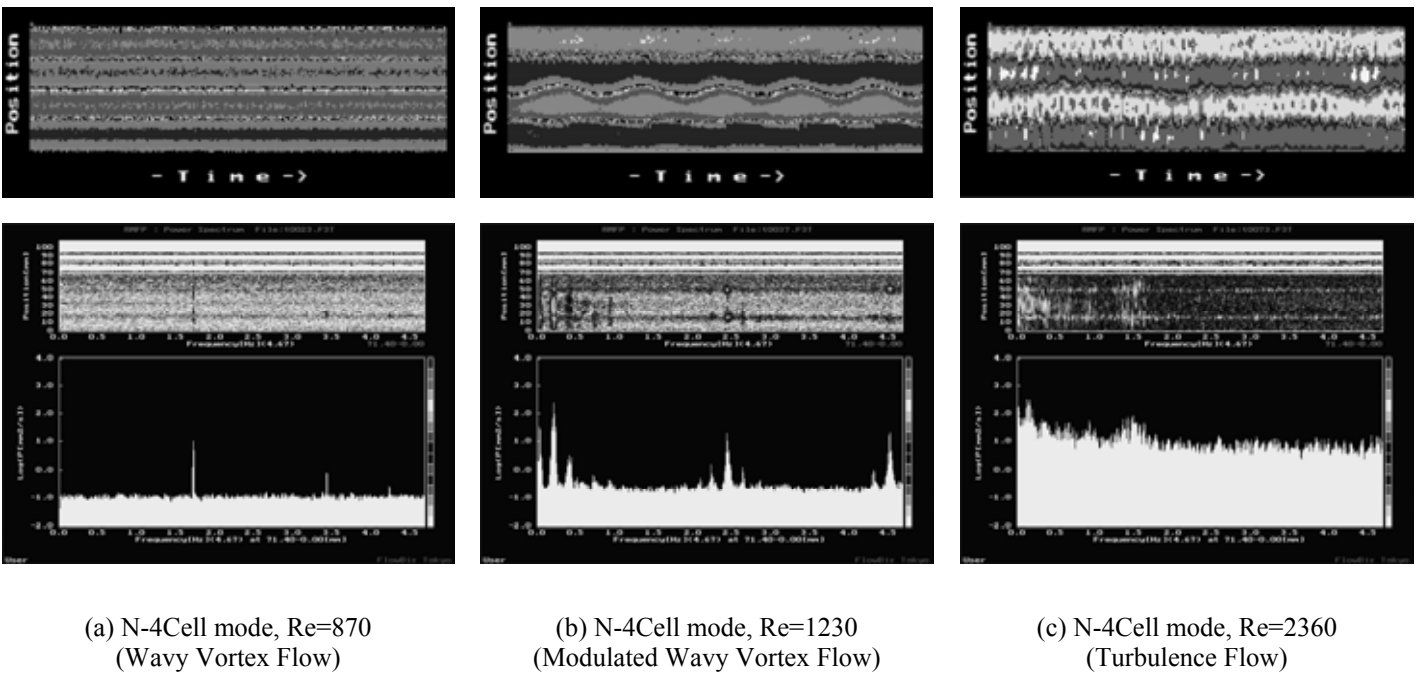
Fig. 6 Velocity fields and the corresponding space-averaged power spectra at η=0.375

With the increase in Re, the flow instability occurs and deforms the Taylor vortex to produce a time-dependent non-axisymmetric flow called the wavy vortex flow (WVF). With further increasing the Re, an additional wave mode appears which modulates the WVF; this flow is called the modulated wavy vortex flow (MWF).

Fig. 5 and Fig. 6 show the velocity fields and the corresponding space-averaged power spectra in the WVF and MWF and turbulence flow for N-4Cell mode at η=0.667 and η=0.375, respectively. The velocity levels in those figures are represented by the color contour. For WVF, oscillation with basic wave frequency of 1.32Hz is appeared clearly from both velocity field and its power spectra in Fig. 5(a), while the basic wave frequency of 1.6 Hz is observed only from power spectra in Fig. 6(a). With increasing of Re, the basic wave frequency is shifted to higher level. At η=0.667 in Fig. 5(b), the additional frequency of 1.05Hz is appeared together with the existing basic wave frequency of 1.87Hz for Re=900. At η=0.375 in Fig.6(b), the broader shape of power spectra is appeared with increasing of Re upto 1230. Further increasing of Re, flow field become complete turbulence as illustrated in Fig. 5(c) and 6(c). Thus, the characteristics of vortex flow can be obtained by FFT analysis.
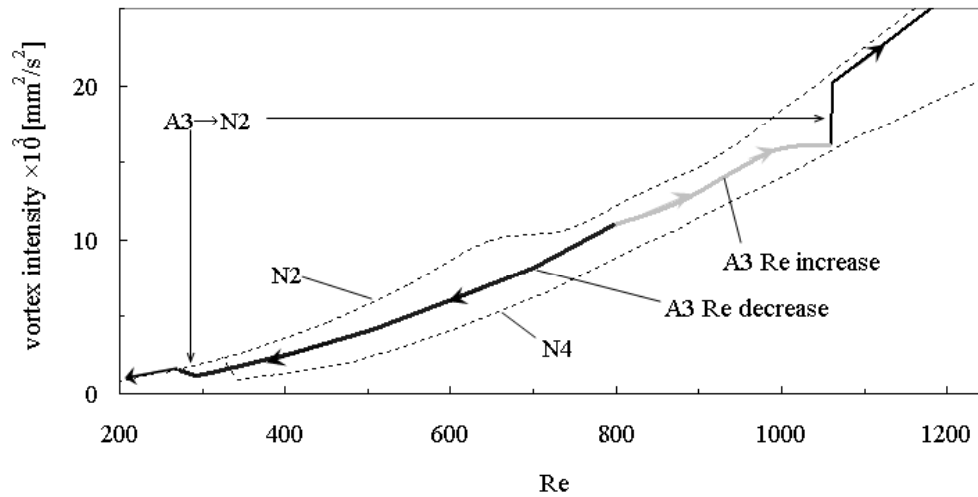
Fig. 7 Influence of bifurcation of Vortex intensity to Reynolds number at η=0.667

Using an ultrasonic velocity profiler, successive instantaneous and mean velocity profiles were obtained.

At N-2Cell mode, there is no significant difference of vortex intensity in the transition with the variation of Re. However the dependency of Re on vortex intensity is observed for N-4Cell and A-3Cell case. For example, Fig. 7 shows the bifurcation of vortex intensity for A-3Cell in term of Re. An upper and lower dotted lines represent vortex intensity for N-2Cell and N-4Cell respectively. With the increase of Re from Re=800, the characteristic of vortex intensity for A-3Cell approaches to the behavior for N-4Cell at Re=1060, then it switches to the behavior for N-2Cell when further increase of Re. During the increasing of Re from 800 to 1060, vortex intensity is departed from the original path at Re =1000. This can be explained by the influence of instability. In the other hand, the vortex intensity for A-3Cell approaches to behavior for N-2Cell when Re decreases. This bifurcation is the irreverible process.

CONCLUDING REMARKS

Spatio-temporal velocity profile of Taylor-couette flow at small aspect ratio was obtained by UVP measurement. Furthermore, the characteristic of each cell modes and spectrum transition of bifurcation were confirmed. Finally, bifurcation in term of Re was clarified by considering the measured vortex intensity.

REFERENCES

1. S.T.Wreley and R.M.Luepton, 1999, Internal particle motion in a Taylor Couette rotating filter, *Physics of Fluid*, 11-2, pp.325-333.

2. I.Nakamura et al., 1988, Experiment on a Taylor Vortex Flow in a Gap with a Small Aspect Ratio (2nd Report, Instability of Taylor Vortex Flows), *JSME International Journal*, 54-505, B, pp.2425-2432.

3. T.B.Benjamin, 1978, Bifurcation phenomena in steady ows of a viscous uid. II. Experiments, *Proc.R.Soc. London A*, 359, pp.27-43.

4. G.Pfister et al., 1988, Bifurcation phenomena in Taylor-Couette flow in a very short annulus, *J.Fluid Mech.*, 191, pp.1-18.

5. Y.Takeda, 1999, Quasi-periodic state and transition to turbulence in a rotating Couette system, *J. Fluid Mech.*, 389, pp.81-99.

ULTRASONIC MEASUREMENTS IN ICE SLURRY GENERATION

BY DIRECT CONTACT EVAPORATION

Didier Vuarnoz*, D. Ata-Caesar*, Osmann Sari*, Peter William Egolf*

*EIVD, Route de Cheseaux 1, CH-1401 Yverdon-les-Bains, dvuarnoz@eivd.ch

ABSTRACT

Important reductions of refrigerant amounts can be achieved by using secondary refrigeration fluids. Ice slurry is a two-phase fluid and thus, compared to single phase secondary refrigeration fluids, offers the advantage of the latent heat of fusion when the ice phase melts during heat exchange. Therefore, the challenges that the introduction of ice slurry as a common thermal fluid is facing are, in the first place, how to generate ice slurry in an efficient and ecological way. Optimal design of a direct contact ice slurry generator requires studying the injection and the mechanisms of the evaporation of the refrigerant in the aqueous solution. The evaporation chamber is the main domain of our investigations presented in this paper. Some aspects of the evolution of the liquid-to-gas phase-change of the refrigerant, and of the liquid to solid phase-change of the water are presented in this article. Basic theory, velocity profiles achieved by <u>U</u>ltrasonic <u>D</u>oppler <u>M</u>ethod (UDM), and extracted values from measurements help to understand how to optimise the process of ice creation by an expanding jet of refrigerant in a column of water.

Keywords: Ice-slurry, jet, bubbles, drop, drobble, refrigerant.

INTRODUCTION

Ice slurry consists of numerous ice particles with an average size below 1mm, suspended in a carrier fluid. It is therefore a two-phase colloidal suspension, classed in the family of the <u>P</u>hase <u>C</u>hange <u>S</u>lurries PCS. There are two main different methods of producing ice slurry: the heterogeneous nucleation and the homogeneous nucleation. In this paper we deal only with the *homogeneous nucleation. Direct injection*, where the non-miscible refrigerant (dispersed phase) is injected into the brine fluid (continuous phase), is an interesting method in terms of energy and cost efficiency. (Chuard & Fortuin, 1999) with C4F8, (Wobst and Vollmer, 1999) with R600a and (K. Kiatsiriroat *et al*., 2003) produced ice slurry using this type of generator.

In most research approaches, the first approximation to study direct contact evaporation is based on the study of single drops evaporating in an immiscible medium. A detailed review of the state of the art was performed by (Lugo, 2004). It has been confirmed experimentally, that the configuration of a single drop during evaporation is that given in (Sideman & Taitel, 1964). As soon as the drop starts to evaporate, the liquid forms a meniscus at the bottom of the vapour bubble which begins to rise. Trajectories of rising bubbles were studied by (Zun, 1986), (Tomiyama *et al*., 1993) and (Sletta *et al*., 04). Theoretical and experimental single drop studies have been carried out by many authors. (Sideman & Taitel 1964) used the general drop-bubble configuration to solve the energy equation; they give an expression of the average Nusselt number (Nu) as a function of the Peclet number (Pe) and the opening angle β (fig. 2); they assume that heat transfer only takes place at the liquid-liquid interface of the evaporating drop.

They validate their expressions with experimental results obtained with pentane and butane drops injected into distilled or sea water. (Tochitani *et al*., 1977) studied the evaporation of single drops of pentane and furan in aqueous glycerol. The same authors compare the experimental heat transfer characteristics with a Stokes flow model. Heat transfer coefficients are determined using the liquid-liquid interfacial area or the total surface area of the evaporating drop as the heat exchange surface. (Shimizu et Mori, 1988) dealt with the evaporation of single drops of R113 and n-pentane injected into water under pressures up to 0.48 MPa. The heat flow rate is determined from the volume variation; the authors propose two configurations: 1) the drop consists of saturated liquid and saturated vapour of the dispersed phase (explanation given in the remainder); and 2) the drop consists of saturated liquid of dispersed phase and saturated vapours of both the water and the dispersed phase.

The main objective of this study is, to investigate if Ultrasonic Doppler measurements are adequate to better understand the interrelated phenomena involved in such injection and evaporation of the refrigerant including the ice creation. (Ata-Caesar, 2004) performed a complete study on the choice of the refrigerant for this ice generation technology. For laboratory safety reasons however, the present studies were done with the refrigerant C_4F_8.

BASIC THEORY

The injection

The configuration of the injected refrigerant can be classified into the four flow regimes shown in fig. 1 (Clift et al. 1978). With interfacial tension as a parameter, the regimes are a function of the nozzle characteristics and the flow rate of the

injected fluid. Based on the following definition of the injection Reynolds number as proposed in (1):

$$Re_{inj} = \delta_c * D_{inj} * U_{inj} / \mu_c \qquad (1)$$

(Meister and Scheele, 1969) point out three flow regimes. For Re_{inj} below 300 the regime is drop to drop. For Re_{inj} between 300 and 3000 the injected fluid configures in a column-like flow pattern. The last case is the turbulent regime, often denoted atomization. We have investigated the drop to drop regime.
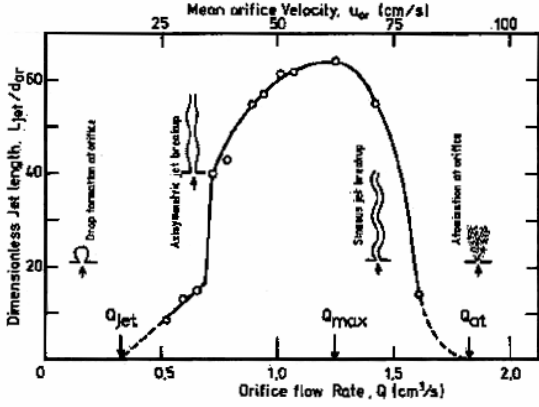

Fig. 1: Injection regime as a function of the mass flow and the nozzle characteristics.

The evaporation
To schematize the evolution of the evaporating drop, a simplified model was used (Lugo, 2004) to describe the geometry of the evaporating refrigerant drop (fig 2). The word "drobble" in the following text refers to a liquid drop during evaporation.
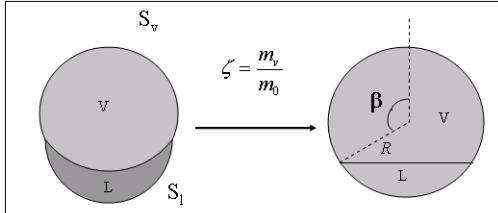

Fig. 2: Geometrical description of a drop during evaporation. The drop quality (ζ) is the ratio of the vapour to initial drop mass.

The radius as a function of drobble quality is expressed by:

$$R^3 = R_0^{\,3} \left[1 + \zeta \left(\frac{\rho_l}{\rho_v} - 1 \right) \right] \qquad (2)$$

The bubble opening angle as a function of drobble quality is expressed by:

$$3\cos\beta - \cos^3\beta + 2 = \frac{4(1 - \zeta)}{1 + \zeta \left(\dfrac{\rho_l}{\rho_v} - 1 \right)} \qquad (3)$$

where β is the opening angle, R and R_0 are the radius and the initial radius, ρ_l and ρ_v are refrigerant liquid and vapour densities. These equations can be used to predict the growth of the drobble. The drobble velocity U is obtained by simplifying and solving the following momentum equation:

$$\rho_d V_d U \frac{dU}{dz} = (\rho_c - \rho_d)\tfrac{4}{3}\pi R^3 g - \frac{\pi}{2}\rho_c C_D R^2 U^2 \qquad (4)$$

where g is the gravity, V is the volume, C_D is the drag coefficient, ρ_c is the carrier fluid density, z is the vertical coordinate and index d stands for "dispersed phase" (related to the system drop + bubble). Rigorously, other terms should appear in this equation (added mass, parachute effect, etc.) but they prove to be negligible as the evaporation starts. The motion is mainly controlled by buoyancy and drag forces. There are many expressions for the drag coefficient of drops and bubbles, but many authors use only some formulae for air bubbles. Heat transfer is governed by:

$$\dot{Q} = S_{hex} h (T_c - T_d) = U \rho_d V_d \Delta h_v \frac{d\zeta}{dz} \qquad (5)$$

where $\dot{Q}$ is the heat exchanged between the carrier fluid and the particle per unit time, S_{hex} and h are the heat transfer surface and the heat transfer coefficient (they vary widely from one author to another), T_c and T_d are the temperature of the carrier fluid and the particle temperatures (for the evaporation of a single drop, both are assumed to be constant) and Δh_v is the enthalpy of vaporization of the refrigerant.

EXPERIMENTAL METHOD

The experimental setup
Our experimental setup for ice slurry generation (fig. 3) is identical to the one of (Chuard & Fortuin 1999).
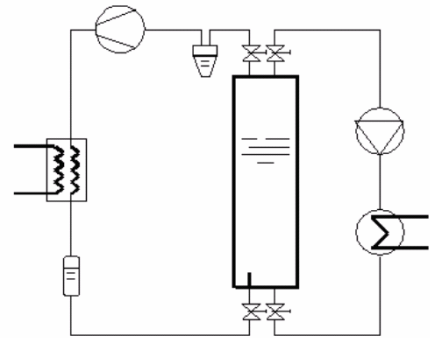

Fig. 3: Schematic drawing of the direct injection system.

In this vapour compression cycle direct contact evaporation is applied. Technical differences from the conventional installations are the evaporation chamber and the injection of refrigerant. The injection is performed through a nozzle, which causes not only the expansion of the refrigerant but also the movement and turbulence of the mixture in the evaporation chamber. A tube in Plexiglas of 400mm diameter was fixed 3 cm above the nozzle to concentrate the injected flux of refrigerant. The refrigerant expands and evaporates inside the evaporation chamber at constant pressure and constant temperature (<0°C). The vapour rises through the contents of the chamber and the compressor sucks it away. During the evaporation, the latent heat of vaporization is withdrawn from the surrounding carrier fluid. At locations where this cooling effect leads to temperatures slightly below the freezing temperature of the aqueous solution, the water in the solution begins to freeze to tiny ice particles, which are suspended in the remaining unfrozen aqueous solution. This way, a certain amount of the water of the solution can be transformed to finely dispersed ice. The remaining aqueous solution has a

higher concentration of freezing depressing agent and stays liquid.

The applied measurement device for experimentally studying the injection is an Ultrasonic Velocity Profiler UVP-XW3. The positions of the UVP probes are detailed in fig. 4. The UVP measurements were performed separately for each height.
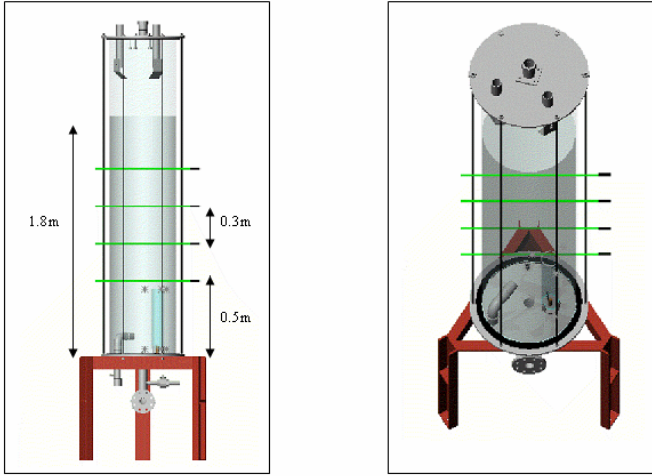

Fig. 4: Drawing of the evaporation chamber with the position of the four ultrasonic transductors of 2 MHz.

RESULTS AND DISCUSSION

One way to show the results of a UVP measurement is the colour plot showed in fig. 5. From this plot, the diameter, velocity and horizontal position of drobbles can be extracted. Table 1 shows average values determined from recorded data such as in fig. 5 and fig. 6. The velocity, size and drobble position along the ultrasonic beam are listed for the four heights where measurements were taken.
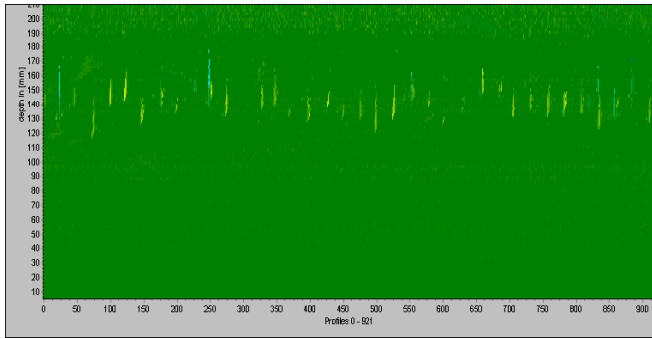

Fig. 5: UDM series of thousand velocity profile measurements of drop to drop injection regime at z = 800mm above the injection nozzle.
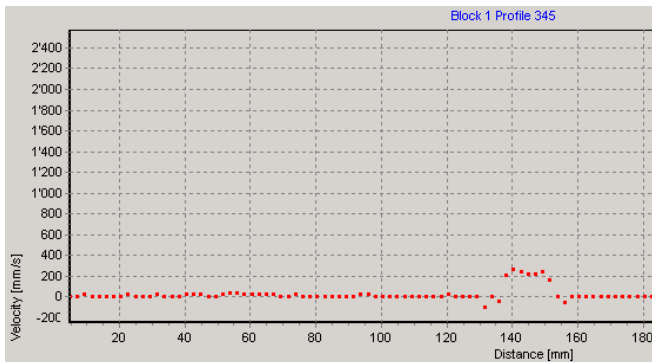

Fig 6: Velocity profile used for the determination of the diameter and velocity of the drobbles at z = 800mm.

Level	Z [m]	D [mm]	U [m/s]	x_{max} [mm]	f_{inj} [Hz]
1	0.5	22.2	0.366	-3.9 / 4.5	0.737
2	0.8	26.6	0.432	-12.4/ 10.8	3.119
3	1.1	23.7	0.448	-17.4/ 16.1	0.758
4	1.4	24.9	0.397	-21. 6 / 18.7	1.4

Table 1: Synthesis of mean values determined from data of Ultrasonic Doppler Method investigation.

The probability that the trajectory of a drobble crosses the ultrasonic beam (diameter = X mm) decreases with the distance between the nozzle and the investigated position. The drobble diameter for each level is determined from the maximal trace of each measurement series. Figure 7 shows the drobble diameter versus column height determined with UVP (points). The measured value at the second level deviates rather strongly though. The dashed line indicates the rapid drobble growth shortly after injection of the liquid drop.
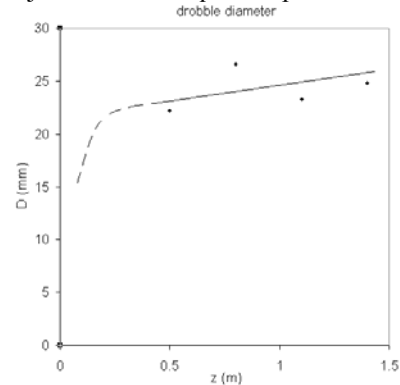

Fig. 7: Experimental results of the drobble diameter versus the distance z.

Figure 8 shows the drop velocity as a function of the column height determined with UVP (points). The tendency is shown with the line. The measured value at the highest level deviates rather strongly though. The dashed line indicates the strong drobble acceleration due to its rapid growth shortly after injection of the liquid drop.
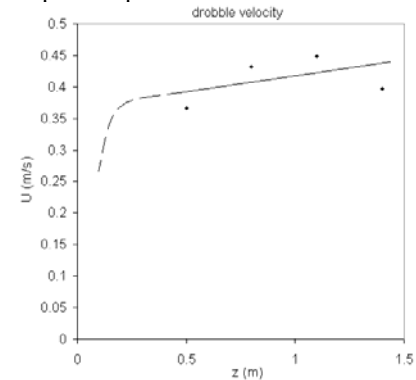

Fig. 8: Experimental results of the drop velocity versus the distance z.

A two dimensional description of the drobble trajectory can be determined by looking at the position of each particle appearing in the measured velocity profile series (as in fig. 6). For each investigated level, the two particles found at the largest opposing distances from the nozzle axis are represented in figure 9.
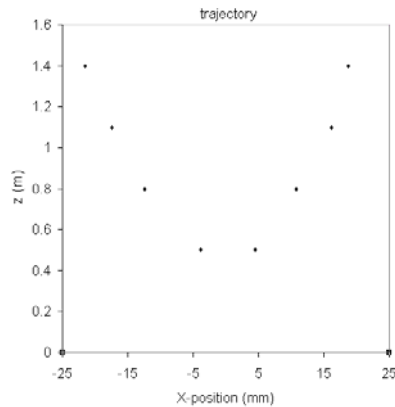
Fig. 9: Maximal lateral position versus column height z obtained UVP. The axis of the nozzle is located at X = 0.

Ultrasonic Doppler measurements appear to be suitable for investigating the fluid dynamic behaviour of refrigerant drops evaporating in a non-miscible fluid as occurs in the evaporation chamber of a direct contact ice slurry generator. Comparison of the UDM experimental results with numerical simulations of the aforementioned fluid dynamic behaviour can provide an efficient approach towards utilising UDM in experimental multiphase fluid dynamics investigations. At present, commercial Computational Fluid Dynamic (CFD) codes can be efficiently applied to investigate bubbly flows, drag on particles and the influence of turbulence on flow patterns. However, the phenomena occurring during the evaporation of liquid drops in a liquid surrounding are not yet implemented in commercial CFD codes. This limitation calls for specialized numerical simulation codes, which take the drop to bubble phase change into account, in order to be able to compare theoretical to experimental results for the entire drop to bubble evolution. Numerical investigations (Lugo, 2004) have shown remarkable dependence of the drobble behaviour on the initial conditions of the injected refrigerant drop, such as the initial diameter and velocity. These necessary parameters for reasonable theoretical investigations are although difficult to determine.

CONCLUSIONS AND OUTLOOK

The Ultrasonic Doppler Method has been applied to the process of ice slurry generation by direct injection of a refrigerant into an aqueous solution. Some theory of the physics involved, such as the injection regime and the evaporation processes, has been shown. The main objective of this work has been to investigate the fluid dynamic behaviour of evaporating refrigerant drops in an immiscible fluid and the approach taken has been to evaluate how suitable the UDM technique is for such investigations.
The diameter, the velocity and the position of evaporating refrigerant drops were determined from the results of Ultrasonic Doppler measurements. The determined values agree well with numerical results. For better comparison with numerical simulation, improved studies of the initial conditions of the injected refrigerant drop are needed.

ACKNOWLEDGEMENT

REFERENCES

1. Chuard M., Fortuin J., 1999, COLDECO – A new technology system for production and storage of ice. *Proceedings of the First Workshop on Ice Slurries*. IIF/IIR : 140-146.

2. Wobs E., Vollmer D., 1999, Ice slurry generation by direct evaporating of refrigerant. In: Proceedings of the First Workshop on Ice Slurries. IIF/IIR : 126-132.

3. Kiatsisriroat T., Vithayasai S., Vorayos N., Nuntaphan A., Vorayos N., 2003, Heat transfer prediction for a direct contact ice thermal energy storage. *Energy Conversion Management* 44 : 497-508.

4. Lugo, R., 2004, Contribution à l'étude de deux methods de fabrication de coulis de glace par contact direct: Evaporation sous vide et injection directe. Thèse du Conservatoire National des Arts et Métiers.

5. Sideman S., Taitel Y., 1964, Direct-contact heat transfer with change of phase: evaporation of drops in an immiscible liquid medium. *Int. J. Heat Mass Transfer* 7: 1273-1289.

6. Zun, I., 1986, The non-rectilinear motion of bubbles rising through a stagnant and disturbed liquid. *Proc. World Cong. III of Chem. Eng.* , vol II. 214-217.

7. J. Sletta, D.Vuarnoz, O. Sari, D. Ata-Caesar, P.W. Egolf, , 2004, Production de « coulis de glace » à germination spontanée : Système COLDECO®, Rapport Scientifique Final HES-SO.

8. Tomiyama A., Zun I., Sou A., Sakaguchi T., 1993, Numerical analysis of bubble motion with the VOF method. *Nucl. Eng. Des.* 141: 69-82.

9. Tochitani Y., Nagagawa T., Mori Y., Komotori K., 1977, Vaporization of single liquid drops in a immiscible liquid. Part II: Heat transfer characteristics. *Wärme-und Stoffübertragung.* 10:71-79.

10. Shimizu Y., Mori Y. Evaporation of single drops in an inmiscible liquid at elevated pressure. Experimental study with n-pentane and R113 drops in water. *Int. J. Heat Mass Tran*sfer 31:1843-1851.

11. Ata-Caesar, D., Sletta, J., Sari, O., Egolf, P.W., 2004, Refrigerant choice for ice-slurry production in direct contact heat exchangers, *Proc. of the Sixth Gustav Lorentzen Conference on Natural Working Fluids of the International Institute of Refrigeration*, Glasgow, 29th of Aug. – 1st of Sept. 2004.

NOMENCLATURE
Latin symbols
C_D drag coefficient
D   mean diameter (m)
g gravity (m s^{-2})
h heat transfer coefficient (W m^{-2} K^{-1})
Δh_v enthalpy of vaporization (kJ kg^{-1})
$\dot{Q}$ power (W)
R   radius (m)
S_{hex} heat exchange surface (m^2)
T   temperature (°C)
U   velocity (m s^{-1})
V   volume (m^3)
z   vertical coordinate (m)
Greek symbols
β   opening angle
ρ   density (kg/m^3)
ζ   drop quality
μ   dynamic viscosity (Pa s)
Subscripts
c continuous phase
d dispersed phase
l dispersed liquid phase
v dispersed vapour phase
inj   injection

SPATIAL AND TEMPORAL STRUCTURE OF A TIME DEPENDENT PIPE FLOW

Y. Sato*, Y. Takeda*, D. Sugiyama*

* Div. of Mechanical Science, Graduate School of Engineering, Hokkaido University, Kita-13 Nishi-8, Sapporo, Japan,
E-mail: yohei@ring-me.eng.hokudai.ac.jp

ABSTRACT

Time dependent velocity distribution of an oscillating pipe flow has been measured by ultrasound Doppler method. Velocity field showed typical pulsatile flow nature as totally different from a stationary pipe flow.

Time domain Fourier transfer was used to obtain temporal characteristics of this flow, as being space dependent power spectrum. By decomposing temporal characteristics and analyzing their spatial dependence of each model, we found the energy is more concentrated in the boundary region (named as HPA – Higher Power Area), and it appears that turbulence starts to be generated in this area by increasing Reynolds number.

Keywords: Oscillating flow, Spacio-temporal Measurement, Weakly Turbulent flow, HPA

INTRODUCTION

The theoretical solution of purely oscillating flow was determined by Uchida [1], and Annular Effect was known as preceding of the phase near the wall of the pipe. Experiments on oscillating pipe flow have been carried out by Christian von Kerczek [2] for the Stokes layer in oscillating flow and Merkli & Thoman [3], Hino [4] for transition to turbulent flow.

In earlier experiments, it was possible to measure at only one spatial point at the same time. In this experiment, Ultrasonic Doppler Method (UDM) made possible measurement on a line at the same time. The spatial structure of the oscillating pipe flow can be available with UDM.

STABILITY DIAGRAM

Figure 1 shows the stability diagram of purely oscillating pipe flow. The types of oscillating pipe flow can be classified in terms of the Reynolds number R_δ and Stokes parameter λ into laminar flow, weekly turbulent flow and conditionally turbulent flow. In weakly turbulent flow, turbulence is generated weekly. In conditionally turbulent flow, turbulence is generated suddenly in the decelerating phase. R_δ is defined as $R_\delta = U\delta/\nu$ using the Stokes-layer thickness $\delta = (2\nu/\omega)^{1/2}$ and the cross-sectional mean velocity amplitude $U = A\omega$. λ is defined as $\lambda = 1/2d(\omega/2\nu)^{1/2}$. ($\nu$=kinematic viscosity, ω=angular frequency, A=amplitude and d=inner diameter of the pipe)
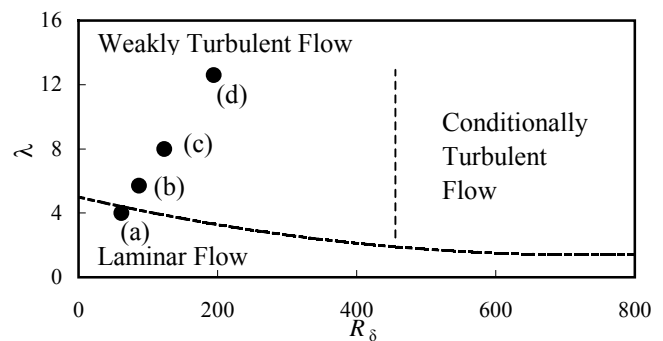

Figure 1. Stability Diagram, Hino *et al.* [4]

EXPERIMENTAL ARRANGEMENT

The general arrangement of the equipment is shown in Figure 2. The pipe is connected to the reservoir at one end. The oscillations are driven by an oscillating piston at the other end.
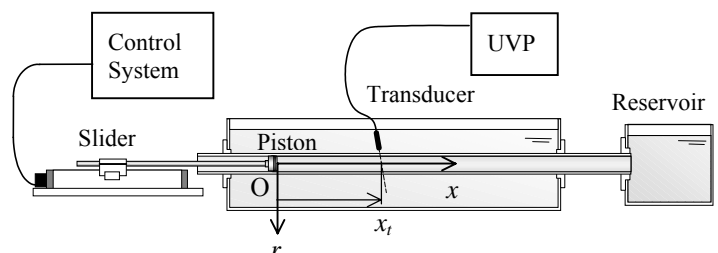

Figure 2.Experimental arrangement and coordinate axis

A liner motion stepping motor makes the monotonic oscillation of piston. The pipe has an inner diameter of 26 mm and a length of 2000 mm. The measuring section is in a large water tank to prevent changing of temperature.

Velocity was measured by Ultrasonic Velocity Profiler (UVP) with a basic frequency 4 MHz. The transducer is fixed above the pipe with an angle of 78° between the ultrasonic beam axis and the pipe axis. The tracer is Grilex5P1 (ρ_t=1.05g/cm^3). 20 % Glycerol-water solution is used for the fluid to make the density of fluid closer to the density of tracer.

Coordinate axes are shown in Figure 2. The origin O is set on the center of the pipe. The x-axis has the direction of the axis of the pipe. The r-axis has the direction of the radius of the pipe. The x-component of the piston x_t is the intersection of the x-axis and the ultrasonic beam axis.

The piston moves with sin-wave $x=A \sin\omega t$ (x =position of piston head, A =amplitude of sin-wave, ω =angular frequency and t=time). A was kept constant A=100 [mm]. ω was set at 0.31, 0.62, 1.25 and 3.14 [rad]. Then R_δ=61.5, 87.0, 123.0 and 194.5 and λ=4.0, 5.7, 8.0 and 12.6 (Figure. 1 (a) ~ (d)). The measuring points are set every $\Delta r/D$=0.028 from r/D=-0.5 to r/D=0.5 every $\Delta x/D$=0.769 from x/D=5 to x/D=23.4.

EXPERIMENTAL RESULTS AND ANALYSIS

Figure 3 shows an example of an instantaneous velocity profile in the accelerating phase. The velocity near the wall is higher than center (Annular effect). Figure 4 is a typical example of the velocity-time series at one spatial point showing a regular sinusoidal motion.

Each time series data was analyzed by FFT in order to see the temporal characteristics of the flow.

Then, analyzed data was averaged over x-axis for 5 < x/D < 23.4. The space dependent power spectra are shown in Figure 5 for various Reynolds number. The coordinate is the radial position and the abscissa is frequency. The collar represents the magnitude of the power. These graphs show the distribution of the power on the r-axis. The power of the base frequency is much higher than the others at every position. When R_δ and λ are increased, the higher order harmonics can be recognized clearly especially near the wall.
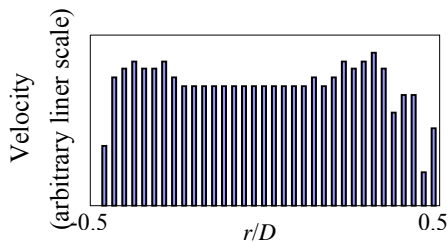

Figure 3. Example of velocity profile
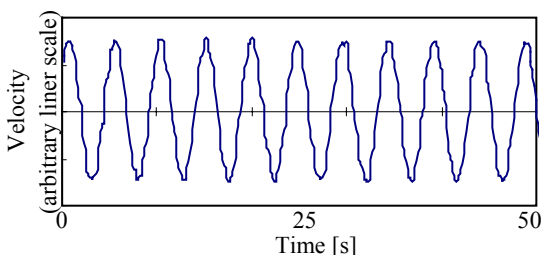(R_δ=123.0, λ=8.0, x/D=21.15, θ=1.3π)

Figure 4. Example of velocity-time series
(R_δ=123.0, λ=8.0, x/D=21.15, r/D=0)
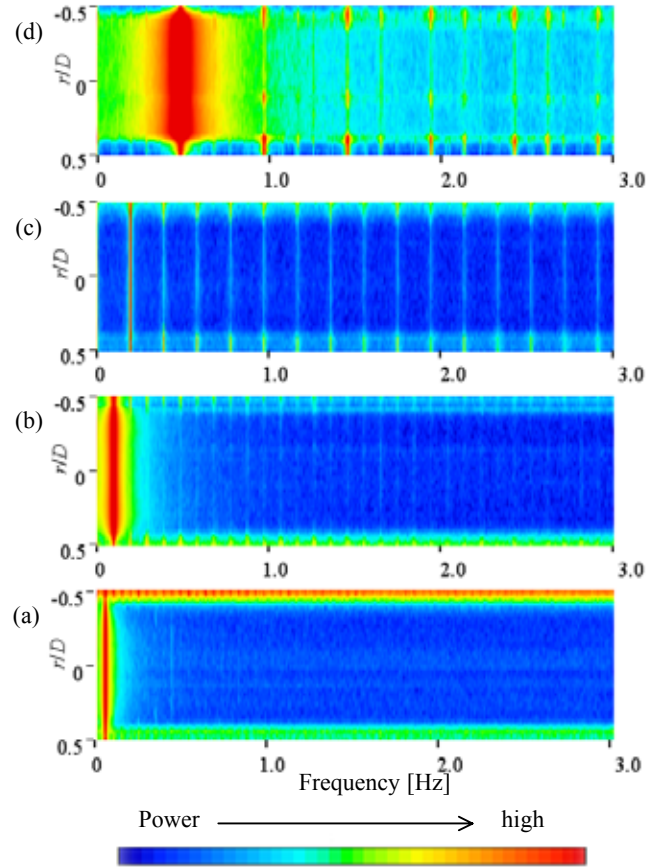

Figure 5. Space dependent power spectrum
(a) R_δ=61.5, λ=4.0 (b) R_δ=87.0, λ=5.7
(c) R_δ=123.0, λ=8.0 (d) R_δ=194.5, λ=12.6

DISCUSSION

Figure 6 shows the spatial distribution of the power of the base frequency at various Reynolds number. The distribution has one broad peak in the inner region of the pipe at R_δ=61.5, λ =4.0 (a). The distribution has two peaks outside of the central region at R_δ=87.0, λ=5.7 (b). We call those peaks Higher Power Area (HPA). Two HPAs appear too at R_δ=123.0, λ =8.0 (c). But the location is closer to the wall and the space between each HPA is wider than (b). The distribution looks like a trapezoid at R_δ=194.5, λ=12.6 (d). For all cases power is lower just next to the wall.

Figure 7 shows the similar spatial distribution of the power of the second harmonic mode. Two HPAs appear near the wall, but their location is closer to the wall than that of the base frequency. The distribution looks almost flat in the inner region for all cases.

The case (a) corresponds to laminar flow according to Hino [4] and Fig.1. The spatial distribution of the base frequency is higher in the inner region. This seems reasonable since oscillation is driven by a sinusoidal motion of the piston and the energy is given to fluid uniformly. On contrary for (c) to (d), Most of the power is distributed near the wall. This indicates that this mode is generated by being caused by a boundary layer. It may be considered that the energy of the basic mode is transferred to this higher harmonic mode inside

this boundary layer, and as a result, the power of the base frequency is much lower than in the inner region.

From this result, flow transition from laminar to turbulent flow might be defined as following. For laminar flow the energy is concentrated only on the basic mode and there is no HPA of the fundamental frequency and are the power of the higher harmonic mode is low. When R_δ and λ are increased, HPA appears with fundamental frequency outside of the central region as well as for the higher harmonic mode. The HPA of harmonic mode appears just next to the wall at (b) and is moving to the central region of the pipe by increasing R_δ. The power itself appears to increase. Consequently, the flow is considered to transit to weekly turbulent flow.

This result also indicates that the boundary layer is given the energy from the basic mode through the higher harmonic mode by nonlinear mechanisms because the power of fundamental mode is lower relative to other region and that of the harmonic frequency is higher near the wall. In other word, the fact that the power of fundamental frequency is higher near the wall when R_δ and λ are increased means the flow in this area is following the motion of the piston more faithfully. It corresponds to see the annular effect. However when R_δ and λ are small, the peak of the power of base frequency is at the center. Annular Effect may not be seen in laminar flow.

CONCLUSION

Spatial and temporal characteristics of the oscillating pipe flow was investigated. From the space dependent power spectra, flow transition might be defined using the appearance of HPA and the behavior of their location. The transition scheme observed seems to support the earlier investigation. It suggests a possible future work on the flow transition based on the energy transfer among various harmonic modes.

REFERENCES

1. Uchida S. The pulsating viscous flow superposed on the steady laminar motion of incompressible fluid in a circular pipe: *Z.Angrew.Math.Phys*. 1956, **7**, 403-422

2. Kerczek CV and Davis SH: Liner stability theory of oscillatory Stokes layers , *J.Fluid Mech*. 1974, **62** (4), 193-207

3. Merkli P and Thomann H: Transition to turbulence in oscillating pipe flow , *J.Fluid Mech*. 1975, **68** (3), 567-575

4. Hino M, Sawamoto M, Takasu S: Experiments on transition to turbulence in an oscillatory pipe flow , *J.Fluid Mech*. 1976, **75** (2), 193-207

5. Elkholy AH. Sinusoidal excitation of viscous fluids in pipes: *Int. J. Pres*. Ves. & Piping 70 1997, 161-165
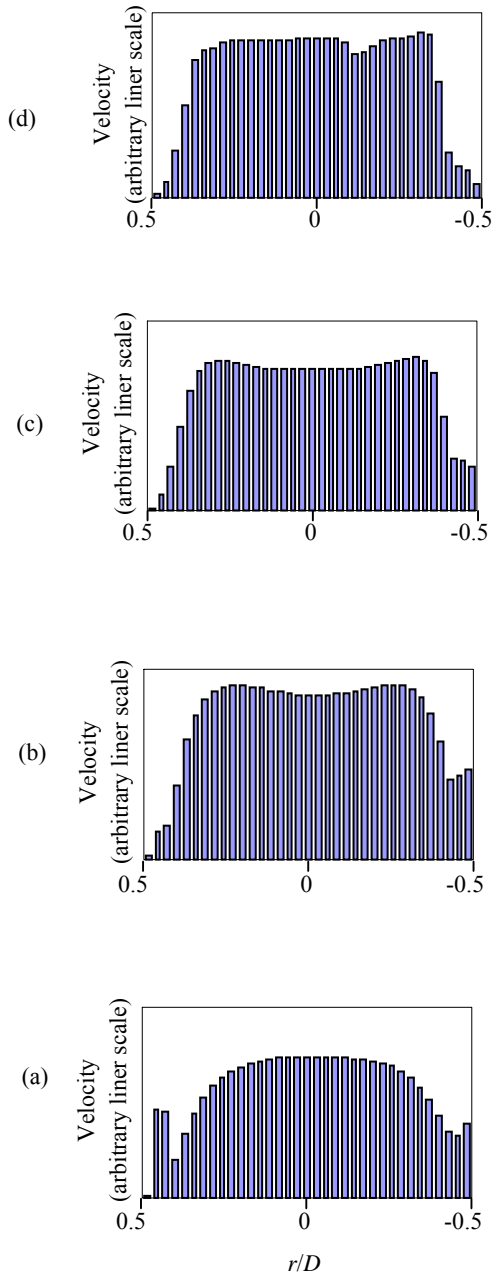
Figure 6. Spatial distribution of the power of base frequency

(a) R_δ=61.5, λ=4.0 (b) R_δ=87.0, λ=5.7
(c) R_δ=123.0, λ=8.0 (d) R_δ=194.5, λ=12.6
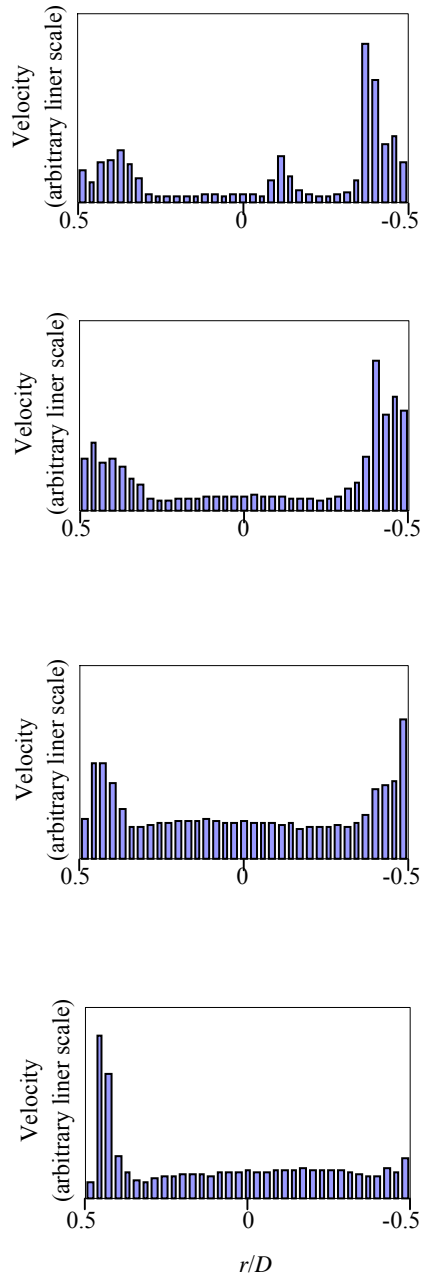
Figure 7. Spatial distribution of the power of second harmonic

(a) R_δ=61.5, λ=4.0 (b) R_δ=87.0, λ=5.7
(c) R_δ=123.0, λ=8.0 (d) R_δ=194.5, λ=12.6